Suraj Jaiswal

COUPLING MULTIBODY DYNAMICS AND HYDRAULIC ACTUATORS FOR INDIRECT KALMAN FILTERING AND REAL-TIME SIMULATION

ACTA UNIVERSITATIS LAPPEENRANTAENSIS 981

Suraj Jaiswal

COUPLING MULTIBODY DYNAMICS AND HYDRAULIC ACTUATORS FOR INDIRECT KALMAN FILTERING AND REAL-TIME SIMULATION

Dissertation for the degree of Doctor of Science (Technology) to be presented with due permission for public examination and criticism in the Auditorium 1316 at Lappeenranta-Lahti University of Technology LUT, Lappeenranta, Finland on the 15th of October 2021, at noon.

Acta Universitatis
Lappeenrantaensis 981

Supervisors Professor Aki Mikkola
LUT School of Energy Systems
Lappeenranta-Lahti University of Technology LUT
Finland

Professor Jussi Sopanen
LUT School of Energy Systems
Lappeenranta-Lahti University of Technology LUT
Finland

Reviewers Assistant Professor Frank Naets
Department of Mechanical Engineering
Katholieke Universiteit Leuven
Belgium

Associate Professor Daniel García Vallejo
Department of Mechanical Engineering and Manufacturing
University of Seville
Spain

Opponents Professor Paulo Flores
Department of Mechanical Engineering
University of Minho
Portugal

Assistant Professor Frank Naets
Department of Mechanical Engineering
Katholieke Universiteit Leuven
Belgium

ISBN 978-952-335-713-6
ISBN 978-952-335-714-3 (PDF)
ISSN-L 1456-4491
ISSN 1456-4491

Lappeenranta-Lahti University of Technology LUT
LUT University Press 2021

Abstract

Suraj Jaiswal
Coupling multibody dynamics and hydraulic actuators for indirect Kalman filtering and real-time simulation
Lappeenranta 2021
70 pages
Acta Universitatis Lappeenrantaensis 981
Diss. Lappeenranta-Lahti University of Technology LUT
ISBN 978-952-335-713-6, ISBN 978-952-335-714-3 (PDF), ISSN-L 1456-4491, ISSN 1456-4491

The computer simulation of complex mechanical systems can be performed using multibody dynamics. Multibody models often include a description of hydraulic actuators, which can introduce numerical stiffness into the models. This numerical stiffness problem can be alleviated by properly selecting either the multibody model or the friction model of a hydraulic cylinder. Furthermore, the actual dynamic state of such models can be inferred using information-fusing techniques such as nonlinear Kalman filters, where information from a physical system can be combined with its multibody model. This synergy can result in advanced simulation-based solutions. Additionally, the real-time capabilities of coupled multibody and hydraulic models can be utilized in product development, user training, and other product processes.

The objective of this study is to couple multibody dynamics and hydraulic actuators for indirect Kalman filtering and real-time simulation in the framework of heavy machinery. In this regard, efficient formulations for the coupled simulation of multibody and hydraulic models are developed here in a monolithic framework. The simulation models are further combined with an indirect Kalman filter to estimate actual dynamic states, thereby, representing a real system. Furthermore, the application of the real-time capabilities for coupled multibody and hydraulic models are demonstrated in the areas of user training and product development. This study incorporates both academic and industrial examples of hydraulically actuated systems. The results demonstrate the accuracy, efficiency, utility, and wide applicability for the developed simulation-based solutions.

Keywords: multibody dynamics, hydraulic actuators, friction models, nonlinear Kalman filters, real-time simulation

Acknowledgements

I would like to express my sincere gratitude to Prof. Aki Mikkola and Prof. Jussi Sopanen for trusting me at the first place with this work. Prof. Mikkola deserves a special mention because he made a difficult topic, such as multibody dynamics, simple and easy to follow. I have always admired his teaching abilities. Prof. Sopanen also deserves a special mention because he has always been proactive in helping me with every work even at a very basic level. His insights on almost every topic are just amazing and mind blowing. I thank both my supervisors for inspiring and helping me in all these years.

I acknowledge the great efforts made by the reviewers of this work, Assoc. Prof. Frank Naets and Asst. Prof. Daniel García Vallejo. The comments made by them have helped me to improve the quality of this work. I also thank in advance the opponents for this dissertation, Prof. Paulo Flores and Assoc. Prof. Frank Naets. I am very grateful that Prof. Flores could be a part of this work because I have always been an admirer for his work on contact modeling and would like to learn it from him someday.

My research visit to the Laboratory of Mechanical Engineering, University of A Coruña, Ferrol, Spain was made possible because of Prof. Javier Cuadrado and Prof. Emilio Sanjurjo. It was my absolute pleasure to have met Prof. Cuadrado in person because his work has always kept me motivated and passionate about multibody dynamics. Prof. Sanjurjo deserves a special mention because he has always helped me to understand Kalman filters. Every discussion I have had with him in the past two years have been enlightening and informative. During my stay at Ferrol, Prof. Francisco González has been an absolute friend, and I extend my special gratitude to thank him and everyone in the laboratory.

Most importantly, I express my gratitude to my mother Mrs. Pushpa Jaiswal, father Mr. Gagan Jaiswal, brother Vinay, sister-in-law Prity, sister Roshni, and nieces Nitya and Yati for their unconditional love and support in all my aspirations in life. It is because of their sacrifices that I was able to move abroad, follow my passion, and finally, achieve a doctoral degree in science. I will always be thankful to my family. Furthermore, I would like to especially acknowledge the immense support of my wife Heena without whom this work was simply not possible. This work literally took her patience, time, support, and even feedbacks. I am very blessed and grateful for your understanding, your never-ending encouragement, and for always being there for me.

At last, this work is my endeavor to contribute to the body of knowledge. This work is carried out in the Department of Mechanical Engineering at Lappeenranta-Lahti University of Technology LUT, Finland, between January 2018 and May 2021.

Suraj Jaiswal
August 2021
Lappeenranta, Finland

This work is dedicated to the only special person of my life...

Contents

List of publications

This article-based dissertation is based on the following peer-reviewed articles that are published in internationally recognized scientific journals. The reprint of each article is included at the end of the dissertation. All the articles are published under open-access publishing agreements. The rights to reprint and include the articles in the dissertation have been granted by the respective publishers in accordance with the publishing agreements.

Publication I

Jaiswal, S., Rahikainen, J., Khadim, Q., Sopanen, J., Mikkola, A.: Comparing double-step and penalty-based semirecursive formulations for hydraulically actuated multibody systems in a monolithic approach. *Multibody System Dynamics*, 52(2), 169–191 (2021)

Publication II

Jaiswal, S., Sopanen, J., Mikkola, A.: Efficiency comparison of various friction models of a hydraulic cylinder in the framework of multibody system dynamics. *Nonlinear Dynamics*, 104(4), 3497–3515 (2021)

Publication III (Submitted)

Jaiswal, S., Sanjurjo, E., Cuadrado, J., Sopanen, J., Mikkola, A.: State estimator based on an indirect Kalman filter for a hydraulically actuated multibody system. *Multibody System Dynamics*, (December 10, 2020)

Publication IV

Jaiswal, S., Åman, R., Sopanen, J., Mikkola, A.: Real-time multibody model-based heads-up display unit of a tractor. *IEEE Access*, 9, 57645–57657 (2021)

Publication V

Jaiswal, S., Korkealaakso, P., Åman, R., Sopanen, J., Mikkola, A.: Deformable terrain model for the real-time multibody simulation of a tractor with a hydraulically driven front-loader. *IEEE Access*, 7, 172694–172708 (2019)

Publication VI

Jaiswal, S., Islam, M., Hannola, L., Sopanen, J., Mikkola, A.: Gamification procedure based on real-time multibody simulation. *International Review on Modelling and Simulations*, 11(5), 259–266 (2018)

Author's contribution

Mr. Suraj Jaiswal is the principal author, investigator, and corresponding author in all the articles. All the articles and this dissertation are written under the supervision of Prof. Aki Mikkola and Prof. Jussi Sopanen from LUT University, Finland. It should be noted that Publication III was carried out under the guided supervision of Prof. Emilio Sanjurjo and Prof. Javier Cuadrado from University of A Coruña, Spain.

In *Publication I*, the topic of the paper was decided jointly by Prof. Mikkola and Prof. Sopanen. The methods, implementations, and results and analysis were proposed and carried out by Mr. Jaiswal. In writing, the introduction was written by Dr. Jarkko Rahikainen while the rest of the paper was written by Mr. Jaiswal. The guidance and assistance for the paper were provided by Dr. Rahikainen, Prof. Sopanen, and Prof. Mikkola.

In *Publication II*, the topic of the self-motivated paper was decided by Mr. Jaiswal. The methods, implementations, results and analysis, and the entire paper writing process were proposed and carried out by Mr. Jaiswal. The assistance for the paper was provided by Prof. Sopanen and Prof. Mikkola.

In *Publication III*, the topic of the paper was decided as a joint effort between Mr. Jaiswal and Prof. Sanjurjo. The method was proposed jointly by Mr. Jaiswal and Prof. Sanjurjo, whereas the implementations and results and analysis were carried out by Mr. Jaiswal. The entire paper was written by Mr. Jaiswal. The guidance and assistance for the paper were provided by Prof. Sanjurjo, Prof. Cuadrado, Prof. Sopanen, and Prof. Mikkola.

In *Publication IV*, the topic of the self-motivated paper was decided by Mr. Jaiswal. The methods, implementations, results and analysis, and the entire paper writing process were proposed and carried out by Mr. Jaiswal. It should be noted that a third party multibody simulation software was used in the process. The assistance for the paper was provided by Prof. Sopanen and Prof. Mikkola.

In *Publication V*, the topic of the paper was decided jointly by Prof. Mikkola and Prof. Sopanen. The deformable terrain model was proposed and implemented by Dr. Pasi Korkealaakso while the tractor model was implemented by Mr. Jaiswal. Dr. Åman provided modeling details of the tractor model. The results and analysis and the entire writing process were carried out by Mr. Jaiswal. The guidance and assistance for the paper were provided by Prof. Sopanen and Prof. Mikkola.

In *Publication VI*, the topic of the paper was decided jointly by Prof. Lea Hannola and Prof. Mikkola. The gamification methodology was proposed by Mr. Md Iftekharul Islam while its implementation on an excavator model and the results and analysis was carried out by Mr. Jaiswal. It should be noted that a third party multibody simulation software was used. The entire paper was written by Mr. Jaiswal. The guidance and assistance for the paper were provided by Prof. Hannola, Prof. Sopanen, and Prof. Mikkola.

Supplementary studies

The ideas from some of the publications above are presented or accepted in international conferences as extended abstracts and presentations. In addition, a book chapter is published based on the idea of a related topic. The list of supplementary studies includes

- Jaiswal, S., Islam, M., Hannola, L., Sopanen, J., Mikkola, A.: Real-time multibody simulation based gamification procedure for product processes. In *The 9th Asian Conference on Multibody Dynamics (ACMD)*, Xi'an, China, August 19–23, 2018
- Jaiswal, S., Sopanen, J., Mikkola, A.: A study of different friction force models of a hydraulic actuator in a combined multibody and hydraulic model. In *International Symposium on Co-Simulation and Solver Coupling in Dynamics (COSIM)*, Online event, May 24–25, 2021
- Jaiswal, S., Tarkiainen, A., Choudhury, T., Sopanen, J., Mikkola, A.: Gamification and the marketing of agricultural machinery. In *Real-time Simulation for Sustainable Production: Enhancing User Experience and Creating Business Value*, Routledge (2021)
- Jaiswal, S., Sopanen, J., Mikkola, A.: Modeling heads-up display unit of a tractor using a real-time multibody model. In *International Conference on Machine Design (MD)*, Porto, Portugal, September 9–10, 2021
- Jaiswal, S., Rahikainen, J., Khadim, Q., Sopanen, J., Mikkola, A.: Comparing semi-recursive multibody formulations for hydraulically driven mechanisms. In *ECCOMAS Thematic Conference on Multibody Dynamics*, Budapest, Hungary, December 12–15, 2021
- Jaiswal, S., Åman, R., Sopanen, J., Mikkola, A.: Heads-up display based on the real-time multibody simulation of a tractor. In *The 6th Joint International Conference on Multibody System Dynamics and The 10th Asian Conference on Multibody System Dynamics (IMSD–ACMD)*, New Delhi, India, October 16–20, 2022
- Mohammadi M., Khadim Q., Jaiswal, S., Mikkola, A.: Environment modeling using photogrammetry for the real-time multibody simulation of a vehicle. In *The 6th Joint International Conference on Multibody System Dynamics and The 10th Asian Conference on Multibody System Dynamics (IMSD–ACMD)*, New Delhi, India, October 16–20, 2022

Nomenclature

Latin symbols

$\sim$	Tilde representing the skew-symmetric matrix of a vector
$*$	Asterisk representing the virtual velocities
$\hat{}$	Hat representing the estimated value
$^{\mathrm{T}}$	Transpose operation
$\mathbf{0}$	Zero matrix
A, B, P, T	Port
A_1, A_2	Area of a cylinder chamber
A_t	Area of a throttle valve
$\mathbf{A}$	Rotation matrix
$\mathbf{b}$, $\mathbf{d}$	Joint type dependent vector
B_{e_s}	Effective bulk modulus
B_k	Bulk modulus of a hydraulic sub-volume V_k
B_{oil}	Bulk modulus of oil
$\mathbf{B}$	Transformation matrix
C_d	Flow discharge coefficient of a throttle valve
C_{v_d}	Semi-empirical flow rate constant of a directional control valve
C_{v_t}	Semi-empirical flow rate coefficient of a throttle valve
$\bar{\mathbf{C}}$	Matrix containing damping contributions in the system
$f(\cdot)$	Viscous friction function
f_j	Relative joint degrees of freedom between body j and the base
$\acute{f}(\cdot)$	Nonlinear function
$\mathbf{f}$	Vector of external forces
$\mathbf{f_x}$	Jacobian matrix of the state transition model
$\acute{\mathbf{f}}(\cdot)$	Function of nonlinear equations
$\bar{\mathbf{f}}(\cdot)$	State transition model
F, G, N, Q	Point
F_c	Coulomb friction
F_{cyl}	Force produced by a hydraulic cylinder
F_s	Static friction
F_μ	Total friction force caused by sealing
$\mathbf{F}_n$	Normal contact force vector
$\mathbf{F}_\mu$	Total friction force vector
$g(\cdot)$	Function describing the Stribeck effect
$\mathbf{g}$	Position vector of the center of mass
$\dot{\mathbf{g}}$	Velocity vector of the center of mass
$\ddot{\mathbf{g}}$	Acceleration vector of the center of mass
h	Iteration step
$\mathbf{h}(\cdot)$	Measurement model
$\mathbf{h_x}$	Jacobian matrix of the measurement model

$\bar{\mathbf{h}}$	Lubricant film thickness vector
$\bar{\mathbf{h}}_{ss}$	Lubricant film thickness steady-state vector
$\dot{\bar{\mathbf{h}}}$	Time derivative of the lubricant film thickness
$\mathbf{I}$	Identity matrix
j	A body
$\mathbf{J}$	Inertia tensor in the inertial reference frame
$\bar{\mathbf{J}}$	Inertia tensor in the body reference frame
k	Time-step
K_f	Proportional constant
$\bar{\mathbf{K}}$	Matrix containing stiffness contributions in the system
$\mathbf{K}$	Kalman gain matrix
l, l_2, l_3	Length
m	Mass of a body
$\mathbf{M}$, $\bar{\mathbf{M}}$, $\mathbf{M}^\Sigma$, $\bar{\mathbf{M}}^\Sigma$, $\overline{\bar{\mathbf{M}}^\Sigma}$, $\overline{\mathbf{M}^\Sigma}$	Mass matrix
n	Exponent for the Stribeck curve
n_c	Total number of hydraulic sub-volumes
n_f	Total number of volume flow rates
n_j	Number of joints in the path from body j to the base
n_p	Number of hydraulic pressures
$\mathbf{n}$	Unit vector in the direction of the revolute axis
N_b	Number of bodies
N_f	Degrees of freedom of a closed-loop system
N_m	Number of loop-closure constraint equations
$\mathbf{o}$	Actual measurement vector
p_P	Pump pressure
p_s, p_1, p_2	Hydraulic pressure
p_T	Tank pressure
$\dot{p}_s$	Pressure build-up
$\mathbf{p}$	Vector of hydraulic pressures
$\dot{\mathbf{p}}$	Vector of pressure build-ups
$\mathbf{P}^-$	Covariance matrix of the predicted state mean
$\mathbf{P}^+$	Covariance matrix of the corrected state mean
$\mathbf{q}$	Average bristle deflection vector
$\dot{\mathbf{q}}$	Time derivative of the average bristle deflection vector
Q_d	Volume flow rate through a directional control valve
Q_{s_1}, Q_{in}	Incoming volume flow rate
Q_{s_2}, Q_{s_3}, Q_{out}	Outgoing volume flow rate
Q_{s_k}, Q_{d1}, Q_{3d}	Volume flow rate
Q_t	Volume flow rate through a simple throttle valve
$\mathbf{Q}$, $\bar{\mathbf{Q}}$, $\mathbf{Q}^\Sigma$, $\bar{\mathbf{Q}}^\Sigma$, $\overline{\bar{\mathbf{Q}}^\Sigma}$, $\overline{\mathbf{Q}^\Sigma}$	External force vector
$\mathbf{r}$	Position vector of the revolute joint in the inertial reference frame

$\mathbb{R}$	Real numbers
$\bar{\mathbf{R}}$, $\mathbf{R}$, $\mathbf{R_z}$	Velocity transformation matrix
$\mathbf{R}_\mathrm{d}$	Diagonal matrix containing vectors $\mathbf{b}_j$
$\mathbf{R}_j^{rev}$	Sub-matrix of the velocity transformation matrix for a revolute joint
$\dot{\bar{\mathbf{R}}}\dot{\mathbf{z}}$	Vector containing vectors $\mathbf{d}_j$
sgn $(\cdot)$	Signum function
$\mathbf{s}$	Actuator length vector
$\dot{\mathbf{s}}$	Velocity of a reference point
$\ddot{\mathbf{s}}$	Acceleration of a reference point
$\mathbf{S}$	Covariance matrix of the innovation
t	Time
$\mathbf{T}$	Path matrix
$\mathbf{u}_0$	Vector of pressure variation equations
$\mathbf{u}_1$, $\mathbf{u}_2$	Vector of average bristle deflection variation equations
$\mathbf{u}_3$	Vector of lubricant film thickness variation equations
U	Relative spool position
U_{ref}	Reference voltage signal for a reference spool position
$\dot{U}$	Time derivative of the relative spool position
v_s	Stribeck velocity
v_t	Relative tangential velocity
$\mathbf{v}_b$	Threshold velocity vector
$\mathbf{v}_t$	Relative tangential velocity vector
V_k	Hydraulic sub-volume forming a control volume V_s
V_s	Hydraulic control volume
$\mathbf{W}$	Matrix used in augmented Lagrangian method with projections
x	Actuator length
$\dot{x}$	Piston velocity
$\bar{x}_0$	Point of derivative approximation
$\mathbf{x}$	State vector
$\bar{\mathbf{x}}$	Vector of primary variables in simulation model
$\hat{\mathbf{x}}^-$	Predicted state mean, also called ‘a priori’ state estimation
$\hat{\mathbf{x}}^+$	Corrected state mean, also called ‘a posteriori’ state estimation
$\mathbf{y}$	Innovation vector
$\mathbf{Y}$, $\mathbf{Z}$	Vector of Cartesian velocities
$\dot{\mathbf{Y}}$, $\dot{\mathbf{Z}}$	Vector of Cartesian accelerations
z	Relative joint coordinate
$\mathbf{z}$	Vector of relative joint coordinates
$\mathbf{z}^\mathrm{d}$	Vector of dependent relative joint coordinates
$\mathbf{z}^\mathrm{i}$	Vector of independent relative joint coordinates
$\dot{z}$	Relative joint velocity
$\dot{\mathbf{z}}$, $\dot{\mathbf{z}}'$	Vector of relative joint velocities
$\dot{\mathbf{z}}^\mathrm{d}$	Vector of dependent relative joint velocities
$\dot{\mathbf{z}}^\mathrm{i}$	Vector of independent relative joint velocities

$\ddot{z}$	Relative joint acceleration
$\ddot{\mathbf{z}}$, $\ddot{\mathbf{z}}^{'}$	Vector of relative joint accelerations
$\ddot{\mathbf{z}}^{\mathrm{i}}$	Vector of independent relative joint accelerations

Greek alphabets

α	Penalty factor
$\boldsymbol{\alpha}$	Diagonal matrix containing values of penalty factors
Δp	Pressure difference
$\Delta\mathbf{p}$	Errors in hydraulic pressures
$\Delta\dot{\mathbf{p}}$	Errors in hydraulic pressure build-ups
Δt	Time-step size
$\Delta\bar{\mathbf{x}}$	Difference in the vector of primary variables
$\Delta\mathbf{z}$	Errors in relative joint coordinates
$\Delta\mathbf{z}^{\mathrm{d}}$	Errors in dependent relative joint coordinates
$\Delta\mathbf{z}^{\mathrm{i}}$	Errors in independent relative joint coordinates
$\Delta\dot{\mathbf{z}}^{\mathrm{i}}$	Errors in independent relative joint velocities
$\Delta\ddot{\mathbf{z}}^{\mathrm{i}}$	Errors in independent relative joint accelerations
ϵ	Differentiation increment
$\boldsymbol{\lambda}$	Vector of Lagrange multipliers
μ_c	Coefficient of Coulomb friction
μ_s	Coefficient of static friction
$\boldsymbol{\mu}$	Diagonal matrix containing values of damping ratios
ξ	Parameter for curve shape
ρ	Oil density
σ_0	Stiffness of elastic bristles
σ_1	Damping of elastic bristles
σ_2	Coefficient of viscous friction
$\sigma_{\mathbf{p}}^{'}$	Standard deviation of the measurement noise at pressure levels
$\sigma_{\mathbf{z}}^{'}$	Standard deviation of the measurement noise at position levels
$\sigma_{\mathbf{p},D}^{2}$	Variance at the pressure level
$\sigma_{\ddot{\mathbf{z}}}^{2}$	Variance at the acceleration level
$\sum^{P}$	Covariance matrix of plant noise
$\sum^{S}$	Covariance matrix of measurement noise
$\tau,\ \tau_h,\ \tau_{h0},\ \tau_{hn},$ τ_{hp}	Time constant
$\boldsymbol{\tau}$	Vector of external moments with respect to the center of mass
$\boldsymbol{\Phi}$	Loop-closure constraint equations
$\boldsymbol{\Phi}_{\mathbf{z}}$	Jacobian matrix of constraint equations
$\boldsymbol{\Phi}_{\mathbf{z}}^{\mathrm{d}}$	Dependent columns of the Jacobian matrix $\boldsymbol{\Phi}_{\mathbf{z}}$
$\boldsymbol{\Phi}_{\mathbf{z}}^{\mathrm{i}}$	Independent columns of the Jacobian matrix $\boldsymbol{\Phi}_{\mathbf{z}}$
$\dot{\boldsymbol{\Phi}}$	First order time derivatives of constraint equations
$\dot{\boldsymbol{\Phi}}_{\mathbf{z}}$	Derivative of $\boldsymbol{\Phi}_{\mathbf{z}}$ with respect to time

$\ddot{\mathbf{\Phi}}$	Second order time derivatives of constraint equations
$\boldsymbol{\omega}$	Angular velocity
$\dot{\boldsymbol{\omega}}$	Angular acceleration
$\mathbf{\Omega}$	Diagonal matrix containing values of natural frequencies

Abbreviation

HUD	Heads-up display

1 Introduction

The computer simulation of complex mechanical systems, such as heavy machinery, can be performed using multibody dynamics. In this approach, the equations of motion are often coupled with models of other physical nature such as hydraulic actuators. Modern multibody methods have explored the real-time capability of such coupled multibody models. Even though such coupled models can accurately describe reality, it is impossible to achieve a perfect model because of unknown forces or uncertain parameters that may affect the dynamics. Nevertheless, actual dynamic states can be inferred using information-fusing techniques such as nonlinear Kalman filters, where information from a physical system is combined with its multibody model. This approach can be utilized in predicting maintenance needs and optimizing machine performances as shown in Fig. 1.1.

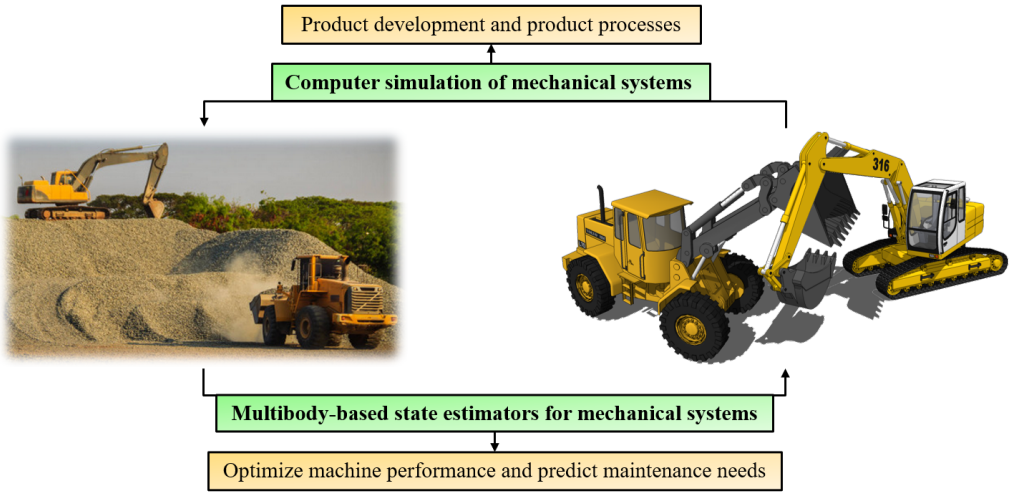

Figure 1.1: Conceptual overview of this study.

1.1 Research motivation

The heavy machinery industry in Finland is a technology leader enjoying global demand. Companies such as Valtra, Sandvik, Rocla, and Konecranes are continuously developing autonomous solutions for the construction, mining, and container handling industries. Digitalization, followed by the expansion of autonomous solutions, is becoming crucial as it can affect almost everything from operational activities to the design and features of products and services. At present, the heavy machinery industry is undergoing a major transformation such that the physical and virtual worlds are becoming more interdependent and interconnected. This synergy can result in advanced simulation-based solutions that can change both products and related services. It can find its application in product development, user training, emerging digital twins, and artificial intelligence.

1.2 State of the art

In simulating heavy machinery, multibody dynamics often includes models of another physical nature, such as hydraulic actuators. The modeling of hydraulic actuators often introduces numerical stiffness into the models. The friction model of a hydraulic cylinder can add more numerical stiffness [46]. This problem is a significant aspect to consider in modeling because it can lead to poor numerical efficiency, especially, in real-time applications. Furthermore, such coupled multibody models can be combined with nonlinear Kalman filters in designing state estimators. In the subsequent subsections, a brief literature review on multibody dynamics, hydraulic actuators, friction force models, and multibody-based state estimators are provided.

1.2.1 Multibody dynamics

A multibody system can be described as an assembly of bodies that are usually connected using idealized kinematic joints allowing a possible relative movement [41]. In many cases, the bodies are not in direct contact, but are rather connected by some possible force elements such as actuators, springs, and dampers [31]. Multibody systems can be classified as open-loop and closed-loop systems. A closed-loop system can be expressed as an open-loop system by introducing a temporary cut-joint to open the loop. Later, this cut-joint is incorporated into the dynamics of the system in the form of constraints. The scope of this study is limited to the dynamics of rigid bodies only and this limits the applicability of the used methods in this study for certain applications.

In multibody dynamics, simulation methods can be categorized into two main groups according to the selected coordinates [41]. Firstly, the multibody methods that are based on global coordinates, where the absolute positions, velocities, and accelerations of each body are used. Secondly, the multibody methods that utilize relative coordinates. For real-time applications, the use of relative coordinates is often considered, because it can lead to a computationally efficient approach. However, the selection of a method is case-dependent as demonstrated in [32]. Moreover, computational efficiency can be significantly affected by many factors such as implementation details [33], the use of automated differentiation tools [18], and the use of sparse and parallelization techniques [37]. However, the scope of this study is limited to the use of relative coordinates because it can be suitable for real-time applications [51, 52].

Within the methods based on relative coordinates, the semi-recursive multibody formulation is often used in the literature [8, 55]. In a semi-recursive formulation, the equations of motion are described using the dynamics of an open-loop system incorporated with the loop-closure constraints. The dynamics of an open-loop system can be described using the principle of virtual work. Whereas loop-closure constraints can be incorporated in many different ways [30, 41]. In this study, the augmented Lagrangian method with projections [10], the coordinate partitioning method [60], and the penalty method [41] will be employed. Semi-recursive formulations have been successfully used in many practical applications such as in real-time vehicle simulations [52, 59].

1.2.2 Hydraulic actuators

Hydraulic actuators are highly nonlinear systems that have gained considerable recognition in multibody dynamics for applications such as heavy machinery [49, 57]. Pressures in a hydraulic circuit can be modeled using the lumped fluid theory [71], where a hydraulic circuit is assumed to be divided into discrete volumes with equally distributed pressures. In this approach, hydraulic pressures can be integrated using differential equations, where effective bulk moduli are divided by small volumes. This type of description can introduce numerical stiffness into the multibody equations of motion [56]. Moreover, the friction models of hydraulic actuators can introduce additional numerical stiffness [46]. Consequently, the time integration of coupled multibody models may become cumbersome, especially, in real-time applications [8, 58].

1.2.3 Friction force models

Friction force models can be categorized into two main groups as static and dynamic models [45, 54]. Static friction models describe only the steady-state relation between the friction force and the relative velocity [7]. The exponential Stribeck friction model [15] is popular. However, it can lead to numerical problems because of the discontinuity of friction at zero relative velocity. To overcome this numerical problem, many alternative continuous friction models have been developed [2, 12, 17]. For example, Bengisu–Akay friction model [12] utilized two separate equations for the adhesion regime and Stribeck effect. The Brown–McPhee model [17], proposed a continuous velocity-based friction model suitable for computationally challenging applications.

Dynamic friction models evaluate friction forces based on the actual state of contact and the contact history [7, 46] using extra state variables, such as average bristle deflection, and relative velocity. Unlike most static models, dynamic friction models consider frictional phenomena such as pre-slip displacement [13] and frictional lag. They eliminate the discontinuity at zero relative velocity. Based on the Dahl friction model [26], a number of friction models have been proposed, such as the reset integrator model [35], LuGre model [28], Leuven model [66], and generalized Maxwell slip model [1, 43]. Subsequently, a modified LuGre friction model [72] was developed to incorporate the lubricant film dynamics using a first-order lag element in which the time-constant is varied between the deceleration, acceleration, and dwell periods.

In the literature, several studies have been carried out that utilize different seal friction models for simulation of hydraulic actuators. For example, the exponential Stribeck friction model [15] was used in [69, 70] and the stick-slip friction model [3, 4] in [47]. Furthermore, the dynamic friction behavior of hydraulic actuators was studied using the LuGre friction model in [50, 69], and a modified LuGre friction model [72] in [68, 69]. It was found in [72] that compared with the LuGre friction model, the modified LuGre friction model [72] can simulate the real friction characteristics of a hydraulic actuator with a higher accuracy. Furthermore, the study in [73] combined a pressure-dependent function with the LuGre friction model to study multibody simulation of a hydraulic actuator.

1.2.4 Multibody-based state estimators

Various studies on multibody-based state estimators have been carried out in the last decade. In this regard, a number of estimating techniques have been used in the literature [14, 22], such as Kalman filters [34, 64] and particle filters [5, 20]. Applying Kalman filters to multibody models is not trivial because of their different mathematical structures. The Kalman filter was originally formulated for first order, linear, and unconstrained systems [42]. Whereas in general, multibody models are second order, nonlinear, and constrained systems [41]. Therefore, it is an open field of research for multibody models, especially, in the framework of hydraulic actuators.

The methods within the family of nonlinear Kalman filters can be categorized into two groups as independent- and dependent-coordinate methods [64]. In independent-coordinate methods, the state vector of a filter contains only independent elements, which is the case with most probabilistic estimators in estimation and control theory [34]. In their application to multibody dynamics, the independent positions and velocities of a multibody model are the state vector of a filter [67]. Dependent-coordinate methods [27, 65] can handle intra-state vector dependencies, as found in the case of multibody models. In their application to multibody models, either the constraints are incorporated as perfect measurements, or unconstrained estimation is projected over the constraints manifold [64]. The scope of this study is limited to independent-coordinate methods because of using relative coordinates in multibody models.

Among the methods in independent coordinates, multibody model-based state estimators were pioneered in [22] and [25]. Here, the structure of multibody equations was adapted to fit into an extended Kalman filter in continuous-time frames such that, the state-transition and state-update stages are seamlessly fused together. Estimators that work in discrete-time frames; such as in the discrete extended Kalman filter [67], unscented Kalman filter [53], and indirect Kalman filters [62]; consider these stages as two separate steps. In these filters, the state-transition stage relies on the plant transition model, whereas the state-update stage includes information from the actual measurements [67]. Compared with the above-mentioned filters, an indirect Kalman filter provides a computationally efficient approach, which is unaffected by an increased system size [63].

An indirect Kalman filter considers error states instead of the conventional full states, and therefore, it is also referred to as an error-state extended Kalman filter. In the framework of multibody dynamics, three indirect Kalman filters were developed in [62], where the first and second variants incorporate a simplified and an exact form of the plant transition model, respectively. In the third variant, the second variant was extended to incorporate input force estimations such that it outperformed all other previous approaches, especially, for planar mechanisms. The input force estimation approach has even found its application in an automobile application [59, 61]. It should be noted that the above indirect Kalman filters were independent of integrators used in the multibody simulation models.

1.3 Objective and scope

The objective of this study is to couple multibody dynamic models and hydraulic actuator models for indirect Kalman filtering and real-time simulation in the framework of heavy machinery. The objective is subdivided into three categories. The first category focuses on investigating efficient formulations for the coupled simulation of multibody and hydraulic models in monolithic frameworks. The second category focuses on combining the simulation model developed above with the measurements from physical systems using an indirect Kalman filter. Academic examples are illustrated in the first two categories, such as a four-bar mechanism, which is very common in hydraulically driven systems. The third category focuses on exploring the use of real-time capabilities of detailed multibody models in user training and product development. Industrial examples such as a tractor and an excavator are illustrated in the third category.

1.4 Scientific contributions

A total of six peer-reviewed journal articles are included in this dissertation. Based on the objective, the scientific contributions of this dissertation are grouped into three categories. The first category focuses on efficient formulations for the monolithically coupled simulation of multibody and hydraulic models in the framework of hydraulically actuated systems. In this regard, **Publication I** introduced and compared two semi-recursive multibody formulations that are coupled with the hydraulic actuators model. **Publication II** introduced and compared various friction models of a hydraulic cylinder in the coupled simulation of multibody and hydraulic models. The above two publications demonstrated that the proper selection of either the multibody formulations or the friction models can improve numerical efficiency.

The second category focuses on combining simulation models with physical systems for hydraulically driven systems using an indirect Kalman filter. In this regard, **Publication III** developed a state estimator by combining a coupled multibody and hydraulic model with an error-state extended Kalman filter. The state estimator considered modeling errors in the force and pressure models because of their uncertainty in modeling. The measurements are obtained from a simulation model, which provides the ground truth, with an addition of white Gaussian noise to represent the noise properties of real sensors. It should be noted that measurements are not performed on a real system and they are numerical as stated earlier. The estimator utilized four sensor configurations at different sampling rates. The proposed state estimator was shown to accurately estimate the work cycle of the illustrated case study.

The third category focuses on utilizing the real-time capabilities of detailed multibody models in user training and product development. In this regard, **Publication IV** introduced a detailed real-time multibody model-based heads-up display (HUD) unit of a tractor. The HUD unit proved to be effective in moving an amount of sand from one place to another. Furthermore, **Publication V** introduced a real-time capable deformable terrain

model that can interact with the dynamics of the tractor model. The simulated hydraulic actuator forces agreed with the static forces computed analytically. **Publication VI** introduced a gamification procedure to possibly identify the design need of an excavator in the framework of real-time multibody simulation. This approach is a possible source of information for product development.

1.5 Dissertation outline

This dissertation contains five sections. The structure for the rest of the dissertation is organized as follows:

- Section 2 describes multibody formulations, hydraulic actuators modeling, friction models, and the coupling of multibody and hydraulic models.
- Section 3 describes a state estimator based on an indirect Kalman filter for hydraulically actuated mechanical systems.
- Section 4 illustrates a summary of the research findings using academic and industrial examples.
- Section 5 provides a conclusion, and it highlights possibilities for future work.

2 Multibody modeling

The dynamics of a constrained mechanical system can be modeled using semi-recursive multibody formulations. Multibody models often include a description of hydraulic actuators, which can introduce numerical stiffness into the models. In this study, hydraulic actuators are modeled using the lumped fluid theory [71], whereas friction in a hydraulic cylinder is described using both static and dynamic friction models. In this study, the mass of a hydraulic cylinder is assumed to be negligible because it is not considered as a separate body. Instead, the internal dynamics of hydraulic actuators are computed, and the resultant force is fed into the multibody equations of motion in a monolithic approach. It should be noted that, only a fixed step-size integrator is considered in this study, because the scope of this study covers real-time simulation.

2.1 Semi-recursive multibody formulations

In semi-recursive formulations, the dynamics of a closed-loop system is formulated by incorporating loop-closure constraints in the dynamics of an open-loop system. A closed-loop system is converted into an open-loop by a temporary cutting of certain joints as shown in Fig. 2.1. Open-loop dynamics are formulated in Cartesian coordinates first and then switched to relative joint coordinates using a velocity transformation matrix. The reference point used to define the Cartesian velocities and accelerations of each body can be the center of mass of the body; a point on the moving body that instantaneously coincides with the origin of the inertial reference frame; or the origin of the reference frame attached to the moving body. Furthermore, the loop-closure constraints can be incorporated using the augmented Lagrangian method with projections, the coordinate partitioning method, or the penalty method.

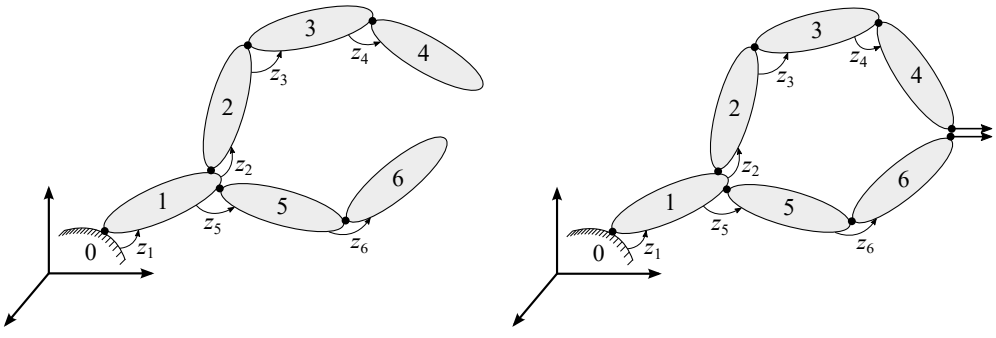

Figure 2.1: Illustration of a multibody system. (a) An open-loop system. (b) A closed-loop system.

2.1.1 Multibody kinematics

Consider an open-loop system of N_b rigid bodies with any number of branches, that is, a tree-structure mechanism as shown in Fig. 2.1a. The kinematics of the open-loop system can be expressed recursively, either from the base to the leaves as in this study or from leaves to the base, by applying the classical kinematic relations [24, 41]. The Cartesian velocities, $\mathbf{Z}_j$, and the Cartesian accelerations, $\dot{\mathbf{Z}}_j$, of a reference point on a body j can be defined as

$$\mathbf{Z}_j = \begin{bmatrix} \dot{\mathbf{s}}_j \\ \boldsymbol{\omega}_j \end{bmatrix}, \quad \dot{\mathbf{Z}}_j = \begin{bmatrix} \ddot{\mathbf{s}}_j \\ \dot{\boldsymbol{\omega}}_j \end{bmatrix}, \tag{2.1}$$

where $\dot{\mathbf{s}}_j$ and $\ddot{\mathbf{s}}_j$ are the respective velocity and acceleration of the reference point on body j that instantaneously coincides with the origin of the inertial reference frame, and $\boldsymbol{\omega}_j$ and $\dot{\boldsymbol{\omega}}_j$ are the angular velocity and angular acceleration of body j, respectively. Furthermore, the Cartesian velocities, $\mathbf{Y}_j$, and the Cartesian accelerations, $\dot{\mathbf{Y}}_j$, of the center of mass of body j can be written in terms of $\mathbf{Z}_j$ and $\dot{\mathbf{Z}}_j$ as [40]

$$\mathbf{Y}_j = \begin{bmatrix} \dot{\mathbf{g}}_j \\ \boldsymbol{\omega}_j \end{bmatrix} = \begin{bmatrix} \mathbf{I}_3 & -\widetilde{\mathbf{g}}_j \\ \mathbf{0} & \mathbf{I}_3 \end{bmatrix} \begin{bmatrix} \dot{\mathbf{s}}_j \\ \boldsymbol{\omega}_j \end{bmatrix}, \tag{2.2}$$

$$\dot{\mathbf{Y}}_j = \begin{bmatrix} \ddot{\mathbf{g}}_j \\ \dot{\boldsymbol{\omega}}_j \end{bmatrix} = \begin{bmatrix} \mathbf{I}_3 & -\widetilde{\mathbf{g}}_j \\ \mathbf{0} & \mathbf{I}_3 \end{bmatrix} \begin{bmatrix} \ddot{\mathbf{s}}_j \\ \dot{\boldsymbol{\omega}}_j \end{bmatrix} + \begin{bmatrix} \widetilde{\boldsymbol{\omega}}_j \widetilde{\boldsymbol{\omega}}_j \mathbf{g}_j \\ \mathbf{0} \end{bmatrix}, \tag{2.3}$$

where $\mathbf{g}_j$, $\dot{\mathbf{g}}_j$, and $\ddot{\mathbf{g}}_j$ are the position, velocity, and acceleration of the center of mass of body j in the inertial reference frame, respectively, a tilde ($\sim$) represents the skew-symmetric matrix of a vector, and $\mathbf{I}$ is an identity matrix.

For the open-loop system, the Cartesian velocities $\mathbf{Z}_j$ and the Cartesian accelerations $\dot{\mathbf{Z}}_j$ can be expressed recursively in terms of the reference points of the previous bodies as [40]

$$\mathbf{Z}_j = \mathbf{Z}_{j-1} + \mathbf{b}_j \dot{z}_j, \tag{2.4}$$

$$\dot{\mathbf{Z}}_j = \dot{\mathbf{Z}}_{j-1} + \mathbf{b}_j \ddot{z}_j + \mathbf{d}_j, \tag{2.5}$$

where the scalars z_j, $\dot{z}_j$, and $\ddot{z}_j$ are the relative joint coordinate, velocity, and acceleration of the joint between bodies $j-1$ and j, respectively, whereas $\mathbf{b}_j$ and $\mathbf{d}_j = \dot{\mathbf{b}}_j \dot{z}_j$ are the vectors depending on the type of joint [24] between bodies $j-1$ and j. It should be noted that the indexes $j-1$ and j may not be successive because the system may branch. It is assumed here that only revolute and prismatic joints are considered because other joints can be expressed as a combination of these joints using massless intermediate bodies. If the center of mass is considered as the reference point, the Cartesian velocities $\mathbf{Y}_j$ and the Cartesian accelerations $\dot{\mathbf{Y}}_j$ can be expressed recursively using an additional transformation matrix $\mathbf{B}_j$ as [40]

$$\mathbf{Y}_j = \mathbf{B}_j \mathbf{Y}_{j-1} + \mathbf{b}_j \dot{z}_j, \tag{2.6}$$

$$\dot{\mathbf{Y}}_j = \mathbf{B}_j \dot{\mathbf{Y}}_{j-1} + \mathbf{b}_j \ddot{z}_j + \mathbf{d}_j. \tag{2.7}$$

The Cartesian velocities $\mathbf{Z}_j$ can be mapped onto a set of relative joint velocities using a velocity transformation matrix $\bar{\mathbf{R}} \in \mathbb{R}^{6N_b \times N_b}$ as [24, 40]

$$\mathbf{Z} = \bar{\mathbf{R}}\dot{\mathbf{z}} = \mathbf{T}\mathbf{R}_{\mathrm{d}}\dot{\mathbf{z}}, \tag{2.8}$$

$$\dot{\mathbf{Z}} = \bar{\mathbf{R}}\ddot{\mathbf{z}} + \dot{\bar{\mathbf{R}}}\dot{\mathbf{z}} = \mathbf{T}\mathbf{R}_{\mathrm{d}}\ddot{\mathbf{z}} + \mathbf{T}\dot{\mathbf{R}}_{\mathrm{d}}\dot{\mathbf{z}}, \tag{2.9}$$

where $\mathbf{z} \in \mathbb{R}^{N_b}$, $\dot{\mathbf{z}} \in \mathbb{R}^{N_b}$, and $\ddot{\mathbf{z}} \in \mathbb{R}^{N_b}$ are the respective vectors of the relative joint coordinates, velocities, and accelerations, $\mathbf{T} \in \mathbb{R}^{6N_b \times 6N_b}$ is the constant path matrix representing the tree topology of the open-loop system, and $\mathbf{R}_{\mathrm{d}} \in \mathbb{R}^{6N_b \times N_b}$ is a block diagonal matrix whose elements are the vectors $\mathbf{b}_j$ arranged in an ascending order. In this study, the path matrix $\mathbf{T}$ is a lower block triangular matrix [24] whose elements from diagonal to left are the identity matrix $\mathbf{I}_6$ for the corresponding body between the considered body and root. The term $\dot{\bar{\mathbf{R}}}\dot{\mathbf{z}}$ in Eq. (2.9) is simply a vector containing the vectors $\mathbf{d}_j$ [24]. It should be noted that $\mathbf{Z} = \left[\mathbf{Z}_1^{\mathrm{T}}, \mathbf{Z}_2^{\mathrm{T}}, \ldots, \mathbf{Z}_{N_b}^{\mathrm{T}}\right]^{\mathrm{T}}$ and $\dot{\mathbf{Z}} = \left[\dot{\mathbf{Z}}_1^{\mathrm{T}}, \dot{\mathbf{Z}}_2^{\mathrm{T}}, \ldots, \dot{\mathbf{Z}}_{N_b}^{\mathrm{T}}\right]^{\mathrm{T}}$.

Alternatively, the Cartesian velocities $\mathbf{Y}_j$ can be mapped onto a set of relative joint velocities using a velocity transformation matrix $\mathbf{R} \in \mathbb{R}^{6N_b \times N_b}$ as [6]

$$\mathbf{Y} = \mathbf{R}\dot{\mathbf{z}}, \tag{2.10}$$

$$\dot{\mathbf{Y}} = \mathbf{R}\ddot{\mathbf{z}} + \dot{\mathbf{R}}\dot{\mathbf{z}}, \tag{2.11}$$

where the term $\dot{\mathbf{R}}\dot{\mathbf{z}}$ are the Cartesian accelerations $\dot{\mathbf{Y}}$ computed with the true relative joint velocities $\dot{\mathbf{z}}$ and the zero relative joint accelerations, $\ddot{\mathbf{z}} = \mathbf{0}$. The computation of the matrix $\mathbf{R}$ is crucial in formulations using this approach. The rows of matrix $\mathbf{R}$ that affect each body can be computed in parallel using the body-by-body technique as in [6]. In general, the row of matrix $\mathbf{R}$ corresponding to body j can be written as $\mathbf{R}_j \in \mathbb{R}^{6 \times f_j}$, where f_j is the relative joint degrees of freedom found in the path from body j to the base. It should be noted that for joints that cause no motion to body j, the corresponding zero columns of matrix $\mathbf{R}$ are eliminated in forming the matrix $\mathbf{R}_j$. The matrix $\mathbf{R}_j$ can be written as

$$\mathbf{R}_j = \left[\mathbf{R}_j^1, \mathbf{R}_j^2, \ldots \mathbf{R}_j^{n_j}\right], \tag{2.12}$$

where n_j is the number of joints in the path from body j to the base. In Eq. (2.12), the subindexes are used for bodies and the superindexes are used for joints. The dimension of each sub-matrix in Eq. (2.12) is six by the degrees of freedom of the joint. For example, the sub-matrix $\mathbf{R}_j^{rev}$ for a revolute joint can be written as

$$\mathbf{R}_j^{rev} = \begin{bmatrix} \widetilde{\mathbf{n}}\left(\mathbf{g}_j - \mathbf{r}\right) \\ \mathbf{n} \end{bmatrix}_{6\times 1}, \tag{2.13}$$

where $\mathbf{n}$ is the unit vector in the direction of the revolute axis and $\mathbf{r}$ is the position vector of a reference point in the revolute joint in the inertial reference frame. The expression of the sub-matrices in Eq. (2.12) for different types of joints are presented in [6].

2.1.2 Open-loop dynamics

Using the principle of virtual work, the virtual power of the inertia and external forces acting on the open-loop system can be written as [6]

$$\sum_{j=1}^{N_b} \mathbf{Y}_j^{*\mathrm{T}} \left(\mathbf{M}_j \dot{\mathbf{Y}}_j - \mathbf{Q}_j \right) = \mathbf{0}, \tag{2.14}$$

or it can be rewritten using Eqs. (2.2) and (2.3) as [40]

$$\sum_{j=1}^{N_b} \mathbf{Z}_j^{*\mathrm{T}} \left(\bar{\mathbf{M}}_j \dot{\mathbf{Z}}_j - \bar{\mathbf{Q}}_j \right) = \mathbf{0}, \tag{2.15}$$

where an asterisk (*) denotes the virtual velocities that are assumed to be kinematically admissible, the mass matrices $\mathbf{M}_j$ and $\bar{\mathbf{M}}_j$ can be written as [6, 40]

$$\mathbf{M}_j = \begin{bmatrix} m_j \mathbf{I}_3 & \mathbf{0} \\ \mathbf{0} & \mathbf{J}_j \end{bmatrix}, \quad \bar{\mathbf{M}}_j = \begin{bmatrix} m_j \mathbf{I}_3 & -m_j \widetilde{\mathbf{g}}_j \\ m_j \widetilde{\mathbf{g}}_j & \mathbf{J}_j - m_j \widetilde{\mathbf{g}}_j \widetilde{\mathbf{g}}_j \end{bmatrix}, \tag{2.16}$$

and the external force vectors $\mathbf{Q}_j$ and $\bar{\mathbf{Q}}_j$ can be written as [6, 40]

$$\mathbf{Q}_j = \begin{bmatrix} \mathbf{f}_j \\ \boldsymbol{\tau}_j \end{bmatrix}, \quad \bar{\mathbf{Q}}_j = \begin{bmatrix} \mathbf{f}_j - \widetilde{\boldsymbol{\omega}}_j \left(\widetilde{\boldsymbol{\omega}}_j m_j \mathbf{g}_j \right) \\ \boldsymbol{\tau}_j - \widetilde{\boldsymbol{\omega}}_j \mathbf{J}_j \boldsymbol{\omega}_j + \widetilde{\mathbf{g}}_j \left(\mathbf{f}_j - \widetilde{\boldsymbol{\omega}}_j \left(\widetilde{\boldsymbol{\omega}}_j m_j \mathbf{g}_j \right) \right) \end{bmatrix}. \tag{2.17}$$

In Eqs. (2.16) and (2.17), m_j is the mass of body j, $\mathbf{J}_j$ is the inertia tensor of body j, $\mathbf{f}_j$ is the vector of external forces applied on body j, and $\boldsymbol{\tau}_j$ is the vector of external moments with respect to the center of mass of body j. The inertia tensor $\mathbf{J}_j$ in the inertial reference frame can be written as $\mathbf{J}_j = \mathbf{A}_j^{\mathrm{T}} \bar{\mathbf{J}}_j \mathbf{A}_j$, with $\mathbf{A}_j$ being the rotation matrix of body j and $\bar{\mathbf{J}}_j$ being the constant inertia tensor in the body reference frame of body j.

The equations of motion for the open-loop system can be written by substituting Eqs. (2.8) and (2.9) in Eq. (2.15) as [40]

$$\mathbf{R}_{\mathrm{d}}^{\mathrm{T}} \mathbf{T}^{\mathrm{T}} \bar{\mathbf{M}} \mathbf{T} \mathbf{R}_{\mathrm{d}} \ddot{\mathbf{z}} = \mathbf{R}_{\mathrm{d}}^{\mathrm{T}} \mathbf{T}^{\mathrm{T}} \left(\bar{\mathbf{Q}} - \bar{\mathbf{M}} \mathbf{T} \dot{\mathbf{R}}_{\mathrm{d}} \dot{\mathbf{z}} \right) \quad \Rightarrow \quad \bar{\mathbf{M}}^{\Sigma} \ddot{\mathbf{z}} = \bar{\mathbf{Q}}^{\Sigma}, \tag{2.18}$$

where $\bar{\mathbf{M}} \in \mathbb{R}^{6N_b \times 6N_b}$ is the composite diagonal mass matrix constituting the matrices $\bar{\mathbf{M}}_j$, $\bar{\mathbf{Q}} \in \mathbb{R}^{6N_b}$ is the composite external force vector constituting the vectors $\bar{\mathbf{Q}}_j$, $\bar{\mathbf{M}}^{\Sigma} = \left(\mathbf{R}_{\mathrm{d}}^{\mathrm{T}} \mathbf{T}^{\mathrm{T}} \bar{\mathbf{M}} \mathbf{T} \mathbf{R}_{\mathrm{d}} \right)$, and $\bar{\mathbf{Q}}^{\Sigma} = \left[\mathbf{R}_{\mathrm{d}}^{\mathrm{T}} \mathbf{T}^{\mathrm{T}} \left(\bar{\mathbf{Q}} - \bar{\mathbf{M}} \mathbf{T} \dot{\mathbf{R}}_{\mathrm{d}} \dot{\mathbf{z}} \right) \right]$. Alternatively, the equations of motion for the open-loop system can be written by substituting Eqs. (2.10) and (2.11) in Eq. (2.14) as [6]

$$\mathbf{R}^{\mathrm{T}} \mathbf{M} \mathbf{R} \ddot{\mathbf{z}} = \mathbf{R}^{\mathrm{T}} \left(\mathbf{Q} - \mathbf{M} \dot{\mathbf{R}} \dot{\mathbf{z}} \right) \quad \Rightarrow \quad \mathbf{M}^{\Sigma} \ddot{\mathbf{z}} = \mathbf{Q}^{\Sigma}, \tag{2.19}$$

where $\mathbf{M} \in \mathbb{R}^{6N_b \times 6N_b}$ is the composite diagonal mass matrix constituting the matrices $\mathbf{M}_j$, $\mathbf{Q} \in \mathbb{R}^{6N_b}$ is the composite external force vector constituting the vectors $\mathbf{Q}_j$, $\mathbf{M}^{\Sigma} = \left(\mathbf{R}^{\mathrm{T}} \mathbf{M} \mathbf{R} \right)$, and $\mathbf{Q}^{\Sigma} = \left[\mathbf{R}^{\mathrm{T}} \left(\mathbf{Q} - \mathbf{M} \dot{\mathbf{R}} \dot{\mathbf{z}} \right) \right]$.

2.1.3 Closed-loop dynamics–Augmented Lagrangian with projections

In this approach, the loop-closure constraints are incorporated in the dynamics of the open-loop system using the index-3 augmented Lagrangian method with projections as in [11, 23]. A set of N_m constraint equations $\mathbf{\Phi} = \mathbf{0}$ are used for the closure of the open-loop. For simplicity, the constraints are assumed to be holonomic and scleronomic. The constraint equations $\mathbf{\Phi} = \mathbf{0}$ can be expressed in terms of the relative joint coordinates as $\mathbf{\Phi}(\mathbf{z}) = \mathbf{0}$. The equations of motion for the closed-loop system can be written using Eq. (2.18) as

$$\left.\begin{aligned} \bar{\mathbf{M}}^{\Sigma}\ddot{\mathbf{z}} + \mathbf{\Phi}_{\mathbf{z}}^{\mathrm{T}}\alpha\mathbf{\Phi} + \mathbf{\Phi}_{\mathbf{z}}^{\mathrm{T}}\boldsymbol{\lambda} &= \bar{\mathbf{Q}}^{\Sigma} \\ \boldsymbol{\lambda}^{(h+1)} &= \boldsymbol{\lambda}^{(h)} + \alpha\mathbf{\Phi}^{(h+1)} \end{aligned}\right\}, \tag{2.20}$$

where $\mathbf{\Phi}_{\mathbf{z}}$ is the Jacobian matrix of $\mathbf{\Phi}(\mathbf{z}) = \mathbf{0}$, α is the penalty factor that can be set the same for all constraints, $\boldsymbol{\lambda}$ is the vector of iterated Lagrange multipliers, h is the iteration step, $\bar{\mathbf{M}}^{\Sigma} = \left(\mathbf{R}_{\mathrm{d}}^{\mathrm{T}}\mathbf{T}^{\mathrm{T}}\bar{\mathbf{M}}\mathbf{T}\mathbf{R}_{\mathrm{d}}\right)$, and $\bar{\mathbf{Q}}^{\Sigma} = \left[\mathbf{R}_{\mathrm{d}}^{\mathrm{T}}\mathbf{T}^{\mathrm{T}}\left(\bar{\mathbf{Q}} - \bar{\mathbf{M}}\mathbf{T}\dot{\mathbf{R}}_{\mathrm{d}}\dot{\mathbf{z}}\right)\right]$. The value of $\boldsymbol{\lambda}^{(0)}$ is taken to be equal to the iterated value of $\boldsymbol{\lambda}$ in the previous time-step.

In this method, the time integration scheme is carried out using an implicit single-step trapezoidal rule [23]. After the integration process, the relative joint velocities $\dot{\mathbf{z}}$ and accelerations $\ddot{\mathbf{z}}$ are corrected using the mass-damping-stiffness-orthogonal projections as [11, 23]

$$\left[\mathbf{W} + \frac{\Delta t^2}{4}\mathbf{\Phi}_{\mathbf{z}}^{\mathrm{T}}\alpha\mathbf{\Phi}_{\mathbf{z}}\right]\dot{\mathbf{z}} = \mathbf{W}\dot{\mathbf{z}}', \tag{2.21}$$

$$\left[\mathbf{W} + \frac{\Delta t^2}{4}\mathbf{\Phi}_{\mathbf{z}}^{\mathrm{T}}\alpha\mathbf{\Phi}_{\mathbf{z}}\right]\ddot{\mathbf{z}} = \mathbf{W}\ddot{\mathbf{z}}' - \frac{\Delta t^2}{4}\mathbf{\Phi}_{\mathbf{z}}^{\mathrm{T}}\alpha\left(\dot{\mathbf{\Phi}}_{\mathbf{z}}\dot{\mathbf{z}}\right), \tag{2.22}$$

where Δt is the time-step size, $\dot{\mathbf{z}}'$ and $\ddot{\mathbf{z}}'$ are the respective relative joint velocities and accelerations obtained from the Newton–Raphson iteration after achieving convergence, $\dot{\mathbf{\Phi}}_{\mathbf{z}}$ is the derivative of $\mathbf{\Phi}_{\mathbf{z}}$ with respect to time t, and $\mathbf{W}$ can be written as

$$\mathbf{W} = \bar{\mathbf{M}}^{\Sigma} + \frac{\Delta t}{2}\bar{\mathbf{C}} + \frac{\Delta t^2}{4}\bar{\mathbf{K}}, \tag{2.23}$$

where $\bar{\mathbf{C}}$ and $\bar{\mathbf{K}}$ are the damping and stiffness contributions in the system that can be written as

$$\bar{\mathbf{C}} = -\frac{\partial\bar{\mathbf{Q}}^{\Sigma}}{\partial\dot{\mathbf{z}}}, \tag{2.24}$$

and

$$\bar{\mathbf{K}} = -\frac{\partial\bar{\mathbf{Q}}^{\Sigma}}{\partial\mathbf{z}}. \tag{2.25}$$

It should be noted that this method can handle redundant constraints and can provide solutions in the vicinity of singular configurations. Furthermore, to account for rheonomic constraints using this approach, the reader is referred to [23] and [57].

2.1.4 Closed-loop dynamics–Coordinate partitioning method

In this approach, the loop-closure constraints are incorporated in the dynamics of the open-loop system using the coordinate partitioning method as in [19, 40]. In the literature [19], this approach is also referred to as the double-step semi-recursive formulation because it utilizes two velocity transformation matrices, one in Eq. (2.8) and the other is presented in this subsection. A set of N_m constraint equations $\mathbf{\Phi}(\mathbf{z}) = \mathbf{0}$ are used for the closure of the open-loop. For simplicity, the constraints are assumed to be holonomic and scleronomic.

In this method, the relative joint velocities can be mapped on a set of independent relative joint velocities using a velocity transformation matrix $\mathbf{R_z} \in \mathbb{R}^{N_b \times N_f}$ as [40, 41]

$$\dot{\mathbf{z}} = \mathbf{R_z}\dot{\mathbf{z}}^{\mathrm{i}} \quad \Rightarrow \quad \begin{bmatrix} \dot{\mathbf{z}}^{\mathrm{d}} \\ \dot{\mathbf{z}}^{\mathrm{i}} \end{bmatrix} = \begin{bmatrix} -\left(\mathbf{\Phi}_{\mathbf{z}}^{\mathrm{d}}\right)^{-1}\mathbf{\Phi}_{\mathbf{z}}^{\mathrm{i}} \\ \mathbf{I} \end{bmatrix} \dot{\mathbf{z}}^{\mathrm{i}}, \tag{2.26}$$

$$\ddot{\mathbf{z}} = \mathbf{R_z}\ddot{\mathbf{z}}^{\mathrm{i}} + \dot{\mathbf{R}}_{\mathbf{z}}\dot{\mathbf{z}}^{\mathrm{i}}, \tag{2.27}$$

where N_f are the degrees of freedom of the closed-loop system, $\dot{\mathbf{z}}^{\mathrm{i}} \in \mathbb{R}^{N_f}$ and $\dot{\mathbf{z}}^{\mathrm{d}} \in \mathbb{R}^{N_m}$ are the independent and dependent relative joint velocities, respectively, $\mathbf{\Phi}_{\mathbf{z}}^{\mathrm{i}} \in \mathbb{R}^{N_m \times N_f}$ and $\mathbf{\Phi}_{\mathbf{z}}^{\mathrm{d}} \in \mathbb{R}^{N_m \times N_m}$ are the respective independent and dependent columns of the Jacobian matrix $\mathbf{\Phi_z}$, and $\ddot{\mathbf{z}}^{\mathrm{i}} \in \mathbb{R}^{N_f}$ are the independent relative joint accelerations. It is assumed that redundant constraints or singular configurations do not exist reassuring that the inverse of $\mathbf{\Phi}_{\mathbf{z}}^{\mathrm{d}}$ can be found. The independent relative joint coordinates can be identified using the Gaussian elimination [38] with full pivoting to the Jacobian matrix $\mathbf{\Phi_z}$ as in [29] and [41].

The equations of motion for the closed-loop system can be written by substituting Eqs. (2.26) and (2.27) in Eq. (2.18) as

$$\mathbf{R}_{\mathrm{z}}^{\mathrm{T}}\bar{\mathbf{M}}^{\Sigma}\mathbf{R}_{\mathrm{z}}\ddot{\mathbf{z}}^{\mathrm{i}} = \mathbf{R}_{\mathrm{z}}^{\mathrm{T}}\left(\bar{\mathbf{Q}}^{\Sigma} - \bar{\mathbf{M}}^{\Sigma}\dot{\mathbf{R}}_{\mathbf{z}}\dot{\mathbf{z}}^{\mathrm{i}}\right), \tag{2.28}$$

where $\bar{\mathbf{M}}^{\Sigma} = \left(\mathbf{R}_{\mathrm{d}}^{\mathrm{T}}\mathbf{T}^{\mathrm{T}}\bar{\mathbf{M}}\mathbf{T}\mathbf{R}_{\mathrm{d}}\right)$ and $\bar{\mathbf{Q}}^{\Sigma} = \left[\mathbf{R}_{\mathrm{d}}^{\mathrm{T}}\mathbf{T}^{\mathrm{T}}\left(\bar{\mathbf{Q}} - \bar{\mathbf{M}}\mathbf{T}\dot{\mathbf{R}}_{\mathrm{d}}\dot{\mathbf{z}}\right)\right]$. The computation of the derivatives of the velocity transformation matrices is avoided by rewriting Eq. (2.28) as [19]

$$\left.\begin{aligned} &\mathbf{R}_{\mathrm{z}}^{\mathrm{T}}\mathbf{R}_{\mathrm{d}}^{\mathrm{T}}\mathbf{T}^{\mathrm{T}}\bar{\mathbf{M}}\mathbf{T}\mathbf{R}_{\mathrm{d}}\mathbf{R}_{\mathrm{z}}\ddot{\mathbf{z}}^{\mathrm{i}} = \mathbf{R}_{\mathrm{z}}^{\mathrm{T}}\mathbf{R}_{\mathrm{d}}^{\mathrm{T}}\left(\mathbf{T}^{\mathrm{T}}\bar{\mathbf{Q}} - \mathbf{T}^{\mathrm{T}}\bar{\mathbf{M}}\bar{\mathbf{D}}\right) \\ &\bar{\mathbf{D}} = \mathbf{T}\mathbf{R}_{\mathrm{d}}\begin{bmatrix} -\left(\mathbf{\Phi}_{\mathbf{z}}^{\mathrm{d}}\right)^{-1}\left(\dot{\mathbf{\Phi}}_{\mathbf{z}}\dot{\mathbf{z}}\right) \\ \mathbf{0} \end{bmatrix} + \mathbf{T}\dot{\mathbf{R}}_{\mathrm{d}}\dot{\mathbf{z}} \end{aligned}\right\} \quad \Rightarrow \quad \overline{\bar{\mathbf{M}}^{\Sigma}}\ddot{\mathbf{z}}^{\mathrm{i}} = \overline{\bar{\mathbf{Q}}^{\Sigma}}, \tag{2.29}$$

where $\bar{\mathbf{D}} \in \mathbb{R}^{6N_b}$ contains the Cartesian accelerations $\dot{\mathbf{Z}}$ computed with the true relative joint velocities $\dot{\mathbf{z}}$ and the zero independent relative joint accelerations ($\ddot{\mathbf{z}}^{\mathrm{i}} = \mathbf{0}$). This method can be used with both explicit and implicit integrators. It should be noted that to account for rheonomic constraints using this approach, the reader is referred to [40].

2.1.5 Closed-loop dynamics–Penalty method

In this approach, the loop-closure constraints are incorporated in the dynamics of the open-loop system using the penalty method as in [6, 10]. A set of N_m constraint equations $\mathbf{\Phi}(\mathbf{z}) = \mathbf{0}$ are used for the closure of the open-loop. For simplicity, the constraints are assumed to be holonomic and scleronomic. In this method, it is assumed that the constraint forces acting at the location of the cut-joint compensate for the constraint violations by acting in the violation direction. Furthermore, the magnitude of these forces are assumed proportional to a linear combination of the value of constraints and their first and second time derivatives.

The equations of motion for the closed-loop system can be written by directly introducing constraints penalized by a large factor in Eq. (2.19) as

$$\mathbf{M}^{\Sigma}\ddot{\mathbf{z}} + \mathbf{\Phi}_{\mathbf{z}}^{\mathrm{T}}\boldsymbol{\alpha}\left(\ddot{\mathbf{\Phi}} + 2\boldsymbol{\Omega}\boldsymbol{\mu}\dot{\mathbf{\Phi}} + \boldsymbol{\Omega}^2\mathbf{\Phi}\right) = \mathbf{Q}^{\Sigma}, \tag{2.30}$$

where $\mathbf{\Phi}_{\mathbf{z}}$ is the Jacobian matrix of $\mathbf{\Phi}(\mathbf{z}) = \mathbf{0}$, $\boldsymbol{\alpha} \in \mathbb{R}^{N_m \times N_m}$, $\boldsymbol{\Omega} \in \mathbb{R}^{N_m \times N_m}$, and $\boldsymbol{\mu} \in \mathbb{R}^{N_m \times N_m}$ are the diagonal matrices containing values of the penalty factors, natural frequencies, and damping ratios at each constraint conditions, respectively, the terms $\dot{\mathbf{\Phi}}$ and $\ddot{\mathbf{\Phi}}$ are the respective first and second order time derivatives of the constraints $\mathbf{\Phi}(\mathbf{z}) = \mathbf{0}$, $\mathbf{M}^{\Sigma} = (\mathbf{R}^{\mathrm{T}}\mathbf{M}\mathbf{R})$, and $\mathbf{Q}^{\Sigma} = \left[\mathbf{R}^{\mathrm{T}}\left(\mathbf{Q} - \mathbf{M}\dot{\mathbf{R}}\dot{\mathbf{z}}\right)\right]$. The second term on the left side of Eqs. (2.30) represents the forces produced by the penalty system to avoid the violation of the constraints $\mathbf{\Phi}$, $\dot{\mathbf{\Phi}}$, and $\ddot{\mathbf{\Phi}}$. The terms $\dot{\mathbf{\Phi}}$ and $\ddot{\mathbf{\Phi}}$ can be written as

$$\dot{\mathbf{\Phi}} = \mathbf{\Phi}_{\mathbf{z}}\dot{\mathbf{z}}, \tag{2.31}$$

$$\ddot{\mathbf{\Phi}} = \mathbf{\Phi}_{\mathbf{z}}\ddot{\mathbf{z}} + \dot{\mathbf{\Phi}}_{\mathbf{z}}\dot{\mathbf{z}}, \tag{2.32}$$

where $\dot{\mathbf{\Phi}}_{\mathbf{z}}$ is the derivative of $\mathbf{\Phi}_{\mathbf{z}}$ with respect to time t. It should be noted that the time-dependent constraints are not incorporated in Eqs. (2.31) and (2.32) because constraints are assumed scleronomic. To account for rheonomic constraints using this approach, the reader is referred to [6] and [10]. The equations of motion for the closed-loop system can be rewritten by substituting Eqs. (2.31) and (2.32) in Eq. (2.30) as

$$\left(\mathbf{M}^{\Sigma} + \mathbf{\Phi}_{\mathbf{z}}^{\mathrm{T}}\boldsymbol{\alpha}\mathbf{\Phi}_{\mathbf{z}}\right)\ddot{\mathbf{z}} = \mathbf{Q}^{\Sigma} - \mathbf{\Phi}_{\mathbf{z}}^{\mathrm{T}}\boldsymbol{\alpha}\left(\dot{\mathbf{\Phi}}_{\mathbf{z}}\dot{\mathbf{z}} + 2\boldsymbol{\Omega}\boldsymbol{\mu}\mathbf{\Phi}_{\mathbf{z}}\dot{\mathbf{z}} + \boldsymbol{\Omega}^2\mathbf{\Phi}\right) \quad \Rightarrow \quad \overline{\mathbf{M}^{\Sigma}}\ddot{\mathbf{z}}^{\mathrm{i}} = \overline{\mathbf{Q}^{\Sigma}}. \tag{2.33}$$

A large value of the penalty factors $\boldsymbol{\alpha}$ ensures a better fulfillment of constraints, however, it may cause numerical ill-conditioning. The values of natural frequencies $\boldsymbol{\Omega}$ and damping ratios $\boldsymbol{\mu}$ can vary because a general procedure determining their values is lacking, and it may cause inconsequential solutions in some cases. For the same value of penalty terms used for each constraint, the terms $\boldsymbol{\alpha}$, $\boldsymbol{\Omega}$, and $\boldsymbol{\mu}$ become identity matrices multiplied by the respective penalty values. It should be noted that this method can handle redundant constraints and can provide solutions in the vicinity of singular configurations.

2.2 Modeling of hydraulic actuators

The scope of this work focuses on linear hydraulic actuators and only double acting hydraulic cylinders are considered as shown in Sect. 2.2.2. In this study, the lumped fluid theory is used to compute the pressures in a hydraulic circuit [71]. In this approach, a hydraulic circuit is partitioned into discrete volumes where the hydraulic pressures are assumed to be equally distributed. Thus, the effects of acoustic waves are assumed to be insignificant. Figure 2.2 illustrates the modeling concept, where an incoming flow Q_{s_1}, and outgoing flows Q_{s_2} and Q_{s_3}, are associated with a hydraulic control volume, V_s. The hydraulic pressure p_s, within a hydraulic control volume V_s, can be computed as

$$\dot{p}_s = \frac{B_{e_s}}{V_s}\left(-\frac{dV_s}{dt} + \sum_{k=1}^{n_f} Q_{s_k}\right), \tag{2.34}$$

where $\dot{p}_s$ is the pressure build-up, B_{e_s} is the effective bulk modulus, $\frac{dV_s}{dt}$ is the change of volume with respect to time t that usually represents the cylinder or piston movement, Q_{s_k} is the incoming and outgoing volume flow rates associated to the control volume V_s, and n_f is the total number of such volume flow rates. The effective bulk modulus B_{e_s}, can be computed as

$$B_{e_s} = \left(\frac{1}{B_{oil}} + \sum_{k=1}^{n_c} \frac{V_k}{V_s B_k}\right)^{-1}, \tag{2.35}$$

where B_{oil} is the bulk modulus of oil, B_k is the bulk modulus of the container of a sub-volume V_k that forms the control volume V_s, and n_c is the total number of such sub-volumes.

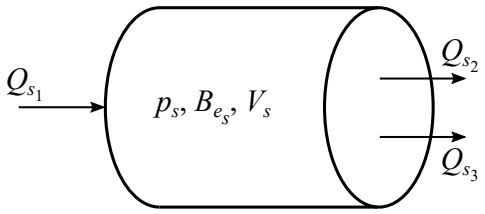

Figure 2.2: Modeling illustration of the lumped fluid theory.

2.2.1 Throttle and directional control valves

In this study, valves in a hydraulic circuit are described using a semi-empirical modeling approach [36]. In this approach, the volume flow rate, Q_t, through a simple throttle valve can be written as

$$Q_t = C_{v_t} \operatorname{sgn}(\Delta p)\sqrt{|\ \Delta p\ |}, \tag{2.36}$$

where C_{v_t} is the semi-empirical flow rate coefficient of the valve, $\operatorname{sgn}(\cdot)$ is the signum function, and Δp is the pressure difference over the valve. The value of C_{v_t} in Eq. (2.36)

can be evaluated as [57] $C_{v_t} = C_d A_t \sqrt{\frac{2}{\rho}}$, where C_d is the flow discharge coefficient, A_t is the area of the throttle valve, and ρ is the oil density.

Similarly, the volume flow rate, Q_d, through a directional control valve can be written as

$$Q_d = C_{v_d} U \operatorname{sgn}(\Delta p) \sqrt{|\ \Delta p\ |}, \tag{2.37}$$

where C_{v_d} is the semi-empirical flow rate constant of the valve and U is the relative spool position. The value of C_{v_d} in Eq. (2.37) can be procured from the manufacturer's catalogue. The relative spool position, expressed in voltage, can be computed using its time derivative $\dot{U}$ as

$$\dot{U} = \frac{U_{ref} - U}{\tau}, \tag{2.38}$$

where U_{ref} is the reference voltage signal for the reference spool position and τ is the time constant. The value of τ in Eq. (2.38) can be procured from the Bode-diagram of the valve describing the valve spool dynamics. Note that Eqs. (2.36) and (2.37) account for a turbulent volume flow. In this study, the volume flow is assumed laminar for a pressure difference of less than two bar, and Eqs. (2.36) and (2.37) are modified to follow a linear relation between the volume flow rate and the pressure difference.

2.2.2 Double acting hydraulic cylinders

A double acting hydraulic cylinder is shown in Fig. 2.3, whose motion causes volume flows that can be expressed as

$$Q_{in} = \dot{x} A_1, \quad Q_{out} = \dot{x} A_2, \tag{2.39}$$

where Q_{in} and Q_{out} are the respective incoming and outgoing volume flow rates of the cylinder, $\dot{x}$ is the piston velocity, and A_1 and A_2 are the respective areas on the piston and piston-rod sides of the cylinder. In Fig. 2.3, x is the actuator length. The force, F_{cyl}, produced by the cylinder can be written as

$$F_{cyl} = p_1 A_1 - p_2 A_2 - F_\mu, \tag{2.40}$$

where p_1 and p_2 are the respective chamber pressures on the piston and piston-rod sides of the cylinder and F_μ is the total seal friction.

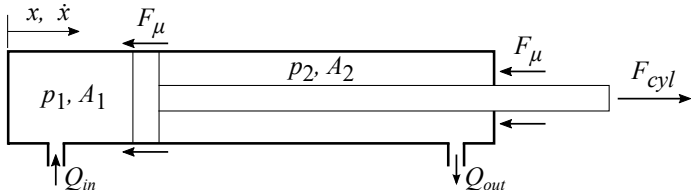

Figure 2.3: Schematic figure of a double acting hydraulic cylinder.

2.3 Modeling of friction force

Friction is defined as a force opposing the relative motion between two surfaces in contact. Several friction models in the literature capture a combination of the Coulomb, stiction, viscous, and Stribeck effects. Most static friction models may suffer from numerical instability because of the discontinuity of friction at zero relative velocity. However, many alternate continuous models in the category of static friction models have been developed to overcome this numerical instability as shown in Fig. 2.4. In Fig. 2.4, F_c and F_s are the respective Coulomb and static friction, and v_s and v_t are the Stribeck and relative tangential velocities, respectively. In this category, the Bengisu–Akay [12] and Brown–McPhee [17] friction models are considered in this study.

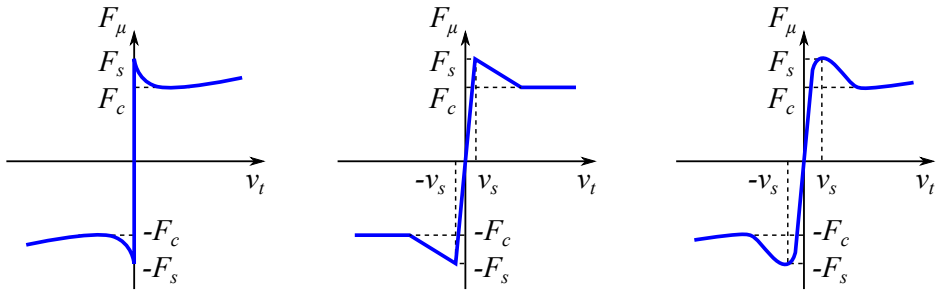

Figure 2.4: Depiction of the Stribeck friction model (left [15]), and alternate friction models (middle [45] and right [12, 17]) eliminating discontinuity at zero relative velocity.

Dynamic friction models consider the pre-slip displacement [13], and thus, they eliminate the discontinuity of friction at zero relative velocity. In the category of dynamic friction models, the average bristle deflection is often considered, representing the behavior of surface asperities during contact [28, 46]. The bristles behave like springs during the sticking phase. In this category, the LuGre [28] and modified LuGre [72] friction models are considered in this study.

2.3.1 Bengisu–Akay friction model

Friction can be approximated using the Coulomb friction law, which has established that the friction force magnitude depends on the relative tangential velocity between the contact surfaces. It is established in the literature that the static friction is greater than the kinetic or Coulomb friction and it continuously decreases with an increasing relative tangential velocity. This phenomenon is known as the Stribeck effect [39] and it is shown in Fig. 2.4. Considering numerical stability at zero relative velocity, friction can be modeled using two separate equations for the adhesion regime and the Stribeck effect as [12, 45]

$$\mathbf{F}_\mu = \begin{cases} \left(-\frac{F_s}{v_s{}^2}\left(|\mathbf{v}_t| - v_s\right)^2 + F_s\right) \operatorname{sgn}(\mathbf{v}_t) & |\mathbf{v}_t| < v_s, \\ \left(F_c + \left(F_s - F_c\right) e^{-\xi(|\mathbf{v}_t| - v_s)}\right) \operatorname{sgn}(\mathbf{v}_t) & |\mathbf{v}_t| \geq v_s, \end{cases} \tag{2.41}$$

where F_c is the Coulomb friction, F_s is the static friction, v_s is the Stribeck velocity, ξ is a positive parameter representing a negative slope of the sliding regime, $\mathbf{v}_t$ is the relative tangential velocity vector between contact surfaces, and $\mathbf{F}_\mu$ is the total friction force vector. In Eq. (2.41), $F_c = \mu_c |\mathbf{F}_n|$ and $F_s = \mu_s |\mathbf{F}_n|$, where $\mathbf{F}_n$ is the normal contact force vector, and μ_c and μ_s are the respective coefficients of Coulomb and static friction.

It should be noted that viscous friction is not considered in Eq. (2.41). Viscous friction cannot be ignored in case of a hydraulic cylinder where lubricants are present, such as in this study. Therefore, a corrected version of the Bengisu–Akay friction model incorporating viscous friction is presented in this study as

$$\mathbf{F}_\mu = \begin{cases} \left(-\frac{F_s}{v_s{}^2}\left(|\mathbf{v}_t| - v_s\right)^2 + F_s\right) \operatorname{sgn}(\mathbf{v}_t) & |\mathbf{v}_t| < v_s, \\ \left(F_c + (F_s - F_c)\, e^{-\xi(|\mathbf{v}_t| - v_s)}\right) \operatorname{sgn}(\mathbf{v}_t) + f(\mathbf{v}_t) & |\mathbf{v}_t| \geq v_s, \end{cases} \tag{2.42}$$

where $f(\mathbf{v}_t)$ is the viscous friction function, which in lubricated contacts is generally considered linear as [28, 46]

$$f(\mathbf{v}_t) = \sigma_2 \mathbf{v}_t, \tag{2.43}$$

where σ_2 is the coefficient of viscous friction. The incorporation of viscous friction is crucial, especially, in the presence of a fluid lubricant or at a high relative velocity [45]. This model is illustrated on the right side of Fig. 2.4. This model may burden the computational efficiency because for a large slope at zero relative velocity, small time-steps are required to properly capture the friction effects at low velocities.

2.3.2 Brown–McPhee friction model

A suitable alternative to the classical Stribeck friction model that avoids discontinuity at zero relative velocity was proposed by Brown and McPhee [17]. This model incorporates the Coulomb, stiction, and viscous frictions, and it is valid for both positive and negative relative tangential velocities. This velocity-dependent continuous friction model can be written as [17]

$$\mathbf{F}_\mu = \left(F_c \tanh\left(4\frac{|\mathbf{v}_t|}{v_s}\right) + (F_s - F_c)\, \frac{\frac{|\mathbf{v}_t|}{v_s}}{\left(\frac{1}{4}\left(\frac{|\mathbf{v}_t|}{v_s}\right)^2 + \frac{3}{4}\right)^2} \right) \operatorname{sgn}(\mathbf{v}_t) + \sigma_2 \mathbf{v}_t \tanh(4). \tag{2.44}$$

Here, the Coulomb friction term approaches F_c as $|\mathbf{v}_t|$ increases from zero to v_s. Whereas the static friction term representing the stiction and Stribeck effects achieves the maximum of $(F_s - F_c)$ at $|\mathbf{v}_t| = v_s$ and then decreases to zero at large relative tangential velocities, where the Coulomb and viscous frictions are dominant. The viscous friction term is linearly scaled with the velocity and it is physically attributed to the thin-film viscous friction [17]. This model is illustrated on the right side of Fig. 2.4. It should be noted that this model is suitable for real-time simulations and optimization problems [17].

2.3.3 LuGre friction model

The LuGre (Lund–Grenoble) friction model considers interactions of elastic bristles on one surface with rigid bristles on another surface as shown in Fig. 2.5. It utilizes the average bristle deflection in modeling. The LuGre model [28] is an extension of the Dahl model [26] that captures the Stribeck and stiction effects. On applying a tangential force, elastic bristles start to deflect like a spring giving rise to the sticking phase. A sufficiently large value of the tangential force causes large deflections for some of the bristles, giving rise to the slipping phase [28].

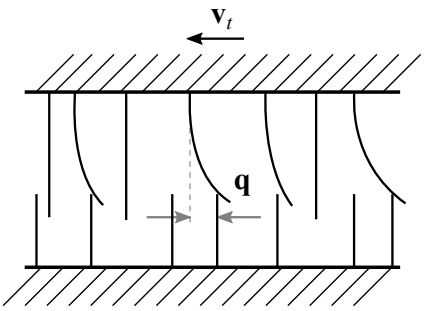

Figure 2.5: Interaction of bristles between two surfaces.

In the LuGre friction model, the average bristle deflection is quantified by introducing an internal state variable, $\mathbf{q}$. The model can be expressed as [28, 45]

$$\dot{\mathbf{q}} = \mathbf{v}_t - \frac{\sigma_0 |\mathbf{v}_t|}{g(\mathbf{v}_t)} \mathbf{q}, \tag{2.45}$$

with

$$g(\mathbf{v}_t) = F_c + (F_s - F_c)\, e^{-\left(\frac{|\mathbf{v}_t|}{v_s}\right)^n}, \tag{2.46}$$

where $\mathbf{q}$ and $\dot{\mathbf{q}}$ are the average bristle deflection vector and its time derivative, respectively, σ_0 is the stiffness of elastic bristles, and n is the exponent affecting the slope of the Stribeck curve. Here, the function $g(\mathbf{v}_t)$ describes the Stribeck effect [28, 69] and it is a function of the relative tangential velocity. The friction force generated from the bending of bristles can be written as

$$\mathbf{F}_\mu = \sigma_0 \mathbf{q} + \sigma_1 \dot{\mathbf{q}} + \sigma_2 \mathbf{v}_t, \tag{2.47}$$

where σ_1 is the damping of elastic bristles and σ_2 is the coefficient of viscous friction. The damping of elastic bristles can be a constant or a function of the relative tangential velocity, however, it is assumed constant in this study.

2.3.4 Modified LuGre friction model

In this model, the LuGre friction model in Sect. 2.3.3 is modified by incorporating the dynamics of the lubricant film formation [72]. The lubricant film dynamics is computed

using a first-order lag element in which the time-constant is varied between the deceleration, acceleration, and dwell periods [72]. Therefore, the friction force in this model is obtained as a combination of the bristle model in Sect. 2.3.3 and the lubricant film dynamics.

Similar to the LuGre friction model, the average bristle deflection is quantified by an internal state variable such that [72]

$$\dot{\mathbf{q}} = \mathbf{v}_t - \frac{\sigma_0 |\mathbf{v}_t|}{g(\mathbf{v}_t, \bar{\mathbf{h}})}\mathbf{q}, \tag{2.48}$$

with

$$g(\mathbf{v}_t, \bar{\mathbf{h}}) = F_c + \left[(1 - |\bar{\mathbf{h}}|)F_s - F_c\right] e^{-\left(\frac{|\mathbf{v}_t|}{v_s}\right)^n}, \tag{2.49}$$

where $\bar{\mathbf{h}}$ is a vector of dimensionless parameters describing the lubricant film thickness. Here, the function $g(\mathbf{v}_t, \bar{\mathbf{h}})$ describing the Stribeck effect is a function of the relative tangential velocity and the lubricant film thickness parameter.

The lubricant film dynamics can be computed using the time derivative of the lubricant film thickness $\dot{\bar{\mathbf{h}}}$ as [68, 72]

$$\dot{\bar{\mathbf{h}}} = \frac{1}{\tau_h}\left(\bar{\mathbf{h}}_{ss} - \bar{\mathbf{h}}\right), \tag{2.50}$$

with

$$\tau_h = \begin{cases} \tau_{hp} & \left(|\mathbf{v}_t| \neq 0, \quad |\bar{\mathbf{h}}| \leq |\bar{\mathbf{h}}_{ss}|\right), \\ \tau_{hn} & \left(|\mathbf{v}_t| \neq 0, \quad |\bar{\mathbf{h}}| > |\bar{\mathbf{h}}_{ss}|\right), \\ \tau_{h0} & \left(|\mathbf{v}_t| = 0\right), \end{cases} \tag{2.51}$$

$$|\bar{\mathbf{h}}_{ss}| = \begin{cases} K_f |\mathbf{v}_t|^{\frac{2}{3}} & \left(|\mathbf{v}_t| \leq |\mathbf{v}_b|\right), \\ K_f |\mathbf{v}_b|^{\frac{2}{3}} & \left(|\mathbf{v}_t| > |\mathbf{v}_b|\right), \end{cases} \tag{2.52}$$

$$K_f = \left(1 - \frac{F_c}{F_s}\right) |\mathbf{v}_b|^{-\frac{2}{3}}, \tag{2.53}$$

where $\bar{\mathbf{h}}_{ss}$ is the dimensionless parameter describing the steady-state of the lubricant film thickness, τ_{hp}, τ_{hn}, τ_{h0} are the time constants for the acceleration, deceleration, and dwell periods, respectively, K_f is a proportional constant, and $\mathbf{v}_b$ is the threshold velocity at which the magnitude of the steady state friction force becomes almost minimum [68, 72]. Here, the condition $|\bar{\mathbf{h}}| \leq |\bar{\mathbf{h}}_{ss}|$ represents the acceleration period, whereas the condition $|\bar{\mathbf{h}}| > |\bar{\mathbf{h}}_{ss}|$ represents the deceleration period. In this model, the lubricant film thickness is assumed to increase with an increasing relative tangential velocity only in the negative resistance regime using the condition $|\mathbf{v}_t| \leq |\mathbf{v}_b|$ in Eq. (2.52), otherwise, it is assumed to be a constant maximum value [72]. The friction force generated from the bending of bristles and the lubricant film dynamics can be written as

$$\mathbf{F}_\mu = \sigma_0 \mathbf{q} + \sigma_1 \dot{\mathbf{q}} + \sigma_2 \mathbf{v}_t. \tag{2.54}$$

2.4 Coupling of multibody dynamics and hydraulic actuators

In this study, the coupling of multibody dynamics with hydraulic actuators is performed in monolithic frameworks. This section is divided into two parts. In the first part, the penalty-based semi-recursive formulation (the augmented Lagrangian method with projections) and the double-step semi-recursive formulation (the coordinate partitioning method) are coupled with the lumped fluid theory. In the second part, various friction models of a hydraulic cylinder are coupled with the equations of motion of the combined penalty-based semi-recursive formulation and lumped fluid theory described in the first part.

2.4.1 Coupling for various semi-recursive multibody formulations

The multibody formulations described in Sect. 2.1.3 and Sect. 2.1.4 are extended to incorporate the dynamics of hydraulic actuators described in Sect. 2.2 in a monolithic approach. The coupling of the semi-recursive multibody formulations with the lumped fluid theory is inspired by [49, 57]. The external force vectors $\bar{\mathbf{Q}}^{\Sigma}$ in Eq. (2.20) and $\overline{\bar{\mathbf{Q}}^{\Sigma}}$ in Eq. (2.29) are now dependent on pressures, and the system of equations has to be incremented with the pressure variation equations leading to the coupled system of equations as

$$\left.\begin{aligned} \bar{\mathbf{M}}^{\Sigma}\ddot{\mathbf{z}} + \boldsymbol{\Phi}_{\mathbf{z}}^{\mathrm{T}}\alpha\boldsymbol{\Phi} + \boldsymbol{\Phi}_{\mathbf{z}}^{\mathrm{T}}\boldsymbol{\lambda} &= \bar{\mathbf{Q}}^{\Sigma}\left(\mathbf{z}, \dot{\mathbf{z}}, \mathbf{p}\right) \\ \boldsymbol{\lambda}^{(h+1)} &= \boldsymbol{\lambda}^{(h)} + \alpha\boldsymbol{\Phi}^{(h+1)} \\ \dot{\mathbf{p}} &= \mathbf{u}_0\left(\mathbf{z}, \dot{\mathbf{z}}, \mathbf{p}\right) \end{aligned}\right\} \tag{2.55}$$

(penalty-based semi-recursive approach),

$$\left.\begin{aligned} \overline{\bar{\mathbf{M}}^{\Sigma}}\ddot{\mathbf{z}}^{\mathrm{i}} &= \overline{\bar{\mathbf{Q}}^{\Sigma}}\left(\mathbf{z}, \dot{\mathbf{z}}, \mathbf{p}\right) \\ \dot{\mathbf{p}} &= \mathbf{u}_0\left(\mathbf{z}, \dot{\mathbf{z}}, \mathbf{p}\right) \end{aligned}\right\} \tag{2.56}$$

(double-step semi-recursive approach),

where $\mathbf{p}$ is the vector of hydraulic pressures, $\dot{\mathbf{p}}$ is the vector of pressure build-ups, and $\mathbf{u}_0$ are the pressure variation equations. It should be noted that $\bar{\mathbf{M}}^{\Sigma} = \left(\mathbf{R}_{\mathrm{d}}^{\mathrm{T}}\mathbf{T}^{\mathrm{T}}\bar{\mathbf{M}}\mathbf{T}\mathbf{R}_{\mathrm{d}}\right)$, $\bar{\mathbf{Q}}^{\Sigma} = \left[\mathbf{R}_{\mathrm{d}}^{\mathrm{T}}\mathbf{T}^{\mathrm{T}}\left(\bar{\mathbf{Q}} - \bar{\mathbf{M}}\mathbf{T}\dot{\mathbf{R}}_{\mathrm{d}}\dot{\mathbf{z}}\right)\right]$, $\overline{\bar{\mathbf{M}}^{\Sigma}} = \left(\mathbf{R}_{\mathrm{z}}^{\mathrm{T}}\bar{\mathbf{M}}^{\Sigma}\mathbf{R}_{\mathrm{z}}\right)$, and $\overline{\bar{\mathbf{Q}}^{\Sigma}} = \left[\mathbf{R}_{\mathrm{z}}^{\mathrm{T}}\left(\bar{\mathbf{Q}}^{\Sigma} - \bar{\mathbf{M}}^{\Sigma}\dot{\mathbf{R}}_{\mathbf{z}}\dot{\mathbf{z}}^{\mathrm{i}}\right)\right]$. It is assumed here that the dependency of $\bar{\mathbf{Q}}^{\Sigma}$, $\overline{\bar{\mathbf{Q}}^{\Sigma}}$, and $\mathbf{u}_0$ with respect to the vectors $\mathbf{z}$, $\dot{\mathbf{z}}$, and $\mathbf{p}$ are known.

In this study, both the coupled models above are integrated using an implicit single-step trapezoidal rule [44] as in [9]. It has already been established in [9, 21] that the trapezoidal rule performs satisfactorily for multibody models by considering the positions as primary variables instead of the accelerations. Similarly, the hydraulic pressures are considered primary variables when applying the trapezoidal rule in this study. By applying the trapezoidal rule to Eqs. (2.55) and (2.56), a nonlinear system of equations are formed

that can be denoted as $\acute{\mathbf{f}}\left(\bar{\mathbf{x}}\right) = \mathbf{0}$ such that

$$\left.\begin{array}{l} \bar{\mathbf{x}} = \left[\mathbf{z}^{\mathrm{T}}, \mathbf{p}^{\mathrm{T}}\right]^{\mathrm{T}} \\ \quad \text{(penalty-based semi-recursive approach)} \\ \bar{\mathbf{x}} = \left[\left(\mathbf{z}^{\mathrm{i}}\right)^{\mathrm{T}}, \mathbf{p}^{\mathrm{T}}\right]^{\mathrm{T}} \\ \quad \text{(double-step semi-recursive approach)} \end{array}\right\}. \tag{2.57}$$

Such nonlinear system of equations, $\acute{\mathbf{f}}\left(\bar{\mathbf{x}}\right) = \mathbf{0}$, can be iteratively solved using the Newton–Raphson method as

$$\left[\frac{\partial \acute{\mathbf{f}}\left(\bar{\mathbf{x}}\right)}{\partial \bar{\mathbf{x}}}\right]_{k+1}^{(h)} \Delta\bar{\mathbf{x}}_{k+1}^{(h)} = -\left[\acute{\mathbf{f}}\left(\bar{\mathbf{x}}\right)\right]_{k+1}^{(h)}, \tag{2.58}$$

where h is the iteration step, k is the time-step, $\left[\acute{\mathbf{f}}\left(\bar{\mathbf{x}}\right)\right]$ is the residual vector, $\left[\frac{\partial \acute{\mathbf{f}}(\bar{\mathbf{x}})}{\partial \bar{\mathbf{x}}}\right]$ is the tangent matrix, and $\Delta\bar{\mathbf{x}}$ is the difference in the vector of primary variables $\bar{\mathbf{x}}$. Here, $\left[\acute{\mathbf{f}}\left(\bar{\mathbf{x}}\right)\right]$ can be written as

$$\left[\acute{\mathbf{f}}\left(\bar{\mathbf{x}}\right)\right] = \frac{\Delta t^2}{4}\begin{bmatrix} \bar{\mathbf{M}}^{\Sigma}\ddot{\mathbf{z}} + \boldsymbol{\Phi}_{\mathbf{z}}^{\mathrm{T}}\alpha\boldsymbol{\Phi} + \boldsymbol{\Phi}_{\mathbf{z}}^{\mathrm{T}}\boldsymbol{\lambda} - \bar{\mathbf{Q}}^{\Sigma} \\ \dot{\mathbf{p}} - \mathbf{u}_0 \end{bmatrix} \tag{2.59}$$

(penalty-based semi-recursive approach),

$$\left[\acute{\mathbf{f}}\left(\bar{\mathbf{x}}\right)\right] = \frac{\Delta t^2}{4}\begin{bmatrix} \overline{\bar{\mathbf{M}}^{\Sigma}}\ddot{\mathbf{z}}^{\mathrm{i}} - \overline{\bar{\mathbf{Q}}^{\Sigma}} \\ \dot{\mathbf{p}} - \mathbf{u}_0 \end{bmatrix} \tag{2.60}$$

(double-step semi-recursive approach),

where $\boldsymbol{\lambda}$ is obtained as shown in Eq. (2.55), whereas the approximated tangent matrix $\left[\frac{\partial \acute{\mathbf{f}}(\bar{\mathbf{x}})}{\partial \bar{\mathbf{x}}}\right]$ can be obtained numerically using the forward differentiation rule as

$$\frac{d\acute{f}\left(\bar{x}_0\right)}{d\bar{x}} \approx \frac{\acute{f}\left(\bar{x}_0 + \epsilon\right) - \acute{f}\left(\bar{x}_0\right)}{\epsilon}, \tag{2.61}$$

where $\acute{f}\left(\cdot\right)$ is the nonlinear function, $\bar{x}_0$ is the point at which the derivative is approximated, and ϵ is the differentiation increment. Here, a central difference scheme may provide a better approximation of the tangent matrix and can be considered in future studies. To avoid ill-conditioning of the tangent matrix, ϵ is computed as in [55]

$$\epsilon = 1 \times 10^{-8} \max\left(1 \times 10^{-2}, \mid \bar{x}_0 \mid\right), \tag{2.62}$$

where 1×10^{-2} limits the minimum value for the differentiation increment to 1×10^{-10}. It should be noted that Eq. (2.62) is a modification of a method presented in [16]. In the penalty-based semi-recursive approach, the relative joint velocities and accelerations are corrected after every integration step using the projections shown in Eqs. (2.21) and (2.22).

2.4.2 Coupling for various friction models of a hydraulic cylinder

In a monolithic approach, the combined multibody and hydraulic models described in Eq. (2.55) is extended to incorporate the dynamics of friction models of a hydraulic cylinder described in Sect. 2.3. The external force vector $\bar{\mathbf{Q}}^{\Sigma}$ in Eq. (2.55) is incremented with the friction force models in Eqs. (2.42), (2.44), (2.47), and (2.54) leading to the coupled system of equations as

$$\left.\begin{aligned} \bar{\mathbf{M}}^{\Sigma}\ddot{\mathbf{z}} + \boldsymbol{\Phi}_{\mathbf{z}}^{\mathrm{T}}\alpha\boldsymbol{\Phi} + \boldsymbol{\Phi}_{\mathbf{z}}^{\mathrm{T}}\boldsymbol{\lambda} &= \bar{\mathbf{Q}}^{\Sigma}\left(\mathbf{z}, \dot{\mathbf{z}}, \mathbf{p}, \mathbf{F}_{\mu}\right) \\ \boldsymbol{\lambda}^{(h+1)} &= \boldsymbol{\lambda}^{(h)} + \alpha\boldsymbol{\Phi}^{(h+1)} \\ \dot{\mathbf{p}} &= \mathbf{u}_0\left(\mathbf{z}, \dot{\mathbf{z}}, \mathbf{p}\right) \end{aligned}\right\} \tag{2.63}$$

(Bengisu–Akay and Brown–McPhee approaches),

$$\left.\begin{aligned} \bar{\mathbf{M}}^{\Sigma}\ddot{\mathbf{z}} + \boldsymbol{\Phi}_{\mathbf{z}}^{\mathrm{T}}\alpha\boldsymbol{\Phi} + \boldsymbol{\Phi}_{\mathbf{z}}^{\mathrm{T}}\boldsymbol{\lambda} &= \bar{\mathbf{Q}}^{\Sigma}\left(\mathbf{z}, \dot{\mathbf{z}}, \mathbf{p}, \mathbf{F}_{\mu}\right) \\ \boldsymbol{\lambda}^{(h+1)} &= \boldsymbol{\lambda}^{(h)} + \alpha\boldsymbol{\Phi}^{(h+1)} \\ \dot{\mathbf{p}} &= \mathbf{u}_0\left(\mathbf{z}, \dot{\mathbf{z}}, \mathbf{p}\right) \\ \dot{\mathbf{q}} &= \mathbf{u}_1\left(\mathbf{z}, \dot{\mathbf{z}}, \mathbf{q}\right) \end{aligned}\right\} \tag{2.64}$$

(LuGre approach),

$$\left.\begin{aligned} \bar{\mathbf{M}}^{\Sigma}\ddot{\mathbf{z}} + \boldsymbol{\Phi}_{\mathbf{z}}^{\mathrm{T}}\alpha\boldsymbol{\Phi} + \boldsymbol{\Phi}_{\mathbf{z}}^{\mathrm{T}}\boldsymbol{\lambda} &= \bar{\mathbf{Q}}^{\Sigma}\left(\mathbf{z}, \dot{\mathbf{z}}, \mathbf{p}, \mathbf{F}_{\mu}\right) \\ \boldsymbol{\lambda}^{(h+1)} &= \boldsymbol{\lambda}^{(h)} + \alpha\boldsymbol{\Phi}^{(h+1)} \\ \dot{\mathbf{p}} &= \mathbf{u}_0\left(\mathbf{z}, \dot{\mathbf{z}}, \mathbf{p}\right) \\ \dot{\mathbf{q}} &= \mathbf{u}_2\left(\mathbf{z}, \dot{\mathbf{z}}, \mathbf{q}, \bar{\mathbf{h}}\right) \\ \dot{\bar{\mathbf{h}}} &= \mathbf{u}_3\left(\mathbf{z}, \dot{\mathbf{z}}, \bar{\mathbf{h}}\right) \end{aligned}\right\} \tag{2.65}$$

(modified LuGre approach),

where $\mathbf{u}_1$ and $\mathbf{u}_2$ are the respective equations of average bristle deflection variation in the LuGre and modified LuGre friction models, and $\mathbf{u}_3$ are the equations of lubricant film thickness variation in the modified LuGre friction model. It is assumed here that the dependency of $\bar{\mathbf{Q}}^{\Sigma}$ with respect to $\mathbf{z}$, $\dot{\mathbf{z}}$, $\mathbf{p}$, and $\mathbf{F}_{\mu}$ are known. It should be noted that the inclusion of static friction force $\mathbf{F}_{\mu}$ in Eq. (2.63) is a straightforward task because it is dependent only on $\mathbf{z}$ and $\dot{\mathbf{z}}$. Whereas for the LuGre and modified LuGre approaches, the inclusion of friction force $\mathbf{F}_{\mu}$ requires extra state variables as shown in Eqs. (2.64) and (2.65). The use of dynamic friction models can introduce numerical stiffness to the system, which may decrease the numerical efficiency of the simulation.

The frictional state variables $\mathbf{q}$ and $\bar{\mathbf{h}}$ in Eqs. (2.64) and (2.65) can be integrated over time either with the equations of motion as shown in Eqs. (2.64) and (2.65), or they can be integrated locally during resolution of the friction problem. In this study, all the coupled models above are integrated using an implicit single-step trapezoidal rule [44] as in Sect. 2.4.1. Accordingly, the average bristle deflection and the lubricant film thickness are considered primary variables when applying the trapezoidal rule. By applying the

trapezoidal rule to Eqs. (2.63), (2.64), and (2.65), a set of nonlinear system of equations are formed that can be denoted as $\acute{\mathbf{f}}(\bar{\mathbf{x}}) = \mathbf{0}$ such that

$$\left.\begin{array}{l} \bar{\mathbf{x}} = \left[\mathbf{z}^{\mathrm{T}},\ \mathbf{p}^{\mathrm{T}}\right]^{\mathrm{T}} \\ \quad \text{(Bengisu–Akay and Brown–McPhee approaches)} \\ \bar{\mathbf{x}} = \left[\mathbf{z}^{\mathrm{T}},\ \mathbf{p}^{\mathrm{T}},\ \mathbf{q}^{\mathrm{T}}\right]^{\mathrm{T}} \\ \quad \text{(LuGre approach)} \\ \bar{\mathbf{x}} = \left[\mathbf{z}^{\mathrm{T}},\ \mathbf{p}^{\mathrm{T}},\ \mathbf{q}^{\mathrm{T}},\ \bar{\mathbf{h}}^{\mathrm{T}}\right]^{\mathrm{T}} \\ \quad \text{(modified LuGre approach)} \end{array}\right\}. \tag{2.66}$$

Such nonlinear systems of equations, $\acute{\mathbf{f}}(\bar{\mathbf{x}}) = \mathbf{0}$, can be iteratively solved using the Newton–Raphson method as in Eq. (2.58), where the residual vector $\left[\acute{\mathbf{f}}(\bar{\mathbf{x}})\right]$ can be written as

$$\left[\acute{\mathbf{f}}(\bar{\mathbf{x}})\right] = \frac{\Delta t^2}{4}\begin{bmatrix} \bar{\mathbf{M}}^{\Sigma}\ddot{\mathbf{z}} + \boldsymbol{\Phi}_{\mathbf{z}}^{\mathrm{T}}\alpha\boldsymbol{\Phi} + \boldsymbol{\Phi}_{\mathbf{z}}^{\mathrm{T}}\boldsymbol{\lambda} - \bar{\mathbf{Q}}^{\Sigma} \\ \dot{\mathbf{p}} - \mathbf{u}_0 \end{bmatrix} \tag{2.67}$$

(Bengisu–Akay and Brown–McPhee approaches),

$$\left[\acute{\mathbf{f}}(\bar{\mathbf{x}})\right] = \frac{\Delta t^2}{4}\begin{bmatrix} \bar{\mathbf{M}}^{\Sigma}\ddot{\mathbf{z}} + \boldsymbol{\Phi}_{\mathbf{z}}^{\mathrm{T}}\alpha\boldsymbol{\Phi} + \boldsymbol{\Phi}_{\mathbf{z}}^{\mathrm{T}}\boldsymbol{\lambda} - \bar{\mathbf{Q}}^{\Sigma} \\ \dot{\mathbf{p}} - \mathbf{u}_0 \\ \dot{\mathbf{q}} - \mathbf{u}_1 \end{bmatrix} \tag{2.68}$$

(LuGre approach),

$$\left[\acute{\mathbf{f}}(\bar{\mathbf{x}})\right] = \frac{\Delta t^2}{4}\begin{bmatrix} \bar{\mathbf{M}}^{\Sigma}\ddot{\mathbf{z}} + \boldsymbol{\Phi}_{\mathbf{z}}^{\mathrm{T}}\alpha\boldsymbol{\Phi} + \boldsymbol{\Phi}_{\mathbf{z}}^{\mathrm{T}}\boldsymbol{\lambda} - \bar{\mathbf{Q}}^{\Sigma} \\ \dot{\mathbf{p}} - \mathbf{u}_0 \\ \dot{\mathbf{q}} - \mathbf{u}_2 \\ \dot{\bar{\mathbf{h}}} - \mathbf{u}_3 \end{bmatrix} \tag{2.69}$$

(modified LuGre approach),

such that $\boldsymbol{\lambda}$ is obtained as shown in Eq. (2.20), and the approximated tangent matrix can be obtained numerically using Eqs. (2.61) and (2.62).

3 State estimator based on an indirect Kalman filter

In this study, the state estimator is based on the well-known extended Kalman filter [64, 34]. However, an indirect (error-state) filtering approach is used here [59, 62]. In indirect filters, the errors of state variables are estimated instead of directly estimating the state variables. In this approach, a coupled multibody simulation model is run without modifications and the indirect filter estimates the drift of this simulation model with respect to the available measurements. After every measurement, the simulation model is corrected with the estimated errors as shown in Fig. 3.1. This filtering approach allows one to use any coupled multibody formulation and integrator. However, some terms of the coupled multibody formulations can be used to propagate the covariance matrix of the estimation error and to map the sensor models into independent coordinates space.

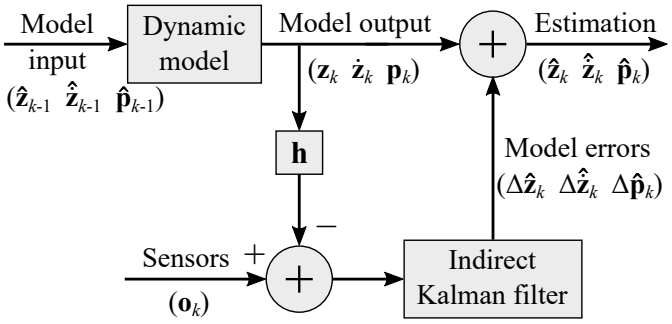

Figure 3.1: Simplified scheme of the indirect Kalman filter in a time-step k.

3.1 Error-state extended Kalman filter

In this approach, one step of a coupled multibody model is first simulated in each time-step obtaining the positions, velocities, and pressures as $\mathbf{z}$, $\dot{\mathbf{z}}$, and $\mathbf{p}$, respectively. Next, the estimation algorithm is performed on a state vector, $\mathbf{x}$, that can be written as

$$\mathbf{x} = \left[\left(\Delta\mathbf{z}^{\mathrm{i}}\right)^{\mathrm{T}}, \left(\Delta\dot{\mathbf{z}}^{\mathrm{i}}\right)^{\mathrm{T}}, (\Delta\mathbf{p})^{\mathrm{T}} \right]^{\mathrm{T}}, \tag{3.1}$$

which consists of the errors in the independent positions, independent velocities, and pressures, respectively. The filter algorithm consists of two stages as a prediction stage (state-transition) and a correction stage (state-update) [67]. The prediction stage relies on the transition model of the dynamic system, while the correction stage relies on the information from the measurements.

The prediction stage in a time-step k can be performed as [62, 63]

$$\hat{\mathbf{x}}_k^- = \mathbf{0}, \tag{3.2}$$

$$\mathbf{P}_k^- = (\mathbf{f_x})_{k-1}\,\mathbf{P}_{k-1}^+\,(\mathbf{f_x})_{k-1}^{\mathrm{T}} + \left(\sum^P\right)_{k-1}, \tag{3.3}$$

where $\hat{\mathbf{x}}^-$ and $\hat{\mathbf{x}}^+$ are the respective predicted and corrected means of the state that are also called 'a priori' and 'a posteriori' state estimations, respectively, $\mathbf{P}^-$ and $\mathbf{P}^+$ are their respective associated covariance matrices, $\mathbf{f_x}$ is the Jacobian matrix of the transition model $\bar{\mathbf{f}}(\cdot)$, and $\sum^P$ is the covariance matrix of the plant noise describing additional uncertainties. Here, the simulation model is assumed to do a perfect work in tracking the real system, thus, $\hat{\mathbf{x}}_k^-$ is always null. The value of $\sum^P$ is physically attributed to the incorrect forces and errors in modeling, such as incorrect inertia values and initial conditions. The transition matrix, $\mathbf{f_x}$, which follows a forward Euler integration can be written as

$$\mathbf{f_x} = \frac{\partial}{\partial\{\hat{\mathbf{z}}^{\mathrm{i}}, \hat{\dot{\mathbf{z}}}^{\mathrm{i}}, \hat{\mathbf{p}}\}} \begin{bmatrix} \hat{\mathbf{z}}^{\mathrm{i}} + \Delta t\hat{\dot{\mathbf{z}}}^{\mathrm{i}} + \frac{1}{2}\Delta t^2\hat{\ddot{\mathbf{z}}}^{\mathrm{i}} \\ \hat{\dot{\mathbf{z}}}^{\mathrm{i}} + \Delta t\hat{\ddot{\mathbf{z}}}^{\mathrm{i}} \\ \hat{\mathbf{p}} + \Delta t\dot{\mathbf{p}} \end{bmatrix} \simeq \left[\begin{array}{c|c|c} \mathbf{I}_{N_f} + \frac{1}{2}\frac{\partial\Delta\ddot{\mathbf{z}}^{\mathrm{i}}}{\partial\mathbf{z}^{\mathrm{i}}}\Delta t^2 & \mathbf{I}_{N_f}\Delta t + \frac{1}{2}\frac{\partial\Delta\ddot{\mathbf{z}}^{\mathrm{i}}}{\partial\dot{\mathbf{z}}^{\mathrm{i}}}\Delta t^2 & \frac{1}{2}\frac{\partial\Delta\ddot{\mathbf{z}}^{\mathrm{i}}}{\partial\mathbf{p}}\Delta t^2 \\ \hline \frac{\partial\Delta\ddot{\mathbf{z}}^{\mathrm{i}}}{\partial\mathbf{z}^{\mathrm{i}}}\Delta t & \mathbf{I}_{N_f} + \frac{\partial\Delta\ddot{\mathbf{z}}^{\mathrm{i}}}{\partial\dot{\mathbf{z}}^{\mathrm{i}}}\Delta t & \frac{\partial\Delta\ddot{\mathbf{z}}^{\mathrm{i}}}{\partial\mathbf{p}}\Delta t \\ \hline \mathbf{0}_{n_p\times N_f} & \mathbf{0}_{n_p\times N_f} & \mathbf{I}_{n_p} \end{array}\right], \tag{3.4}$$

where $\mathbf{0}$ is a zero matrix, n_p is the number of hydraulic pressures, and the terms $\frac{\partial\Delta\ddot{\mathbf{z}}^{\mathrm{i}}}{\partial\mathbf{z}^{\mathrm{i}}}$, $\frac{\partial\Delta\ddot{\mathbf{z}}^{\mathrm{i}}}{\partial\dot{\mathbf{z}}^{\mathrm{i}}}$, and $\frac{\partial\Delta\ddot{\mathbf{z}}^{\mathrm{i}}}{\partial\mathbf{p}}$ consider the variation of the acceleration error with the position, velocity, and pressure errors. The blocks in position $(3,1)$ and $(3,2)$ of Eq. (3.4) are set to $\mathbf{0}$ because the evolution of the pressure error is unknown. Furthermore, it is assumed for simplicity that $\frac{\partial\Delta\dot{\mathbf{p}}}{\partial\mathbf{p}} = \mathbf{0}$. For complex force models, the partial derivatives in Eq. (3.4) can be computed numerically using the forward differentiation rule as in this study.

The correction stage in a time-step k can be performed as [62, 63]

$$\mathbf{y}_k = \mathbf{o}_k - \mathbf{h}\left(\mathbf{z}_k, \dot{\mathbf{z}}_k, \mathbf{p}_k\right), \tag{3.5}$$

$$\mathbf{S}_k = (\mathbf{h_x})_k\,\mathbf{P}_k^-\,(\mathbf{h_x})_k^{\mathrm{T}} + \left(\sum^S\right)_k, \tag{3.6}$$

$$\mathbf{K}_k = \mathbf{P}_k^-\,(\mathbf{h_x})_k^{\mathrm{T}}\,\mathbf{S}_k^{-1}, \tag{3.7}$$

$$\hat{\mathbf{x}}_k^+ = \mathbf{0} + \mathbf{K}_k\mathbf{y}_k, \tag{3.8}$$

$$\mathbf{P}_k^+ = \left[\mathbf{I}_{(2N_f+n_p)} - \mathbf{K}_k\,(\mathbf{h_x})_k\right]\mathbf{P}_k^-, \tag{3.9}$$

where $\mathbf{y}$ is the innovation vector, $\mathbf{S}$ is its associated covariance matrix, $\mathbf{o}$ is the actual measurement vector, $\mathbf{h}(\cdot)$ and $\mathbf{h_x}$ are the measurement model and its Jacobian matrix, respectively, $\sum^S$ is the covariance matrix of the measurement noise, and $\mathbf{K}$ is the Kalman gain matrix. It should be noted that the virtual measurements are built using the positions, velocities, and pressures of the coupled multibody model instead of the filter states. Furthermore, $\mathbf{h_x}$ is obtained as in an equivalent conventional Kalman filter because the partial derivatives with respect to the state errors have the same value as with respect to the states.

After the correction stage, the estimated errors of the independent positions, independent velocities, and pressures are obtained as $\Delta\hat{\mathbf{z}}^{\mathrm{i}}$, $\Delta\hat{\dot{\mathbf{z}}}^{\mathrm{i}}$, and $\Delta\hat{\mathbf{p}}$, respectively. Accordingly, the

independent positions, independent velocities, and pressures are estimated as

$$\left.\begin{aligned} \hat{\mathbf{z}}^{\mathrm{i}}_k &= \mathbf{z}^{\mathrm{i}}_k + \Delta\hat{\mathbf{z}}^{\mathrm{i}}_k \\ \hat{\dot{\mathbf{z}}}^{\mathrm{i}}{}_k &= \dot{\mathbf{z}}^{\mathrm{i}}_k + \Delta\hat{\dot{\mathbf{z}}}^{\mathrm{i}}{}_k \\ \hat{\mathbf{p}}_k &= \mathbf{p}_k + \Delta\hat{\mathbf{p}}_k \end{aligned}\right\}, \tag{3.10}$$

where $\mathbf{z}^{\mathrm{i}}$, $\dot{\mathbf{z}}^{\mathrm{i}}$, and $\mathbf{p}$ are the respective independent positions, independent velocities, and pressures predicted by the simulation model (the coupled multibody model) prior to corrections, and $\hat{\mathbf{z}}^{\mathrm{i}}$, $\hat{\dot{\mathbf{z}}}^{\mathrm{i}}$, and $\hat{\mathbf{p}}$ are their estimated values, respectively.

To update the output of the coupled multibody model, the errors of all the dependent positions and dependent velocities can be obtained using the constraints manifold. The position problem should be solved iteratively, however, it can be computationally expensive. As the corrections in this study are expected to be small, a linearization of the position problem is solved as

$$\boldsymbol{\Phi}_{\mathbf{z}}\Delta\mathbf{z} = \mathbf{0}. \tag{3.11}$$

Accordingly, the complete set of the estimated error of positions can be written as

$$\Delta\hat{\mathbf{z}}^{\mathrm{d}} = -\left(\boldsymbol{\Phi}^{\mathrm{d}}_{\mathbf{z}}\right)^{-1}\boldsymbol{\Phi}^{\mathrm{i}}_{\mathbf{z}}\Delta\hat{\mathbf{z}}^{\mathrm{i}}, \tag{3.12}$$

$$\Delta\hat{\mathbf{z}} = \left[\left(\Delta\hat{\mathbf{z}}^{\mathrm{d}}\right)^{\mathrm{T}}, \left(\Delta\hat{\mathbf{z}}^{\mathrm{i}}\right)^{\mathrm{T}}\right]^{\mathrm{T}}, \tag{3.13}$$

where $\Delta\hat{\mathbf{z}}^{\mathrm{d}}$ is the estimated error of the dependent positions. Therefore, the position output from the coupled multibody model is updated as

$$\hat{\mathbf{z}}_k = \mathbf{z}_k + \Delta\hat{\mathbf{z}}_k, \tag{3.14}$$

where $\hat{\mathbf{z}}$ are the estimated positions. This approach of solving the position problem is an approximation, and thus, a perfect fulfillment of the position constraints is not expected. However, this approach is usually acceptable for most applications because the corrections are performed at every time-step [62]. Nevertheless, the exact position problem must be solved when the highest possible accuracy is required. After the positions update, the velocity output from the coupled multibody model is updated using the velocity problem as

$$\hat{\dot{\mathbf{z}}}^{\mathrm{d}} = -\left(\boldsymbol{\Phi}^{\mathrm{d}}_{\mathbf{z}}\right)^{-1}\boldsymbol{\Phi}^{\mathrm{i}}_{\mathbf{z}}\hat{\dot{\mathbf{z}}}^{\mathrm{i}}, \tag{3.15}$$

$$\hat{\dot{\mathbf{z}}}_k = \left[\left(\hat{\dot{\mathbf{z}}}^{\mathrm{d}}{}_k\right)^{\mathrm{T}}, \left(\hat{\dot{\mathbf{z}}}^{\mathrm{i}}{}_k\right)^{\mathrm{T}}\right]^{\mathrm{T}}, \tag{3.16}$$

where $\hat{\dot{\mathbf{z}}}^{\mathrm{d}}$ are the estimated dependent velocities and $\hat{\dot{\mathbf{z}}}$ are the estimated velocities. Once the output from the simulation model is updated, the expected errors for the next time-step become null, that is, $\hat{\mathbf{x}}^{-}_{k+1} = \mathbf{0}$.

3.2 Covariance matrices of plant and measurement noises

In the application of the Kalman filter, the tuning of the algorithm parameters is paramount, especially, the covariance matrices of the plant and measurement noises. In dealing with nonlinear systems, an improper tuning of these matrices can make an estimator unstable even if all other filter parameters are suitably tuned.

3.2.1 Structure of plant noise

In multibody modeling, geometrical properties can be accurately defined, however, modeling of forces and mass distributions may be cumbersome. Consequently, the model deviates from reality and errors occur at the acceleration level. Therefore, only the acceleration noise is included in the plant noise of a multibody model as in [62, 63]. It should be noted that additional integrator errors or multibody formulation errors are assumed to be negligible compared with the previous errors. The structure of $\sum^P$ for a multibody model with the position and velocity estimations in a discrete filter can be computed as [63]

$$\sum^P = \begin{bmatrix} \sigma^2_{\ddot{\mathbf{z}}} \frac{\Delta t^3}{3} \mathbf{I}_{N_f} & \sigma^2_{\ddot{\mathbf{z}}} \frac{\Delta t^2}{2} \mathbf{I}_{N_f} \\ \sigma^2_{\ddot{\mathbf{z}}} \frac{\Delta t^2}{2} \mathbf{I}_{N_f} & \sigma^2_{\ddot{\mathbf{z}}} \Delta t \mathbf{I}_{N_f} \end{bmatrix}, \tag{3.17}$$

where $\sigma^2_{\ddot{\mathbf{z}}}$ is the variance at the acceleration level introduced in a continuous filter. In a coupled multibody model, the pressure noise from the hydraulic subsystem can be directly introduced in the discrete filter, that is, in Eq. (3.17), as

$$\sum^P = \begin{bmatrix} \sigma^2_{\ddot{\mathbf{z}}} \frac{\Delta t^3}{3} \mathbf{I}_{N_f} & \sigma^2_{\ddot{\mathbf{z}}} \frac{\Delta t^2}{2} \mathbf{I}_{N_f} & \mathbf{0}_{N_f \times n_p} \\ \sigma^2_{\ddot{\mathbf{z}}} \frac{\Delta t^2}{2} \mathbf{I}_{N_f} & \sigma^2_{\ddot{\mathbf{z}}} \Delta t \mathbf{I}_{N_f} & \mathbf{0}_{N_f \times n_p} \\ \mathbf{0}_{n_p \times N_f} & \mathbf{0}_{n_p \times N_f} & \sigma^2_{\mathbf{p},D} \mathbf{I}_{n_p} \end{bmatrix}, \tag{3.18}$$

where $\sigma^2_{\mathbf{p},D}$ is the variance at the pressure level. The values of $\sigma^2_{\ddot{\mathbf{z}}}$ and $\sigma^2_{\mathbf{p},D}$ are tuned by trial and error, and $\sigma^2_{\mathbf{p},D}$ should be modified proportional to the simulation time-step.

3.2.2 Structure of measurement noise

In this study, measurements are obtained from a simulation model, which acts as a real system providing the ground truth, with an addition of white Gaussian noise to imitate the noise properties of real sensors. Thus, the noise properties are perfectly known, and they can be used to obtain the covariance matrix of the measurement noise as a diagonal matrix. The structure of $\sum^S$ with the position and pressure sensors can be written as

$$\sum^S = \begin{bmatrix} \left(\sigma'_{\mathbf{z}}\right)^2 \mathbf{I}_{N_f} & \mathbf{0}_{N_f \times n_p} \\ \mathbf{0}_{n_p \times N_f} & \left(\sigma'_{\mathbf{p}}\right)^2 \mathbf{I}_{n_p} \end{bmatrix}, \tag{3.19}$$

where $\sigma'_{\mathbf{z}}$ and $\sigma'_{\mathbf{p}}$ are the standard deviations of the measurement noise at the position and pressure levels, respectively.

4 Tests and results

This section presents a summary of simulation results obtained in **Publications I** to **VI** by implementing the proposed methods in the respective numerical examples. **Publications I** and **II** employed the approaches proposed in Sects. 2.4.1 and 2.4.2, respectively. **Publication III** applied the state estimator proposed in Sect. 3 for hydraulically driven systems. Even though planar mechanisms are illustrated in the above three publications, general methods are presented in this study that can be applied to three-dimensional mechanisms as well. Furthermore, **Publications IV** to **VI** employed the penalty method introduced in Sect. 2.1.5 for the multibody modeling and hydraulic actuators are modeled as illustrated in Sect. 2.2. For the detailed implementation of numerical simulation examples, the reader is referred to the respective publication provided at the end of the dissertation.

4.1 Comparing semi-recursive multibody formulations

This subsection presents a summary of comparing the double-step and penalty-based semi-recursive formulations (the coordinate partitioning and augmented Lagrangian with projections methods) in the framework of monolithically coupled hydraulic actuators. The detailed results can be found in **Publication I**, where hydraulically actuated four-bar and quick-return mechanisms shown in Figs. 4.1 and 4.2, respectively, are considered as case studies. A hydraulic cylinder is attached between points F and G in Fig. 4.1 and between points N and Q in Fig. 4.2. The cylinder length l is the sum of the respective chamber lengths l_2 and l_3, and $\mathbf{s}$ is the actuator length vector. In Figs. 4.1 and 4.2, p_P and p_T are the respective pump and tank pressures, and Q_{d1} and Q_{3d} are the volume flow rates across ports A, B, P, and T. In **Publication I**, the two coupled multibody approaches, namely, the double-step and penalty-based semi-recursive approaches, are compared based on the simulation work cycle, energy balance, constraint violation, and numerical efficiency.

In the presented case studies, the relative joint coordinates in both approaches showed a good agreement with respect to each other. Whereas the respective hydraulic pressures in both approaches were identical because the same hydraulic circuit was used. The independent coordinates in the double-step approach are identified using the Gaussian elimination with full pivoting technique because their inadequate identification leads to ill-conditioned matrices, thus, causing integration errors. The adequate identification of the independent and dependent coordinates in the double-step approach is therefore considered a relative drawback, compared with the penalty-based approach, because the latter utilizes a full set of coordinates.

The energy balance computed using the kinetic energy, potential energy, and actuator work in both approaches demonstrated a relatively good agreement as shown in Fig. 4.3. In Fig. 4.3, the directional control valve openings are highlighted in purple and cyan for the respective mechanisms. In both approaches, the constraints are fulfilled with good accuracy for both the mechanisms. The relative advantage of the double-step approach is the fulfillment of constraints to the level of machine precision or the predefined precision,

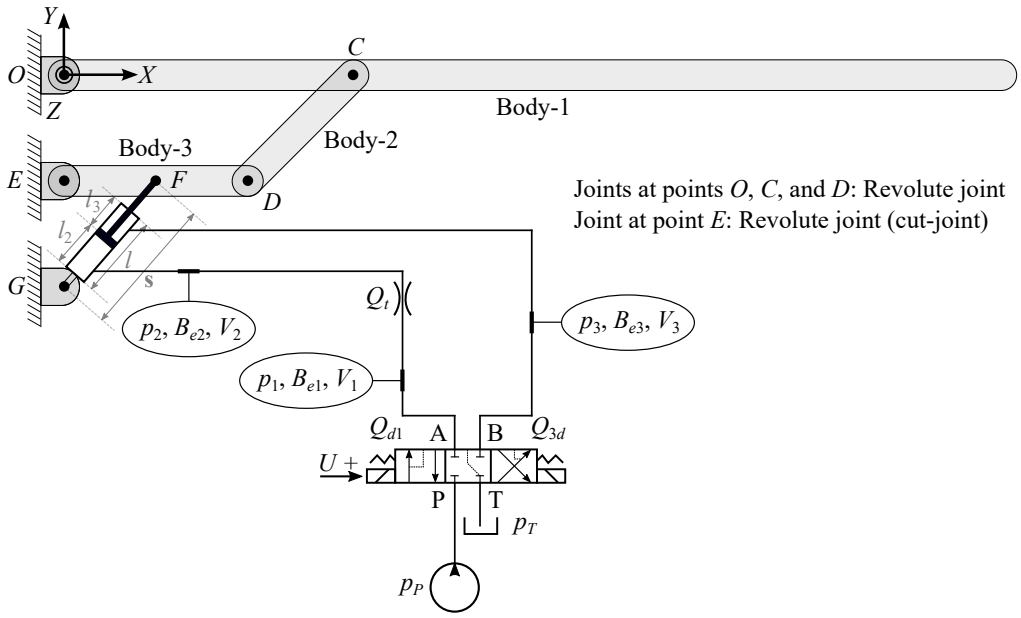

Figure 4.1: A hydraulically actuated four-bar mechanism used in **Publication I**.

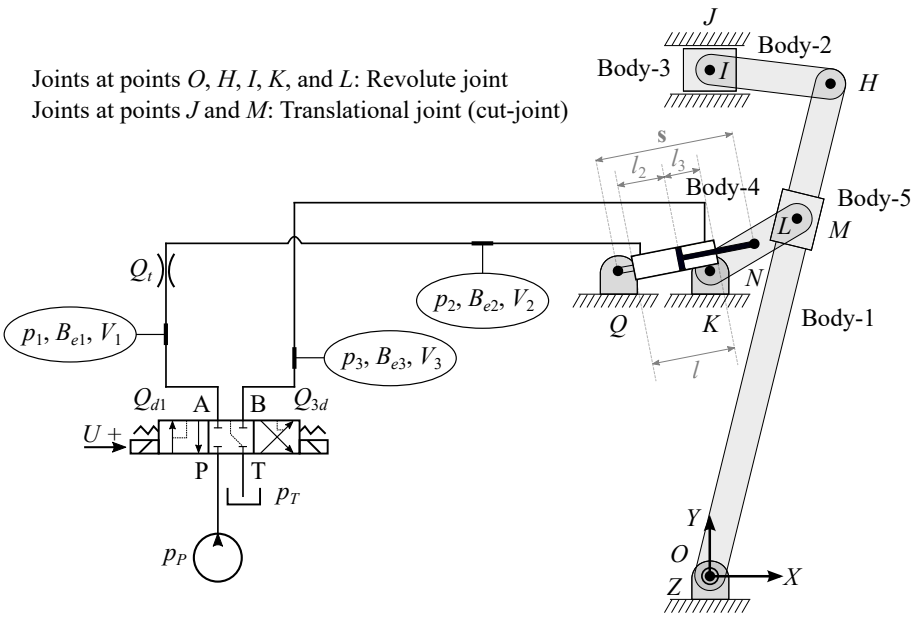

Figure 4.2: A hydraulically actuated quick-return mechanism used in **Publication I**.

thus, maintaining a good error control. The penalty-based approach is relatively more relaxed on the fulfillment of constraints and it can be improved using a larger penalty factor, but it will introduce some numerical ill-conditioning. The relative disadvantage in the double-step approach is the assumption that redundant constraints and singular configurations do not exist. The penalty-based approach, however, can handle redundant constraints and can deliver accurate solutions in the vicinity of singular configurations [30].

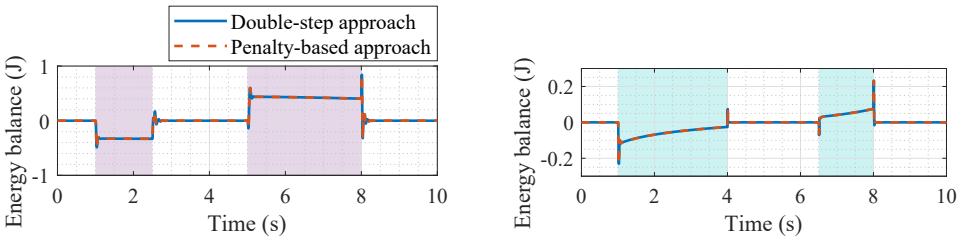

Figure 4.3: Comparison of energy balances in the double-step and penalty-based approaches with a time-step of 1 ms. (a) Four-bar mechanism. (b) Quick-return mechanism.

For the presented case studies, the numerical efficiencies of both approaches are compared in Fig. 4.4. The maximum iterations in both approaches occurred during the opening and closing of the directional control valve. Even though the average iterations in the double-step approach were lower than the penalty-based approach, its integration time was relatively greater and it is in accordance with the literature [30, 48]. The poor numerical efficiency of the double-step approach is attributed to the iterative solution of the position problem. It should be noted that the implementations in **Publication I** are performed in the Matlab environment, and therefore, the numerical efficiency results may be unreliable. The numerical efficiencies and real-time capabilities of both approaches can be investigated by implementing them in a lower-level programming language, such as C or Fortran, and it is expected to produce a generalized evaluation on real-time capabilities.

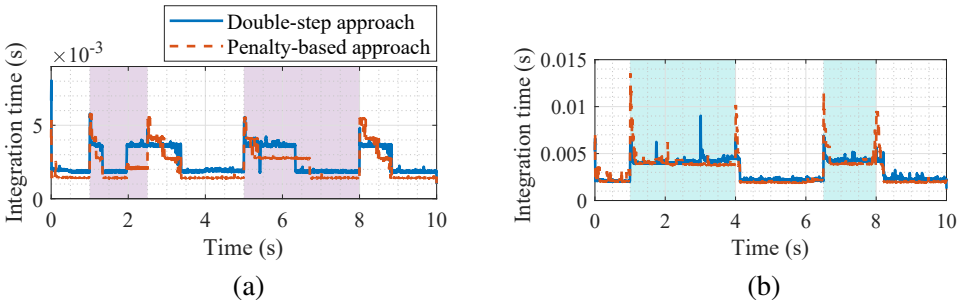

Figure 4.4: Comparison of numerical efficiencies with a time-step of 1 ms. (a) Four-bar mechanism. (b) Quick-return mechanism.

4.2 Comparing friction models of a hydraulic cylinder

This subsection presents a summary of comparing various friction models of a hydraulic cylinder in the framework of monolithically coupled multibody and hydraulic models. The detailed results can be found in **Publication II**, where a hydraulically actuated four-bar mechanism shown in Fig. 4.5 is considered as a case study. The hydraulic circuit used in this case is identical to the one used in **Publication I** described in Sect. 4.1. In **Publication II**, the four coupled system approaches, namely, the Bengisu–Akay, Brown–McPhee, LuGre, and modified LuGre approaches are compared based on the simulation work cycle, friction force, energy balance, and numerical efficiency.

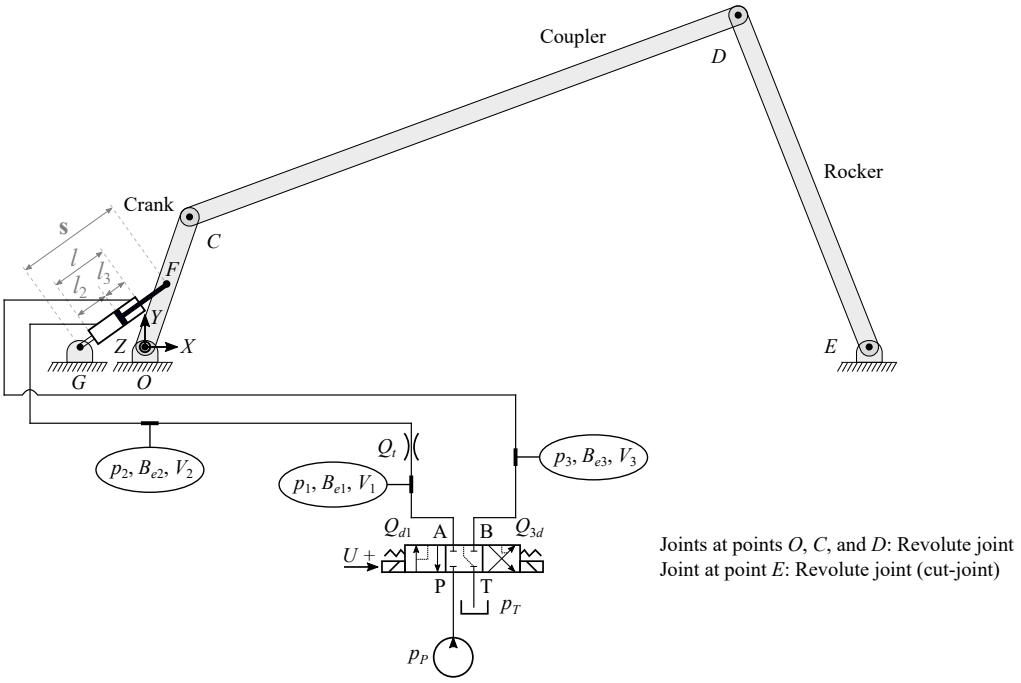

Figure 4.5: A hydraulically actuated four-bar mechanism used in **Publication II**.

In the presented case study, the selection of different friction models caused relatively small differences in relative joint coordinates and hydraulic pressures. Such small differences can be an important aspect to consider in applications where high precision and/or low vibration is a prerequisite. Thus, a friction model may significantly affect the control system performance. Furthermore, the energy balance in all four approaches showed a good agreement with respect to each other. In the static and dynamic friction approaches, the respective peak energy drifts are 0.37% and 0.36% of the respective maximum cylinder work. It occurred at the opening of the directional control valve at around 1 s. The hydraulic system is analogous to a stiff spring supporting the four-bar structure.

A comparison of the friction force models of the hydraulic cylinder is shown in Fig. 4.6a. All friction models are continuous at zero relative piston velocity avoiding numerical instabilities. The friction–velocity characteristics in the Bengisu–Akay and Brown–McPhee approaches match with their definitions incorporating the Coulomb, stiction, Stribeck, and viscous friction effects. Whereas the LuGre and modified LuGre approaches incorporate the pre-slip displacement and the frictional lag. The pre-slip displacement can help to determine the static friction as well as the Stribeck effect in the steady state.

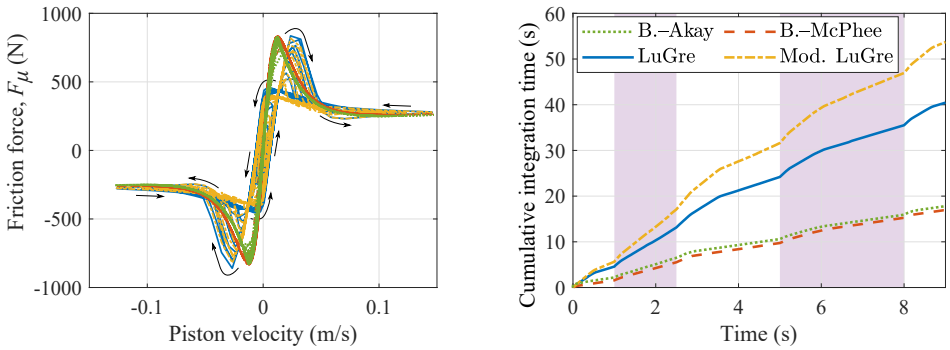

Figure 4.6: Comparison of friction models-based four coupled system approaches with a time-step of 1 ms. (a) Friction force characteristic. (b) Numerical efficiency.

For the presented case study, the numerical efficiencies of all four approaches are compared in Fig. 4.6b and Table 4.1. All the approaches are implemented in the Matlab environment. In Fig. 4.6b, the directional control valve openings are highlighted in purple. The maximum iterations occurred during the opening and closing of the directional control valve. The poorest numerical efficiency of the modified LuGre approach is attributed to the use of two frictional state variables. It is followed by the LuGre approach. The poor numerical efficiency of the Bengisu–Akay approach is attributed to a change in friction equations during simulation. The Brown–McPhee approach is relatively the most efficient approach and it is a potential candidate for real-time applications [17]. Real-time capabilities of the Brown–McPhee approach can be investigated by implementing it in a lower-level programming language, such as C or Fortran.

Table 4.1: Comparison of iterations and the integration time.

Approach	Average iterations	Maximum iterations	Integration time
B.–Akay	1.43	3	17.81 s
B.–McPhee	1.42	3	16.97 s
LuGre	1.60	3	40.45 s
Mod. LuGre	1.62	5	53.72 s

4.3 State estimator for coupled multibody and hydraulics models

This subsection presents a summary of the state estimator developed by combining a coupled multibody model with an error-state extended Kalman filter in the framework of hydraulically driven systems. The detailed results can be found in **Publication III**, where a hydraulically actuated four-bar mechanism shown in Fig. 4.7 is considered as a case study. The hydraulic circuit used in this case is similar to the one used in **Publication II** described in Sect. 4.2. In **Publication III**, the state estimator considered four sensor configurations as shown in Table 4.2 at four different sampling rates of the sensors (100 Hz, 200 Hz, 500 Hz, and 1000 Hz). The estimator is evaluated based on the accuracy of the work cycle and hydraulic pressures.

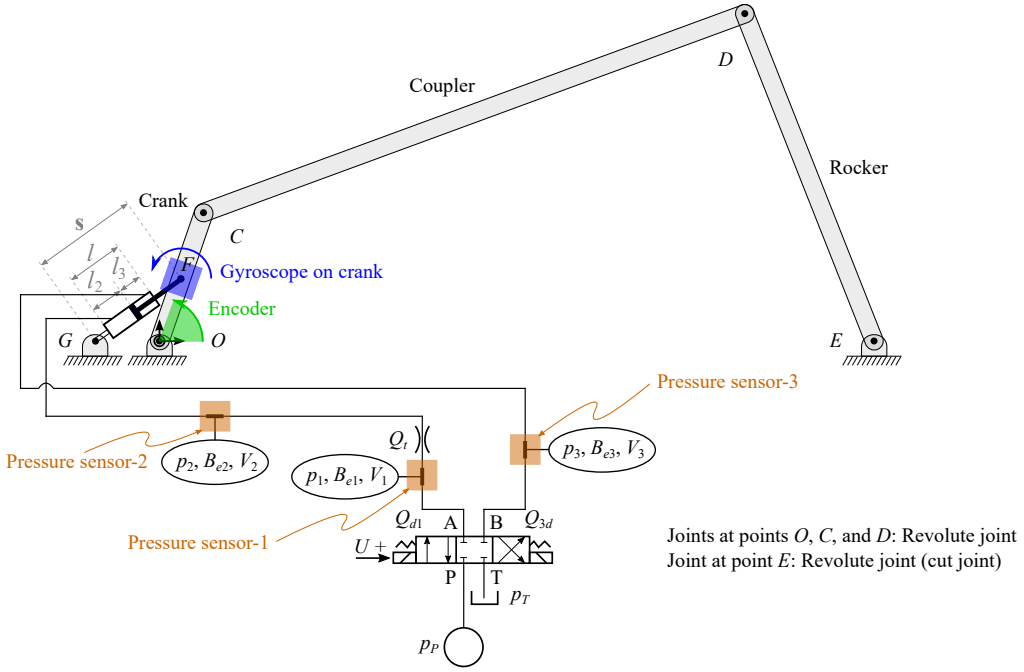

Figure 4.7: A hydraulically actuated four-bar mechanism used in **Publication III**.

Table 4.2: Sensor combinations used in **Publication III**.

	Position sensor	Velocity sensor	Pressure sensors
Sensor set-1	Crank	-	p_1, p_2, and p_3
Sensor set-2	Crank	Crank	p_1, p_2, and p_3
Sensor set-3	Crank	Crank	p_1 and p_2
Sensor set-4	Crank	Crank	p_1 and p_3

In the presented case study, the root-mean-square errors of the state estimations are computed for four sensor configurations at different sampling rates. The root-mean-square errors are computed in % with respect to the absolute maximum values of the real system. It is observed that the sensor configuration that utilized all the sensors (sensor set-2) provided a relatively better estimation. Furthermore, the estimation accuracy degraded with the lower sampling rates of the sensors. It should be noted that the different sensor combinations are tested under the same conditions of the plant noise.

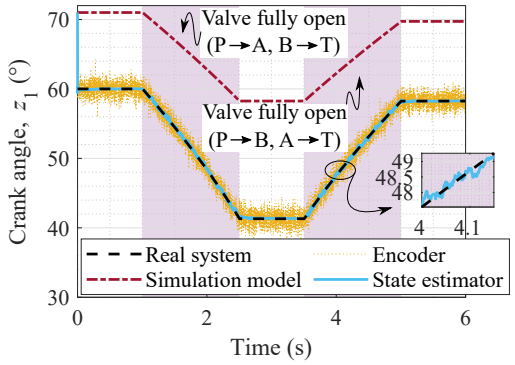

Figure 4.8: Comparison of the crank angle with sensor set-1 providing data at 1000 Hz.

The accuracy of the crank angle estimation with sensor set-1 is shown in Fig. 4.8. The state estimator provided a more accurate estimation of the crank angle compared to the encoder measurement as shown in Fig. 4.8. Furthermore, the 95% confidence interval was consistent with the estimations, that is, it shrank with accurate estimations and it grew by less accurate estimations. The 95% confidence interval is computed as $\pm 1.96\sigma$, where σ is the standard deviation computed from the covariance matrix $\mathbf{P}^+$ of the associated estimation. The estimations at the position and velocity levels are further improved by adding a velocity sensor (gyroscope) from sensor set-1 to sensor set-2. At 200 Hz sampling rate of the sensors in sensor set-1, an expected behavior of a saw-tooth shape of the 95% confidence interval is observed. It implies that the covariance grows when there are no measurements and it shrinks when there are measurements available.

Similarly, the accuracy of the hydraulic pressure estimations is provided in **Publication III**. It is observed that the estimations of the hydraulic pressures are slightly improved in comparison with the pressure sensor measurements. It should be noted that the use of a velocity sensor (gyroscope on the crank) in sensor sets 3 and 4 enabled the removal of a pressure sensor from either end of the hydraulic cylinder in sensor set-1, which would otherwise have been difficult. At a lower sensor sampling rate (200 Hz), the 95% confidence interval of the pressure estimations follows a similar saw-tooth shape evolution as in the case of position and velocity estimations.

4.4 Real-time multibody model-based heads-up display of a tractor

This subsection presents a summary of introducing a detailed real-time multibody model-based heads-up display unit. The detailed results can be found in **Publication IV**, where a tractor model shown in Fig. 4.9 is considered as a case study. The tractor model has nine degrees of freedom where the lifting and tilting of the front-loader are controlled using hydraulic actuators. In **Publication IV**, the elements of the HUD unit include a tachometer, speedometer, roll inclinometer, gear indicator, fuel gauge, and bucket height, tilt, and weight indicators as shown in Fig. 4.10. The utility of the HUD unit is demonstrated by a goal of moving sand from one location to another.

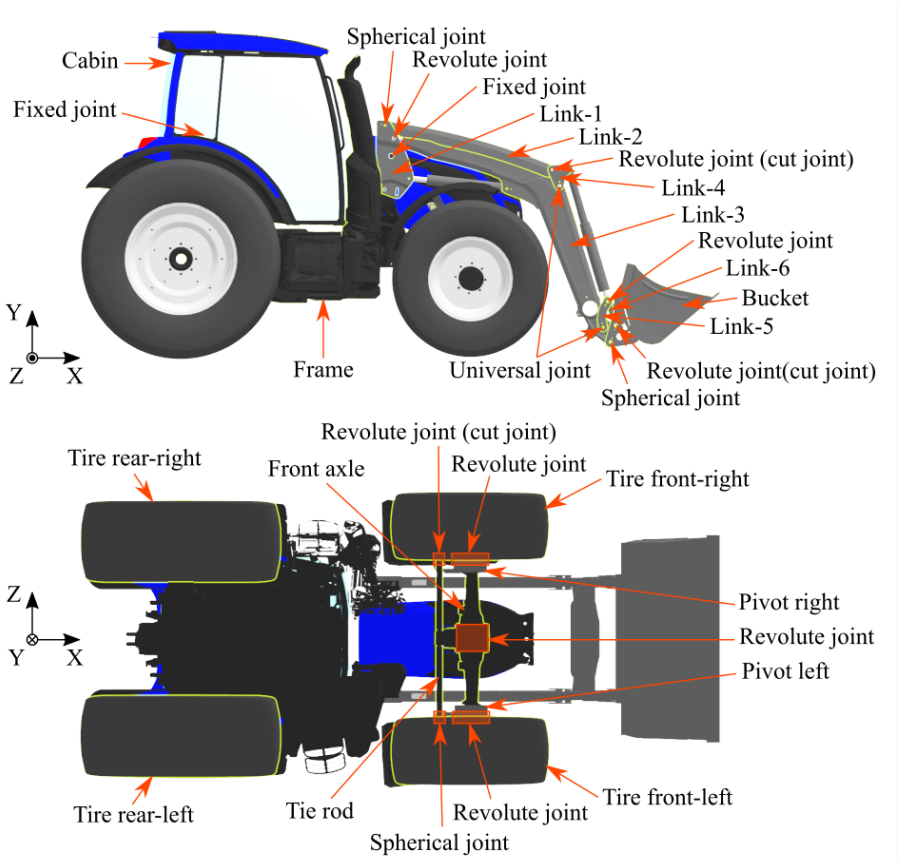

Figure 4.9: Connecting components of a tractor model used in **Publication IV**.

In the presented case study, the simulation frames of the HUD unit provided data such as the weight, height, and tilt of the bucket. As shown in Fig. 4.11a, the bucket was filled with 450 kg, 100 kg, 200 kg, and 600 kg of sand in the respective attempts. Before the digging operation, the height and tilt angle of the bucket are adjusted to the recommended values marked on the respective analog gauges. A deviation from the recommended val-

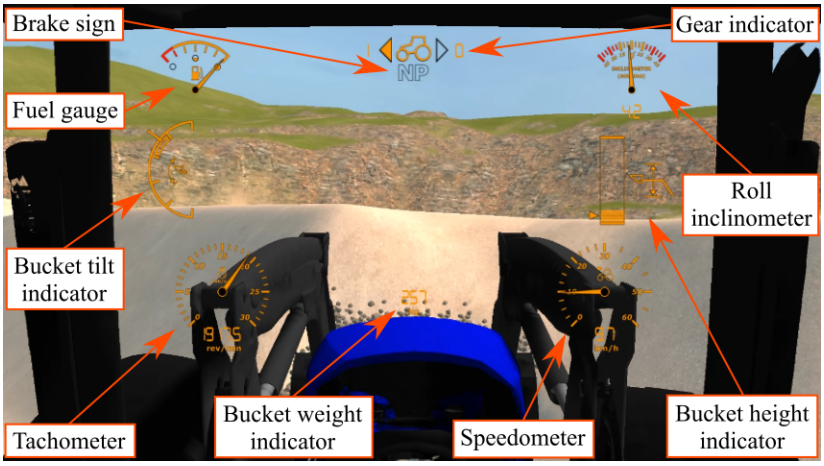

Figure 4.10: Heads-up display unit of the tractor used in **Publication IV**.

ues resulted in different amounts of sand in the bucket. However, the performance of the driver can be improved with every turn. The HUD unit can therefore help in getting accustomed to controls and perform better, by providing a quantitative picture of the surroundings of the tractor. It can be used in user training and other product processes.

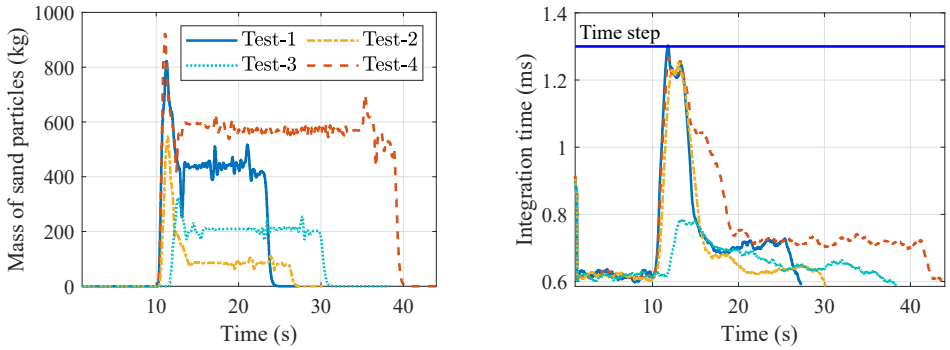

Figure 4.11: Simulation results in performing a goal of moving sand from one place to another. (a) Data of the bucket weight indicator. (b) Numerical efficiency of the system.

For the presented case study, Fig. 4.11b demonstrates the numerical efficiency of the model and it is real-time enabled. This implies that an output can be received as soon as inputs are provided in the simulation environment. All the simulations were performed in a C++ environment (compiler: Microsoft Visual Studio, version 14.1). Furthermore, the robustness of the HUD unit is demonstrated by simulating the critical conditions of limited fuel and a limited rolling angle in real-time. In future work, a qualitative evaluation can be performed to provide firm conclusions about the HUD usability through user evaluations.

4.5 Deformable terrain model for real-time simulation

This subsection presents a summary of introducing a real-time capable deformable terrain model that can interact with the dynamics of heavy machinery. The detailed results can be found in **Publication V**, where the deformable terrain interacts with the tractor model used in **Publication IV** as a case study. The terrain can interact with objects such as the bucket and tires of the tractor as shown in Fig. 4.12. As a demonstration, the tractor loads and transfers sand material from the deformable sand field following a three-dimensional maneuver. In **Publication V**, the overall model is evaluated by analyzing real-time capabilities and actuator forces during the digging and dumping operations.

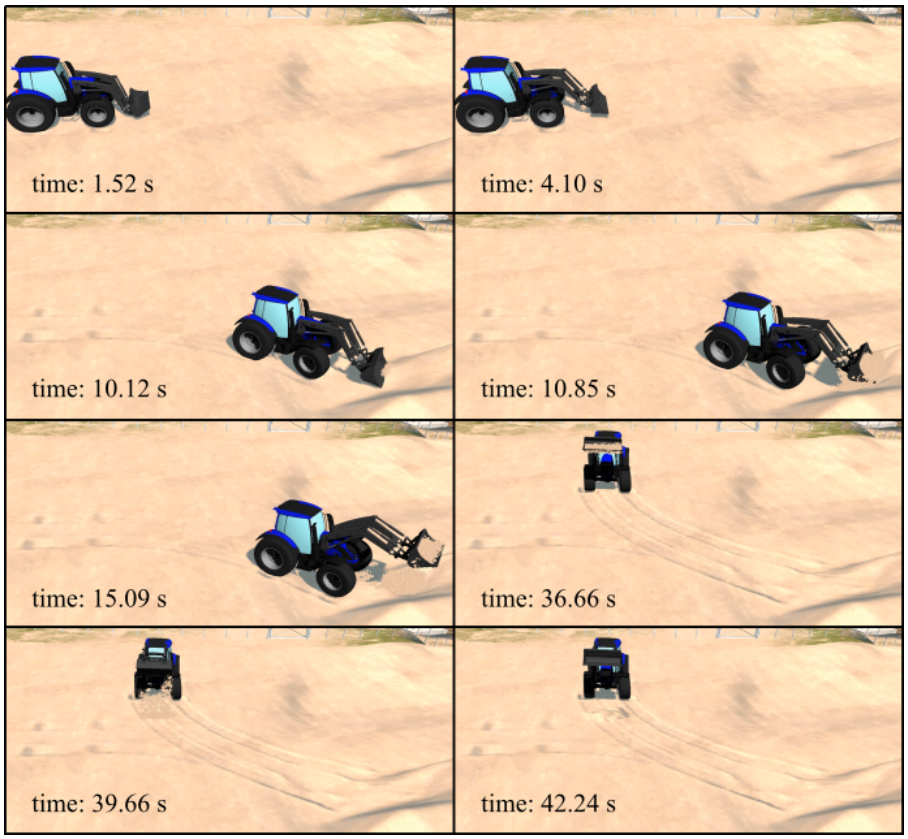

Figure 4.12: Interaction of the tractor with the deformable terrain used in **Publication V**.

In the presented case study, the bucket is filled with approximately 600 kg of sand from a sand pile. During the digging operation, the static sand field is converted into granular sand particles, whilst during the dumping operation, the dumped granular sand particles are merged back into the static sand field on reaching an equilibrium state. Similarly, the granular sand particles that were unpicked during the digging operation, were also merged back into the sand field. The sand field model allowed a visually and physically

correct bucket-filling process, that is, the bucket was filled using physically correct mass particles. The tires of the tractor compressed the sand field, forming a contact patch on the undulating deformable ground as shown in Fig. 4.12.

The numerical efficiency of the overall model along with the performance of the terrain and multibody models is shown in Fig. 4.13a. It should be noted that the performances of the models are measured in terms of the computational efficiency, that is, the integration time. The overall model is real-time capable because the integration time for each time-step is less than the simulation time-step (1.2 ms). Furthermore, the integration time of the coupled multibody and hydraulics model fluctuated between 0.26 ms and 0.43 ms; whereas it varied for the terrain model depending on the compression of the sand field and generation/handling of sand particles. It should be noted that the integration time of the terrain model is higher when sand particles are present, otherwise, it would be lower than the coupled multibody model. Moreover, a large number of sand particles would result in a higher integration time.

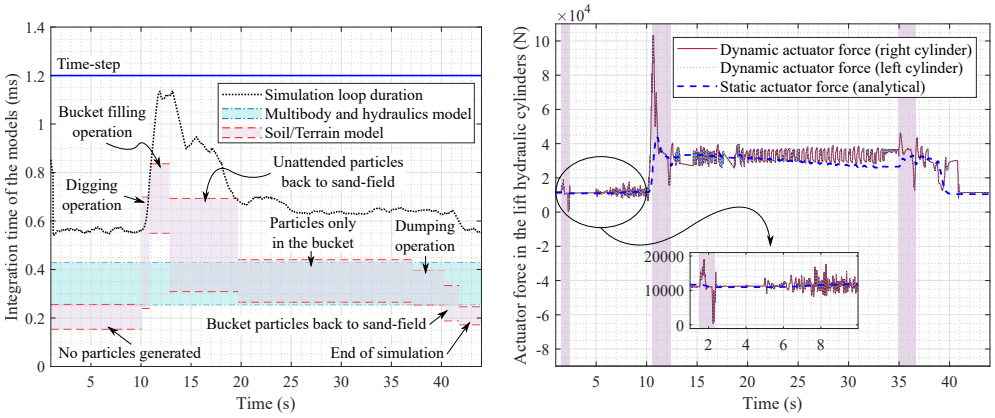

Figure 4.13: Simulation results in digging and dumping sand material from the sand field. (a) Numerical efficiency of the system. (b) Lift actuator forces throughout the simulation.

For the presented case study, the lift actuator forces during the simulation are shown in Fig. 4.13b, demonstrating the interaction of the coupled multibody model with the terrain model. The tractor model utilized two hydraulic lift cylinders, and in Fig. 4.13b, the lifting and lowering operations of the bucket are highlighted in purple. During the digging operation between 10.12 s and 10.85 s, a high order actuator force occurred representing a harsh operation of the bucket collision with the sand pile. The extra weight of the sand particles in the bucket between 10.85 s to 37.20 s is supported using the hydraulic actuator forces. During this duration, the actuator forces fluctuated because of the vibrations of sand particles in the bucket. The simulated actuator forces showed a good agreement with the static actuator force, which is computed analytically without considering the dynamics. A similar analysis was carried out for the tilt actuator forces.

4.6 Gamification procedure based on real-time multibody simulation

This subsection presents a summary of using a gamification procedure in possibly identifying the design needs of heavy machinery in the framework of real-time multibody simulation. The detailed results can be found in **Publication VI**, where an excavator model shown in Fig. 4.14 is considered as a case study. The excavator model has 11 degrees of freedom where six hydraulic cylinders control the excavator arm. In the customizable excavator model, different sizes of the bucket and the hydraulic cylinder of the dipper arm can be selected. The model is gamified as shown in Fig. 4.15 incorporating game elements, such as a goal of filling sand in an industrial hopper, utility poles as obstacles, limited fuel as a challenge, a timer as a time constraint, and visualization graphics as the fantasy element. In **Publication VI**, user experiences are analyzed to identify the possibility of improving the excavator design.

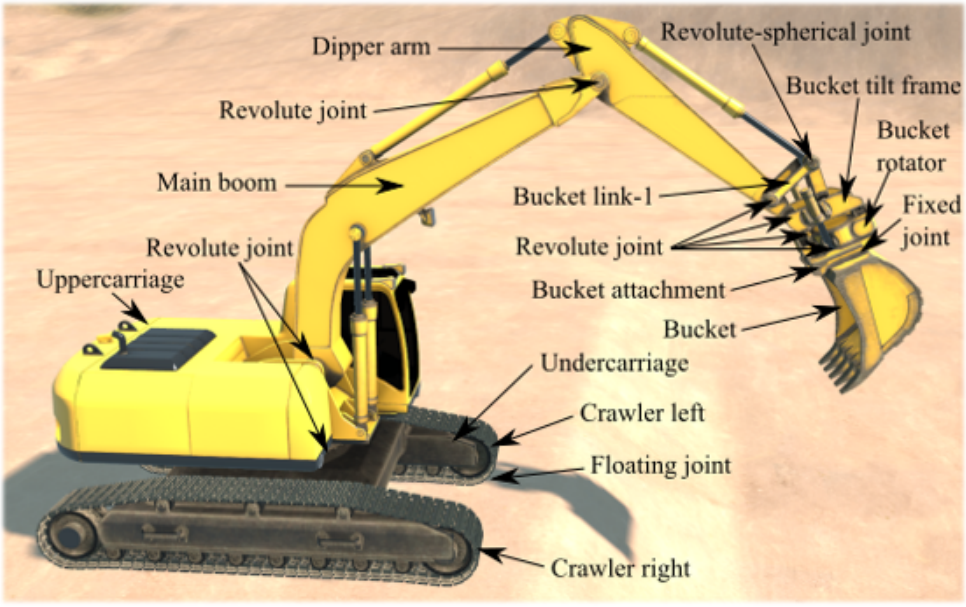

Figure 4.14: Connecting components of an excavator model used in **Publication VI**.

In the presented case study, a total of 16 users performed the goal of filling two tons of sand in the industrial hopper thrice. A leaderboard was created based on the average time consumption, fuel consumption, and number of hits with obstacles. Based on the leaderboard, the arm movements of the winner, the second to last, and the last person are compared as shown in Fig. 4.16a. It should be noted that the arm movement is referred to as the distance between the center of the upper-carriage and the center of the bucket. It is analyzed that a user consumed less time when the arm movement had relatively more fluctuation and less deviation. This source of information may be a significant aspect to consider in redesigning the arm length of the excavator when performing regular tasks.

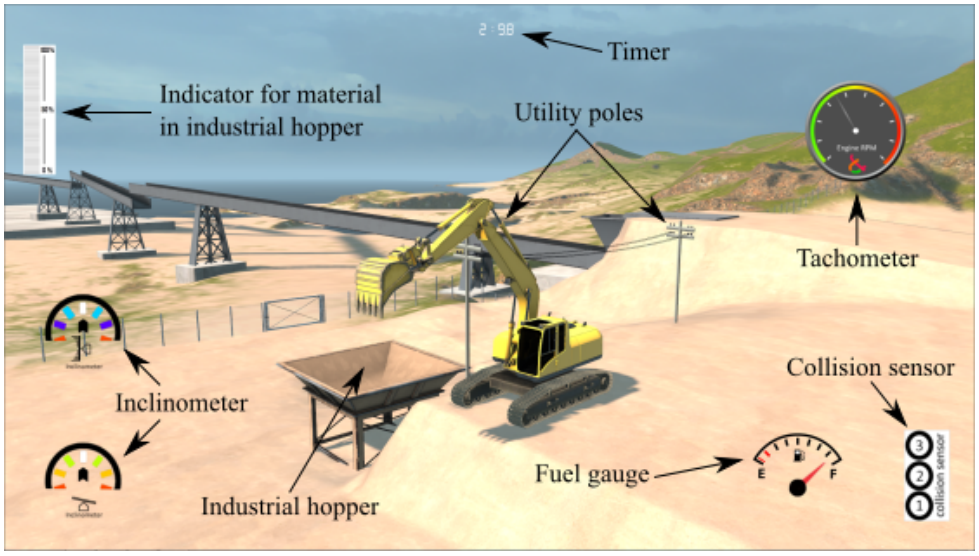

Figure 4.15: Gamified user interface for the excavator model used in **Publication VI**.

For demonstration, Fig. 4.16b shows the performance of a user upon selecting different sizes of the hydraulic cylinder with a large bucket in the successive attempts. It is observed that a combination of a medium cylinder with a large bucket resulted in an improved performance. Similar analysis could be drawn from the performance of other users indicating that this cylinder-bucket combination may be the most suitable combination for the presented goal. Such source of information may help in designing the correct sizes of the hydraulic cylinder and the bucket in performing a certain task. Furthermore, a qualitative analysis in the form of user feedback through interviews and feedback forms may identify additional design needs, such as a small screen inside the cabin.

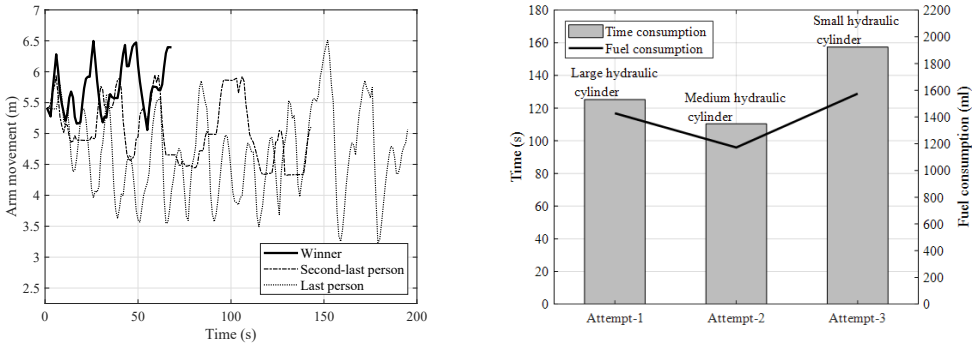

(a) (b)

Figure 4.16: Simulation results of the gamified excavator model. (a) A comparison of the arm movements. (b) Performance of a user in three successive attempts.

4.7 Summary of the findings

The summary of the findings of this study is listed in Table 4.3.

Table 4.3: Summary of the findings of this study.

Objective	Findings
Coupling multibody and hydraulic models	A multibody model selection can improve the numerical efficiency as shown in **Publication I** • The penalty-based approach is numerically more efficient in comparison with the double-step approach A friction model selection of a hydraulic cylinder can improve the numerical efficiency as shown in **Publication II** • The Brown–McPhee approach is relatively the most efficient approach
State estimator based on an indirect Kalman filter	The state estimator can accurately estimate the simulated work cycle as shown in **Publication III** • The use of a velocity sensor allowed the removal of a hydraulic cylinder pressure sensor
Utilizing real-time capabilities in user training and product development	Real-time multibody models can be used to model and virtually test new HUD units as shown in **Publication IV** • The HUD unit provided a quantitative picture of the surroundings of the tractor supporting user training A real-time capable deformable terrain model can interact with a tractor model as shown in **Publication V** • The dynamic actuator forces were in agreement with the static forces computed analytically, and the real-time capability was dependent on the terrain model Gamification can be combined with the real-time multibody model of an excavator as shown in **Publication VI** • This approach can identify the design needs of the excavator as a proof of the concept

5 Conclusion

The objective of this study was to couple multibody dynamic models and hydraulic actuator models for indirect Kalman filtering and real-time simulation in the framework of heavy machinery. The objective was subdivided into three categories. The first category focused on the efficiencies of the coupled simulation of multibody and hydraulic models. In this regard, **Publication I** introduced and compared the double-step and penalty-based semi-recursive formulations, that is, the coordinate partitioning and augmented Lagrangian with projections methods, in the framework of monolithically coupled hydraulic actuators. For the presented case studies, the penalty-based approach had various advantages and was numerically more efficient in comparison with the double-step approach. **Publication II** introduced and compared various friction models of a hydraulic cylinder in the framework of monolithically coupled multibody and hydraulic models. The approaches with the dynamic friction models showed the poorest numerical efficiencies, whereas the Brown–McPhee approach was relatively the most efficient approach.

The second category focused on combining a coupled multibody model developed above with the measurements from physical systems using an indirect Kalman filter. In this regard, **Publication III** developed a state estimator by combining a coupled multibody model with an error-state extended Kalman filter in the framework of hydraulically driven systems. The estimator utilized four sensor configurations at different sampling rates. Here, measurements were obtained from a simulation model, which provided the ground truth, with an addition of white Gaussian noise to represent the noise properties of real sensors. The state estimator provided a more accurate estimation compared with the measurements, especially, at the position level. The addition of a velocity sensor to a working sensor set improved the overall estimation quality. Moreover, it enabled the removal of one of the pressure sensors from either end of the hydraulic cylinder, which would otherwise be difficult. The sensor configuration that utilized all the sensors provided a better estimation and estimation accuracy degraded with the lower sampling rates of the sensors.

The third category focused on utilizing the real-time capabilities of the coupled multibody models in user training and product development. In this regard, **Publication IV** introduced a detailed real-time multibody model-based heads-up display unit of a tractor. The HUD unit assisted a driver in moving sand by providing a quantitative picture of the surroundings of the tractor. **Publication V** introduced a real-time capable deformable terrain model that can interact with the dynamics of a tractor. The simulated bucket and sand pile collision caused a high order fluctuating actuator force demonstrating a harsh operation. The dynamic actuator forces showed a good agreement with the static actuator forces. **Publication VI** introduced a gamification procedure to possibly identify the design needs of an excavator in the framework of real-time multibody simulation. In the gamified excavator model, user experiences were analyzed identifying the design need, such as the excavator arm length and the hydraulic cylinder and bucket sizes, as a proof of the concept.

In future works, the approaches taken in **Publications I** and **II** can be implemented in a low-level programming language, such as C or Fortran, to provide more concrete conclusions about their numerical efficiencies and real-time capabilities. Furthermore, the proposed estimator in **Publication III** can be extended to real world systems, such as a hydraulic crane. The estimation of hydraulic forces acting on a coupled multibody model can also be considered in future works. It should be noted that on considering real experimental examples, there may occur various difficulties such as no exact solutions, measurement errors, different sampling rates of sensors, and a priori unknown level of experimental effects. In **Publication IV**, a qualitative evaluation procedure can be carried out to provide more conclusive results about the usability of the HUD model through user evaluations. The simulation model in **Publication V** can be tested against experimental data. In **Publication VI**, it would be interesting to investigate the varying nature of user actions while using the exact same artifact under similar conditions.

References

[1] Al-Bender, F., Lampaert, V., Swevers, J.: The generalized Maxwell-slip model: A novel model for friction simulation and compensation. IEEE Transactions on Automatic Control **50**(11), 1883–1887 (2005)

[2] Andersson, S., Söderberg, A., Björklund, S.: Friction models for sliding dry, boundary and mixed lubricated contacts. Tribology International **40**(4), 580–587 (2007)

[3] Armstrong-Helouvry, B.: Control of machines with friction. Springer Science & Business Media (2012)

[4] Armstrong-Helouvry, B., Dupont, P., De Wit, C.C.: A survey of models, analysis tools and compensation methods for the control of machines with friction. Automatica **30**(7), 1083–1138 (1994)

[5] Arulampalam, M.S., Maskell, S., Gordon, N., Clapp, T.: A tutorial on particle filters for online nonlinear/non-gaussian Bayesian tracking. IEEE Transactions on Signal Processing **50**(2), 174–188 (2002)

[6] Avello, A., Jimenez, J.M., Bayo, E., Jalon, J.G.D.: A simple and highly parallelizable method for real-time dynamic simulation based on velocity transformation. Computer Methods in Applied Mechanics and Engineering **107**(3), 313–339 (1993)

[7] Awrejcewicz, J., Olejnik, P.: Analysis of dynamic systems with various friction laws. Applied Mechanics Reviews **58**(6), 389–411 (2005)

[8] Baharudin, M.E.: Real-time simulation of multibody systems with applications for working mobile vehicles. Ph.D. thesis, Lappeenranta University of Technology (2016)

[9] Bayo, E., Jalon, J.G.D., Avello, A., Cuadrado, J.: An efficient computational method for real time multibody dynamic simulation in fully cartesian coordinates. Computer Methods in Applied Mechanics and Engineering **92**(3), 377–395 (1991)

[10] Bayo, E., Jalon, J.G.D., Serna, M.A.: A modified Lagrangian formulation for the dynamic analysis of constrained mechanical systems. Computer Methods in Applied Mechanics and Engineering **71**(2), 183–195 (1988)

[11] Bayo, E., Ledesma, R.: Augmented Lagrangian and mass-orthogonal projection methods for constrained multibody dynamics. Nonlinear Dynamics **9**(1-2), 113–130 (1996)

[12] Bengisu, M., Akay, A.: Stability of friction-induced vibrations in multi-degree-of-freedom systems. Journal of Sound and Vibration **171**(4), 557–570 (1994)

[13] Berger, E.: Friction modeling for dynamic system simulation. Applied Mechanics Review **55**(6), 535–577 (2002)

[14] Blanco-Claraco, J.L., Torres-Moreno, J.L., Giménez-Fernández, A.: Multibody dynamic systems as Bayesian networks: Applications to robust state estimation of mechanisms. Multibody System Dynamics **34**(2), 103–128 (2015)

[15] Bo, L.C., Pavelescu, D.: The friction-speed relation and its influence on the critical velocity of stick-slip motion. Wear **82**(3), 277–289 (1982)

[16] Brenan, K.E., Campbell, S.L., Petzold, L.R.: Numerical solution of initial-value problems in differential-algebraic equations. Siam (1996)

[17] Brown, P., McPhee, J.: A continuous velocity-based friction model for dynamics and control with physically meaningful parameters. Journal of Computational and Nonlinear Dynamics **11**(5), 054502(1–6) (2016)

[18] Callejo, A., Narayanan, S.H.K., Jalon, J.G.D., Norris, B.: Performance of automatic differentiation tools in the dynamic simulation of multibody systems. Advances in Engineering Software **73**, 35–44 (2014)

[19] Callejo, A., Pan, Y., Ricón, J.L., Kövecses, J., Jalon, J.G.D.: Comparison of semi-recursive and subsystem synthesis algorithms for the efficient simulation of multibody systems. Journal of Computational and Nonlinear Dynamic **12**(1), 011020(1–11) (2017)

[20] Carpenter, J., Clifford, P., Fearnhead, P.: Improved particle filter for nonlinear problems. IEE Proceedings-Radar, Sonar and Navigation **146**(1), 2–7 (1999)

[21] Cuadrado, J., Cardenal, J., Bayo, E.: Modeling and solution methods for efficient real-time simulation of multibody dynamics. Multibody System Dynamics **1**(3), 259–280 (1997)

[22] Cuadrado, J., Dopico, D., Barreiro, A., Delgado, E.: Real-time state observers based on multibody models and the extended Kalman filter. Journal of Mechanical Science and Technology **23**(4), 894–900 (2009)

[23] Cuadrado, J., Dopico, D., González, M., Naya, M.Á.: A combined penalty and recursive real-time formulation for multibody dynamics. Journal of Mechanical Design **126**(4), 602–608 (2004)

[24] Cuadrado, J., Dopico, D., Naya, M.Á., González, M.: Real-time multibody dynamics and applications. In: Simulation Techniques for Applied Dynamics, pp. 247–311. Springer (2008)

[25] Cuadrado, J., Dopico, D., Perez, J.A., Pastorino, R.: Automotive observers based on multibody models and the extended Kalman filter. Multibody System Dynamics **27**(1), 3–19 (2012)

[26] Dahl, P.R.: Solid friction damping of mechanical vibrations. American Institute of Aeronautics and Astronautics **14**(12), 1675–1682 (1976)

[27] De Geeter, J., Van Brussel, H., De Schutter, J., Decréton, M.: A smoothly constrained Kalman filter. IEEE Transactions on Pattern Analysis and Machine Intelligence **19**(10), 1171–1177 (1997)

[28] De Wit, C.C., Olsson, H., Astrom, K.J., Lischinsky, P.: A new model for control of systems with friction. IEEE Transactions on Automatic Control **40**(3), 419–425 (1995)

[29] Fisette, P., Vaneghem, B.: Numerical integration of multibody system dynamic equations using the coordinate partitioning method in an implicit Newmark scheme. Computer Methods in Applied Mechanics and Engineering **135**(1–2), 85–105 (1996)

[30] Flores, P., Ambrosio, J., Claro, J.P., Lankarani, H.M.: Kinematics and dynamics of multibody systems with imperfect joints: Models and case studies. Springer Science & Business Media (2008)

[31] Flores, P., Lankarani, H.M.: Contact force models for multibody dynamics. Springer (2016)

[32] González, F., Dopico, D., Pastorino, R., Cuadrado, J.: Behaviour of augmented Lagrangian and Hamiltonian methods for multibody dynamics in the proximity of singular configurations. Nonlinear Dynamics **85**(3), 1491–1508 (2016)

[33] González, F., Naya, M.Á., Luaces, A., González, M.: On the effect of multirate co-simulation techniques in the efficiency and accuracy of multibody system dynamics. Multibody System Dynamics **25**(4), 461–483 (2011)

[34] Grewal, M.S., Andrews, A.P.: Kalman filtering: Theory and practice with MATLAB. John Wiley & Sons (2014)

[35] Haessig, D.A., Friedland, B.: On the modeling and simulation of friction. Journal of Dynamic Systems, Measurement, and Control **113**(3), 354–362 (1991)

[36] Handroos, H.M., Vilenius, M.J.: Flexible semi-empirical models for hydraulic flow control valves. Journal of Mechanical Design **113**(3), 232–238 (1991)

[37] Hidalgo, A.F., Jalon, J.G.D.: Real-time dynamic simulations of large road vehicles using dense, sparse, and parallelization techniques. Journal of Computational and Nonlinear Dynamics **10**(3), 031005(1–15) (2015)

[38] Higham, N.J.: Gaussian elimination. Wiley Interdisciplinary Reviews: Computational Statistics **3**(3), 230–238 (2011)

[39] Jacobson, B.: The Stribeck memorial lecture. Tribology International **36**(11), 781–789 (2003)

[40] Jalon, J.G.D., Alvarez, E., Ribera, F.A.D., Rodriguez, I., Funes, F.J.: A fast and simple semi-recursive formulation for multi-rigid-body systems. Computational Methods in Applied Sciences **2**, 1–23 (2005)

[41] Jalon, J.G.D., Bayo, E.: Kinematic and dynamic simulation of multibody systems: The real-time challenge. Springer-Verlag (1994)

[42] Kalman, R.E.: A new approach to linear filtering and prediction problems. Journal of Basic Engineering **82**(1), 35–45 (1960)

[43] Lampaert, V., Al-Bender, F., Swevers, J.: A generalized Maxwell-slip friction model appropriate for control purposes. In: Proceedings of the International Conference on Physics and Control, pp. 1170–1177. Saint Petersburg, Russia (2003)

[44] Linge, S., Langtangen, H.P.: Programming for computations-MATLAB/Octave: A gentle introduction to numerical simulations with MATLAB/Octave. Springer (2016)

[45] Marques, F., Flores, P., Claro, J.P., Lankarani, H.M.: A survey and comparison of several friction force models for dynamic analysis of multibody mechanical systems. Nonlinear Dynamics **86**(3), 1407–1443 (2016)

[46] Marques, F., Flores, P., Claro, J.P., Lankarani, H.M.: Modeling and analysis of friction including rolling effects in multibody dynamics: A review. Multibody System Dynamics **45**(2), 223–244 (2019)

[47] Márton, L., Fodor, S., Sepehri, N.: A practical method for friction identification in hydraulic actuators. Mechatronics **21**(1), 350–356 (2011)

[48] Matikainen, M.K., Von Hertzen, R., Mikkola, A., Gerstmayr, J.: Elimination of high frequencies in the absolute nodal coordinate formulation. Proceedings of the Institution of Mechanical Engineers, Part K: Journal of Multi-body Dynamics **224**(1), 103–116 (2010)

[49] Naya, M.Á., Cuadrado, J., Dopico, D., Lugris, U.: An efficient unified method for the combined simulation of multibody and hydraulic dynamics: Comparison with simplified and co-integration approaches. Archive of Mechanical Engineering **58**(2), 223–243 (2011)

[50] Owen, W.S., Croft, E.A.: The reduction of stick-slip friction in hydraulic actuators. IEEE/ASME Transactions on Mechatronics **8**(3), 362–371 (2003)

[51] Pan, Y., Dai, W., Huang, L., Li, Z., Mikkola, A.: Iterative refinement algorithm for efficient velocities and accelerations solutions in closed-loop multibody dynamics. Mechanical Systems and Signal Processing **152**, 107463(1–13) (2021)

[52] Pan, Y., Xiang, S., He, Y., Zhao, J., Mikkola, A.: The validation of a semi-recursive vehicle dynamics model for a real-time simulation. Mechanism and Machine Theory **151**, 103907(1–18) (2020)

[53] Pastorino, R., Richiedei, D., Cuadrado, J., Trevisani, A.: State estimation using multibody models and non-linear Kalman filters. International Journal of Non-Linear Mechanics **53**, 83–90 (2013)

[54] Pennestrì, E., Rossi, V., Salvini, P., Valentini, P.P.: Review and comparison of dry friction force models. Nonlinear Dynamics **83**(4), 1785–1801 (2016)

[55] Rahikainen, J.: On the dynamic simulation of coupled multibody and hydraulic systems for real-time applications. Ph.D. thesis, Lappeenranta University of Technology (2019)

[56] Rahikainen, J., Kiani, M., Sopanen, J., Jalali, P., Mikkola, A.: Computationally efficient approach for simulation of multibody and hydraulic dynamics. Mechanism and Machine Theory **130**, 435–446 (2018)

[57] Rahikainen, J., Mikkola, A., Sopanen, J., Gerstmayr, J.: Combined semi-recursive formulation and lumped fluid method for monolithic simulation of multibody and hydraulic dynamics. Multibody System Dynamics **44**(3), 293–311 (2018)

[58] Rodríguez, A.J., Pastorino, R., Carro-Lagoa, Á., Janssens, K., Naya, M.Á.: Hardware acceleration of multibody simulations for real-time embedded applications. Multibody System Dynamics **51**(4), 455–473 (2021)

[59] Rodríguez, A.J., Sanjurjo, E., Pastorino, R., Naya, M.Á.: State, parameter, and input observers based on multibody models and Kalman filters for vehicle dynamics. Mechanical Systems and Signal Processing **155**, 107544(1–17) (2021)

[60] Rodríguez, J.I., Jiménez, J.M., Funes, F.J., Jalon, J.G.D.: Recursive and residual algorithms for the efficient numerical integration of multibody systems. Multibody System Dynamics **11**(4), 295–320 (2004)

[61] Sanjurjo, E.: State observers based on detailed multibody models applied to an automobile. Ph.D. thesis, University of A Coruña (2016)

[62] Sanjurjo, E., Dopico, D., Luaces, A., Naya, M.Á.: State and force observers based on multibody models and the indirect Kalman filter. Mechanical Systems and Signal Processing **106**, 210–228 (2018)

[63] Sanjurjo, E., Naya, M.Á., Blanco-Claraco, J.L., Torres-Moreno, J.L., Giménez-Fernández, A.: Accuracy and efficiency comparison of various nonlinear Kalman filters applied to multibody models. Nonlinear Dynamics **88**(3), 1935–1951 (2017)

[64] Simon, D.: Optimal state estimation: Kalman, H infinity, and nonlinear approaches. John Wiley & Sons (2006)

[65] Simon, D., Chia, T.L.: Kalman filtering with state equality constraints. IEEE Transactions on Aerospace and Electronic Systems **38**(1), 128–136 (2002)

[66] Swevers, J., Al-Bender, F., Ganseman, C.G., Projogo, T.: An integrated friction model structure with improved presliding behavior for accurate friction compensation. IEEE Transactions on Automatic Control **45**(4), 675–686 (2000)

[67] Torres, J., Blanco, J., Sanjurjo, E., Naya, M.Á., Giménez, A.: Towards benchmarking of state estimators for multibody dynamics. In: The 3rd Joint International Conference on Multibody System Dynamics. The 7th Asian Conference on Multibody Dynamics, pp. 261–262. Busan, Korea (2014)

[68] Tran, X.B., Hafizah, N., Yanada, H.: Modeling of dynamic friction behaviors of hydraulic cylinders. Mechatronics **22**(1), 65–75 (2012)

[69] Tran, X.B., Khaing, W.H., Endo, H., Yanada, H.: Effect of friction model on simulation of hydraulic actuator. Proceedings of the Institution of Mechanical Engineers, Part I: Journal of Systems and Control Engineering **228**(9), 690–698 (2014)

[70] Tran, X.B., Nguyen, V.L., Tran, K.D.: Effects of friction models on simulation of pneumatic cylinder. Mechanical Sciences **10**(2), 517–528 (2019)

[71] Watton, J.: Fluid power systems: Modeling, simulation, analog, and microcomputer control. Prentice Hall (1989)

[72] Yanada, H., Sekikawa, Y.: Modeling of dynamic behaviors of friction. Mechatronics **18**(7), 330–339 (2008)

[73] Ylinen, A., Marjamäki, H., Mäkinen, J.: A hydraulic cylinder model for multibody simulations. Computers & Structures **138**, 62–72 (2014)

Publication I

Jaiswal, S., Rahikainen, J., Khadim, Q., Sopanen, J., and Mikkola, A.
Comparing double-step and penalty-based semirecursive formulations for hydraulically actuated multibody systems in a monolithic approach

Reprinted with permission from
Multibody System Dynamics
Vol. 52(2), pp. 169–191, 2021

Multibody Syst Dyn (2021) 52:169–191
https://doi.org/10.1007/s11044-020-09776-4

Comparing double-step and penalty-based semirecursive formulations for hydraulically actuated multibody systems in a monolithic approach

Suraj Jaiswal[1] · Jarkko Rahikainen[1] · Qasim Khadim[1] · Jussi Sopanen[1] · Aki Mikkola[1]

Received: 18 March 2020 / Accepted: 26 December 2020 / Published online: 21 January 2021

Abstract The simulation of mechanical systems often requires modeling of systems of other physical nature, such as hydraulics. In such systems, the numerical stiffness introduced by the hydraulics can become a significant aspect to consider in the modeling, as it can negatively effect to the computational efficiency. The hydraulic system can be described by using the lumped fluid theory. In this approach, a pressure can be integrated from a differential equation in which effective bulk modulus is divided by a volume size. This representation can lead to numerical stiffness as a consequence of which time integration of a hydraulically driven system becomes cumbersome. In this regard, the used multibody formulation plays an important role, as there are many different procedures for the constraint enforcement and different sets of coordinates to choose from. This paper introduces the double-step semirecursive approach and compares it with a penalty-based semirecursive approach in case of coupled multibody and hydraulic dynamics within the monolithic framework. To this end, hydraulically actuated four-bar and quick-return mechanisms are analyzed as case studies. The two approaches are compared in terms of the work cycle, energy balance, constraint violation, and numerical efficiency of the mechanisms. It is concluded that the penalty-based semirecursive approach has a number of advantages compared with the double-step semirecursive approach, which is in accordance with the literature.

S. Jaiswal
suraj.jaiswal@lut.fi

J. Rahikainen
jarkko.rahikainen@lut.fi

Q. Khadim
qasim.khadim@lut.fi

J. Sopanen
jussi.sopanen@lut.fi

A. Mikkola
aki.mikkola@lut.fi

[1] Department of Mechanical Engineering, Lappeenranta University of Technology, Yliopistonkatu 34, 53850 Lappeenranta, Finland

Keywords Multibody system dynamics · Double-step semirecursive formulation · Penalty-based semirecursive formulation · Hydraulic actuators · Monolithic simulation

1 Introduction

The computer simulation of dynamic systems has proven its value in product development, from early prototyping phase to user training, and emerging digital twins and artificial intelligence applications. In practice, the modeling of mechanisms can be carried out by using multibody system dynamics in which equations of motion describe a force equilibrium for the mechanical system under investigation. The use of multibody system dynamics also allows describing actuator models such as hydraulics or electric drives.

The multibody methods can be, in general, categorized to two main groups according to the selected coordinates [25]. Firstly, there is the group of formulations based on global coordinates, where the absolute positions, velocities, and accelerations of each body are used. In the second case, relative coordinates are employed. Should high computational efficiency be required, as is the case in real-time applications, such as those presented in [22, 23], the use of the relative coordinates is often considered to be an appropriate approach. The selection of an approach is case-dependent, as demonstrated in [17]. The computational efficiency can be significantly effected by implementation details [18], and, among others, the use of the automated differentiation tools [6], and sparse and parallelization techniques [20].

Within the family of methods based on the relative coordinates, the semirecursive approach is often used. In the semirecursive approach, closed loops need to be handled by employing constraint equations. Constraint equations, in turn, can be accounted in the semirecursive approach in many different ways, such as by using the Lagrange multiplier method, the penalty-based approach as proposed by Cuadrado et al. [10] or the double-step approach, which is using a coordinate partitioning as proposed by Rodríguez et al. [33]. The latter two approaches are originated from Featherstone's articulated inertia method [13]. The penalty-based approach utilizes the index-3 augmented Lagrangian formulation with projections [3, 9] to enforce the constraints. After their original introductions, both methods have also been successfully used in practical applications, such as in real-time vehicle simulations [20, 29]. In this study, the double-step approach based on coordinate partitioning method [24, 33] is referred as the double-step semirecursive formulation, and the penalty-based augmented Lagrangian approach [9, 10] is referred as the penalty-based semirecursive formulation.

Regarding the solution of the multiphysics problem that system-level simulations require, two main approaches exist in the literature. A straightforward one is the monolithic approach, or sometimes referred as unified scheme, where a single set of differential equations is formed and integrated forward in time as a whole. In an alternative approach, namely cosimulation approach, in turn, the system is split into two or more subsystems that are each integrated separately. In this approach, the required variables, such as the state variables, are communicated in predetermined time intervals. Multiple instances of both approaches can be found from the literature. Cosimulation, due to the discrete time information exchange and the resulting coupling error, has especially been under keen research interest in recent years [16, 36]. The studies include important aspects, such as the multirate cosimulation [18], cosimulation configuration [4, 30], and energy-based coupling error minimization [4, 34, 35]. Monolithic schemes, in turn, have been under less active development since the simple coupling requires less research effort. Nevertheless, in [12] a multiphysics model

was derived for a semiactive car suspension. Naya et al. [28], in turn, presented a monolithic method for a coupled multibody and hydraulic simulation based on the index-3 augmented Lagrangian [3], followed later in [32] and [31], where the index-3 semirecursive formulation [10] was used.

In the case of a coupled multibody and hydraulic dynamics, which is a common case in mobile working machinery, one of the key aspects to consider is the numerical stiffness introduced by the hydraulics. This problem can be alleviated by proper selection of a multibody approach. While these aspects have been discussed in some sources, such as in [32], few comparisons between the available methods in this context exist in the literature. In the context of the absolute nodal coordinate formulation, in turn, a study in this direction has been done by Matikainen et al. [27], where coordinate partitioning, Lagrange multiplier method with Baumgarte's stabilization, and penalty formulation were used for constraint enforcement. The results indicated best performance for the Lagrange multiplier method, closely followed by the penalty-based approach, while less efficient solution was sought with the coordinate partitioning method.

The objective of this paper is to introduce the double-step semirecursive formulation [24] and compare it with the penalty-based semirecursive formulation [10, 32] in the framework of hydraulically driven systems. A monolithic scheme for the coupled simulation of the double-step semirecursive formulation and hydraulic systems is introduced in this study. As explained earlier, the modeling of hydraulic actuators often leads to numerically stiff systems. In this study, the hydraulic system will be described by using the lumped fluid theory. While variable-step integrators often provide more efficient solutions, especially with stiff systems when compared with fixed step-size solutions, since the author's interests lie within the field of real-time simulation, only fixed step-sizes are considered in this work. The coupled systems are referred after the name of the multibody formulations used, such as the double-step semirecursive approach and the penalty-based semirecursive approach. As case studies, hydraulically actuated four-bar and quick-return mechanisms are illustrated. Using the numerical examples, the two approaches are compared based on the work cycle, energy balance, constraint violation, and numerical efficiency of the mechanisms.

2 Semirecursive multibody formulations

The dynamics of a constrained mechanical system can be described by using a multibody system dynamics approach. In the semirecursive formulations, the dynamics of the open-loop multibody systems are formulated in relative joint coordinates, which are independent. In the case of closed-loop multibody systems, in turn, the relative joint coordinates are not independent and cut-joint method is often used to open the loop. In this study, the cut-joint constraints are incorporated by using the coordinate partitioning method [24, 33], referred as the double-step semirecursive formulation, and by using the penalty-based augmented Lagrangian method [2, 9], referred as the penalty-based semirecursive formulation. Since the system is hydraulically actuated, the internal dynamics of the hydraulics are computed and the resultant force, as well as the stroke and stroke velocity, is used to combine the hydraulics to the multibody equations of motion. Therefore, in this study, the constraints are assumed scleronomic. Should kinematic constraints be needed, both methods can easily be extended to rheonomous systems, as shown in the literature [10, 24].

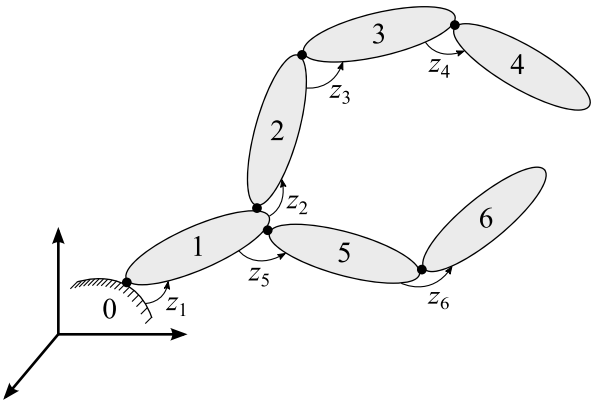

Fig. 1 An example of an open-loop system

2.1 Semirecursive formulation for an open-loop system

In the semirecursive formulation, a system is considered as an open-loop multibody system with N_b bodies. The following Cartesian velocity $\mathbf{Z}_j$ and acceleration $\dot{\mathbf{Z}}_j$ are used to describe the absolute velocity and acceleration of each body [24]

$$\mathbf{Z}_j \equiv \begin{bmatrix} \dot{\mathbf{s}}_j \\ \boldsymbol{\omega}_j \end{bmatrix}, \qquad \dot{\mathbf{Z}}_j \equiv \begin{bmatrix} \ddot{\mathbf{s}}_j \\ \dot{\boldsymbol{\omega}}_j \end{bmatrix}, \tag{1}$$

where $\dot{\mathbf{s}}_j$ and $\ddot{\mathbf{s}}_j$ are, respectively, the velocity and acceleration of the point of the body j, which at that particular time is coincident with the origin of the inertial reference frame, and $\boldsymbol{\omega}_j$ and $\dot{\boldsymbol{\omega}}_j$ are the angular velocity and angular acceleration, respectively, of the body j. In this approach, the kinematics of the open-loop system is calculated in a recursive form, either from the base to the leaves, as performed in this study, or from leaves to base, by applying the classical kinematic relations as in [11]. Figure 1 shows an example of an open-loop system. In general case, the position of the system can be described by using the relative joint coordinates $\mathbf{z} = \left[z_1, z_2, \ldots, z_{N_b}\right]^{\mathrm{T}}$.

The absolute velocity $\mathbf{Z}_j$ and acceleration $\dot{\mathbf{Z}}_j$ for body $j \in [1, N_b]$ can be recursively expressed in terms of the previous bodies as [24]

$$\mathbf{Z}_j = \mathbf{Z}_{j-1} + \mathbf{b}_j \dot{z}_j, \tag{2}$$

$$\dot{\mathbf{Z}}_j = \dot{\mathbf{Z}}_{j-1} + \mathbf{b}_j \ddot{z}_j + \mathbf{d}_j, \tag{3}$$

where the scalars $\dot{z}_j$ and $\ddot{z}_j$ are the first and second time derivatives, respectively, of the relative joint coordinate z_j, and the vectors $\mathbf{b}_j$ and $\mathbf{d}_j$ depend on the type of joint [11] that connects the bodies $j-1$ and j. Note that the indexes $j-1$ and j may not be successive, as the system may branch.

The absolute velocities $\mathbf{Z} \in \mathbb{R}^{6N_b}$ and accelerations $\dot{\mathbf{Z}} \in \mathbb{R}^{6N_b}$ of the open-loop system can respectively be expressed in the matrix forms as $\mathbf{Z} = \left[\mathbf{Z}_1^{\mathrm{T}}, \mathbf{Z}_2^{\mathrm{T}}, \ldots, \mathbf{Z}_{N_b}^{\mathrm{T}}\right]^{\mathrm{T}}$ and $\dot{\mathbf{Z}} = \left[\dot{\mathbf{Z}}_1^{\mathrm{T}}, \dot{\mathbf{Z}}_2^{\mathrm{T}}, \ldots, \dot{\mathbf{Z}}_{N_b}^{\mathrm{T}}\right]^{\mathrm{T}}$. A velocity transformation matrix $\mathbf{R} \in \mathbb{R}^{6N_b \times N_b}$ that maps the absolute velocities into a set of relative joint velocities can be written as [11, 24]

$$\mathbf{Z} = \mathbf{R}\dot{\mathbf{z}} = \mathbf{T}\mathbf{R}_{\mathrm{d}}\dot{\mathbf{z}}, \tag{4}$$

$$\dot{\mathbf{Z}} = \mathbf{R}\ddot{\mathbf{z}} + \dot{\mathbf{R}}\dot{\mathbf{z}} = \mathbf{T}\mathbf{R}_{\mathrm{d}}\ddot{\mathbf{z}} + \mathbf{T}\dot{\mathbf{R}}_{\mathrm{d}}\dot{\mathbf{z}}, \tag{5}$$

where $\dot{\mathbf{z}} \in \mathbb{R}^{N_b}$ is the vector of relative joint velocities, $\mathbf{T} \in \mathbb{R}^{6N_b \times 6N_b}$ is the path matrix that represents the topology of the open-loop system, and $\mathbf{R}_{\mathrm{d}} \in \mathbb{R}^{6N_b \times N_b}$ is a diagonal matrix whose elements are the vectors $\mathbf{b}_j$ arranged in an ascending order. The path matrix $\mathbf{T}$ is a lower block-triangular matrix [11] whose elements from diagonal to left are (6×6) identity matrices $\mathbf{I}_6$, if the corresponding body is in between the considered body and the root of the system. Note that the term $\dot{\mathbf{R}}\dot{\mathbf{z}}$ in Eq. (5) can be expressed in terms of the vectors $\mathbf{d}_j$ by using Eq. (3) [11].

The absolute velocity $\mathbf{Y}_j$ and acceleration $\dot{\mathbf{Y}}_j$ of the center of mass of body j can be written as

$$\mathbf{Y}_j = \begin{bmatrix} \dot{\mathbf{g}}_j \\ \boldsymbol{\omega}_j \end{bmatrix} = \begin{bmatrix} \mathbf{I}_3 & -\widetilde{\mathbf{g}}_j \\ \mathbf{0} & \mathbf{I}_3 \end{bmatrix} \begin{bmatrix} \dot{\mathbf{s}}_j \\ \boldsymbol{\omega}_j \end{bmatrix} = \mathbf{D}_j \mathbf{Z}_j, \tag{6}$$

and

$$\dot{\mathbf{Y}}_j = \begin{bmatrix} \ddot{\mathbf{g}}_j \\ \dot{\boldsymbol{\omega}}_j \end{bmatrix} = \begin{bmatrix} \mathbf{I}_3 & -\widetilde{\mathbf{g}}_j \\ \mathbf{0} & \mathbf{I}_3 \end{bmatrix} \begin{bmatrix} \ddot{\mathbf{s}}_j \\ \dot{\boldsymbol{\omega}}_j \end{bmatrix} + \begin{bmatrix} \widetilde{\boldsymbol{\omega}}_j \widetilde{\boldsymbol{\omega}}_j \mathbf{g}_j \\ \mathbf{0} \end{bmatrix} = \mathbf{D}_j \dot{\mathbf{Z}}_j + \mathbf{e}_j, \tag{7}$$

where $\mathbf{g}_j$ is the position vector of the center of mass of body j with respect to the inertial reference frame, $\mathbf{I}_3$ is a (3×3) identity matrix, and $\dot{\mathbf{g}}_j$, $\ddot{\mathbf{g}}_j$, and $\widetilde{\mathbf{g}}_j$, respectively, are the first and second time derivative, and the skew-symmetric matrix of the position vector $\mathbf{g}_j$. By using Eqs. (6) and (7), the virtual power of the inertia and external forces acting on the open-loop system can be written as [24]

$$\sum_{j=1}^{N_b} \mathbf{Y}_j^{*\mathrm{T}} \left(\mathbf{M}_j \dot{\mathbf{Y}}_j - \mathbf{Q}_j \right) = \sum_{j=1}^{N_b} \mathbf{Z}_j^{*\mathrm{T}} \left(\bar{\mathbf{M}}_j \dot{\mathbf{Z}}_j - \bar{\mathbf{Q}}_j \right) = 0, \tag{8}$$

where the virtual velocities are denoted with an asterisk (*), and the matrices $\mathbf{M}_j$, $\bar{\mathbf{M}}_j$, and $\bar{\mathbf{Q}}_j$ can be written as

$$\mathbf{M}_j = \begin{bmatrix} m_j \mathbf{I}_3 & \mathbf{0} \\ \mathbf{0} & \mathbf{J}_j \end{bmatrix}, \qquad \bar{\mathbf{M}}_j = \begin{bmatrix} m_j \mathbf{I}_3 & -m_j \widetilde{\mathbf{g}}_j \\ m_j \widetilde{\mathbf{g}}_j & \mathbf{J}_j - m_j \widetilde{\mathbf{g}}_j \widetilde{\mathbf{g}}_j \end{bmatrix}, \tag{9}$$

and

$$\bar{\mathbf{Q}}_j = \begin{bmatrix} \mathbf{f}_j - \widetilde{\boldsymbol{\omega}}_j \left(\widetilde{\boldsymbol{\omega}}_j m_j \mathbf{g}_j \right) \\ \boldsymbol{\tau}_j - \widetilde{\boldsymbol{\omega}}_j \mathbf{J}_j \boldsymbol{\omega}_j + \widetilde{\mathbf{g}}_j \left(\mathbf{f}_j - \widetilde{\boldsymbol{\omega}}_j \left(\widetilde{\boldsymbol{\omega}}_j m_j \mathbf{g}_j \right) \right) \end{bmatrix}, \tag{10}$$

where m_j is the mass of body j and $\mathbf{J}_j$ is the inertia tensor of body j. The inertia tensor $\mathbf{J}_j$ can be written as $\mathbf{J}_j = \mathbf{A}_j^{\mathrm{T}} \bar{\mathbf{J}}_j \mathbf{A}_j$, where $\bar{\mathbf{J}}_j$ is the constant inertia tensor in the body reference frame of body j and $\mathbf{J}_j$ is expressed in the inertial reference frame. Note that both $\mathbf{J}_j$ and $\bar{\mathbf{J}}_j$ are defined with respect to the center of mass of body j. In Eq. (10), $\mathbf{f}_j$ is the vector of external forces applied on body j and $\boldsymbol{\tau}_j$ is the vector of external moments with respect to the center of mass of body j. By substituting Eqs. (4) and (5) in Eq. (8), a set of ordinary differential equations that describes the motion of the open-loop system can be written as [24]

$$\mathbf{R}_{\mathrm{d}}^{\mathrm{T}} \mathbf{T}^{\mathrm{T}} \bar{\mathbf{M}} \mathbf{T} \mathbf{R}_{\mathrm{d}} \ddot{\mathbf{z}} = \mathbf{R}_{\mathrm{d}}^{\mathrm{T}} \mathbf{T}^{\mathrm{T}} \left(\bar{\mathbf{Q}} - \bar{\mathbf{M}} \mathbf{T} \dot{\mathbf{R}}_{\mathrm{d}} \dot{\mathbf{z}} \right), \tag{11}$$

where $\bar{\mathbf{M}} \in \mathbb{R}^{6N_b \times 6N_b}$ is a diagonal matrix that consists of the mass matrices $\bar{\mathbf{M}}_j$, and $\bar{\mathbf{Q}} \in \mathbb{R}^{6N_b}$ is a column vector that consists of the force vectors $\bar{\mathbf{Q}}_j$. Equation (11) can be rewritten

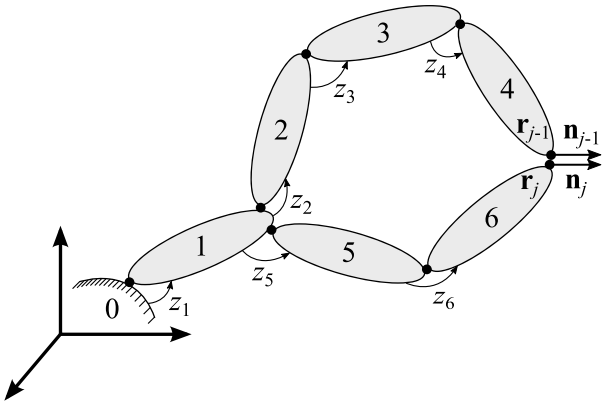

Fig. 2 An example of a closed-loop system

as

$$\mathbf{M}'\ddot{\mathbf{z}} = \mathbf{Q}', \tag{12}$$

where $\mathbf{M}' = \mathbf{R}_{\mathrm{d}}^{\mathrm{T}}\mathbf{T}^{\mathrm{T}}\bar{\mathbf{M}}\mathbf{T}\mathbf{R}_{\mathrm{d}}$ and $\mathbf{Q}' = \mathbf{R}_{\mathrm{d}}^{\mathrm{T}}\mathbf{T}^{\mathrm{T}}\left(\bar{\mathbf{Q}} - \bar{\mathbf{M}}\mathbf{T}\dot{\mathbf{R}}_{\mathrm{d}}\dot{\mathbf{z}}\right)$.

2.2 Double-step semirecursive formulation

In the double-step semirecursive formulation, the constraints are introduced by using the coordinate partitioning method [24]. This method can be used in frameworks of the explicit and implicit integrators. A set of m constraint equations $\mathbf{\Phi} = \mathbf{0}$ are used for the closure of an open-loop. For the sake of simplicity, the constraint equations are assumed holonomic and scleronomic. To account for rheonomic constraints, the reader is referred to [24]. The constraint equations $\mathbf{\Phi} = \mathbf{0}$ can be expressed in terms of the relative joint coordinates as $\mathbf{\Phi}(\mathbf{z}) = \mathbf{0}$. Figure 2 shows an example of a closed-loop system.

By using the coordinate partitioning method, the dependent velocities can be written in terms of the system's degrees of freedom f as [25]

$$\dot{\mathbf{z}}^{\mathrm{d}} = -\left(\mathbf{\Phi}_{\mathbf{z}}^{\mathrm{d}}\right)^{-1}\mathbf{\Phi}_{\mathbf{z}}^{\mathrm{i}}\dot{\mathbf{z}}^{\mathrm{i}}, \tag{13}$$

where $\mathbf{\Phi}_{\mathbf{z}}^{\mathrm{d}} \in \mathbb{R}^{m\times m}$ and $\mathbf{\Phi}_{\mathbf{z}}^{\mathrm{i}} \in \mathbb{R}^{m\times f}$ are, respectively, the dependent and independent columns of Jacobian matrix $\mathbf{\Phi}_{\mathbf{z}}$, and $\dot{\mathbf{z}}^{\mathrm{d}} \in \mathbb{R}^{m}$ and $\dot{\mathbf{z}}^{\mathrm{i}} \in \mathbb{R}^{f}$ are, respectively, the dependent and independent relative joint velocities. It is assumed that neither redundant constraints nor singular configurations exist, which guarantees that the inverse of $\mathbf{\Phi}_{\mathbf{z}}^{\mathrm{d}}$ can be found. A velocity transformation matrix $\mathbf{R}_{\mathbf{z}} \in \mathbb{R}^{N_b\times f}$ is introduced to transform the dependent relative joint velocities into independent ones as [25]

$$\begin{bmatrix}\dot{\mathbf{z}}^{\mathrm{d}}\\ \dot{\mathbf{z}}^{\mathrm{i}}\end{bmatrix} = \begin{bmatrix}-\left(\mathbf{\Phi}_{\mathbf{z}}^{\mathrm{d}}\right)^{-1}\mathbf{\Phi}_{\mathbf{z}}^{\mathrm{i}}\\ \mathbf{I}\end{bmatrix}\dot{\mathbf{z}}^{\mathrm{i}} \equiv \mathbf{R}_{\mathbf{z}}\dot{\mathbf{z}}^{\mathrm{i}}. \tag{14}$$

Similarly, accelerations can be written as

$$\ddot{\mathbf{z}} = \mathbf{R}_{\mathbf{z}}\ddot{\mathbf{z}}^{\mathrm{i}} + \dot{\mathbf{R}}_{\mathbf{z}}\dot{\mathbf{z}}^{\mathrm{i}}, \tag{15}$$

where $\ddot{\mathbf{z}}^{\mathrm{i}} \in \mathbb{R}^{f}$ are the independent relative joint accelerations. In this study, the independent relative joint coordinates are identified by using the Gaussian elimination with full

pivoting to the Jacobian matrix $\mathbf{\Phi_z}$. Note that Gaussian elimination with full pivoting is a lower–upper (LU) matrix factorization technique, where the rows and columns of a matrix are interchanged to use the largest element (in absolute value) in the matrix as the pivot [21]. Accordingly, the $(N_b - m)$ columns of the Jacobian matrix $\mathbf{\Phi_z}$, where the m pivots do not appear, determines the independent relative joint coordinates [15, 25]. Fisette and Vaneghem utilized the same technique in the identification of dependent and independent coordinates [14]. This can be considered as a relative drawback of the double-step semirecursive formulation because the penalty-based semirecursive formulation utilizes the full set of coordinates. By substituting Eqs. (14) and (15) into Eq. (11), the dynamic equations of the closed-loop system can be written as [7]

$$\mathbf{R}_z^{\mathrm{T}}\mathbf{M}'\mathbf{R}_z\ddot{\mathbf{z}}^{\mathrm{i}} = \mathbf{R}_z^{\mathrm{T}}\mathbf{R}_{\mathrm{d}}^{\mathrm{T}}\left(\mathbf{T}^{\mathrm{T}}\bar{\mathbf{Q}} - \mathbf{T}^{\mathrm{T}}\bar{\mathbf{M}}\mathbf{D}\right), \tag{16}$$

where $\mathbf{D} \equiv \mathbf{T}\mathbf{R}_{\mathrm{d}}\begin{bmatrix} -\left(\mathbf{\Phi}_{\mathbf{z}}^{\mathrm{d}}\right)^{-1}\left(\dot{\mathbf{\Phi}}_{\mathbf{z}}\dot{\mathbf{z}}\right) \\ \mathbf{0} \end{bmatrix} + \mathbf{T}\dot{\mathbf{R}}_{\mathrm{d}}\dot{\mathbf{z}}$ are the absolute accelerations, when vector $\ddot{\mathbf{z}}$ in Eq. (5) is set to zero. Equation (16) can be expressed in a simplified form as

$$\mathbf{M}''\ddot{\mathbf{z}}^{\mathrm{i}} = \mathbf{Q}'', \tag{17}$$

where $\mathbf{M}'' = \mathbf{R}_z^{\mathrm{T}}\mathbf{M}'\mathbf{R}_z$ and $\mathbf{Q}'' = \mathbf{R}_z^{\mathrm{T}}\mathbf{R}_{\mathrm{d}}^{\mathrm{T}}\left(\mathbf{T}^{\mathrm{T}}\bar{\mathbf{Q}} - \mathbf{T}^{\mathrm{T}}\bar{\mathbf{M}}\mathbf{D}\right)$. Note that the relation between $\mathbf{Q}'$ and $\mathbf{Q}''$ can be written as $\mathbf{Q}'' = \mathbf{R}_z^{\mathrm{T}}\mathbf{Q}' - \mathbf{R}_z^{\mathrm{T}}\mathbf{M}'\mathbf{R}_z\dot{\mathbf{R}}_z\dot{\mathbf{z}}^{\mathrm{i}}$.

2.3 Penalty-based semirecursive formulation

In the penalty-based semirecursive formulation, the constraints are introduced by using the penalty-based augmented Lagrangian method [10]. In this formulation, the time integration scheme is carried out by using the trapezoidal rule. The loop-closure constraints, a set of m constraint equations $\mathbf{\Phi} = \mathbf{0}$, are introduced in Eq. (12) with a penalty method similar to the index-3 augmented Lagrangian with projections to satisfy the constraints on velocity and acceleration levels [3, 9]. The equations of motion for the closed-loop system can be written as

$$\mathbf{M}'\ddot{\mathbf{z}} + \mathbf{\Phi}_{\mathbf{z}}^{\mathrm{T}}\alpha\mathbf{\Phi} + \mathbf{\Phi}_{\mathbf{z}}^{\mathrm{T}}\boldsymbol{\lambda} = \mathbf{Q}', \tag{18}$$

where $\mathbf{\Phi_z}$ is the Jacobian matrix of $\mathbf{\Phi}(\mathbf{z}) = \mathbf{0}$, α is the penalty factor that can be set the same for all constraints, and $\boldsymbol{\lambda}$ is the vector of iterated Lagrange multipliers. In this method, these multipliers are obtained at each time-step k as

$$\boldsymbol{\lambda}_k^{(h+1)} = \boldsymbol{\lambda}_k^{(h)} + \alpha\mathbf{\Phi}_k^{(h+1)}, \tag{19}$$

where h is the iteration step. The value of $\boldsymbol{\lambda}_k^{(0)}$ is the final value of $\boldsymbol{\lambda}_{k-1}$, calculated in the previous time-step [10]. As mentioned earlier, the system is integrated by using an implicit single-step trapezoidal scheme [10]. In this approach, the relative joint velocities $\dot{\mathbf{z}}$ and accelerations $\ddot{\mathbf{z}}$ are corrected by using the mass-damping-stiffness-orthogonal projections as [3, 9]

$$\left[\mathbf{W} + \frac{\Delta t^2}{4}\mathbf{\Phi}_{\mathbf{z}}^{\mathrm{T}}\alpha\mathbf{\Phi}_{\mathbf{z}}\right]\dot{\mathbf{z}} = \mathbf{W}\dot{\mathbf{z}}', \tag{20}$$

$$\left[\mathbf{W} + \frac{\Delta t^2}{4}\mathbf{\Phi}_{\mathbf{z}}^{\mathrm{T}}\alpha\mathbf{\Phi}_{\mathbf{z}}\right]\ddot{\mathbf{z}} = \mathbf{W}\ddot{\mathbf{z}}' - \frac{\Delta t^2}{4}\mathbf{\Phi}_{\mathbf{z}}^{\mathrm{T}}\alpha\left(\dot{\mathbf{\Phi}}_{\mathbf{z}}\dot{\mathbf{z}}\right), \tag{21}$$

where $\dot{\mathbf{z}}'$ and $\ddot{\mathbf{z}}'$ are, respectively, the relative joint velocities and accelerations obtained from the Newton–Raphson iteration, and $\mathbf{W} = \mathbf{M} + \frac{\Delta t}{2}\mathbf{C} + \frac{\Delta t^2}{4}\mathbf{K}$, where $\mathbf{C}$ and $\mathbf{K}$ represent the damping and stiffness contributions in the system. Note that in Eqs. (20) and (21), time-dependent constraint terms are not incorporated because the constraints are assumed sclerono-mic. To account for rheonomic constraints, the reader is referred to [10, 32].

3 Hydraulic actuators

In this study, the hydraulic pressures within a hydraulic circuit is computed by using the lumped fluid theory [37]. By using this approach, a hydraulic circuit is divided into discrete volumes where pressures are assumed to be equally distributed. The effect of acoustic waves is thus assumed to be insignificant. In a hydraulic volume V_k, the pressure p_k can be computed as

$$\dot{p}_k = \frac{B_{e_k}}{V_k} \sum_{s=1}^{n_f} Q_{ks}, \tag{22}$$

where Q_{ks} is the sum of incoming and outgoing flows associated with the volume V_k, n_f is the total number of volume flows going in or out of the volume V_k, and B_{e_k} is the effective bulk modulus associated to the volume V_k. The effective bulk modulus can be written as

$$B_{e_k} = \left(\frac{1}{B_{oil}} + \sum_{s=1}^{n_c} \frac{V_s}{V_k B_s} \right)^{-1}, \tag{23}$$

where B_{oil} is the bulk modulus of oil, n_c is the total number of subvolumes V_s that form the volume V_k, and B_s is the corresponding bulk modulus of the volume V_s.

3.1 Valves

In this study, the valves are described by using a semiempirical modeling method [19]. By using the semiempirical modeling approach, the volume flow rate Q_t through a simple throttle valve can be written as

$$Q_t = C_{v_t} \operatorname{sgn}(\Delta p) \sqrt{|\, \Delta p \,|}, \tag{24}$$

where Δp is the pressure difference over the valve, $\operatorname{sgn}(\Delta p)$ is the sign function that determines the sign of Δp, and C_{v_t} is the semiempirical flow rate coefficient of the throttle valve that can be calculated as

$$C_{v_t} = C_d A_t \sqrt{\frac{2}{\rho}}, \tag{25}$$

where C_d is the flow discharge coefficient, A_t is the area of the throttle valve, and ρ is the density of the oil.

Similarly, the volume flow rate Q_d through a directional control valve can be written as

$$Q_d = C_{v_d} U \operatorname{sgn}(\Delta p) \sqrt{|\, \Delta p \,|}, \tag{26}$$

where C_{v_d} is the semiempirical flow rate constant of the valve procured from the manufacturer catalogues, and U is the relative poppet/spool position. If the pressure difference is

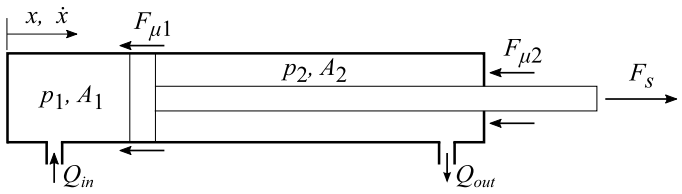

Fig. 3 Schematic figure of a hydraulic cylinder

less than 2 bar, the volume flow is assumed to be laminar, and Eqs. (24) and (26) are modified so that the volume flow and the pressure difference follows a linear relation. Equation (26) is complemented by the following first order differential equation that describes a spool position

$$\dot{U} = \frac{U_{ref} - U}{\tau}, \tag{27}$$

where U_{ref} is the reference voltage signal for the reference spool position, and τ is the time constant, which can be obtained from the Bode-diagram of the valve that describes the dynamics of valve spool.

3.2 Cylinders

The volume flow produced due to the motion of a hydraulic cylinder (shown in Fig. 3) can be written as

$$Q_{in} = \dot{x} A_1, \qquad Q_{out} = \dot{x} A_2, \tag{28}$$

where Q_{in} and Q_{out} are, respectively, the volume flow rate going inside and coming out of the cylinder, $\dot{x}$ is the piston velocity, and A_1 and A_2 are, respectively, the areas on the piston and piston-rod side of the cylinder. The force F_s produced by the cylinder can be written in terms of its dimensions and chambers pressure as

$$F_s = p_1 A_1 - p_2 A_2 - F_\mu, \tag{29}$$

where p_1 and p_2 are, respectively, the pressure on the piston and piston-rod side that can be calculated by using Eq. (22), and F_μ is the total friction force caused by sealing.

4 Coupling of multibody formulations and hydraulic actuators

In this section, the multibody formulations described in Sect. 2 are extended to incorporate the dynamics of the hydraulic actuators described in Sect. 3 in a monolithic approach. The coupling of the double-step semirecursive formulation with the lumped fluid theory is inspired from [28] and [32]. Whereas the coupling of the penalty-based semirecursive formulation with the lumped fluid theory was already carried out in [32]. The force vector $\bar{\mathbf{Q}}$ in Eqs. (17) and (18) is incremented with the pressure variation equations, leading to the combined system of equations as follows

$$\left.\begin{aligned} \mathbf{M}''\dot{\mathbf{z}}^{\mathbf{i}} &= \mathbf{Q}''(\mathbf{z}, \dot{\mathbf{z}}, \mathbf{p}) \\ \dot{\mathbf{p}} &= \mathbf{h}(\mathbf{p}, \mathbf{z}, \dot{\mathbf{z}}) \end{aligned}\right\} \text{(double-step semirecursive approach)}, \tag{30}$$

$$\left.\begin{aligned} \mathbf{M}'\ddot{\mathbf{z}} + \boldsymbol{\Phi}_{\mathbf{z}}^{\mathrm{T}}\alpha\boldsymbol{\Phi} + \boldsymbol{\Phi}_{\mathbf{z}}^{\mathrm{T}}\boldsymbol{\lambda} &= \mathbf{Q}'(\mathbf{z}, \dot{\mathbf{z}}, \mathbf{p}) \\ \boldsymbol{\lambda}^{(h+1)} &= \boldsymbol{\lambda}^{(h)} + \alpha\boldsymbol{\Phi}^{(h+1)} \\ \dot{\mathbf{p}} &= \mathbf{h}(\mathbf{p}, \mathbf{z}, \dot{\mathbf{z}}) \end{aligned}\right\} \text{(penalty-based semirecursive approach)}, \tag{31}$$

where $\mathbf{p}$ is a vector of the pressures in the hydraulic subsystem and $\mathbf{h}(\mathbf{p}, \mathbf{z}, \dot{\mathbf{z}})$ are the pressure variation equations. It is assumed that the dependency of both $\mathbf{Q}'$ and function $\mathbf{h}$ with respect to $\mathbf{z}$, $\dot{\mathbf{z}}$, and $\mathbf{p}$ are known.

In this study, both the approaches are integrated by using an implicit single-step trapezoidal rule [26], which is second order and A-stable method. While the trapezoidal rule was often used in structural dynamics, it was, however, seldom used in multibody system dynamics until the study by Bayo et al. [1]. In the study [1], it was agreed that the trapezoidal rule will lead to poor convergence characteristics when applied to multibody system dynamics in a similar way as other multistep integrators, that is, by considering the accelerations as primary variables. However, Bayo et al. [1] and Cuadrado et al. [8–10] demonstrated that the trapezoidal rule performs very satisfactorily when it is combined directly with the equations of motion by taking the positions as the primary variables, as shown below. Similarly, for the hydraulic subsystem, pressures are taken as the primary variables, as shown in [28, 32]. Note that this study is more inclined to use the above approaches for real-time applications, such as [23], in future studies. Therefore, a single-step integration method is preferred that can use the same computational cost in each integration step [1]. Furthermore, even though the explicit, multistep integrators can be inexpensive and accurate, however, they do not demonstrate good stability, which is a limiting factor for real-time integration [1], especially for stiff systems. Thus, an implicit method is used. Moreover, A-stability is crucial for a numerically stiff system [1], such as presented in this study.

In the double-step semirecursive approach, the trapezoidal rule can be written as

$$\left.\begin{aligned} \mathbf{z}_{k+1}^{\mathrm{i}} &= \mathbf{z}_k^{\mathrm{i}} + \frac{\Delta t}{2}\left(\dot{\mathbf{z}}_k^{\mathrm{i}} + \dot{\mathbf{z}}_{k+1}^{\mathrm{i}}\right) \\ \dot{\mathbf{z}}_{k+1}^{\mathrm{i}} &= \dot{\mathbf{z}}_k^{\mathrm{i}} + \frac{\Delta t}{2}\left(\ddot{\mathbf{z}}_k^{\mathrm{i}} + \ddot{\mathbf{z}}_{k+1}^{\mathrm{i}}\right) \\ \mathbf{p}_{k+1} &= \mathbf{p}_k + \frac{\Delta t}{2}\left(\dot{\mathbf{p}}_k + \dot{\mathbf{p}}_{k+1}\right) \end{aligned}\right\}, \tag{32}$$

where Δt is the time-step, $\mathbf{z}_k^{\mathrm{i}}$ are the independent relative joint coordinates, $\dot{\mathbf{z}}_k^{\mathrm{i}}$ are the independent relative joint velocities, $\ddot{\mathbf{z}}_k^{\mathrm{i}}$ are the independent relative joint accelerations, and $\mathbf{p}_k$ and $\dot{\mathbf{p}}_{k+1}$ are, respectively, the pressures and pressure derivatives. Equation (32) can be rewritten by considering $\mathbf{z}_{k+1}^{\mathrm{i}}$ and $\mathbf{p}_{k+1}$ as the primary variables and, respectively, solving for $\dot{\mathbf{z}}_{k+1}^{\mathrm{i}}$, $\ddot{\mathbf{z}}_{k+1}^{\mathrm{i}}$, and $\dot{\mathbf{p}}_{k+1}$ at time-step $(k+1)$ as

$$\left.\begin{aligned} \dot{\mathbf{z}}_{k+1}^{\mathrm{i}} &= \frac{2}{\Delta t}\mathbf{z}_{k+1}^{\mathrm{i}} + \hat{\dot{\mathbf{z}}}_k^{\mathrm{i}} \\ \ddot{\mathbf{z}}_{k+1}^{\mathrm{i}} &= \frac{4}{\Delta t^2}\mathbf{z}_{k+1}^{\mathrm{i}} + \hat{\ddot{\mathbf{z}}}_k^{\mathrm{i}} \\ \dot{\mathbf{p}}_{k+1} &= \frac{2}{\Delta t}\mathbf{p}_{k+1} + \hat{\dot{\mathbf{p}}}_k \end{aligned}\right\}, \tag{33}$$

where

$$\left.\begin{aligned}\hat{\dot{\mathbf{z}}}^{\mathrm{i}}_k &= -\left(\frac{2}{\Delta t}\mathbf{z}^{\mathrm{i}}_k + \dot{\mathbf{z}}^{\mathrm{i}}_k\right)\\ \hat{\ddot{\mathbf{z}}}^{\mathrm{i}}_k &= -\left(\frac{4}{\Delta t^2}\mathbf{z}^{\mathrm{i}}_k + \frac{4}{\Delta t}\dot{\mathbf{z}}^{\mathrm{i}}_k + \ddot{\mathbf{z}}^{\mathrm{i}}_k\right)\\ \hat{\dot{\mathbf{p}}}_k &= -\left(\frac{2}{\Delta t}\mathbf{p}_k + \dot{\mathbf{p}}_k\right)\end{aligned}\right\}. \tag{34}$$

Note that in the double-step semirecursive approach, the rules $\mathbf{z}^{\mathrm{i}}_{k+1} = \mathbf{z}^{\mathrm{i}}_k + \dot{\mathbf{z}}^{\mathrm{i}}_k \Delta t + \frac{1}{2}\ddot{\mathbf{z}}^{\mathrm{i}}_k \Delta t^2$ and $\mathbf{p}_{k+1} = \mathbf{p}_k + \dot{\mathbf{p}}_k \Delta t$ are applied to $\mathbf{z}^{\mathrm{i}}_{k+1}$ and $\mathbf{p}_{k+1}$, respectively. In the double-step semirecursive approach, given $\mathbf{z}^{\mathrm{i}}_{k+1}$, the dependent relative joint coordinates $\mathbf{z}^{\mathrm{d}}_{k+1}$ are obtained by iteratively solving the loop-closure constraint equations $\mathbf{\Phi}(\mathbf{z}) = \mathbf{0}$, which are highly nonlinear [11]. In this study, the Newton–Raphson method is used to solve the loop-closure position problem and convergence is achieved by providing a reliable estimate for $\mathbf{z}^{\mathrm{d}}_{k+1}$ by using information from the previous time-step as [15] $\mathbf{z}^{\mathrm{d}}_{k+1} = \mathbf{z}^{\mathrm{d}}_k + \dot{\mathbf{z}}^{\mathrm{d}}_k \Delta t + \frac{1}{2}\ddot{\mathbf{z}}^{\mathrm{d}}_k \Delta t^2$. The dependent relative joint velocities $\dot{\mathbf{z}}^{\mathrm{d}}_{k+1}$ and accelerations $\ddot{\mathbf{z}}^{\mathrm{d}}_{k+1}$ are computed from Eqs. (14) and (15), respectively. In the penalty-based semirecursive approach, the full set of relative joint coordinates $\mathbf{z}_{k+1}$, velocities $\dot{\mathbf{z}}_{k+1}$, and accelerations $\ddot{\mathbf{z}}_{k+1}$ are used in the above discussion of Eqs. (32), (33), and (34), instead of $\mathbf{z}^{\mathrm{i}}_{k+1}$, $\dot{\mathbf{z}}^{\mathrm{i}}_{k+1}$, and $\ddot{\mathbf{z}}^{\mathrm{i}}_{k+1}$. The dynamic equilibrium, established at time-step $(k+1)$, for both the approaches can be written as

$$\left.\begin{aligned}\mathbf{M}''\mathbf{z}^{\mathrm{i}}_{k+1} - \frac{\Delta t^2}{4}\mathbf{Q}''_{k+1} + \frac{\Delta t^2}{4}\mathbf{M}''\hat{\ddot{\mathbf{z}}}^{\mathrm{i}}_k = 0\\ \frac{\Delta t}{2}\mathbf{p}_{k+1} - \frac{\Delta t^2}{4}\mathbf{h}_{k+1} + \frac{\Delta t^2}{4}\hat{\dot{\mathbf{p}}}_k = 0\end{aligned}\right\} \text{(double-step semirecursive approach)}, \tag{35}$$

$$\left.\begin{aligned}\mathbf{M}'\mathbf{z}_{k+1} + \frac{\Delta t^2}{4}\mathbf{\Phi}^{\mathrm{T}}_{\mathbf{z}_{k+1}}\left(\alpha\mathbf{\Phi}_{k+1} + \boldsymbol{\lambda}_{k+1}\right) - \frac{\Delta t^2}{4}\mathbf{Q}'_{k+1} + \frac{\Delta t^2}{4}\mathbf{M}'\hat{\dot{\mathbf{z}}}_k = 0\\ \boldsymbol{\lambda}^{(h+1)}_{k+1} = \boldsymbol{\lambda}^{(h)}_{k+1} + \alpha\mathbf{\Phi}^{(h+1)}_{k+1}\\ \frac{\Delta t}{2}\mathbf{p}_{k+1} - \frac{\Delta t^2}{4}\mathbf{h}_{k+1} + \frac{\Delta t^2}{4}\hat{\dot{\mathbf{p}}}_k = 0\end{aligned}\right\} \tag{36}$$

(penalty-based semirecursive approach).

Equations (35) and (36) are a nonlinear system of equations that can be denoted as $\mathbf{f}(\mathbf{x}_{k+1}) = \mathbf{0}$, where $\mathbf{x} = \left[\left(\mathbf{z}^{\mathrm{i}}\right)^{\mathrm{T}}, \mathbf{p}^{\mathrm{T}}\right]^{\mathrm{T}}$ for the double-step semirecursive approach and $\mathbf{x} = \left[\mathbf{z}^{\mathrm{T}}, \mathbf{p}^{\mathrm{T}}\right]^{\mathrm{T}}$ for the penalty-based semirecursive approach. Such a nonlinear system of equations can be iteratively solved by employing the Newton–Raphson method as

$$\left[\frac{\partial \mathbf{f}(\mathbf{x})}{\partial \mathbf{x}}\right]^{(h)}_{k+1} \Delta\mathbf{x}^{(h)}_{k+1} = -\left[\mathbf{f}(\mathbf{x})\right]^{(h)}_{k+1}. \tag{37}$$

The residual vector $\left[\mathbf{f}(\mathbf{x})\right]^{(h)}_{k+1}$ can be written as

$$\left[\mathbf{f}(\mathbf{x})\right]^{(h)}_{k+1} = \frac{\Delta t^2}{4}\left[\begin{matrix}\mathbf{M}''\ddot{\mathbf{z}}^{\mathrm{i}} - \mathbf{Q}''\\ \dot{\mathbf{p}} - \mathbf{h}\end{matrix}\right]^{(h)}_{k+1} \text{(double-step semirecursive approach)}, \tag{38}$$

$$[\mathbf{f}(\mathbf{x})]_{k+1}^{(h)} = \frac{\Delta t^2}{4}\begin{bmatrix}\mathbf{M}'\ddot{\mathbf{z}} + \mathbf{\Phi}_{\mathbf{z}}^{\mathrm{T}}\alpha\mathbf{\Phi} + \mathbf{\Phi}_{\mathbf{z}}^{\mathrm{T}}\boldsymbol{\lambda} - \mathbf{Q}' \\ \dot{\mathbf{p}} - \mathbf{h}\end{bmatrix}_{k+1}^{(h)} \quad \text{(penalty-based semirecursive approach)}, \tag{39}$$

where $\boldsymbol{\lambda}$ is obtained as shown in Eq. (19). The approximated tangent matrix $\left[\frac{\partial \mathbf{f}(\mathbf{x})}{\partial \mathbf{x}}\right]_{k+1}^{(h)}$ can be obtained numerically by using the forward differentiation rule

$$\frac{df(x_0)}{dx} \approx \frac{f(x_0+\epsilon) - f(x_0)}{\epsilon}, \tag{40}$$

where ϵ is the differentiation increment. To avoid ill-conditioning of the tangent matrix, ϵ is computed as in [32], namely

$$\epsilon = 1 \times 10^{-8}\max\left(1 \times 10^{-2}, |\, x_0 \,|\right), \tag{41}$$

where 1×10^{-2} limits the minimum value for the differentiation increment to 1×10^{-10}. Equation (41) is a modification of a method presented in [5]. In the penalty-based semirecursive approach, $\dot{\mathbf{z}}$ and $\ddot{\mathbf{z}}$ are corrected by using the mass-damping-stiffness-orthogonal projections [3, 9] as shown in Eqs. (20) and (21).

5 The case studies of hydraulically actuated four-bar and quick-return mechanisms

In this study, a hydraulically actuated four-bar mechanism, as shown in Fig. 4, and a hydraulically actuated quick-return mechanism, as shown in Fig. 5, are used for a comparative study between the two multibody formulations in a numerically stiff coupled environment. The numerical stiffness in the coupled environment is introduced by the hydraulic subsystem. The mechanisms are modeled, first by using the double-step semirecursive formulation, and later by using the penalty-based semirecursive formulation, as explained in Sect. 2. For the planar system in Fig. 4, three joint coordinates are used in the modeling of the structure and two loop-closure constraints are used for a cut-joint (revolute joint) at point E. Whereas for the planar system in Fig. 5, five joint coordinates are used in the modeling of the structure and four loop-closure constraints are used for two cut-joints (translational joints) at points J and M. Both the mechanisms have one degree of freedom.

In Fig. 4, bodies 1, 2, and 3 are assumed as rectangular beams, whose lengths and masses are $L_1 = 9$ m, $L_2 = \sqrt{2}$ m, and $L_3 = 2$ m, and $m_1 = 225$ kg, $m_2 = 35$ kg, and $m_3 = 50$ kg, respectively. The locations of points E, G, and C in the inertial reference frame are $[0, -1, 0]^{\mathrm{T}}$ m, $[0, -2, 0]^{\mathrm{T}}$ m, and $\left[\frac{L_1}{3}, 0, 0\right]^{\mathrm{T}}$ m, respectively. Point F is located at the center of mass of body-3. In Fig. 4, the relative joint coordinates at points O, C, and D are respectively represented by z_1, z_2 and z_3 that define the orientation of the respective bodies in the inertial reference frame, XYZ. Their initial values are considered as 0^{o}, -135^{o}, and -45^{o}, respectively. To avoid instabilities in the integration process, the initial values of the relative joint velocities are considered 0^{o}/s.

In Fig. 5, bodies 1, 2, and 4 are assumed as rectangular beams and bodies 3 and 5 are assumed as cuboid, whose lengths and masses are $L_1 = 5$ m, $L_2 = 1.2$ m, $L_3 = 0.3$ m, $L_4 = 1$ m, and $L_5 = 0.3$ m, and $m_1 = 25$ kg, $m_2 = 12$ kg, $m_3 = 3$ kg, $m_4 = 100$ kg, and $m_5 = 30$ kg, respectively. The locations of points I, K, and Q in the inertial reference frame are $[0, 5, 0]^{\mathrm{T}}$ m, $[0, 3, 0]^{\mathrm{T}}$ m, and $[-0.96, 3, 0]^{\mathrm{T}}$ m, respectively. Points N and L are

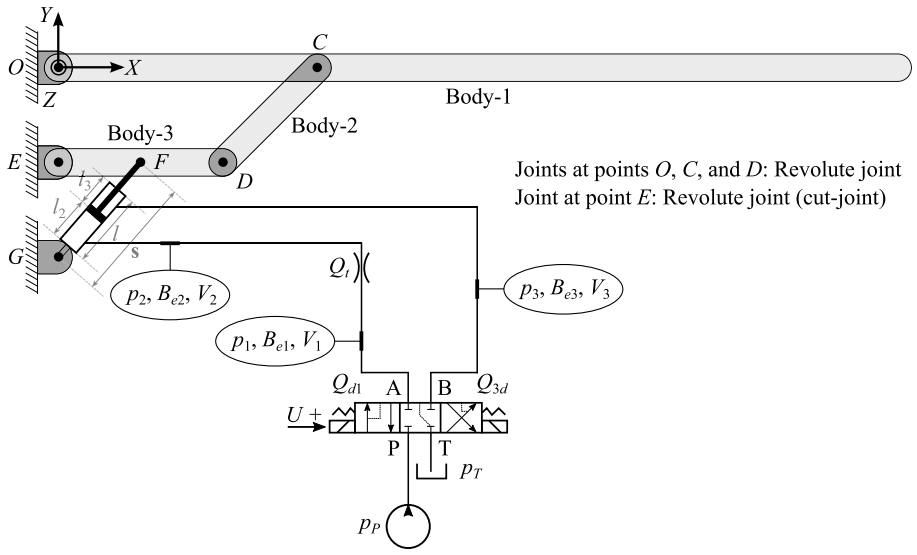

Fig. 4 A four-bar mechanism actuated by a double-acting hydraulic cylinder

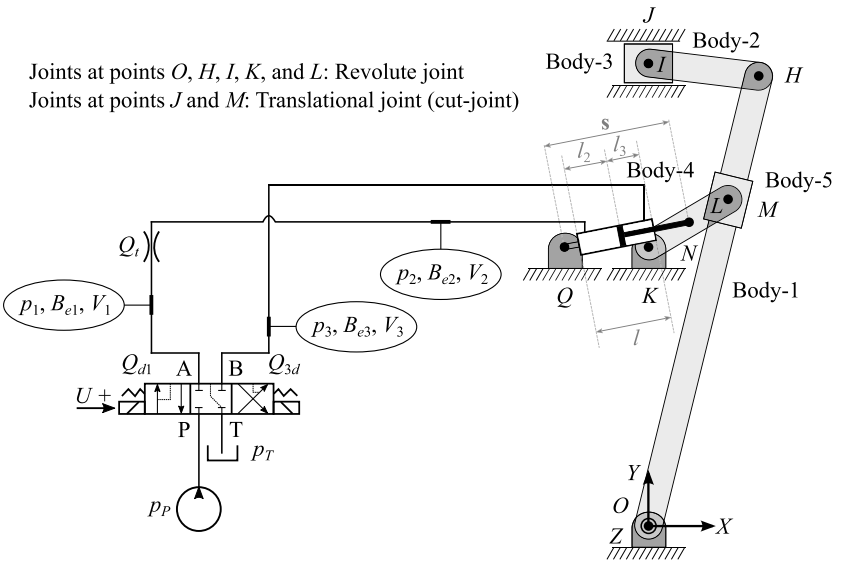

Fig. 5 A quick-return mechanism actuated by a double-acting hydraulic cylinder

located at the center of mass of bodies 4 and 5, respectively. In Fig. 5, the relative joint coordinates at points O, H, I, K, and L are respectively represented by z_1, z_2, z_3, z_4, and z_5 that define the orientation of the respective bodies in the inertial reference frame, XYZ. Their initial values are considered as 76.22°, 96.89°, 6.89°, 30.59°, and 45.63°, respectively. The mass moment of inertia of a rectangular beam and a cuboid are considered as $\frac{mL^2}{12}$ and $\frac{mL^2}{6}$,

respectively, where m is the mass and L is the length. The gravity is assumed to act in the negative Y direction, whose value is $g = 9.81$ m/s^2.

Both mechanisms are actuated by using the hydraulic actuators, as shown in Figs. 4 and 5. For simplicity, identical hydraulic actuators are used in both mechanisms. In this study, a simple hydraulic circuit is accounted, which consists of a pump, with a constant pressure source p_P, a directional control valve, with a control signal U, a throttle valve, a double-acting hydraulic cylinder, connecting hoses, and a tank, with a constant pressure p_T. The control volumes, V_1, V_2, and V_3, used in the modeling of the hydraulic circuit are marked in Fig. 4. The pressure in the respective control volumes are p_1, p_2, and p_3; and their respective effective bulk modulus are B_{e1}, B_{e2}, and B_{e3}, that are calculated by using Eq. (23). For simplicity, the hydraulic circuit is assumed ideal, that is, the leakage is neglected.

In the hydraulic subsystem, the control volumes V_1, V_2, and V_3 are calculated as

$$\left.\begin{aligned} V_1 &= V_{h_1} \\ V_2 &= V_{h_2} + A_2 l_2 \\ V_3 &= V_{h_3} + A_3 l_3 \end{aligned}\right\}, \tag{42}$$

where V_{h_1}, V_{h_2}, and V_{h_3} are the volumes of the respective hoses; A_2 and A_3 are, respectively, the areas of the piston side and the piston-rod side within a cylinder; and l_2 and l_3 are, respectively, the lengths of the chambers of the cylinder, piston and piston-rod side. The length of the hydraulic cylinder is l such that $l_2 + l_3 = l$; and the variable chamber lengths, l_2 and l_3, are calculated as

$$\left.\begin{aligned} l_2 &= l_{2_0} + s_0 - |\,\mathbf{s}\,| \\ l_3 &= l_{3_0} - s_0 + |\,\mathbf{s}\,| \end{aligned}\right\}, \tag{43}$$

where $|\,\mathbf{s}\,|$ is the actuator length of the hydraulic cylinder (see Figs. 4 and 5); s_0 is the actuator length at $t = 0$; and $l_{2_0} = s_0 - l$ and $l_{3_0} = l - l_{2_0}$ are, respectively, the length of the piston and piston-rod side of the cylinder at $t = 0$. The differential equations of the pressures p_1, p_2, and p_3 are computed based on Eq. (22) as

$$\left.\begin{aligned} \dot{p}_1 &= \frac{B_{e1}}{V_1}\,(Q_{d1} - Q_t) \\ \dot{p}_2 &= \frac{B_{e2}}{V_2}\,(Q_t - A_2\dot{s}) \\ \dot{p}_3 &= \frac{B_{e3}}{V_3}\,(A_3\dot{s} - Q_{3d}) \end{aligned}\right\}, \tag{44}$$

where the volume flow rates Q_{d1} and Q_{3d} are calculated from Eq. (26), the volume flow rate Q_t is calculated from Eq. (24), and $\dot{s}$ is the actuator velocity. The actuator length $|\,\mathbf{s}\,|$ and actuator velocity $\dot{s}$ of the hydraulic cylinder are computed as a function of the relative joint coordinates. For example, in Fig. 4, the upper end of the hydraulic cylinder is attached to body-3 at point F, while, the lower end is attached to ground at point G, such that $\mathbf{r}_G = [0, -2, 0]^{\mathrm{T}}$ m. Therefore, $\mathbf{s}$ and $\dot{s}$ for the four-bar mechanism can be computed as

$$\left.\begin{aligned} \mathbf{s} &= \mathbf{r}_F - \mathbf{r}_G \\ \dot{s} &= \frac{d|\,\mathbf{s}\,|}{dt} = \dot{\mathbf{s}} \cdot \frac{\mathbf{s}}{|\,\mathbf{s}\,|} = \dot{\mathbf{r}}_F \cdot \frac{\mathbf{s}}{|\,\mathbf{s}\,|} \end{aligned}\right\}, \tag{45}$$

Table 1 Parameters of the hydraulic circuit

Parameter	Symbol	Value
Pressure of the pump	p_P	7.6 MPa
Pressure of the tank (atmospheric pressure)	p_T	0.1 MPa
Semiempirical flow rate constant of the directional control valve	C_{v_d}	2.138×10^{-8} m^3/s $\sqrt{\text{Pa}}$
Volume of the hose (section-1)	V_{h_1}	4.71×10^{-5} m^3
Volume of the hose (section-2)	V_{h_2}	3.14×10^{-5} m^3
Volume of the hose (section-3)	V_{h_3}	7.85×10^{-5} m^3
Area of the throttle valve	A_t	2.83×10^{-5} m^2
Flow discharge coefficient of the throttle valve	C_d	0.8
Density of the oil	ρ	850 kg/m^3
Bulk modulus of the hoses	B_h	550 MPa
Bulk modulus of the oil	B_{oil}	1500 MPa
Bulk modulus of the hydraulic cylinder	B_c	31500 MPa
Efficiency of the cylinder	η	0.88
Diameter of the piston	d_2	80 mm
Diameter of the piston-rod	d_3	35 mm
Length of the cylinder/piston	l	1.1 m
Initial actuator length	s_0	$\sqrt{2}$ m

where the position $\mathbf{r}_F$ and velocity $\dot{\mathbf{r}}_F$ are calculated by applying the classical kinematic relations as in [11, 22]. For simplicity, the force F_s produced by the hydraulic cylinder in Eq. (29) is expressed in the form of Eq. (10) as $\mathbf{F}_s = \left[\frac{s_X}{|\mathbf{s}|}F_s, \frac{s_Y}{|\mathbf{s}|}F_s, \frac{s_Z}{|\mathbf{s}|}F_s\right]^{\mathrm{T}}$, where s_X, s_Y, and s_Z are the components of vector $\mathbf{s}$ along the axes of the inertial reference frame. The initial value of the force F_{s_0} produced by the hydraulic cylinder is calculated from the static configurations, as shown in Figs. 4 and 5. For example, in case of four-bar mechanism, $F_{s_0} = \sqrt{2}g\,(3m_1 + 2m_2 + m_3)$. In the static configuration, the initial value of pressure p_1 is equal to the initial value of pressure p_2, which can be calculated based on Eq. (29) as $p_2 = \left(F_{s_0} + p_3 A_3\right)/A_2$. Note that the friction is neglected in static configuration and the initial value of pressure p_3 is assumed 3.5 MPa. The directional control valve, parameter U in Eq. (27), controls the movement of the cylinder through volume flows and is actuated for 10 s by using the following reference voltage signal U_{ref} as

$$\text{(Four-bar mechanism)} \quad U_{ref} = \begin{cases} 0, & t < 1 \text{ s}, \quad 2.5 \text{ s} \le t < 5 \text{ s}, \quad t \le 10, \\ 10, & 1 \text{ s} \le t < 2.5 \text{ s}, \\ -10, & 5 \text{ s} \le t < 8 \text{ s}, \end{cases} \tag{46}$$

$$\text{(Quick-return mechanism)} \quad U_{ref} = \begin{cases} 0, & t < 1 \text{ s}, \quad 4 \text{ s} \le t < 6.5 \text{ s}, \quad t \le 10, \\ -10, & 1 \text{ s} \le t < 4 \text{ s}, \\ 10, & 6.5 \text{ s} \le t < 8 \text{ s}, \end{cases} \tag{47}$$

where t is the simulation run time. The parameters of the hydraulic circuit are shown in Table 1.

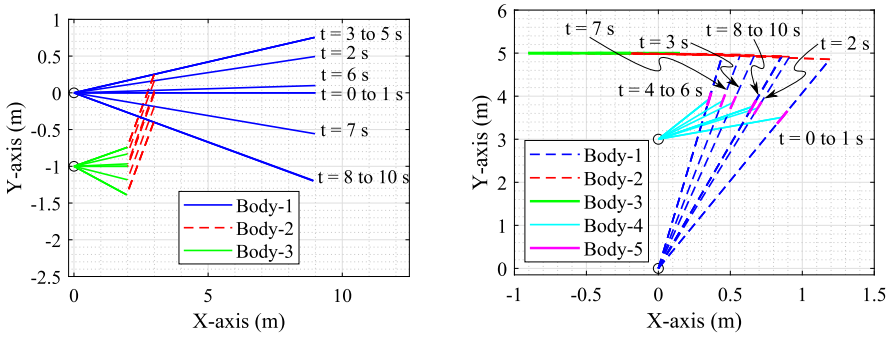

(a) Hydraulically actuated four-bar mechanism (b) Hydraulically actuated quick-return mechanism

Fig. 6 The positions of the mechanisms at every second during the simulation run

The set of variables used to solve the combined system of equations with the proposed integration scheme (Sect. 4) are

$$\left.\begin{aligned} \mathbf{x} &= \left[\left(\mathbf{z}^{\mathrm{i}}\right)^{\mathrm{T}},\ \mathbf{p}^{\mathrm{T}}\right]^{\mathrm{T}} \text{ (double-step semirecursive approach)} \\ \mathbf{x} &= \left[\mathbf{z}^{\mathrm{T}},\ \mathbf{p}^{\mathrm{T}}\right]^{\mathrm{T}} \text{ (penalty-based semirecursive approach)} \end{aligned}\right\}. \tag{48}$$

Note that, in the double-step semirecursive approach (Eq. (48)), $\mathbf{z}^{\mathrm{i}}$ is identified by using the Gaussian elimination with full pivoting to the Jacobian matrix $\mathbf{\Phi}_{\mathbf{z}}$. In this study, the error tolerance is considered as 1×10^{-7} rad for positions and 1×10^{-2} Pa for pressures. The voltage that corresponds to the spool position is integrated by using the trapezoidal rule and its error tolerance is considered as 1×10^{-7} V. Furthermore, the penalty factor α in Eq. (18) is considered as 1×10^{11}. Note that in the penalty-based semirecursive approach, the penalty term is analogous to a spring constant by considering that there is a spring attached to the cut-joint location to fulfill the constraints. Due to the high numerical stiffness introduced by the hydraulics, a high penalty term (spring constant) is used. In this study, both the approaches are implemented in the Matlab environment.

6 Results and discussion

This section presents the simulation results of the hydraulically actuated four-bar and quick-return mechanisms presented in the previous section. Figures 6a and 6b show the simulation frames of the four-bar and quick-return mechanisms, respectively, presenting the position of the bodies at different instants of time. Here, the two approaches, namely, the double-step semirecursive approach and the penalty-based semirecursive approach, are compared based on the simulation work cycle, energy balance, constraint violation, and numerical efficiency.

6.1 The work cycle

In the four-bar mechanism, the hydraulic cylinder lifts the structure between 1–2.5 s and lowers it down between 5–8 s. Whereas in the quick-return mechanism, the hydraulic cylinder pulls the structure between 1–4 s and pushes it between 6.5–8 s. In the subsequent

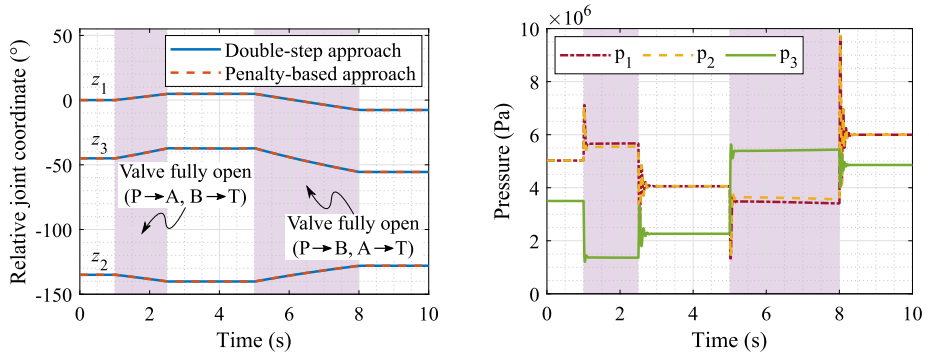

(a) Relative joint coordinates during the simulation (b) Pressures in the hydraulic control volumes

Fig. 7 The relative joint coordinates and pressures for the four-bar mechanism

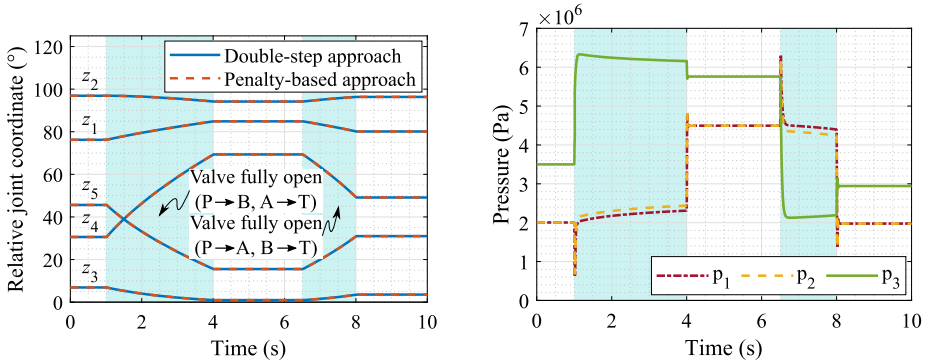

(a) Relative joint coordinates during the simulation (b) Pressures in the hydraulic control volumes

Fig. 8 The relative joint coordinates and pressures for the quick-return mechanism

plots, the regions between the opening and closing of the directional control valve are highlighted in purple for the four-bar mechanism and in cyan for the quick-return mechanism. For both the mechanisms, the relative joint coordinates showed a good agreement in the two approaches, as shown in Figs. 7a and 8a. Thus, the solutions of both the approaches are accurate with respect to each other. The pressures in the hydraulic control volumes are shown in Figs. 7b and 8b, respectively, for the four-bar and quick-return mechanisms. Note that the pressures are identical in both the approaches and the choice of the multibody formulation does not affect the results of the hydraulics.

In the double-step approach, the independent joint coordinate is identified by using the Gaussian elimination with full pivoting on the Jacobian matrix of the constraints. For the presented work cycle, the independent coordinates are identified as z_3 for the four-bar mechanism and as z_4 for the quick-return mechanism, throughout the simulation. In the double-step approach, if the independent and dependent coordinates are not identified adequately, then it can lead to the numerical problems during the integration because of the poor conditioned matrices. Therefore, the adequate identification of the independent and dependent coordinates is considered a relative drawback of the double-step approach compared with the penalty-based approach because the latter uses the full set of coordinates.

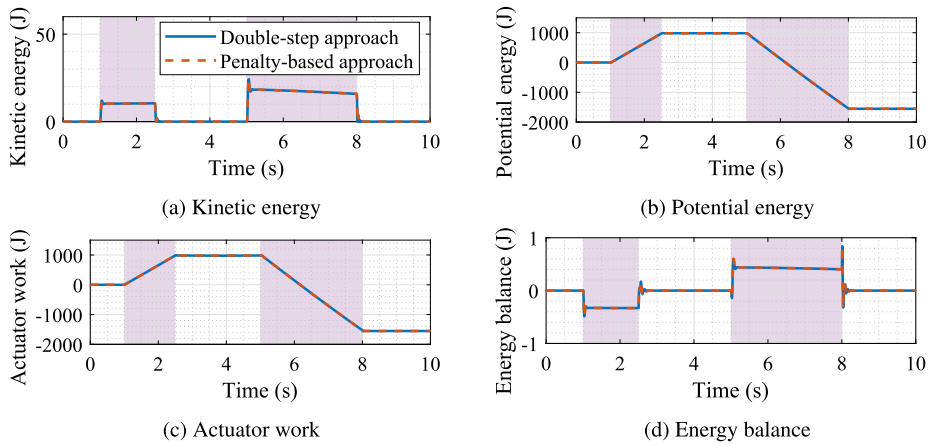

Fig. 9 A comparison of energies for the four-bar mechanism with a time-step of 1 ms

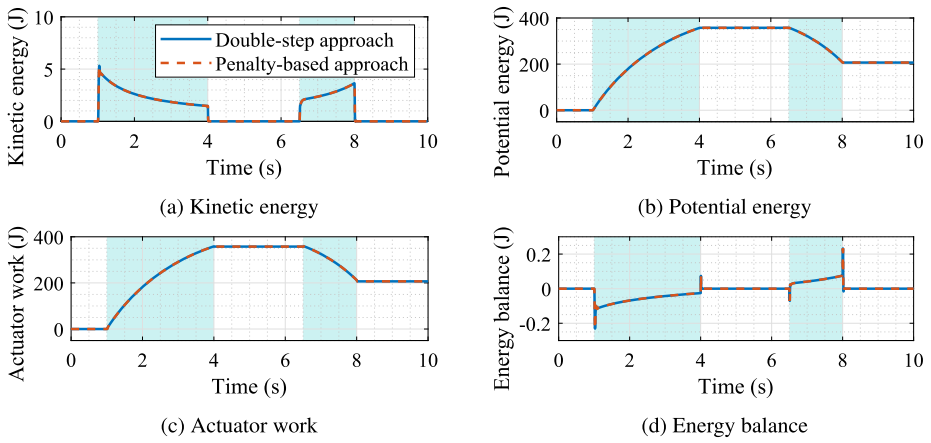

Fig. 10 A comparison of energies for the quick-return mechanism with a time-step of 1 ms

6.2 Energy balance

The energy balances in both the approaches are compared by analyzing the kinetic energy, potential energy, and work done by the actuator. The energy comparison of the four-bar mechanism is shown in Fig. 9 and of the quick-return mechanism is shown in Fig. 10. The energy balance in the double-step and penalty-based approaches showed a good agreement with each other for both the mechanisms. The peak energy drift in case of the four-bar mechanism is 0.84 J, which is 0.09% of the maximum actuator work, 982.95 J, and it occurred at the closing of the valve around 8 s. Whereas in case of the quick-return mechanism, the peak energy drift is 0.23 J, that is, 0.06% of the maximum actuator work, 357.47 J, and it also occurred at the closing of the valve around 8 s. An analogy can be drawn between the hydraulic system and a stiff spring, which supports the structure of the mechanisms.

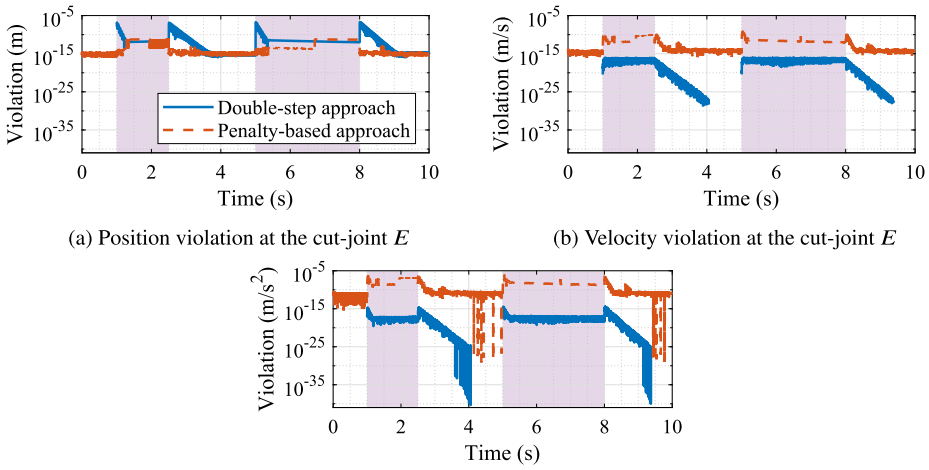

(a) Position violation at the cut-joint E

(b) Velocity violation at the cut-joint E

(c) Acceleration violation at the cut-joint E

Fig. 11 Magnitude of constraint violations for the four-bar mechanism with a time-step of 1 ms

6.3 Constraint violation

The basic difference between the double-step and penalty-based approaches is the way they handle constraints in their multibody formulation. Thus, it is worth showing a comparison of the constraint violations in both the approaches for the two mechanisms as shown in Figs. 11 and 12. Note that in the quick-return mechanism, two cut-joints are used in the modeling, but for demonstration purposes, the results for only one of the cut-joint are presented. In both the approaches, the constraints are fulfilled with good accuracy for both mechanisms. Thus, the robustness of the multibody formulations, as explained in the literature [10, 24], is preserved in the application of a monolithic simulation of coupled multibody and hydraulic systems. Furthermore, the double-step approach fulfills constraints to the level of machine precision, or the precision specified, and it maintains a good error control. Therefore, this can be considered as the relative advantage of the double-step approach compared with the penalty-based approach because the latter approach is relatively more relaxed on the fulfillment of constraints.

In the double-step approach, for a possible mapping between independent and dependent relative joint coordinates, there is an assumption that redundant constraints and singular configurations do not exist. This assumption is a relative disadvantage of the double-step approach compared with the penalty-based approach because the latter approach can handle redundant constraints and can deliver accurate solutions in the vicinity of singular configurations [15].

6.4 Numerical efficiency

The numerical efficiencies of both the approaches are compared in Figs. 13 and 14, for the four-bar and quick-return mechanisms, respectively. In the four-bar mechanism, the average and maximum iterations, and the total integration time for the double-step approach are 1.39, 3, and 27.45 s and for the penalty-based approach are 1.56, 4, 21.54 s. Whereas in the quick-return mechanism, the average and maximum iterations, and the total integration time for the double-step approach are 1.49, 3, and 29.03 s and for the penalty-based approach are 1.57, 6,

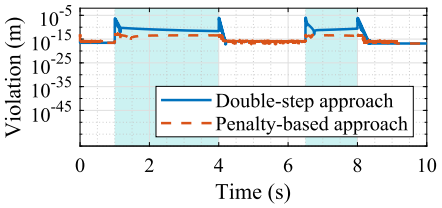

(a) Position violation at the cut-joint M

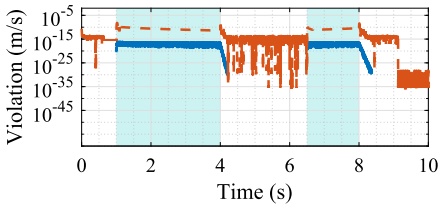

(b) Velocity violation at the cut-joint M

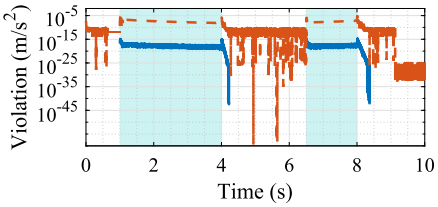

(c) Acceleration violation at the cut-joint M

Fig. 12 Magnitude of constraint violations for the quick-return mechanism with a time-step of 1 ms

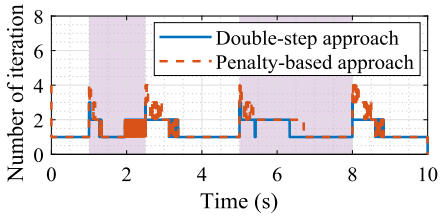

(a) Iterations in the Newton–Raphson method

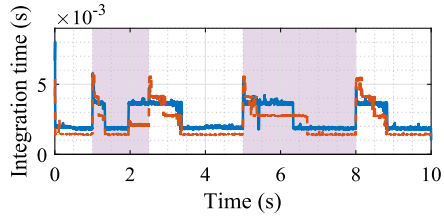

(b) Loop integration time

Fig. 13 A comparison of numerical efficiencies for the four-bar mechanism with a time-step of 1 ms

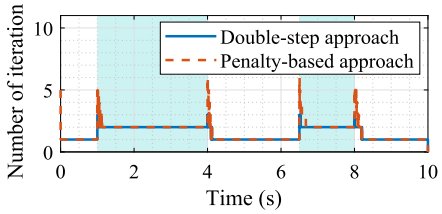

(a) Iterations in the Newton–Raphson method

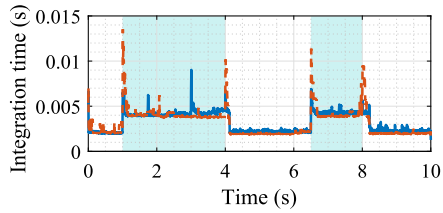

(b) Loop integration time

Fig. 14 A comparison of numerical efficiencies for the quick-return mechanism with a time-step of 1 ms

and 28.47 s. The maximum number of iterations occurred during the opening and closing of the directional control valve. Even though the number of iterations are lower in the double-step approach, its integration time is greater compared with the penalty-based approach, which is in accordance with the literature [15, 27]. The poor numerical efficiency of the double-step approach is attributed to the iterative solution of the dependent joint coordinates by using the Newton–Raphson method.

Note that the examples are implemented in the Matlab environment and for this reason, the result about the integration time may be unreliable because of the implementation details. However, both approaches are carefully implemented such that they have the same number of function calls in each iteration. This was achieved by symbolic precomputation and function generation of the matrix product, as in [32]. Furthermore, both approaches can be potential candidates for real-time applications by implementing them in a lower level language such as C++ or Fortran and by limiting the number of iterations to a lower value.

7 Conclusion

This study introduced the double-step semirecursive formulation and compared it with the penalty-based semirecursive formulation, in a numerically stiff coupled environment. The numerical stiffness was introduced by a hydraulic system. A monolithic scheme for the coupled simulation of the double-step semirecursive formulation and hydraulic systems was introduced in this study. To this end, the hydraulic system was described by using the lumped fluid theory. As case studies, hydraulically actuated four-bar and quick return mechanisms were modeled to compared the double-step semirecursive approach with the penalty-based semirecursive approach. The two approaches were compared based on the work cycle, energy balance, constraint violation, and numerical efficiency of the mechanisms, and similar results were obtained in both the mechanisms.

The relative joint coordinates and energy balances showed a good agreement in both the approaches. In the double-step approach, the adequate identification of the independent and dependent joint coordinates was carried out by using the Gaussian elimination with full pivoting on the Jacobian matrix of the constraints. Its identification is considered a relative drawback compared with the penalty-based approach where the full set of coordinates were used. In both the approaches, the constraints were fulfilled with good accuracy. However, the double-step approach had an advantage of fulfilling the constraints to the level of machine precision, or the precision specified compared with the penalty-based approach. Nevertheless, the double-step approach had an assumption that the redundant constraints and singularity configuration do not exit. This is a relative disadvantage of the double-step approach because the penalty-based approach can handle redundant constraints and can provide accurate solutions in the vicinity of singular configurations. Furthermore, the double-step approach suffered from poor numerical efficiency, which was attributed to the iterative solution of the dependent joint coordinates by using the Newton–Raphson method. To improve the numerical efficiency of the double-step approach, it would be of utmost importance to enhance the iterative solution of dependent coordinates and this is left as a topic for future studies. In conclusion, the penalty-based semirecursive approach has a number of advantages over the double-step semirecursive approach, which is in accordance with the literature [15, 27].

For future studies, alternate multibody formulations can be coupled with hydraulic systems to study on the optimal formulation for simulating coupled multibody and hydraulic systems. Note that the selection of the integrator type is bound to have an effect on the results. In this study, an implicit integrator is used, whereas the double-step semirecursive formulation is usually integrated by using the fourth order Runge–Kutta method, that is, an explicit integrator. Therefore, different integrators can be implemented to study on the optimal integrator choice for such coupled systems. This study utilized the Matlab environment, therefore, to make a firm conclusion on the numerical efficiency of the two approaches, a large-scale, three-dimensional example needs to be investigated in programming languages, such as C++ or Fortran.

Acknowledgements This work was supported in part by the Business Finland [project: Service Business from Physics Based Digital Twins—DigiBuzz], and in part by the Academy of Finland under Grant #316106.

Funding Note Open Access funding provided by LUT University (previously Lappeenranta University of Technology (LUT)).

Conflict of interest The authors declare that they have no conflict of interest.

References

1. Bayo, E., Jalon, J.G.D., Avello, A., Cuadrado, J.: An efficient computational method for real time multibody dynamic simulation in fully cartesian coordinates. Comput. Methods Appl. Mech. Eng. **92**(3), 377–395 (1991)
2. Bayo, E., Jalon, J.G.D., Serna, M.A.: A modified Lagrangian formulation for the dynamic analysis of constrained mechanical systems. Comput. Methods Appl. Mech. Eng. **71**(2), 183–195 (1988)
3. Bayo, E., Ledesma, R.: Augmented Lagrangian and mass-orthogonal projection methods for constrained multibody dynamics. Nonlinear Dyn. **9**(1–2), 113–130 (1996)
4. Benedikt, M., Holzinger, F.R.: Automated configuration for non-iterative co-simulation. In: Proceedings of the 17th International Conference on Thermal, Mechanical, and Multi-Physics Simulation, and Experiments in Microelectronics and Microsystems, Montpellier, France, pp. 1–7 (2016)
5. Brenan, K.E., Campbell, S.L., Petzold, L.R.: Numerical Solution of Initial-Value Problems in Differential-Algebraic Equations, vol. 14. SIAM, Philadelphia (1996)
6. Callejo, A., Narayanan, S.H.K., Jalon, J.G.D., Norris, B.: Performance of automatic differentiation tools in the dynamic simulation of multibody systems. Adv. Eng. Softw. **73**, 35–44 (2014)
7. Callejo, A., Pan, Y., Ricón, J.L., Kövecses, J., Jalon, J.G.D.: Comparison of semi-recursive and subsystem synthesis algorithms for the efficient simulation of multibody systems. J. Comput. Nonlinear Dyn. **12**(1), 011020(1 (2017)
8. Cuadrado, J., Cardenal, J., Bayo, E.: Modeling and solution methods for efficient real-time simulation of multibody dynamics. Multibody Syst. Dyn. **1**(3), 259–280 (1997)
9. Cuadrado, J., Cardenal, J., Morer, P., Bayo, E.: Intelligent simulation of multibody dynamics: space-state and descriptor methods in sequential and parallel computing environments. Multibody Syst. Dyn. **4**(1), 55–73 (2000)
10. Cuadrado, J., Dopico, D., Gonzalez, M., Naya, M.A.: A combined penalty and recursive real-time formulation for multibody dynamics. J. Mech. Des. **126**(4), 602–608 (2004)
11. Cuadrado, J., Dopico, D., Naya, M.A., Gonzalez, M.: Real-time multibody dynamics and applications. In: Simulation Techniques for Applied Dynamics, vol. 507, pp. 247–311. Springer, Berlin (2008)
12. Docquier, N., Poncelet, A., Delannoy, M., Fisette, P.: Multiphysics modelling of multibody systems: application to car semi-active suspensions. Veh. Syst. Dyn. **48**(12), 1439–1460 (2010)
13. Featherstone, R.: The calculation of robot dynamics using articulated-body inertias. Int. J. Robot. Res. **2**(1), 13–30 (1983)
14. Fisette, P., Vaneghem, B.: Numerical integration of multibody system dynamic equations using the coordinate partitioning method in an implicit Newmark scheme. Comput. Methods Appl. Mech. Eng. **135**(1–2), 85–105 (1996)
15. Flores, P., Ambrosio, J., Claro, J.P., Lankarani, H.M.: Kinematics and Dynamics of Multibody Systems with Imperfect Joints: Models and Case Studies, vol. 34. Springer, Berlin (2008)

16. Gomes, C., Thule, C., Broman, D., Larsen, P.G., Vangheluwe, H.: Co-simulation: a survey. ACM Comput. Surv. **51**(3), 1–33 (2018)
17. González, F., Dopico, D., Pastorino, R., Cuadrado, J.: Behaviour of augmented Lagrangian and Hamiltonian methods for multibody dynamics in the proximity of singular configurations. Nonlinear Dyn. **85**(3), 1491–1508 (2016)
18. González, F., Naya, M.Á., Luaces, A., González, M.: On the effect of multirate co-simulation techniques in the efficiency and accuracy of multibody system dynamics. Multibody Syst. Dyn. **25**(4), 461–483 (2011)
19. Handroos, H.M., Vilenius, M.J.: Flexible semi-empirical models for hydraulic flow control valves. J. Mech. Des. **113**(3), 232–238 (1991)
20. Hidalgo, A.F., Jalon, J.G.D.: Real-time dynamic simulations of large road vehicles using dense, sparse, and parallelization techniques. J. Comput. Nonlinear Dyn. **10**(3), 031005 (2015)
21. Higham, N.J.: Gaussian elimination. Wiley Interdiscip. Rev.: Comput. Stat. **3**(3), 230–238 (2011)
22. Jaiswal, S., Islam, M., Hannola, L., Sopanen, J., Mikkola, A.: Gamification procedure based on real-time multibody simulation. Int. Rev. Model. Simul. **11**(5), 259–266 (2018)
23. Jaiswal, S., Korkealaakso, P., Åman, R., Sopanen, J., Mikkola, A.: Deformable terrain model for the real-time multibody simulation of a tractor with a hydraulically driven front-loader. IEEE Access **7**, 172694–172708 (2019)
24. Jalon, J.G.D., Alvarez, E., Ribera, F.A.D., Rodriguez, I., Funes, F.J.: A fast and simple semi-recursive formulation for multi-rigid-body systems. Comput. Methods Appl. Sci. **2**, 1–23 (2005)
25. Jalon, J.G.D., Bayo, E.: Kinematic and Dynamic Simulation of Multibody Systems: The Real-Time Challenge. Springer, Berlin (1994)
26. Linge, S., Langtangen, H.P.: Programming for Computations-MATLAB/Octave: A Gentle Introduction to Numerical Simulations with MATLAB/Octave, vol. 14. Springer, Berlin (2016)
27. Matikainen, M.K., Von Hertzen, R., Mikkola, A., Gerstmayr, J.: Elimination of high frequencies in the absolute nodal coordinate formulation. Proc. Inst. Mech. Eng., Proc., Part K, J. Multi-Body Dyn. **224**(1), 103–116 (2010)
28. Naya, M., Cuadrado, J., Dopico, D., Lugris, U.: An efficient unified method for the combined simulation of multibody and hydraulic dynamics: comparison with simplified and co-integration approaches. Arch. Mech. Eng. **58**(2), 223–243 (2011)
29. Pan, Y., He, Y., Mikkola, A.: Accurate real-time truck simulation via semi-recursive formulation and Adams–Bashforth–Moulton algorithm. Acta Mech. Sin. **35**(3), 641–652 (2019)
30. Rahikainen, J., González, F., Naya, M.Á.: An automated methodology to select functional co-simulation configurations. Multibody Syst. Dyn. **48**(1), 79–103 (2020)
31. Rahikainen, J., Kiani, M., Sopanen, J., Jalali, P., Mikkola, A.: Computationally efficient approach for simulation of multibody and hydraulic dynamics. Mech. Mach. Theory **130**, 435–446 (2018)
32. Rahikainen, J., Mikkola, A., Sopanen, J., Gerstmayr, J.: Combined semi-recursive formulation and lumped fluid method for monolithic simulation of multibody and hydraulic dynamics. Multibody Syst. Dyn. **44**(3), 293–311 (2018)
33. Rodríguez, J.I., Jiménez, J.M., Funes, F.J., Jalon, J.G.D.: Recursive and residual algorithms for the efficient numerical integration of multibody systems. Multibody Syst. Dyn. **11**(4), 295–320 (2004)
34. Sadjina, S., Kyllingstad, L.T., Skjong, S., Pedersen, E.: Energy conservation and power bonds in co-simulations: non-iterative adaptive step size control and error estimation. Eng. Comput. **33**(3), 607–620 (2017)
35. Sadjina, S., Pedersen, E.: Energy conservation and coupling error reduction in non-iterative co-simulations. Eng. Comput. **36**, 1579–1587 (2020)
36. Schweiger, G., Gomes, C., Engel, G., Hafner, I., Schoeggl, J., Posch, A., Nouidui, T.: An empirical survey on co-simulation: promising standards, challenges and research needs. Simul. Model. Pract. Theory **95**, 148–163 (2019)
37. Watton, J.: Fluid Power Systems: Modeling, Simulation, Analog, and Microcomputer Control. Prentice Hall, New York (1989)

Publication II

Jaiswal, S., Sopanen, J., and Mikkola, A.
Efficiency comparison of various friction models of a hydraulic cylinder in the framework of multibody system dynamics

Reprinted with permission from
Nonlinear Dynamics
Vol. 104(4), pp. 3497–3515, 2021

Nonlinear Dyn (2021) 104:3497–3515
https://doi.org/10.1007/s11071-021-06526-9

ORIGINAL PAPER

Efficiency comparison of various friction models of a hydraulic cylinder in the framework of multibody system dynamics

Suraj Jaiswal · **Jussi Sopanen** · **Aki Mikkola**

Received: 20 December 2020 / Accepted: 6 May 2021 / Published online: 1 June 2021

Abstract Dynamic simulation of mechanical systems can be performed using a multibody system dynamics approach. The approach allows to account systems of other physical nature, such as hydraulic actuators. In such systems, the nonlinearity and numerical stiffness introduced by the friction model of the hydraulic cylinders can be an important aspect to consider in the modeling because it can lead to poor computational efficiency. This paper couples various friction models of a hydraulic cylinder with the equations of motion of a hydraulically actuated multibody system in a monolithic framework. To this end, two static friction models, the Bengisu–Akay model and Brown–McPhee model, and two dynamic friction models, the LuGre model and modified LuGre model, are considered in this work. A hydraulically actuated four-bar mechanism is exemplified as a case study. The four modeling approaches are compared based on the work cycle, friction force, energy balance, and numerical efficiency. It is concluded that the Brown–McPhee approach is numerically the most efficient approach and it is well able to describe usual friction characteristics in dynamic simulation of hydraulically actuated multibody systems.

Keywords Multibody system dynamics · Hydraulic actuators · Hydraulic cylinder friction · Static friction models · Dynamic friction models · Monolithic simulation

S. Jaiswal ( )· J. Sopanen · A. Mikkola
Department of Mechanical Engineering, Lappeenranta University of Technology, Yliopistonkatu 34, 53850 Lappeenranta, Finland
e-mail: suraj.jaiswal@lut.fi

J. Sopanen
e-mail: jussi.sopanen@lut.fi

A. Mikkola
e-mail: aki.mikkola@lut.fi

1 Introduction

Dynamic simulation of mechanical systems can be performed using multibody system dynamics. In this approach, the equations of motion describe a force equilibrium for the mechanical system under consideration. This approach allows to describe systems of other physical nature, such as hydraulic actuators [32,33,43]. Hydraulic systems are highly nonlinear systems, which are caused, in part, by the friction model of the hydraulic cylinders. The friction model of the hydraulic cylinders can introduce numerical stiffness [38], and as a consequence, time integration of hydraulically actuated systems may become cumbersome, especially, in real-time applications [30,31,50]. Moreover, a physically incorrect friction model of the hydraulic cylinders can lead to inaccurate simulations and control errors.

Friction models can, in general, be categorized into two main groups, namely, static friction models and dynamic friction models [5,37,45]. Static friction models describe only the steady-state relation between the

friction force and the relative velocity [5]. The well-known friction model was developed by Coulomb in 1785, and over the years, various friction models have been proposed that capture Coulomb, stiction, viscous, and Stribeck [29] friction effects, as in [14,27]. The exponential Stribeck friction model described by Bo and Pavelescu [14] is popular, however, it can lead to numerical problems because of the discontinuity of the friction force at zero relative velocity. To overcome this numerical problem, a separate equation can be used to describe friction at zero relative velocity [2–4,10]. For example, Bengisu and Akay [10] utilize two separate equations for the adhesion regime and Stribeck effect. However, when this approach is adopted, the use of different equations during the simulation can lead to poor numerical efficiency. To address this problem, Brown and McPhee [16] recently developed a continuous velocity-based friction model suitable for computationally challenging applications and optimization problems. Their model [16] does not consider the time lag [11], micro-slip [2] or pre-slip displacement [11], and dwell-time dependence of friction [23]. In this study, the friction models developed by Bengisu and Akay [10] and Brown and McPhee [16] are referred to as the Bengisu–Akay and Brown–McPhee friction models, respectively.

Dynamic friction models evaluate the friction force based on the actual state of contact and the contact history [5,38]. In general, extra state variables, such as the average bristle deflection, are used with relative velocity to model the evolution of the friction force [37]. Unlike most static friction models, dynamic friction models consider frictional phenomena such as pre-slip displacement [11] and frictional lag, and dynamic friction models eliminate the discontinuity at zero relative velocity. The Dahl friction model [20] was the first dynamic friction model in which the friction force is considered proportional to the average bristle deflection. It did not, however, consider the static friction. Based on the Dahl friction model, a number of friction models, such as the reset integrator model [24], Bliman–Sorine model [12,13], LuGre model [21], Leuven model [51], and generalized Maxwell slip model [1,36], are described accounting for various frictional phenomena. The LuGre friction model [21] is widely used and it captures the Stribeck and stiction effects, as well as the pre-slip displacement and frictional lag. Subsequently, a modified LuGre friction model [57] was developed that considered the dynamics of the lubricant film formation. In the modified LuGre friction model, the lubricant film dynamics is computed using a first-order lag element in which the time constant is varied between the deceleration, acceleration, and dwell periods [57]. It should be noted that dynamic friction models can introduce numerical stiffness to systems and, consequently, increasing the computational cost [38].

In the literature, experiments have been conducted to measure the friction force of hydraulic cylinders with different reciprocating seals operating under various conditions [42]. Additionally, a number of studies have been carried out that utilize different seal friction models for simulation of hydraulic cylinders. For example, the exponential Stribeck friction model [14] was used in [53,54] and the stick-slip friction model [3,4] in [39]. Furthermore, the dynamic friction behavior of hydraulic cylinders was studied using the LuGre friction model in [41,53] and a modified LuGre friction model [57] in [52,53]. Yanada and Sekikawa [57] found that compared with the LuGre friction model, the modified LuGre friction model [57] can simulate the real friction characteristics of a hydraulic cylinder with a good accuracy. Other work has used simple pressure-dependent friction models [15,25] that either had discontinuity at zero relative velocity [25] or were case-dependent [15]. Ylinen et al. [58] combined a pressure-dependent function with the LuGre friction model to study multibody simulation of a hydraulic cylinder.

In the framework of multibody system dynamics [35,46], a large number of studies have been presented that demonstrate coupling of multibody systems and hydraulic actuators [22,40]. Coupling has been carried out using either monolithic [48,49] or co-simulation approaches [44,47]. There are even studies using a monolithic approach that demonstrate this coupling for real-time applications, such as [6] and [31]. Despite widespread interest in the field, detailed comparative study on the inclusion of various friction models of a hydraulic cylinder with the equations of motion of hydraulically actuated multibody systems has been overlooked in the literature.

The objective of this paper is to couple various friction models of a hydraulic cylinder with the equations of motion of a hydraulically actuated multibody system in a monolithic framework. To this end, the Bengisu–Akay model [10] and the Brown–McPhee model [16], in the category of static friction models, and the LuGre model [21] and the modified LuGre

model [57], in the category of dynamic friction models, are considered in this work. In the monolithic coupling scheme, the multibody system is described using a semi-recursive formulation [8,18] and the hydraulic system is described using the lumped fluid theory [56]. In the study, only a fixed step-size integrator is considered because the interest of the authors lies in the area of real-time simulation. The coupled systems are referred to with the name of the friction force model used, that is, the Bengisu–Akay approach, Brown–McPhee approach, LuGre approach, and modified LuGre approach. Although a case study of a hydraulically actuated planar four-bar mechanism is shown, the methods presented in this study are general and applicable to three-dimensional mechanisms as well. Using the numerical example, the four approaches are compared based on the simulation work cycle, friction force, energy balance, and numerical efficiency.

2 Multibody system dynamics

In this study, the dynamics of a constrained mechanical system is described using a semi-recursive multibody formulation. In this method, the equations of motion of a system are formulated in the relative joint coordinates using the dynamics of an open-loop system. Closed-loop systems are modeled by employing the cut-joint constraints using the penalty-based augmented Lagrangian method [8,17,18]. The multibody system is hydraulically actuated and the dynamics of the hydraulic system is described using the lumped fluid theory [56]. It should be noted that the hydraulic cylinder–piston is not considered as separate bodies, and therefore, their masses are assumed to be neglectable. Nevertheless, the internal dynamics of the hydraulic system, including the friction model of a hydraulic cylinder, are computed and the resultant force is fed into the multibody equations of motion in a monolithic approach.

2.1 Semi-recursive multibody formulation

Consider an open-loop system, which has N_b bodies. The absolute velocity, $\mathbf{Z}_j$, and acceleration, $\dot{\mathbf{Z}}_j$, of the bodies can be described using Cartesian velocities and accelerations [28,34] as $\mathbf{Z}_j \equiv \left[\dot{\mathbf{s}}_j^{\mathrm{T}}, \boldsymbol{\omega}_j^{\mathrm{T}}\right]^{\mathrm{T}}$ and $\dot{\mathbf{Z}}_j \equiv \left[\ddot{\mathbf{s}}_j^{\mathrm{T}}, \dot{\boldsymbol{\omega}}_j^{\mathrm{T}}\right]^{\mathrm{T}}$. Here, $\dot{\mathbf{s}}_j$ and $\ddot{\mathbf{s}}_j$ are, respectively, the velocities and accelerations of a point on body $j \in [1, N_b]$, which are instantaneously coincident with the origin of the inertial reference frame, and $\boldsymbol{\omega}_j$ and $\dot{\boldsymbol{\omega}}_j$ are their angular counterparts. The kinematics for an open-loop system, shown in Fig. 1a, can be calculated, for example, from the base to the leaves using classical kinematic relations [19]. In Fig. 1, the relative joint coordinates, z_j, represent the position of the bodies. The absolute velocities and accelerations can be recursively expressed with respect to the previous bodies as [34]

$$\mathbf{Z}_j = \mathbf{Z}_{j-1} + \mathbf{b}_j \dot{z}_j, \tag{1}$$

$$\dot{\mathbf{Z}}_j = \dot{\mathbf{Z}}_{j-1} + \mathbf{b}_j \ddot{z}_j + \mathbf{d}_j, \tag{2}$$

where $\dot{z}_j$ and $\ddot{z}_j$ are, respectively, the relative joint velocities and accelerations, and $\mathbf{b}_j$ and $\mathbf{d}_j$ are vectors that depend on the joint-type connecting bodies $j-1$ and j [19]. As the system may branch, the indexes $j-1$ and j may not be successive.

A velocity transformation matrix, $\mathbf{R} \in \mathbb{R}^{6N_b \times N_b}$, can map the absolute velocities, $\mathbf{Z} = \left[\mathbf{Z}_1^{\mathrm{T}}, \mathbf{Z}_2^{\mathrm{T}}, \ldots, \mathbf{Z}_{N_b}^{\mathrm{T}}\right]^{\mathrm{T}}$, into a set of relative joint velocities, $\dot{\mathbf{z}} = \left[\dot{z}_1, \dot{z}_2, \ldots, \dot{z}_{N_b}\right]^{\mathrm{T}}$, as [34]

$$\mathbf{Z} = \mathbf{R}\dot{\mathbf{z}} = \mathbf{T}\mathbf{R}_{\mathrm{d}}\dot{\mathbf{z}}, \tag{3}$$

$$\dot{\mathbf{Z}} = \mathbf{R}\ddot{\mathbf{z}} + \dot{\mathbf{R}}\dot{\mathbf{z}} = \mathbf{T}\mathbf{R}_{\mathrm{d}}\ddot{\mathbf{z}} + \mathbf{T}\dot{\mathbf{R}}_{\mathrm{d}}\dot{\mathbf{z}}, \tag{4}$$

where $\mathbf{T} \in \mathbb{R}^{6N_b \times 6N_b}$ is the constant path matrix that represents the topology of the open-loop system and $\mathbf{R}_{\mathrm{d}} \in \mathbb{R}^{6N_b \times N_b}$ is a diagonal matrix whose elements are vectors $\mathbf{b}_j$, arranged in an ascending order. In Eq. (4), the term $\dot{\mathbf{R}}\dot{\mathbf{z}}$ can be expressed in terms of vectors $\mathbf{d}_j$ using Eq. (2) [19].

In an open-loop system, the virtual power of the inertia and external forces can be written as [34]

$$\sum_{j=1}^{N_b} \mathbf{Z}_j^{*\mathrm{T}} \left(\bar{\mathbf{M}}_j \dot{\mathbf{Z}}_j - \bar{\mathbf{Q}}_j\right) = 0, \tag{5}$$

where an asterisk (*) denotes the virtual velocities, and the mass matrix $\bar{\mathbf{M}}_j$ and force vector $\bar{\mathbf{Q}}_j$ can be expressed as

$$\bar{\mathbf{M}}_j = \begin{bmatrix} m_j \mathbf{I}_3 & -m_j \tilde{\mathbf{g}}_j \\ m_j \tilde{\mathbf{g}}_j & \mathbf{J}_j - m_j \tilde{\mathbf{g}}_j \tilde{\mathbf{g}}_j \end{bmatrix}, \tag{6}$$

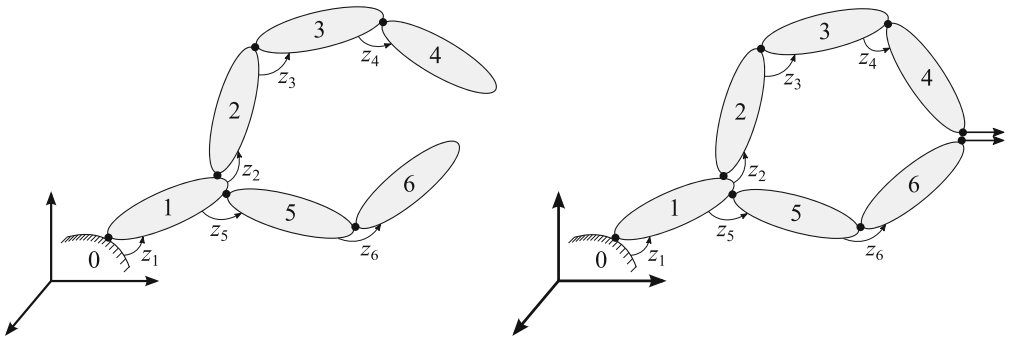

(a) An open-loop multibody system. **(b)** A closed-loop multibody system.

Fig. 1 Illustration of a multibody system

and

$$\bar{\mathbf{Q}}_j = \begin{bmatrix} \mathbf{f}_j - \widetilde{\boldsymbol{\omega}}_j \left(\widetilde{\boldsymbol{\omega}}_j m_j \mathbf{g}_j\right) \\ \boldsymbol{\tau}_j - \widetilde{\boldsymbol{\omega}}_j \mathbf{J}_j \boldsymbol{\omega}_j + \widetilde{\mathbf{g}}_j \left(\mathbf{f}_j - \widetilde{\boldsymbol{\omega}}_j \left(\widetilde{\boldsymbol{\omega}}_j m_j \mathbf{g}_j\right)\right) \end{bmatrix}, \tag{7}$$

where m_j and $\mathbf{J}_j$ are, respectively, the mass and inertia tensor of body j, $\mathbf{I}_3$ is a (3×3) identity matrix, the vector $\mathbf{g}_j$ is the position of the center of mass of body j, a tilde $(\sim)$ denotes the skew-symmetric matrix of a vector, and $\boldsymbol{\tau}_j$ and $\mathbf{f}_j$ are, respectively, the vector of external moments with respect to the center of mass and external forces applied on body j. By substituting Eqs. (3) and (4) in Eq. (5), the equations of motion for the open-loop system can be written as [34]

$$\mathbf{R}_\mathrm{d}^\mathrm{T} \mathbf{T}^\mathrm{T} \bar{\mathbf{M}} \mathbf{T} \mathbf{R}_\mathrm{d} \ddot{\mathbf{z}} = \mathbf{R}_\mathrm{d}^\mathrm{T} \mathbf{T}^\mathrm{T} \left(\bar{\mathbf{Q}} - \bar{\mathbf{M}} \mathbf{T} \dot{\mathbf{R}}_\mathrm{d} \dot{\mathbf{z}}\right), \tag{8}$$

where $\ddot{\mathbf{z}} \in \mathbb{R}^{N_b}$ is the vector of the relative joint accelerations, and $\bar{\mathbf{M}} \in \mathbb{R}^{6N_b \times 6N_b}$ and $\bar{\mathbf{Q}} \in \mathbb{R}^{6N_b}$ are, respectively, a diagonal matrix and a column vector, whose elements are $\bar{\mathbf{M}}_j$ and $\bar{\mathbf{Q}}_j$.

By following the penalty-based augmented Lagrangian method [17,18], a set of m loop-closure constraints, $\boldsymbol{\Phi} = \mathbf{0}$, are incorporated in Eq. (8) and the equations of motion for the closed-loop system can be written as [18,49]

$$\mathbf{M}^\Sigma \ddot{\mathbf{z}} + \boldsymbol{\Phi}_\mathbf{z}^\mathrm{T} \alpha \boldsymbol{\Phi} + \boldsymbol{\Phi}_\mathbf{z}^\mathrm{T} \boldsymbol{\lambda} = \mathbf{Q}^\Sigma, \tag{9}$$

where $\mathbf{M}^\Sigma = \left(\mathbf{R}_\mathrm{d}^\mathrm{T} \mathbf{T}^\mathrm{T} \bar{\mathbf{M}} \mathbf{T} \mathbf{R}_\mathrm{d}\right)$, $\mathbf{Q}^\Sigma = \left[\mathbf{R}_\mathrm{d}^\mathrm{T} \mathbf{T}^\mathrm{T} \left(\bar{\mathbf{Q}} - \bar{\mathbf{M}} \mathbf{T} \dot{\mathbf{R}}_\mathrm{d} \dot{\mathbf{z}}\right)\right]$, α is a penalty factor that can be set to the same value for all constraints, $\boldsymbol{\Phi}_\mathbf{z}$ is the Jacobian matrix of $\boldsymbol{\Phi}(\mathbf{z}) = \mathbf{0}$, and $\boldsymbol{\lambda}$ is the vector of Lagrange multipliers that are iterated at each time-step (k) as

$$\boldsymbol{\lambda}_k^{(h+1)} = \boldsymbol{\lambda}_k^{(h)} + \alpha \boldsymbol{\Phi}_k^{(h+1)}, \tag{10}$$

where h is the iteration step. The value of $\boldsymbol{\lambda}_k^{(0)}$ is the final value of $\boldsymbol{\lambda}_{k-1}$ from the previous time-step. For simplicity, the constraints are assumed to be holonomic. An example of a closed-loop system is shown in Fig. 1b.

In this study, an implicit single-step trapezoidal rule as in [7] is used. In this method, the relative joint velocities, $\dot{\mathbf{z}}$, and accelerations, $\ddot{\mathbf{z}}$, are corrected using mass–damping–stiffness–orthogonal projections as [9,17]

$$\left[\mathbf{W} + \frac{\Delta t^2}{4} \boldsymbol{\Phi}_\mathbf{z}^\mathrm{T} \alpha \boldsymbol{\Phi}_\mathbf{z}\right] \dot{\mathbf{z}} = \mathbf{W} \dot{\mathbf{z}}' - \frac{\Delta t^2}{4} \boldsymbol{\Phi}_\mathbf{z}^\mathrm{T} \alpha \boldsymbol{\Phi}_t, \tag{11}$$

$$\left[\mathbf{W} + \frac{\Delta t^2}{4} \boldsymbol{\Phi}_\mathbf{z}^\mathrm{T} \alpha \boldsymbol{\Phi}_\mathbf{z}\right] \ddot{\mathbf{z}} = \mathbf{W} \ddot{\mathbf{z}}' - \frac{\Delta t^2}{4} \boldsymbol{\Phi}_\mathbf{z}^\mathrm{T} \alpha \left(\dot{\boldsymbol{\Phi}}_\mathbf{z} \dot{\mathbf{z}} + \dot{\boldsymbol{\Phi}}_t\right), \tag{12}$$

where $\dot{\mathbf{z}}'$ and $\ddot{\mathbf{z}}'$ are, respectively, the relative joint velocities and accelerations obtained from the Newton–Raphson iteration, Δt is the time-step, $\mathbf{W} = \mathbf{M} + \frac{\Delta t}{2}\mathbf{C} + \frac{\Delta t^2}{4}\mathbf{K}$, with $\mathbf{C}$ and $\mathbf{K}$ representing, respectively, the contributions of damping and stiffness in the system, and $\boldsymbol{\Phi}_t$ is the partial derivative of the constraints with respect to time t.

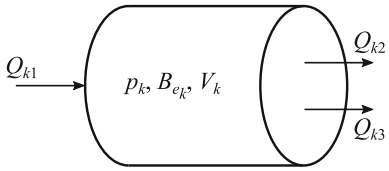

Fig. 2 Modeling concept of hydraulic actuators

2.2 Modeling of hydraulic systems

In this study, the lumped fluid theory [56] is used to describe the hydraulic pressures in a hydraulic circuit. In this approach, a hydraulic circuit is partitioned into discrete volumes where the pressures are assumed to be equally distributed. Thus, the effect of acoustic waves is assumed to be negligible. The modeling concept is illustrated in Fig. 2, where one incoming flow, Q_{k1}, and two outgoing flows, Q_{k2} and Q_{k3}, are associated with a volume, V_k. The pressure, p_k, within a hydraulic volume, V_k, can be expressed as a function of the effective bulk modulus, B_{e_k}, volume, V_k, and incoming and outgoing flows using the following differential equation

$$\dot{p}_k = \frac{B_{e_k}}{V_k} \sum_{s=1}^{n_f} Q_{ks}, \tag{13}$$

where Q_{ks} is the sum of incoming and outgoing flows related to volume V_k, and n_f is the total number of volume flows going in or out of the volume V_k. The effective bulk modulus, B_{e_k}, associated with the volume V_k can be expressed as

$$B_{e_k} = \left(\frac{1}{B_{\text{oil}}} + \sum_{s=1}^{n_c} \frac{V_s}{V_k B_s} \right)^{-1}, \tag{14}$$

where B_{oil} is the bulk modulus of oil, B_s is the bulk modulus of the volume V_s that forms the volume V_k, and n_c is the total number of sub-volumes V_s.

2.2.1 Throttle and directional control valves

In this study, a semi-empirical modeling approach [26] is used to describe the valves in the system. In this approach, the volume flow rate, Q_t, through a simple throttle valve can be expressed as

$$Q_t = C_{v_t} \text{sgn}(\Delta p) \sqrt{|\ \Delta p\ |}, \tag{15}$$

where C_{v_t} is the semi-empirical flow rate coefficient of the throttle valve, Δp is the pressure difference over the valve, and $\text{sgn}(\Delta p)$ is the signum function which determines the sign of Δp. C_{v_t} can be calculated as

$$C_{v_t} = C_d A_t \sqrt{\frac{2}{\rho}}, \tag{16}$$

where ρ is the oil density, A_t is the area of the throttle valve, and C_d is the flow discharge coefficient.

Similarly, the volume flow rate, Q_d, through a directional control valve can be expressed as

$$Q_d = C_{v_d} U \text{sgn}(\Delta p) \sqrt{|\ \Delta p\ |}, \tag{17}$$

where C_{v_d} is the semi-empirical flow rate constant of the valve, and U is the relative spool position. The value of C_{v_d} can be obtained from the manufacturers' catalogues. The volume flow is assumed to be laminar for pressure differences of less than 2 bar, and Eqs. (15) and (17) are modified such that the volume flow and pressure difference follow a linear relation. The spool position can be described using the following differential equation

$$\dot{U} = \frac{U_{\text{ref}} - U}{\tau}, \tag{18}$$

where U_{ref} is the reference voltage signal for the reference spool position, and τ is the time constant. The value of τ can be obtained from the Bode-diagram of the valve, which describes the dynamics of the valve spool.

2.2.2 Double-acting hydraulic cylinder

The motion of a double-acting hydraulic cylinder, shown in Fig. 3, causes volume flows that can be written as

$$Q_{in} = \dot{x} A_1,\ Q_{out} = \dot{x} A_2, \tag{19}$$

where Q_{in} and Q_{out} are, respectively, the incoming and outgoing volume flow rates of the cylinder, $\dot{x}$ is the piston velocity, and A_1 and A_2 are, respectively, the piston and piston-rod areas of the cylinder. The force, F_{cyl}, produced by a cylinder can be written in terms of

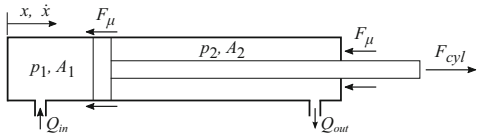

Fig. 3 Schematic figure of a hydraulic cylinder

its dimensions, chamber pressures, and the seal friction as

$$F_{cyl} = p_1 A_1 - p_2 A_2 - F_\mu, \tag{20}$$

where p_1 and p_2 are, respectively, the pressures on the piston and piston-rod sides of the cylinder, and F_μ is the total friction force caused by sealing.

3 Friction force models

Friction force is defined as a force that opposes the relative motion between two surfaces in contact. In the literature, several friction force models have been proposed. These models capture a combination of the Coulomb, stiction, viscous, and Stribeck effects. However, most of the friction models in the static friction model category may suffer from numerical instability because of the discontinuity of the friction force at zero relative tangential velocity. To overcome this numerical inconvenience, many alternative continuous friction models have been developed, for example, as shown in Fig. 4. In the category of static friction models, the Bengisu–Akay and Brown–McPhee friction models [10,16] are considered in this work.

The friction models in the dynamic friction category consider the pre-slip displacement [11]. It is for this reason that these models eliminate the discontinuity of the friction force at zero relative tangential velocity. In general, they consider the evolution of friction force based on the actual state of contact and the contact history [38]. In a dynamic model, an extra state variable, such as the average bristle deflection [21], is used, which represents the behavior of surface asperities during the contact [38]. During the sticking phase, the bristles behave like springs. In the category of dynamic friction models, the LuGre and modified LuGre friction models [21,57] are considered in this work.

3.1 Bengisu–Akay friction model

An approximation of the friction force can be presented by the Coulomb friction law, which established that the magnitude of the friction force depends on the relative tangential velocity between the surfaces in contact. Furthermore, it has been established that the static friction is greater than the kinetic or Coulomb friction and it decreases continuously with the increment of relative tangential velocity. This effect is known as the Stribeck effect [29], as shown in Fig. 4. By considering the numerical stability at zero relative tangential velocity, the friction force can be modeled using two equations, one for the slope and the other for the Stribeck effect, as [10,37]

$$\mathbf{F}_\mu = \begin{cases} \left(-\frac{F_s}{v_s^2}\left(|\mathbf{v}_t| - v_s\right)^2 + F_s\right)\operatorname{sgn}(\mathbf{v}_t) & |\mathbf{v}_t| < v_s, \\ \left(F_c + (F_s - F_c)\, e^{-\xi\left(|\mathbf{v}_t| - v_s\right)}\right)\operatorname{sgn}(\mathbf{v}_t) & |\mathbf{v}_t| \geq v_s, \end{cases} \tag{21}$$

where F_c is the Coulomb friction, F_s is the static friction, $\mathbf{F}_\mu$ is the total friction force, v_s is the Stribeck velocity, $\mathbf{v}_t$ is the relative tangential velocity between the two surfaces in contact, and ξ is a positive parameter that represents the negative slope of the sliding regime. Note that $F_c = \mu_c |\mathbf{F}_n|$ and $F_s = \mu_s |\mathbf{F}_n|$, where μ_c and μ_s are the coefficients of Coulomb and static frictions, respectively, and $\mathbf{F}_n$ is the normal contact force.

It should be noted that the viscous friction is not considered in Eq. (21). However, for a hydraulic cylinder where lubricants are present, as in this study, the viscous friction cannot be ignored. Therefore, a corrected version of the Bengisu–Akay friction model is presented in this study by incorporating the viscous friction as

$$\mathbf{F}_\mu = \begin{cases} \left(-\frac{F_s}{v_s^2}\left(|\mathbf{v}_t| - v_s\right)^2 + F_s\right)\operatorname{sgn}(\mathbf{v}_t) & |\mathbf{v}_t| < v_s, \\ \left(F_c + (F_s - F_c)\, e^{-\xi\left(|\mathbf{v}_t| - v_s\right)}\right)\operatorname{sgn}(\mathbf{v}_t) + f(\mathbf{v}_t) & |\mathbf{v}_t| \geq v_s, \end{cases} \tag{22}$$

where the function $f(\mathbf{v}_t)$ describes the viscous friction. In lubricated contacts, viscous friction is generally considered to be linear viscous friction as [21,38]

$$f(\mathbf{v}_t) = \sigma_2 \mathbf{v}_t, \tag{23}$$

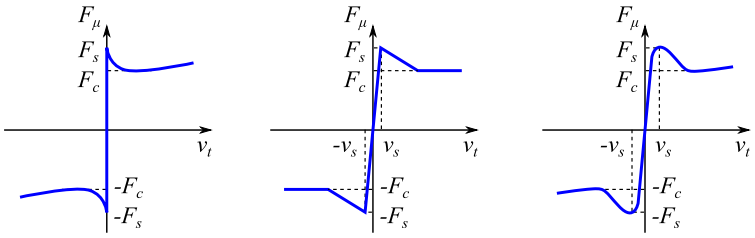

Fig. 4 Representation of the classical Stribeck friction model (left [14]), and two alternative friction models (middle [37] and right [10,16]) to overcome discontinuity at zero relative tangential velocity

where σ_2 is the coefficient of viscous friction. The effect of viscous friction is crucial, especially, in the presence of fluid lubricant or at high relative velocity [37]. A representation of this model is shown on the right side of Fig. 4. It should be noted that if the slope at $\mathbf{v}_t = 0$ in Eq. (22) is large, small time-steps are required to properly capture the friction effects at low velocity. This may burden the computational efficiency.

3.2 Brown–McPhee friction model

A suitable alternate method to the classical Stribeck friction model that avoids the discontinuity at zero relative tangential velocity has been presented by Brown and McPhee [16]. This model incorporates the Coulomb, stiction, and viscous friction, and it is valid for both positive and negative relative tangential velocity. This velocity-dependent continuous differential model can be written as [16]

$$\mathbf{F}_\mu = \left(F_c \tanh\left(4\frac{|\mathbf{v}_t|}{v_s}\right) + (F_s - F_c)\frac{\frac{|\mathbf{v}_t|}{v_s}}{\left(\frac{1}{4}\left(\frac{|\mathbf{v}_t|}{v_s}\right)^2 + \frac{3}{4}\right)^2} \right) \operatorname{sgn}(\mathbf{v}_t) + \sigma_2 \mathbf{v}_t \tanh(4). \tag{24}$$

In Eq. (24), the Coulomb friction term approaches F_c as $|\mathbf{v}_t|$ increases from zero to v_s. Similarly, the static friction term, which represents the stiction and Stribeck effect, has its maximum value as $(F_s - F_c)$ at $|\mathbf{v}_t| = v_s$ and it then decreases to zero for larger relative tangential velocity, where the Coulomb and viscous friction is dominant. Here, the viscous friction term is linearly scaled with velocity and physically corresponds to thin-film viscous friction [16]. A representation of this model is shown on the right side of Fig. 4. This model is suitable for real-time simulations and optimization problems [16].

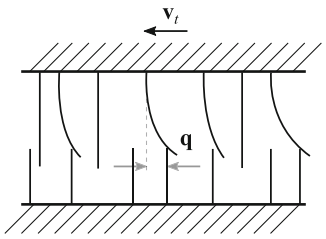

Fig. 5 Interaction of elastic bristles on one surface with rigid bristles on another surface

3.3 LuGre friction model

In LuGre friction model, the friction is considered as an interaction of the bristles between two surfaces, as shown in Fig. 5, and the model utilizes the average bristle deflection. The LuGre (Lund–Grenoble) model [21] is an extension of the Dahl model [20] that captures the Stribeck and stiction effects. When a tangential force is applied, the bristles start to deflect like a spring, giving rise to the sticking phase. The moment the tangential force is sufficiently large, some of the bristles deflect so much that they start to slip [21].

The average bristle deflection is quantified by introducing an internal state variable, $\mathbf{q}$, such that the model can be expressed as [21,37]

$$\dot{\mathbf{q}} = \mathbf{v}_t - \frac{\sigma_0|\mathbf{v}_t|}{g(\mathbf{v}_t)}\mathbf{q}, \tag{25}$$

with

$$g(\mathbf{v}_t) = F_c + (F_s - F_c)\, e^{-\left(\frac{|\mathbf{v}_t|}{v_s}\right)^n}, \tag{26}$$

where $\mathbf{q}$ is the average bristle deflection, $\dot{\mathbf{q}}$ is the rate of average bristle deflection, σ_0 is the stiffness of the elastic bristles, the function $g(\mathbf{v}_t)$ describes the Stribeck effect [21,53], and n is the exponent that affects the slope of the Stribeck curve. The total friction force, $\mathbf{F}_\mu$, generated from the bending of the bristles can be written as

$$\mathbf{F}_\mu = \sigma_0 \mathbf{q} + \sigma_1 \dot{\mathbf{q}} + \sigma_2 \mathbf{v}_t, \tag{27}$$

where σ_1 is the damping of the elastic bristles, which can be a constant or a function of $\mathbf{v}_t$.

3.4 Modified LuGre friction model

In this model, the LuGre friction model (Sect. 3.3) is modified by incorporating the dynamics of the lubricant film formation [57]. The lubricant film dynamics is computed using a first-order lag element in which the time constant is varied between the deceleration, acceleration, and dwell periods [57]. Thus, in this model, the friction is obtained as a combination of the bristle model (Sect. 3.3) and the lubricant film dynamics.

Similar to the LuGre friction model, the average bristle deflection is quantified by an internal state variable, $\mathbf{q}$, such that [57]

$$\dot{\mathbf{q}} = \mathbf{v}_t - \frac{\sigma_0 |\mathbf{v}_t|}{g(\mathbf{v}_t, \mathbf{h})} \mathbf{q}, \tag{28}$$

with

$$g(\mathbf{v}_t, \mathbf{h}) = F_c + [(1 - |\mathbf{h}|) F_s - F_c]\, e^{-\left(\frac{|\mathbf{v}_t|}{v_s}\right)^n}, \tag{29}$$

where $\mathbf{h}$ is the dimensionless lubricant film thickness parameter, and the function $g(\mathbf{v}_t, \mathbf{h})$ describes the Stribeck effect. The lubricant film dynamics can be written as [52,57]

$$\dot{\mathbf{h}} = \frac{1}{\tau_h} (\mathbf{h}_{ss} - \mathbf{h}), \tag{30}$$

with

$$\tau_h = \begin{cases} \tau_{hp} & (|\mathbf{v}_t| \neq 0, \quad |\mathbf{h}| \leq |\mathbf{h}_{ss}|), \\ \tau_{hn} & (|\mathbf{v}_t| \neq 0, \quad |\mathbf{h}| > |\mathbf{h}_{ss}|), \\ \tau_{h0} & (|\mathbf{v}_t| = 0), \end{cases} \tag{31}$$

$$|\mathbf{h}_{ss}| = \begin{cases} K_f |\mathbf{v}_t|^{\frac{2}{3}} & (|\mathbf{v}_t| \leq |\mathbf{v}_b|), \\ K_f |\mathbf{v}_b|^{\frac{2}{3}} & (|\mathbf{v}_t| > |\mathbf{v}_b|), \end{cases} \tag{32}$$

$$K_f = \left(1 - \frac{F_c}{F_s}\right) |\mathbf{v}_b|^{-\frac{2}{3}}, \tag{33}$$

where τ_{hp}, τ_{hn}, τ_{h0} are, respectively, the time constants for the acceleration, deceleration, and dwell periods, $\mathbf{h}_{ss}$ is the dimensionless steady-state lubricant film thickness parameter, K_f is a proportional constant, and $\mathbf{v}_b$ is the velocity at which the magnitude of the steady-state friction force becomes almost minimum [52,57]. In Eq. (31), $|\mathbf{h}| \leq |\mathbf{h}_{ss}|$ represents the acceleration period and $|\mathbf{h}| > |\mathbf{h}_{ss}|$ represents the deceleration period. Here, it is assumed [57] that the lubricant film thickness increases with velocity only in the negative resistance regime, that is, $|\mathbf{v}_t| \leq |\mathbf{v}_b|$, otherwise, it has a constant maximum value, as shown in Eq. (32). The total friction force, $\mathbf{F}_\mu$, generated from the bending of the bristles and lubricant film dynamics can be written as

$$\mathbf{F}_\mu = \sigma_0 \mathbf{q} + \sigma_1 \dot{\mathbf{q}} + \sigma_2 \mathbf{v}_t. \tag{34}$$

4 Coupling the dynamics of the multibody and hydraulic systems

In this section, the multibody formulation in Sect. 2.1 is extended to incorporate the dynamics of the hydraulic system, introduced in Sect. 2.2, with the friction force models of a hydraulic cylinder, introduced in Sect. 3, in a monolithic approach [32,49]. The force vector, $\mathbf{Q}^\Sigma$, in Eq. (9), is incremented with the pressure variation equations and friction force model such that the combined system of equations can be written as

$$\left.\begin{aligned} \mathbf{M}^\Sigma \ddot{\mathbf{z}} + \boldsymbol{\Phi}_{\mathbf{z}}^{\mathrm{T}} \alpha \boldsymbol{\Phi} + \boldsymbol{\Phi}_{\mathbf{z}}^{\mathrm{T}} \boldsymbol{\lambda} &= \mathbf{Q}^\Sigma \left(\mathbf{z}, \dot{\mathbf{z}}, \mathbf{p}, \mathbf{F}_\mu\right) \\ \boldsymbol{\lambda}^{(h+1)} &= \boldsymbol{\lambda}^{(h)} + \alpha \boldsymbol{\Phi}^{(h+1)} \\ \dot{\mathbf{p}} &= \mathbf{u}_0 \left(\mathbf{p}, \mathbf{z}, \dot{\mathbf{z}}\right) \end{aligned}\right\}, \tag{35}$$

where $\mathbf{M}^\Sigma$ and $\mathbf{Q}^\Sigma$ are the respective accumulated mass matrix and accumulated external force vector as shown in Eq. (9), $\mathbf{z} \in \mathbb{R}^{N_b}$ is the vector of the relative joint coordinates, $\dot{\mathbf{p}}$ is the time derivative of the vector of hydraulic pressures, $\mathbf{p}$, and $\mathbf{u}_0 (\mathbf{p}, \mathbf{z}, \dot{\mathbf{z}})$ are the pressure variation equations. Here, it is assumed that the dependency of $\mathbf{Q}^\Sigma$ with respect to $\mathbf{z}$, $\dot{\mathbf{z}}$, $\mathbf{p}$, and $\mathbf{F}_\mu$, and the dependency of function $\mathbf{u}_0$ with respect to $\mathbf{z}$, $\dot{\mathbf{z}}$,

and $\mathbf{p}$ are known. In static friction models, such as the Bengisu–Akay and Brown–McPhee models, the inclusion of friction force, $\mathbf{F}_\mu$, in Eq. (35) is a straightforward task, where $\mathbf{F}_\mu$ is dependent on $\mathbf{z}$ and $\dot{\mathbf{z}}$. However, in dynamic friction models, such as the LuGre and modified LuGre models, the inclusion of $\mathbf{F}_\mu$ in Eq. (35) utilizes extra state variables to describe the friction, such as

$$\left.\begin{array}{l}\dot{\mathbf{q}} = \mathbf{u}_1\left(\mathbf{q}, \mathbf{z}, \dot{\mathbf{z}}\right)\end{array}\right\} \quad \text{(LuGre friction model)}, \tag{36}$$

$$\left.\begin{array}{l}\dot{\mathbf{q}} = \mathbf{u}_2\left(\mathbf{q}, \mathbf{z}, \dot{\mathbf{z}}, \mathbf{h}\right) \\ \dot{\mathbf{h}} = \mathbf{u}_3\left(\mathbf{h}, \mathbf{z}, \dot{\mathbf{z}}\right)\end{array}\right\} \text{(modified LuGre friction model)}, \tag{37}$$

where $\mathbf{u}_1\left(\mathbf{q}, \mathbf{z}, \dot{\mathbf{z}}\right)$ and $\mathbf{u}_2\left(\mathbf{q}, \mathbf{z}, \dot{\mathbf{z}}, \mathbf{h}\right)$ are the equations of average bristle deflection variation in the LuGre and modified LuGre friction models, respectively, and $\mathbf{u}_3\left(\mathbf{h}, \mathbf{z}, \dot{\mathbf{z}}\right)$ are the equations of lubricant film thickness variation. The state variables in Eqs. (36) and (37) can be integrated over time in two ways. In the first approach, which is employed in this study, the frictional state variables can be added to the state variables of the coupled equations of motion in Eq. (35) and integrated as shown in this section. In the second approach, the frictional state variables can be integrated locally during resolution of the friction problem [38]. The use of dynamic friction models can introduce numerical stiffness to the system, which may decrease the numerical efficiency of the simulation.

In this study, coupled systems are integrated [55] using an implicit single-step trapezoidal rule, as in [7]. It has already been established in [7,40] that the trapezoidal rule performs satisfactorily for coupled multibody and hydraulic systems by considering position and pressure as the primary variables instead of accelerations and pressure derivatives. Similarly, average bristle deflection for the LuGre friction model and average bristle deflection and lubricant film thickness for the modified LuGre friction model are considered as primary variables when applying the trapezoidal rule. The implementation details of the trapezoidal rule can be followed from Appendix A. By following Appendix A, the residual vector, $\left[\bar{\mathbf{f}}\left(\mathbf{x}\right)\right]$, can be written as

$$\left[\bar{\mathbf{f}}\left(\mathbf{x}\right)\right] = \frac{\Delta t^2}{4}\begin{bmatrix}\mathbf{M}^{\Sigma}\ddot{\mathbf{z}} + \boldsymbol{\Phi}_{\mathbf{z}}^{\mathrm{T}}\alpha\boldsymbol{\Phi} + \boldsymbol{\Phi}_{\mathbf{z}}^{\mathrm{T}}\boldsymbol{\lambda} - \mathbf{Q}^{\Sigma} \\ \dot{\mathbf{p}} - \mathbf{u}_0\end{bmatrix}$$

(Bengisu–Akay and Brown–McPhee approaches), (38)

$$\left[\bar{\mathbf{f}}\left(\mathbf{x}\right)\right] = \frac{\Delta t^2}{4}\begin{bmatrix}\mathbf{M}^{\Sigma}\ddot{\mathbf{z}} + \boldsymbol{\Phi}_{\mathbf{z}}^{\mathrm{T}}\alpha\boldsymbol{\Phi} + \boldsymbol{\Phi}_{\mathbf{z}}^{\mathrm{T}}\boldsymbol{\lambda} - \mathbf{Q}^{\Sigma} \\ \dot{\mathbf{p}} - \mathbf{u}_0 \\ \dot{\mathbf{q}} - \mathbf{u}_1\end{bmatrix}$$

(LuGre approach), (39)

$$\left[\bar{\mathbf{f}}\left(\mathbf{x}\right)\right] = \frac{\Delta t^2}{4}\begin{bmatrix}\mathbf{M}^{\Sigma}\ddot{\mathbf{z}} + \boldsymbol{\Phi}_{\mathbf{z}}^{\mathrm{T}}\alpha\boldsymbol{\Phi} + \boldsymbol{\Phi}_{\mathbf{z}}^{\mathrm{T}}\boldsymbol{\lambda} - \mathbf{Q}^{\Sigma} \\ \dot{\mathbf{p}} - \mathbf{u}_0 \\ \dot{\mathbf{q}} - \mathbf{u}_2 \\ \dot{\mathbf{h}} - \mathbf{u}_3\end{bmatrix}$$

(modified LuGre approach) (40)

where $\boldsymbol{\lambda}$ is obtained as shown in Eq. (10), whereas the approximated tangent matrix, $\left[\frac{\partial\bar{\mathbf{f}}(\mathbf{x})}{\partial\mathbf{x}}\right]$, can be numerically obtained, as in [32,49], by using the forward differentiation rule as

$$\frac{df\left(x_0\right)}{dx} \approx \frac{f\left(x_0 + \epsilon\right) - f\left(x_0\right)}{\epsilon}, \tag{41}$$

where ϵ is the differentiation increment. To avoid ill-conditioning of the tangent matrix, $\left[\frac{\partial\bar{\mathbf{f}}(\mathbf{x})}{\partial\mathbf{x}}\right]_{k+1}^{(h)}$, ϵ is computed as [49]

$$\epsilon = 1 \times 10^{-8}\max\left(1 \times 10^{-2}, \mid x_0 \mid\right), \tag{42}$$

where 1×10^{-2} limits the minimum value for the differentiation increment to 1×10^{-10}. In the above friction-based approaches, that is, Eqs. (A.2)–(A.4), $\dot{\mathbf{z}}$ and $\ddot{\mathbf{z}}$ are corrected using mass–damping–stiffness–orthogonal projections [9,17], as shown in Eqs. (11) and (12).

5 A case study of a hydraulically actuated four-bar mechanism

In this study, a hydraulically actuated four-bar mechanism, as shown in Fig. 6, is used to illustrate the effect of friction models of a hydraulic cylinder on the four-bar mechanism. The four-bar mechanism is modeled using a semi-recursive formulation, as explained in Sect. 2.1. As can be seen in Fig. 6, three relative joint coordinates, z_1, z_2 and z_3, are used in modeling of the planar structure, and two loop-closure constraints are used for the cut-joint (revolute joint) at point E. The mechanism has one degree of freedom. Note that z_1, z_2 and z_3 represent, respectively, the positions of the crank, coupler, and rocker in the inertial reference frame, XYZ. Their initial values are considered as 60^{o}, -37.90^{o}, and -93.58^{o}, respectively. In the integration process, the initial values of the relative joint velocities are considered to be 0^{o}/s to avoid instabilities. The crank, coupler, and rocker are assumed to be rectangular beams, whose masses and lengths are, respectively, $m_1 = 16$ kg, $m_2 = 64$ kg, and $m_3 = 40$ kg, and $L_1 = 2$ m, $L_2 = 8$ m, and $L_3 = 5$ m. The mass moment of inertia of the bodies is considered as $\frac{mL^2}{12}$. In the XYZ frame, the locations of points E, F and G are, respectively, $\mathbf{r}_E = [10, 0, 0]^{\text{T}}$ m, $\mathbf{r}_F = \left[\frac{L_1}{2}\cos(z_1), \frac{L_1}{2}\sin(z_1), 0\right]^{\text{T}}$ m and $\mathbf{r}_G = \left[-\frac{L_1}{2}, 0, 0\right]^{\text{T}}$ m. Point F is located at the center of mass of the crank.

The four-bar mechanism, as shown in Fig. 6, is hydraulically actuated using a hydraulic circuit that consists of a pump, a tank, a directional control valve, a throttle valve, a double-acting hydraulic cylinder, and connecting hoses. For simplicity, leakage in the hydraulic components is neglected. Following the lumped fluid theory, the hydraulic circuit is partitioned into discrete volumes (shown in Fig. 6), V_1, V_2, and V_3, whose respective pressures p_1, p_2, and p_3 are computed as

$$\left.\begin{aligned} \dot{p}_1 &= \frac{B_{e1}}{V_1}\left(Q_{d1} - Q_t\right) \\ \dot{p}_2 &= \frac{B_{e2}}{V_2}\left(Q_t - A_2\dot{s}\right) \\ \dot{p}_3 &= \frac{B_{e3}}{V_3}\left(A_3\dot{s} - Q_{3d}\right) \end{aligned}\right\}, \tag{43}$$

where Q_{d1} and Q_{3d} are the volume flow rates from the directional control valve (Eq. 17), Q_t is the volume flow rate from the throttle valve (Eq. 15), B_{e1}, B_{e2}, and B_{e3} are the effective bulk modulus of the respective control volumes (Eq. 14), A_2 and A_3 are the areas of the piston and piston-rod sides, respectively, and $\dot{s}$ is the actuator velocity. For the presented hydraulic circuit, the control volumes can be written as

$$\left.\begin{aligned} V_1 &= V_{h_1} \\ V_2 &= V_{h_2} + A_2 l_2 \\ V_3 &= V_{h_3} + A_3 l_3 \end{aligned}\right\}, \tag{44}$$

where V_{h_1}, V_{h_2}, and V_{h_3} are the volumes of the respective hoses, and l_2 and l_3 are the chamber lengths of the piston and piston-rod sides, respectively, which can be calculated as $l_2 = \left((l_2)_{t=0} + |\,\mathbf{s}\,|_{t=0} - |\,\mathbf{s}\,|\right)$ and $l_3 = \left((l_3)_{t=0} - |\,\mathbf{s}\,|_{t=0} + |\,\mathbf{s}\,|\right)$, where $|\,\mathbf{s}\,|$ is the actuator length of the hydraulic cylinder. The values of $\mathbf{s}$ and $\dot{s}$ are, respectively, calculated as

$$\left.\begin{aligned} \mathbf{s} &= \mathbf{r}_F - \mathbf{r}_G \\ \dot{s} &= \frac{d|\,\mathbf{s}\,|}{dt} = \dot{\mathbf{s}}\cdot\frac{\mathbf{s}}{|\,\mathbf{s}\,|} = \dot{\mathbf{r}}_F\cdot\frac{\mathbf{s}}{|\,\mathbf{s}\,|} \end{aligned}\right\}, \tag{45}$$

where $\dot{\mathbf{r}}_F$ is the velocity vector of point F calculated using classical kinematic relations, as in [19,30]. The force, F_c, produced by the hydraulic cylinder (Eq. 20) is expressed as $\mathbf{F}_c = \left[\frac{s_X}{|\mathbf{s}|}F_c, \frac{s_Y}{|\mathbf{s}|}F_c, \frac{s_Z}{|\mathbf{s}|}F_c\right]^{\text{T}}$, where s_X, s_Y, and s_Z are the components of vector $\mathbf{s}$ in the inertial reference frame, XYZ. From the static configuration at $t = 0$, $(F_c)_{t=0} = 681.23$ N, $(p_1)_{t=0} = (p_2)_{t=0}$, and $(p_2)_{t=0} = \left((F_c)_{t=0} + A_3(p_3)_{t=0}\right)/A_2$, where the friction force is assumed as zero and $(p_3)_{t=0}$ as 3.5 MPa. The system is hydraulically actuated for 10 s using the reference voltage signal, U_{ref}, as

$$U_{\text{ref}} = \begin{cases} 0 & t < 1\text{s}, 2.5\text{s} \le t < 5\text{s}, t \le 9\text{s}, \\ 10 & 1\text{s} \le t < 2.5\text{s}, \\ -10 & 5\text{s} \le t < 8\text{s}, \end{cases} \tag{46}$$

where t is the simulation run time. The parameters of the hydraulic circuit are shown in Table 1.

In this study, the coupled system is integrated by incorporating the friction models of the hydraulic cylinder, as shown in Sect. 4. The parameters of the friction models are shown in Table 2, where the values are selected based on typical values found in the literature. Static friction models, that is, the Bengisu–Akay

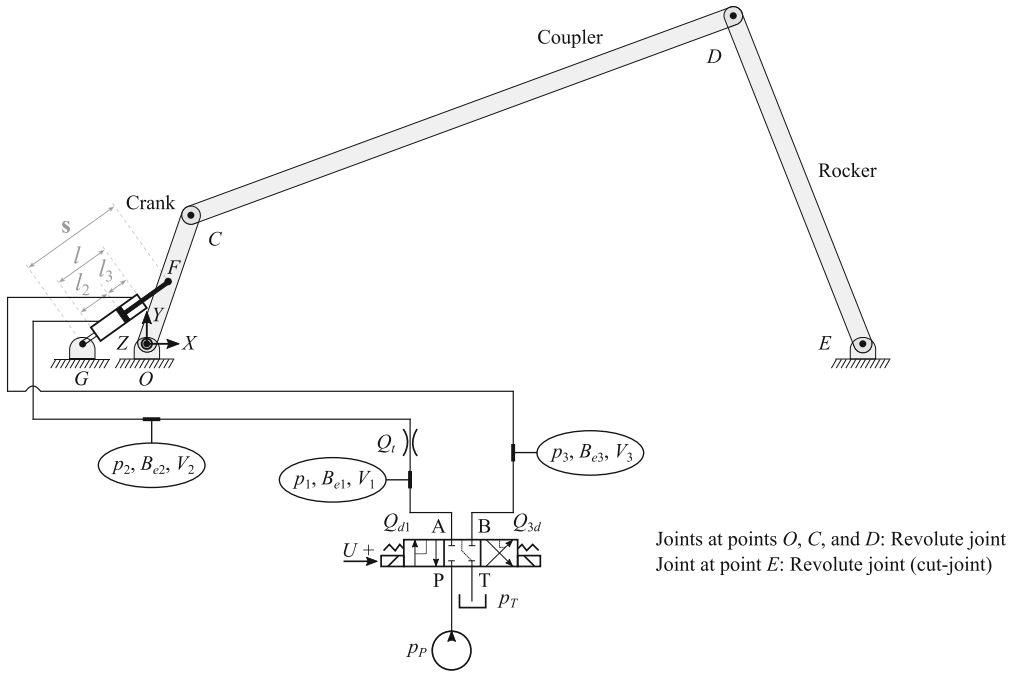

Fig. 6 Four-bar mechanism actuated by a double-acting hydraulic cylinder

Table 1 Parameters of the hydraulic system

Parameter	Symbol	Value
Pressure of the pump	p_P	7.6 MPa
Pressure of the tank (atmospheric pressure)	p_T	0.1 MPa
Semi-empirical flow rate constant of the directional control valve	C_{v_d}	2.138×10^{-8} m^3/s $\sqrt{\text{Pa}}$
Volume of the hose (section-1)	V_{h_1}	4.71×10^{-5} m^3
Volume of the hose (section-2)	V_{h_2}	3.14×10^{-5} m^3
Volume of the hose (section-3)	V_{h_3}	7.85×10^{-5} m^3
Area of the throttle valve	A_t	2.83×10^{-5} m^2
Flow discharge coefficient of the throttle valve	C_d	0.8
Density of the oil	ρ	850 kg/m^3
Bulk modulus of the hoses	B_h	550 MPa
Bulk modulus of the oil	B_{oil}	1500 MPa
Bulk modulus of the hydraulic cylinder	B_c	31500 MPa
Diameter of the piston	d_2	80 mm
Diameter of the piston-rod	d_3	35 mm
Length of the cylinder/piston	l	0.9 m
Initial actuator length	s_0	1.73 m

Table 2 Parameters of friction models of a hydraulic cylinder

Parameter	Symbol	Value	Bengisu–Akay	Brown–McPee	LuGre	Modified LuGre
Coulomb friction	F_c	210 N	✓	✓	✓	✓
Static friction	F_s	830 N	✓	✓	✓	✓
Stribeck velocity	v_s	1.25×10^{-2} m/s	✓	✓	✓	✓
Threshold velocity	v_b	0.70 m/s	-	-	-	✓
Exponent for the Stribeck curve	n	0.5	-	-	✓	✓
Parameter for curve shape	ξ	50 s/m	✓	-	-	-
Stiffness of elastic bristles	σ_0	$\sqrt{54} \times 10^6$ N/m	-	-	✓	✓
Damping of elastic bristles	σ_1	$\sqrt{10} \times 10^4$ Ns/m	-	-	✓	✓
Coefficient of viscous friction	σ_2	330 Ns/m	✓	✓	✓	✓
Time constant for acceleration period	τ_{hp}	0.25 s	-	-	-	✓
Time constant for deceleration period	τ_{hn}	1.50 s	-	-	-	✓
Time constant for dwell period	τ_{h0}	40 s	-	-	-	✓

model and the Brown–McPhee friction model, do not require integration of additional variables other than the positions and pressures of the coupled system. On the other hand, dynamics friction models, that is, the LuGre model and the modified LuGre friction model, require additional variables to be integrated along with the coupled equations of motion. In the proposed integration scheme, the set of variables used to solve the equations of the coupled system (Sect. 4) are

$$\left.\begin{aligned} &\mathbf{x} = \left[\mathbf{z}^{\mathrm{T}},\ \mathbf{p}^{\mathrm{T}}\right]^{\mathrm{T}} \\ &\quad \text{(Bengisu–Akay and Brown–McPhee approaches)} \\ &\mathbf{x} = \left[\mathbf{z}^{\mathrm{T}},\ \mathbf{p}^{\mathrm{T}},\ \mathbf{q}^{\mathrm{T}}\right]^{\mathrm{T}} \\ &\quad \text{(LuGre approach)} \\ &\mathbf{x} = \left[\mathbf{z}^{\mathrm{T}},\ \mathbf{p}^{\mathrm{T}},\ \mathbf{q}^{\mathrm{T}},\ \mathbf{h}^{\mathrm{T}}\right]^{\mathrm{T}} \\ &\quad \text{(modified LuGre approach)} \end{aligned}\right\}. \tag{47}$$

In the trapezoidal integration scheme, the error tolerance for the position is 1×10^{-7} rad; for the average bristle deflection and lubricant film thickness, it is 1×10^{-7} m; and for the pressure 1×10^{-2} Pa. The penalty factor, α, in Eq. (9) is considered as 1×10^{11} in this study. The voltage, which represents the relative spool position, is integrated using the trapezoidal rule, and the error tolerance is considered to be 1×10^{-7} V. All the approaches in this study are implemented in the Matlab environment.

6 Results and discussion

This section presents simulation results of the hydraulically actuated four-bar mechanism, shown in Fig. 6, and demonstrates the effect of friction models of the hydraulic cylinder on the four-bar mechanism. The simulation frames of the four-bar structure at different instants of time, representing the positions of the bodies, are shown in Fig. 7. Here, the four coupled system approaches, namely, the Bengisu–Akay approach, Brown–McPhee approach, LuGre approach, and modified LuGre approach, are compared based on the simulation work cycle, friction force, energy balance, and numerical efficiency. In this study, all the simulations are run with a time-step of 1 ms.

6.1 The work cycle representation

In the presented case study, the hydraulic cylinder tilts the four-bar structure outward between 1 and 2.5 s and inward between 5 and 8 s. In the subsequent plots, the regions between the opening and closing of the directional control valve are highlighted in purple. For demonstration, only the crank angle is presented in Fig. 8a. However, the coupler and rocker angles follow a similar pattern. Similarly, only pressure p_3 is presented in Fig. 8b; pressures p_1 and p_2 follow a similar pattern. Even though the differences in the relative joint coordinates and pressures may be small, they differ based on the friction model utilized in the model-

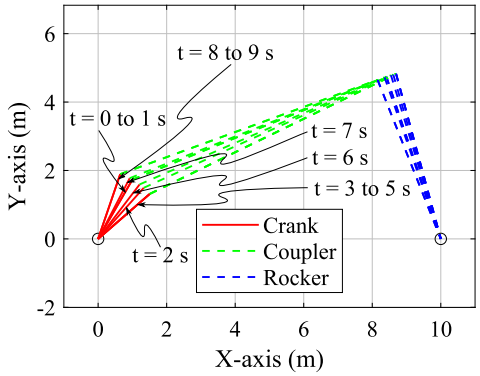

Fig. 7 Position of the four-bar mechanism at every second during the simulation run

ing. Such small differences can be an important aspect to consider in applications where high precision and/or low vibration is a pre-requisite. Thus, the friction model can significantly affect the control system performance. It should be noted that the semi-recursive multibody formulation utilizes the full set of relative joint coordinates in the equations of motion.

6.2 Friction force

A comparison of the friction force models of the hydraulic cylinder is shown in Fig. 9. The friction forces in all four approaches are continuous at zero relative piston velocity, thus, avoiding numerical instabilities. Figure 9b compares the friction–velocity characteristics of the approaches. The curves corresponding to the Bengisu–Akay and Brown–McPhee approaches match with their definitions, as described in Sect. 3, that is, they describe the Coulomb, stiction, Stribeck, and viscous friction effects. The LuGre and modified LuGre approaches evaluate the friction behavior by using extra state variables, such as the average bristle

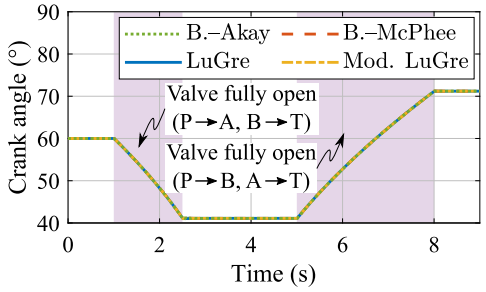

(a) Crank angle.

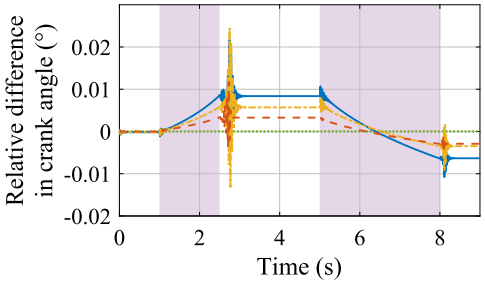

(b) Relative comparison of the crank angle.

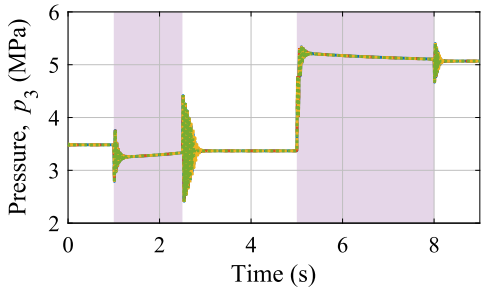

(c) Hydraulic pressure p_3.

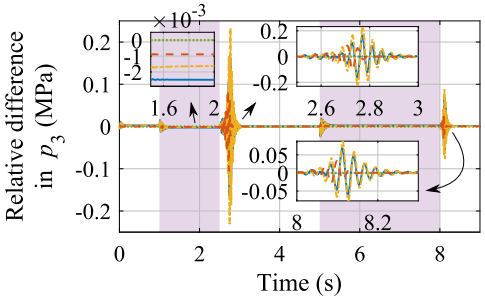

(d) Relative comparison of the hydraulic pressure p_3.

Fig. 8 The work cycle representation of the four-bar mechanism with a time-step of 1 ms

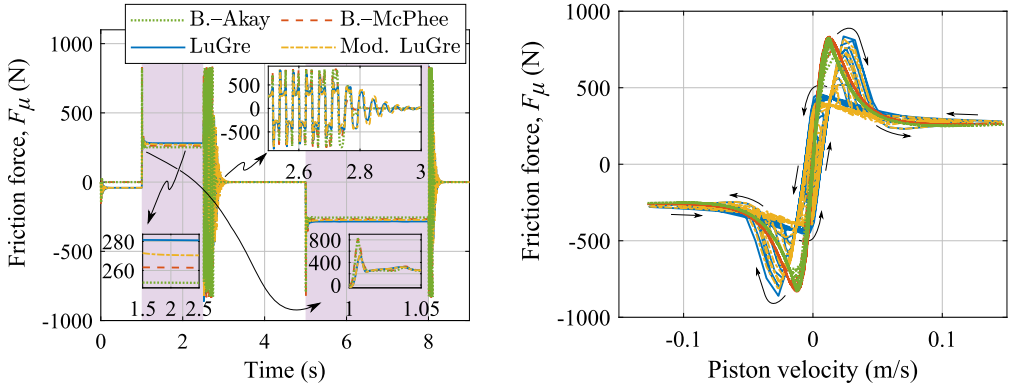

(a) Friction force (F_μ) versus simulation run time characteristic.

(b) Friction force (F_μ) versus piston velocity characteristic.

Fig. 9 Comparison of friction models of the hydraulic cylinder with a simulation time-step of 1 ms

deflection in the LuGre approach and the average bristle deflection and lubricant film thickness in the modified LuGre approach. As shown in Fig. 9b, the latter two approaches can incorporate pre-slip displacement and frictional lag. The pre-slip displacement implies a small motion of the bristles in the elastic range, when the applied force is less than the break-away force [38]. It can help to determine the static friction as well as the Stribeck effect in the steady state. Frictional lag is a delayed behavior of the friction force with respect to velocity such that the friction force is higher for acceleration than during deceleration.

6.3 Energy balance

The energy balance in the approaches is analyzed by comparing the potential energy, kinetic energy, and work done by the hydraulic cylinder. The energy comparison is shown in Fig. 10, where the energy balance in all four studied approaches showed good agreement with respect to each other. With the Bengisu–Akay approach, the peak energy drift is 0.45 J, which is 0.37% of the maximum cylinder work, 121.02 J, whereas with the Brown–McPhee approach, the peak energy drift is 0.45 J, which is 0.37% of the maximum cylinder work, 120.99 J. With the LuGre approach, the peak energy drift is 0.44 J, which is 0.36% of the maximum cylinder work, 120.94 J, and in the modified LuGre approach, the peak energy drift is 0.44 J, which is 0.36% of the maximum cylinder work, 120.97 J. It should be noted that in all four approaches, the peak energy drift occurred at the opening of the directional control valve at around 1 s. An analogy can be drawn between the hydraulic system and a stiff spring supporting the four-bar structure.

6.4 Numerical efficiency

The numerical efficiencies of all four approaches are compared in Figs. 11 and 12, and the average and maximum iterations and total integration time are shown in Table 3. The maximum number of iterations occurred during the opening and closing of the directional control valve. Otherwise, the iterations are mostly one iteration in the Bengisu–Akay and Brown–McPhee approaches and two iterations in the LuGre and modified LuGre approaches. During closing of the directional control valve, the LuGre and modified LuGre approaches required more iterations than the Bengisu–Akay and Brown–McPhee approaches (Fig. 11).

The integration time of the LuGre and modified LuGre approaches is greater than that of the Bengisu–Akay and Brown–McPhee approaches, which is in agreement with the literature [37,38]. The poor numerical efficiency of the LuGre and modified LuGre approaches can be attributed to the numerical stiffness introduced by use of extra state variable(s), such as average bristle deflection in the LuGre approach and

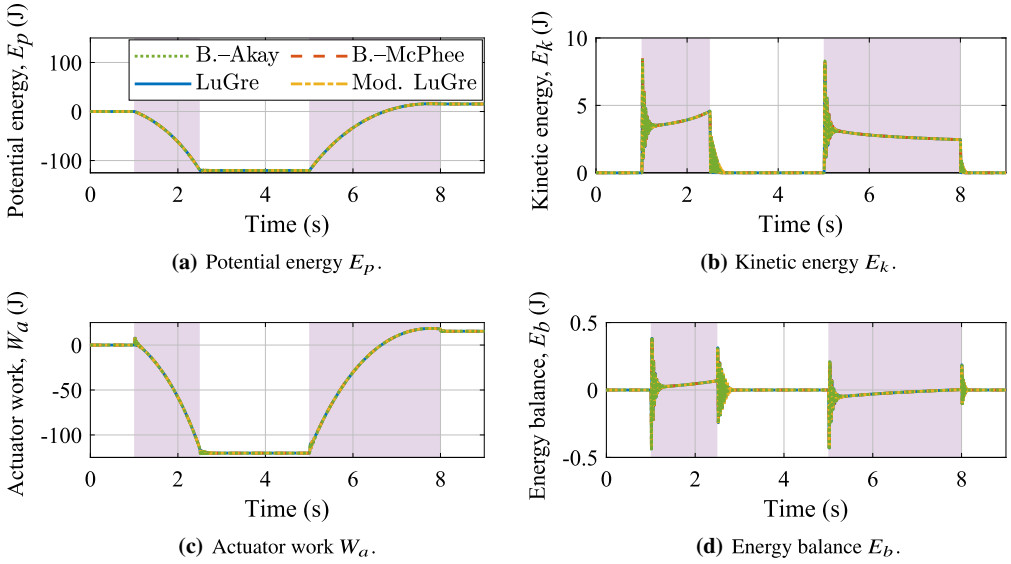

(a) Potential energy E_p. **(b)** Kinetic energy E_k.

(c) Actuator work W_a. **(d)** Energy balance E_b.

Fig. 10 Comparison of energies with a simulation time-step of 1 ms

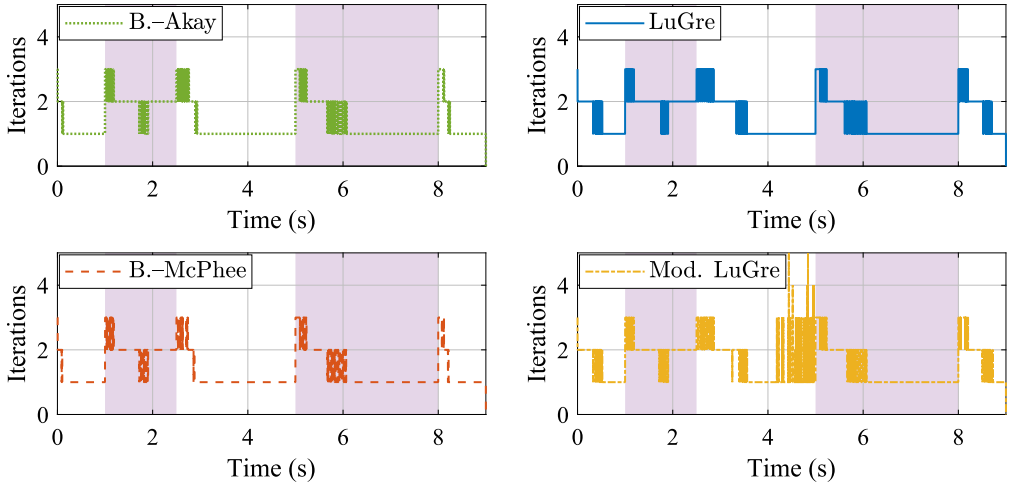

Fig. 11 Number of iterations in the Newton–Raphson method with a time-step of 1 ms

average bristle deflection and lubricant film thickness in the modified LuGre approach. The poor numerical efficiency of the Bengisu–Akay approach compared with the Brown–McPhee approach is attributed to the change in friction equations during the simulation. The Brown–McPhee approach is relatively the most efficient approach and is a potential candidate for real-time applications [16]. Real-time capabilities can be achieved by implementing the approach in a lower language, such as C++ or Fortran, and by limiting the number of iterations to a lower value.

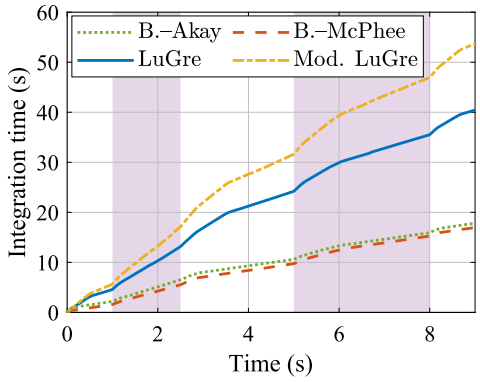

Fig. 12 Comparison of the cumulative integration time with a simulation time-step of 1 ms

Table 3 Comparison of the numerical efficiencies

Approach	Average iterations	Maximum iterations	Integration time
B.–Akay	1.43	3	17.81 s
B.–McPhee	1.42	3	16.97 s
LuGre	1.60	3	40.45 s
Mod. LuGre	1.62	5	53.72 s

7 Conclusion

In simulation of coupled multibody and hydraulic systems, an important aspect in the modeling is the nonlinearity and numerical stiffness introduced by the friction model of a hydraulic cylinder. The objective of this paper was to couple various friction models of a hydraulic cylinder with the equations of motion of a hydraulically actuated multibody system in a monolithic framework. The study considered two static friction models: the Bengisu–Akay model and the Brown–McPhee model, and two dynamic friction models: the LuGre model and the modified LuGre model. Within the monolithic framework, the multibody system was described using a semi-recursive formulation and the hydraulic actuator was described using the lumped fluid theory. A hydraulically actuated four-bar mechanism was examined as a case study and the four approaches were compared based on the work cycle, friction force, energy balance, and numerical efficiency.

The relative joint coordinates and hydraulic pressures were affected by the friction force model selected. This is a significant aspect that should be considered in modeling, especially, in applications where high precision and/or low vibration is a pre-requisite. The Bengisu–Akay and Brown–McPhee approaches showed traditional friction–velocity characteristics, namely the Coulomb, stiction, Stribeck, and viscous friction effects. The LuGre and modified LuGre approaches demonstrated frictional phenomena such as pre-slip displacement and frictional lag. All four approaches studied showed acceptable results for energy balance. The modified LuGre approach had the poorest numerical efficiency, which was attributed to the solution of additional state variables: average bristle deflection and fluid film thickness. The Bengisu–Akay approach was more efficient than the LuGre approach but less efficient than the Brown–McPhee approach because of the change in friction equation during the simulation. It can be concluded that the Brown–McPhee approach appears to be numerically the most efficient approach and it was well able to describe usual friction characteristics in dynamic simulation of hydraulically actuated multibody systems.

In future work, the Brown–McPhee approach could be implemented in a lower language, such as C++ or Fortran, to assess real-time capabilities further. The methods presented in this study may be extended to study of state and force estimators. Studies may also be directed toward coupling the dynamic friction models with other multibody formulations. Future studies can investigate the comparative responses of multibody systems based on the high and low magnitudes of the stiffness/damping of dynamic friction models of a hydraulic cylinder and based on throttling in pressure lines. This can lead to a possible source for a stick-slip behavior between the hydraulic cylinder and piston. Furthermore, static friction models that introduce discontinuity at zero relative velocity can be considered in future studies to demonstrate the numerical instability caused by them.

Acknowledgements The first author acknowledges the immense support of his wife, Heena, as the majority of the research was carried out at his home office.

Funding Open access funding provided by LUT University (previously Lappeenranta University of Technology (LUT)). This work was supported in part by Business Finland (project:

Service Business from Physics Based Digital Twins—DigiBuzz) and in part by the Academy of Finland under Grant #316106.

Declarations

Conflicts of interest The authors declare that they have no conflict of interest.

Availability of data and material Not applicable.

Code availability Not applicable.

Appendix A: Numerical integration scheme

In this study, coupled systems are integrated using an implicit single-step trapezoidal rule. By applying the rule $\mathbf{z}_{k+1} = \mathbf{z}_k + \frac{\Delta t}{2}(\dot{\mathbf{z}}_k + \dot{\mathbf{z}}_{k+1})$ to positions, $\mathbf{z}_{k+1}$, velocities, $\dot{\mathbf{z}}_{k+1}$, pressures, $\mathbf{p}_{k+1}$, average bristle deflections, $\mathbf{q}_{k+1}$, and lubricant film thicknesses, $\mathbf{h}_{k+1}$, the velocities, accelerations, pressure derivatives, rate of average bristle deflections, and lubricant film thickness derivatives at time-step $(k+1)$ can be, respectively, written as

$$\left.\begin{aligned}
\dot{\mathbf{z}}_{k+1} &= \frac{2}{\Delta t}\mathbf{z}_{k+1} - \left(\frac{2}{\Delta t}\mathbf{z}_k + \dot{\mathbf{z}}_k\right) = \frac{2}{\Delta t}\mathbf{z}_{k+1} + \hat{\dot{\mathbf{z}}}_k \\
\ddot{\mathbf{z}}_{k+1} &= \frac{4}{\Delta t^2}\mathbf{z}_{k+1} - \left(\frac{4}{\Delta t^2}\mathbf{z}_k + \frac{4}{\Delta t}\dot{\mathbf{z}}_k + \ddot{\mathbf{z}}_k\right) = \frac{4}{\Delta t^2}\mathbf{z}_{k+1} + \hat{\ddot{\mathbf{z}}}_k \\
\dot{\mathbf{p}}_{k+1} &= \frac{2}{\Delta t}\mathbf{p}_{k+1} - \left(\frac{2}{\Delta t}\mathbf{p}_k + \dot{\mathbf{p}}_k\right) = \frac{2}{\Delta t}\mathbf{p}_{k+1} + \hat{\dot{\mathbf{p}}}_k \\
\dot{\mathbf{q}}_{k+1} &= \frac{2}{\Delta t}\mathbf{q}_{k+1} - \left(\frac{2}{\Delta t}\mathbf{q}_k + \dot{\mathbf{q}}_k\right) = \frac{2}{\Delta t}\mathbf{q}_{k+1} + \hat{\dot{\mathbf{q}}}_k \\
\dot{\mathbf{h}}_{k+1} &= \frac{2}{\Delta t}\mathbf{h}_{k+1} - \left(\frac{2}{\Delta t}\mathbf{h}_k + \dot{\mathbf{h}}_k\right) = \frac{2}{\Delta t}\mathbf{h}_{k+1} + \hat{\dot{\mathbf{h}}}_k
\end{aligned}\right\}. \quad \text{(A.1)}$$

By introducing Eq. (A.1) into Eqs. (35)–(37), the dynamic equilibrium, established at time-step $(k+1)$, for the coupled system can be written as

$$\left.\begin{aligned}
\mathbf{M}^{\Sigma}\mathbf{z}_{k+1} + \frac{\Delta t^2}{4}\left(\boldsymbol{\Phi}_{\mathbf{z}}^{\mathrm{T}}\right)_{k+1}\left(\alpha\boldsymbol{\Phi}_{k+1} + \boldsymbol{\lambda}_{k+1}\right) - \\
\frac{\Delta t^2}{4}\left(\mathbf{Q}^{\Sigma}\right)_{k+1} + \frac{\Delta t^2}{4}\mathbf{M}^{\Sigma}\hat{\ddot{\mathbf{z}}}_k = 0 \\
\boldsymbol{\lambda}_{k+1}^{(h+1)} = \boldsymbol{\lambda}_{k+1}^{(h)} + \alpha\boldsymbol{\Phi}_{k+1}^{(h+1)} \\
\frac{\Delta t}{2}\mathbf{p}_{k+1} - \frac{\Delta t^2}{4}\left(\mathbf{u}_0\right)_{k+1} + \frac{\Delta t^2}{4}\hat{\dot{\mathbf{p}}}_k = 0
\end{aligned}\right\}$$

(Bengisu–Akay and Brown–McPhee approaches), (A.2)

$$\left.\begin{aligned}
\mathbf{M}^{\Sigma}\mathbf{z}_{k+1} + \frac{\Delta t^2}{4}\left(\boldsymbol{\Phi}_{\mathbf{z}}^{\mathrm{T}}\right)_{k+1}\left(\alpha\boldsymbol{\Phi}_{k+1} + \boldsymbol{\lambda}_{k+1}\right) - \\
\frac{\Delta t^2}{4}\left(\mathbf{Q}^{\Sigma}\right)_{k+1} + \frac{\Delta t^2}{4}\mathbf{M}^{\Sigma}\hat{\ddot{\mathbf{z}}}_k = 0 \\
\boldsymbol{\lambda}_{k+1}^{(h+1)} = \boldsymbol{\lambda}_{k+1}^{(h)} + \alpha\boldsymbol{\Phi}_{k+1}^{(h+1)} \\
\frac{\Delta t}{2}\mathbf{p}_{k+1} - \frac{\Delta t^2}{4}\left(\mathbf{u}_0\right)_{k+1} + \frac{\Delta t^2}{4}\hat{\dot{\mathbf{p}}}_k = 0 \\
\frac{\Delta t}{2}\mathbf{q}_{k+1} - \frac{\Delta t^2}{4}\left(\mathbf{u}_1\right)_{k+1} + \frac{\Delta t^2}{4}\hat{\dot{\mathbf{q}}}_k = 0
\end{aligned}\right\}$$

(LuGre approach), (A.3)

$$\left.\begin{aligned}
\mathbf{M}^{\Sigma}\mathbf{z}_{k+1} + \frac{\Delta t^2}{4}\left(\boldsymbol{\Phi}_{\mathbf{z}}^{\mathrm{T}}\right)_{k+1}\left(\alpha\boldsymbol{\Phi}_{k+1} + \boldsymbol{\lambda}_{k+1}\right) - \\
\frac{\Delta t^2}{4}\left(\mathbf{Q}^{\Sigma}\right)_{k+1} + \frac{\Delta t^2}{4}\mathbf{M}^{\Sigma}\hat{\ddot{\mathbf{z}}}_k = 0 \\
\boldsymbol{\lambda}_{k+1}^{(h+1)} = \boldsymbol{\lambda}_{k+1}^{(h)} + \alpha\boldsymbol{\Phi}_{k+1}^{(h+1)} \\
\frac{\Delta t}{2}\mathbf{p}_{k+1} - \frac{\Delta t^2}{4}\left(\mathbf{u}_0\right)_{k+1} + \frac{\Delta t^2}{4}\hat{\dot{\mathbf{p}}}_k = 0 \\
\frac{\Delta t}{2}\mathbf{q}_{k+1} - \frac{\Delta t^2}{4}\left(\mathbf{u}_2\right)_{k+1} + \frac{\Delta t^2}{4}\hat{\dot{\mathbf{q}}}_k = 0 \\
\frac{\Delta t}{2}\mathbf{h}_{k+1} - \frac{\Delta t^2}{4}\left(\mathbf{u}_3\right)_{k+1} + \frac{\Delta t^2}{4}\hat{\dot{\mathbf{h}}}_k = 0
\end{aligned}\right\}$$

(modified LuGre approach). (A.4)

Equations (A.2)–(A.4) are nonlinear system of equations that can be represented as $\bar{\mathbf{f}}(\mathbf{x}_{k+1}) = \mathbf{0}$, where $\mathbf{x} = \left[\mathbf{z}^{\mathrm{T}}, \mathbf{p}^{\mathrm{T}}\right]^{\mathrm{T}}$ for the Bengisu–Akay and Brown–McPhee approaches, $\mathbf{x} = \left[\mathbf{z}^{\mathrm{T}}, \mathbf{p}^{\mathrm{T}}, \mathbf{q}^{\mathrm{T}}\right]^{\mathrm{T}}$ for the LuGre approach, and $\mathbf{x} = \left[\mathbf{z}^{\mathrm{T}}, \mathbf{p}^{\mathrm{T}}, \mathbf{q}^{\mathrm{T}}, \mathbf{h}^{\mathrm{T}}\right]^{\mathrm{T}}$ for the modified LuGre approach. Such nonlinear systems of equations can be solved iteratively using the Newton–Raphson method as [32,49]

$$\left[\frac{\partial \bar{\mathbf{f}}\left(\mathbf{x}\right)}{\partial \mathbf{x}}\right]_{k+1}^{(h)} \Delta \mathbf{x}_{k+1}^{(h)} = -\left[\bar{\mathbf{f}}\left(\mathbf{x}\right)\right]_{k+1}^{(h)}, \tag{A.5}$$

where $\left[\bar{\mathbf{f}}\left(\mathbf{x}\right)\right]$ is the residual vector and $\left[\frac{\partial \bar{\mathbf{f}}(\mathbf{x})}{\partial \mathbf{x}}\right]$ is the approximated tangent matrix.

References

1. Al-Bender, F., Lampaert, V., Swevers, J.: The generalized Maxwell-slip model: a novel model for friction simulation and compensation. IEEE Trans. Autom. Control **50**(11), 1883–1887 (2005)
2. Andersson, S., Söderberg, A., Björklund, S.: Friction models for sliding dry, boundary and mixed lubricated contacts. Tribol. Int. **40**(4), 580–587 (2007)
3. Armstrong-Helouvry, B.: Control of Machines with Friction. Springer, New York (2012)
4. Armstrong-Helouvry, B., Dupont, P., De Wit, C.C.: A survey of models, analysis tools and compensation methods for the control of machines with friction. Automatica **30**(7), 1083–1138 (1994)
5. Awrejcewicz, J., Olejnik, P.: Analysis of dynamic systems with various friction laws. Appl. Mech. Rev. **58**(6), 389–411 (2005)
6. Baharudin, M.E., Rouvinen, A., Korkealaakso, P., Mikkola, A.: Real-time multibody application for tree harvester truck simulator. Proc. Inst. Mech. Eng. Part K J. Multi-Body Dyn. **228**(2), 182–198 (2014)
7. Bayo, E., Jalon, J.G.D., Avello, A., Cuadrado, J.: An efficient computational method for real time multibody dynamic simulation in fully cartesian coordinates. Comput. Methods Appl. Mech. Eng. **92**(3), 377–395 (1991)
8. Bayo, E., Jalon, J.G.D., Serna, M.A.: A modified Lagrangian formulation for the dynamic analysis of constrained mechanical systems. Comput. Methods Appl. Mech. Eng. **71**(2), 183–195 (1988)
9. Bayo, E., Ledesma, R.: Augmented Lagrangian and mass-orthogonal projection methods for constrained multibody dynamics. Nonlinear Dyn. **9**(1–2), 113–130 (1996)
10. Bengisu, M., Akay, A.: Stability of friction-induced vibrations in multi-degree-of-freedom systems. J. Sound Vib. **171**(4), 557–570 (1994)
11. Berger, E.: Friction modeling for dynamic system simulation. Appl. Mech. Rev. **55**(6), 535–577 (2002)
12. Bliman, P.A.: Friction modelling by hysteresis operators: application to Dahl, stiction and Stribeck effects. In: Proceedings of the Conference on Models of Hysteresis, pp. 10–19. Trento, Italy (1991)
13. Bliman, P.A., Sorine, M.: A system-theoretic approach of systems with hysteresis: application to friction modelling and compensation. In: Proceedings of the 2nd European Control Conference, pp. 1844–1849. Groningen, Netherlands (1993)
14. Bo, L.C., Pavelescu, D.: The friction-speed relation and its influence on the critical velocity of stick-slip motion. Wear **82**(3), 277–289 (1982)
15. Bonchis, A., Corke, P.I., Rye, D.C.: A pressure-based, velocity independent, friction model for asymmetric hydraulic cylinders. In: Proceedings of the IEEE International Conference on Robotics and Automation, pp. 1746–1751. Detroit, United States of America (1999)
16. Brown, P., McPhee, J.: A continuous velocity-based friction model for dynamics and control with physically meaningful parameters. J. Comput. Nonlinear Dyn. **11**(5), 054502 (2016)
17. Cuadrado, J., Cardenal, J., Morer, P., Bayo, E.: Intelligent simulation of multibody dynamics: space-state and descriptor methods in sequential and parallel computing environments. Multibody Syst. Dyn. **4**(1), 55–73 (2000)
18. Cuadrado, J., Dopico, D., Gonzalez, M., Naya, M.A.: A combined penalty and recursive real-time formulation for multibody dynamics. J. Mech. Des. **126**(4), 602–608 (2004)
19. Cuadrado, J., Dopico, D., Naya, M.A., Gonzalez, M.: Real-time multibody dynamics and applications. In: Simulation Techniques for Applied Dynamics, vol. 507, pp. 247–311. Springer (2008)
20. Dahl, P.R.: Solid friction damping of mechanical vibrations. Am. Inst. Aeronaut. Astronaut. **14**(12), 1675–1682 (1976)
21. De Wit, C.C., Olsson, H., Astrom, K.J., Lischinsky, P.: A new model for control of systems with friction. IEEE Trans. Autom. Control **40**(3), 419–425 (1995)
22. Fox, B., Jennings, L., Zomaya, A.: On the modelling of actuator dynamics and the computation of prescribed trajectories. Comput. Struct. **80**(7–8), 605–614 (2002)
23. Gonthier, Y., McPhee, J., Lange, C., Piedboeuf, J.C.: A regularized contact model with asymmetric damping and dwell-time dependent friction. Multibody Syst. Dyn. **11**(3), 209–233 (2004)
24. Haessig, D.A., Friedland, B.: On the modeling and simulation of friction. J. Dyn. Syst. Meas. Control **113**(3), 354–362 (1991)
25. Handroos, H.M., Ellman, A.U., Lindberg, I.I.: Dynamics of a counter balance valve controlled mechanical slide. In: Proceedings of the 3rd International Conference on Fluid Power Transmission and Control, pp. 59–65. Hangzhou, China (1993)
26. Handroos, H.M., Vilenius, M.J.: Flexible semi-empirical models for hydraulic flow control valves. J. Mech. Des. **113**(3), 232–238 (1991)
27. Hess, D., Soom, A.: Friction at a lubricated line contact operating at oscillating sliding velocities. J. Tribol. **112**(1), 147–152 (1990)
28. Huston, R., Liu, Y.S., et al.: Use of absolute coordinates in computational multibody dynamics. Comput. Struct. **52**(1), 17–25 (1994)
29. Jacobson, B.: The Stribeck memorial lecture. Tribol. Int. **36**(11), 781–789 (2003)
30. Jaiswal, S., Islam, M., Hannola, L., Sopanen, J., Mikkola, A.: Gamification procedure based on real-time multibody simulation. Int. Rev. Modell. Simul. **11**(5), 259–266 (2018)
31. Jaiswal, S., Korkealaakso, P., Åman, R., Sopanen, J., Mikkola, A.: Deformable terrain model for the real-time multibody simulation of a tractor with a hydraulically driven front-loader. IEEE Access **7**, 172694–172708 (2019)
32. Jaiswal, S., Rahikainen, J., Khadim, Q., Sopanen, J., Mikkola, A.: Comparing double-step and penalty-based semi-recursive formulations for a hydraulically actuated

multibody system in a monolithic approach. Multibody Syst. Dyn. (2021)
33. Jaiswal, S., Sanjurjo, E., Cuadrado, J., Sopanen, J., Mikkola, A.: State estimator based on an indirect kalman filter for a hydraulically actuated multibody system. Multibody Syst. Dyn. (Submitted) (2020)
34. Jalon, J.G.D., Alvarez, E., Ribera, F.A.D., Rodriguez, I., Funes, F.J.: A fast and simple semi-recursive formulation for multi-rigid-body systems. Comput. Methods Appl. Sci. **2**, 1–23 (2005)
35. Jalon, J.G.D., Bayo, E.: Kinematic and Dynamic Simulation of Multibody Systems: The Real-Time Challenge. Springer, Berlin (1994)
36. Lampaert, V., Al-Bender, F., Swevers, J.: A generalized Maxwell-slip friction model appropriate for control purposes. In: Proceedings of the International Conference on Physics and Control, pp. 1170–1177. Saint Petersburg, Russia (2003)
37. Marques, F., Flores, P., Claro, J.P., Lankarani, H.M.: A survey and comparison of several friction force models for dynamic analysis of multibody mechanical systems. Nonlinear Dyn. **86**(3), 1407–1443 (2016)
38. Marques, F., Flores, P., Claro, J.P., Lankarani, H.M.: Modeling and analysis of friction including rolling effects in multibody dynamics: a review. Multibody Syst. Dyn. **45**(2), 223–244 (2019)
39. Márton, L., Fodor, S., Sepehri, N.: A practical method for friction identification in hydraulic actuators. Mechatronics **21**(1), 350–356 (2011)
40. Naya, M.A., Cuadrado, J., Dopico, D., Lugris, U.: An efficient unified method for the combined simulation of multibody and hydraulic dynamics: comparison with simplified and co-integration approaches. Arch. Mech. Eng. **58**(2), 223–243 (2011)
41. Owen, W.S., Croft, E.A.: The reduction of stick-slip friction in hydraulic actuators. IEEE/ASME Trans. Mechatron. **8**(3), 362–371 (2003)
42. Pan, Q., Zeng, Y., Li, Y., Jiang, X., Huang, M.: Experimental investigation of friction behaviors for double-acting hydraulic actuators with different reciprocating seals. Tribol. Int. **153**, 106506 (2021)
43. Park, C.G., Yoo, S., Ahn, H., Kim, J., Shin, D.: A coupled hydraulic and mechanical system simulation for hydraulic excavators. Proc. Inst. Mech. Eng. Part I J. Syst. Control Eng. **234**(4), 527–549 (2020)
44. Peiret, A., González, F., Kövecses, J., Teichmann, M.: Co-simulation of multibody systems with contact using reduced interface models. J. Comput. Nonlinear Dyn. **15**(4), 041001 (2020)
45. Pennestrì, E., Rossi, V., Salvini, P., Valentini, P.P.: Review and comparison of dry friction force models. Nonlinear Dyn. **83**(4), 1785–1801 (2016)
46. Potosakis, N., Paraskevopoulos, E., Natsiavas, S.: Application of an augmented Lagrangian approach to multibody systems with equality motion constraints. Nonlinear Dyn. **99**(1), 753–776 (2020)
47. Rahikainen, J., González, F., Naya, M.Á., Sopanen, J., Mikkola, A.: On the cosimulation of multibody systems and hydraulic dynamics. Multibody Syst. Dyn. **50**, 143–167 (2020)
48. Rahikainen, J., Kiani, M., Sopanen, J., Jalali, P., Mikkola, A.: Computationally efficient approach for simulation of multibody and hydraulic dynamics. Mech. Mach. Theory **130**, 435–446 (2018)
49. Rahikainen, J., Mikkola, A., Sopanen, J., Gerstmayr, J.: Combined semi-recursive formulation and lumped fluid method for monolithic simulation of multibody and hydraulic dynamics. Multibody Syst. Dyn. **44**(3), 293–311 (2018)
50. Rodríguez, A.J., Pastorino, R., Carro-Lagoa, Á., Janssens, K., Naya, M.A.: Hardware acceleration of multibody simulations for real-time embedded applications. Multibody Syst. Dyn. (2020)
51. Swevers, J., Al-Bender, F., Ganseman, C.G., Projogo, T.: An integrated friction model structure with improved presliding behavior for accurate friction compensation. IEEE Trans. Autom. Control **45**(4), 675–686 (2000)
52. Tran, X.B., Hafizah, N., Yanada, H.: Modeling of dynamic friction behaviors of hydraulic cylinders. Mechatronics **22**(1), 65–75 (2012)
53. Tran, X.B., Khaing, W.H., Endo, H., Yanada, H.: Effect of friction model on simulation of hydraulic actuator. Proc. Inst. Mech. Eng. Part I J. Syst. Control Eng. **228**(9), 690–698 (2014)
54. Tran, X.B., Nguyen, V.L., Tran, K.D.: Effects of friction models on simulation of pneumatic cylinder. Mech. Sci. **10**(2), 517–528 (2019)
55. Uhlar, S., Betsch, P.: On the derivation of energy consistent time stepping schemes for friction afflicted multibody systems. Comput. Struct. **88**(11–12), 737–754 (2010)
56. Watton, J.: Fluid Power Systems: Modeling, Simulation, Analog, and Microcomputer Control. Prentice Hall, Hoboken (1989)
57. Yanada, H., Sekikawa, Y.: Modeling of dynamic behaviors of friction. Mechatronics **18**(7), 330–339 (2008)
58. Ylinen, A., Marjamäki, H., Mäkinen, J.: A hydraulic cylinder model for multibody simulations. Comput. Struct. **138**, 62–72 (2014)

Publication III

Jaiswal, S., Sanjurjo, E., Cuadrado, J., Sopanen, J., and Mikkola, A.
State estimator based on an indirect Kalman filter for a hydraulically actuated multibody system

Reprinted with permission from
Submitted in *Multibody System Dynamics* on December 10, 2020

Publication IV

Jaiswal, S., Åman, R., Sopanen, J., and Mikkola, A.
Real-time multibody model-based heads-up display unit of a tractor

Reprinted with permission from
IEEE Access
Vol. 9, pp. 57645–57657, 2021

IEEE Access
Multidisciplinary | Rapid Review | Open Access Journal

Received March 15, 2021, accepted April 6, 2021, date of publication April 12, 2021, date of current version April 20, 2021.

Digital Object Identifier 10.1109/ACCESS.2021.3072452

Real-Time Multibody Model-Based Heads-Up Display Unit of a Tractor

SURAJ JAISWAL[1], RAFAEL ÅMAN[2], JUSSI SOPANEN[1], (Member, IEEE), AND AKI MIKKOLA[1]

[1]Department of Mechanical Engineering, Lappeenranta University of Technology, 53850 Lappeenranta, Finland
[2]Valtra Inc., 44200 Suolahti, Finland

Corresponding author: Suraj Jaiswal (suraj.jaiswal@lut.fi)

This work was supported in part by the Business Finland (Project: Service Business from Physics Based Digital Twins—DigiBuzz), and in part by the Academy of Finland under Grant 316106.

ABSTRACT The concept of heads-up display can be used to provide augmented information onto the windshield of a tractor. The objective of this paper is to introduce a detailed real-time multibody model that is used in the design of a novel heads-up display unit of a tractor. To this end, a tractor is described using a multibody dynamics approach. A heads-up display unit is designed using a series of tasks that are associated with sets of logical conditions and instructions. These conditions and instructions, in turn, determine/design the analog and digital gauges. The gauges are linked with the virtual sensors installed at a number of locations on the tractor. In this study, the heads-up display unit includes elements, such as tachometer, speedometer, roll inclinometer, gear indicator, fuel gauge, and bucket height, tilt, and weight indicators. The effectiveness of the heads-up display unit is determined based on a goal of moving a certain amount of sand from one place to another. The results demonstrate the utility of the heads-up display unit.

INDEX TERMS Multibody dynamics, heads-up display, real-time simulation, tractor model, physics-based model.

I. INTRODUCTION

In the last decade, driving aids such as heads-up displays (HUDs) have gained considerable popularity from vehicle manufacturers [1]–[5]. HUDs present augmented machine data usually on the windshield such that drivers do not have to look away from their conventional viewpoints. In practice, a rapid prototype-based development of such HUDs may be expensive or cumbersome [6]. However, a HUD unit can be modeled from a detailed physics-based model of a vehicle using virtual sensing, that is, by incorporating detailed vehicle dynamics. It can allow vehicle manufacturers to test HUDs for their vehicles using computer simulations even before a physical prototype implementation. Additionally, it can be utilized in user training, research, and other product processes.

A. RELATED WORK–LITERATURE REVIEW

It is well established in the literature that classical dashboard displays or head-down displays (HDDs) cause distractions [7] that can be alleviated by HUDs [8]–[10]. They serve a better alternative to provide machine data and increase road safety [11], [12]. It is demonstrated in [10], [13] that drivers can have faster focal re-accommodation time with HUDs and can maintain a consistent speed control. Moreover, HUDs can help novice drivers to get familiarized with control systems [10] and to enhance the surrounding awareness of a vehicle en-route [14]. The studies on HUDs in general are mainly focused towards the field of cognitive science such as human behavior or user experience [15]. On the contrary, the scope of this study is limited to the development of tool sets to model HUD units.

The literature offers several studies regarding HUD modeling and their evaluation on driving simulators. For example, a HUD-based warning system was proposed in [16] to evaluate drivers' rear-end crash avoidance behavior when a leading vehicle makes an emergency stop under foggy conditions. Similarly, HUD-based speed assistance was developed in [17] to provide speed-guided messages through the entire course of curve driving. The HUDs in [16], [17] were tested on the National Advanced Driving Simulator (NADS MiniSim) [18]. Even though the NADS MiniSim is based on multibody dynamics (usage of which leads to realistic simulations), however, the studies in [16] and [17] overlooked

The associate editor coordinating the review of this manuscript and approving it for publication was Lei Wei.

the connection between HUD modeling and detailed vehicle models. Furthermore, a full-windshield HUD model was proposed in [14] to improve drivers' spatial awareness and response time during navigation under low visibility. This HUD model was extended in [19] by incorporating a gesture recognition system [20] to improve human responses during a potential collision and slow down the plethora of incoming information. The respective multimodal and augmented reality (AR) versions of this HUD model [19] was developed in [21] and [22] to alleviate the cognitive load caused by the existing attention seeking HDDs. The HUD models in [14], [19], [21], [22] were based on a minimalist visual display of real objects, however, these studies ignored the description of vehicle models used in the respective simulators.

Many studies in the literature are focused on examining various HUD models in real vehicles. For example, HUD-based advisory speed assistance was developed in [23] using a learning-based approach to compensate drivers generated speed tracking errors in real-time. Testing was carried out in the Unity game engine and a real vehicle, where simulation results deviated from reality. Similarly, navigation-based AR-HUDs were studied in [24], [25] to examine drivers' performance in simulation [25] and real-world environments. In [24], simulations were carried out in the Unreal Engine and on-road testing was carried out on a HUD-equipped real vehicle, whereas AR-HUD interfaces were developed in Unity. Simulation results even here deviated from real-world tests. Furthermore, fixed and animated designs of AR-HUDs were examined in [26] to evaluate drivers' performance and visual behavior in goal-directed and stimulus-driven tasks. AR graphics were rendered in C++ and QT5 environment and testing was performed on a real vehicle that was equipped with a projection-based volumetric HUD. In all the studies above [23], [24], [26], either tests were performed with real vehicles or simulation outcomes deviated from reality, and the lack of detailed physics-based vehicle dynamics in simulation models can be a possible cause. Studies are even directed towards eliminating the display error of HUD models, such as in [27] and [28]. However, these studies [27], [28] used either a stationary vehicle or utilized real-world driving images and ignored vehicle dynamics.

Multibody dynamics can describe detailed physics-based models of complex systems such like a tractor [29], [30]. This approach allows one to describe a large number of bodies, hydraulic actuators, contact models, and tire models. In the literature, a number of multibody dynamics approaches have been used to describe various heavy-duty vehicles. For example, an excavator was described in [31], [32] and [33], a quadtrac in [34], a tree harvester in [35], and a tractor in [36]. Solution of multibody equations of motion can be synchronized to real-time as shown in [32], [35] and [36]. Moreover, virtual sensors can be built using a multibody model such as in [37], [38].

Despite the previous research efforts as explained above, the limitations of the exiting literature are in two manifolds. First, even though the studies on HUDs provide detailed explanations about HUD modeling, however, its connection with the detailed physics-based model of a vehicle has been overlooked. Second, even though the literature on multibody dynamics can accurately describe real-time capable vehicle dynamics, however, the use of such vehicle models in designing HUD has been neglected. Therefore, this study claims to cover this research gap by introducing HUD modeling based on a detailed physics-based vehicle model.

B. OBJECTIVE AND RESEARCH QUESTIONS

The objective of this paper is to introduce a detailed real-time multibody model-based novel heads-up display unit of a tractor. To this end, a tractor is described using a semi-recursive multibody formulation [39] and the hydraulic actuators are described using the lumped fluid theory [40]. In this study, the contact is described using the object-oriented bounding box and penalty methods [41], [42], and the tires are described using the lumped LuGre model [43], [44]. A heads-up display unit is designed onto the windshield of the tractor using a series of tasks that are associated with sets of logical conditions and instructions. The conditions and instructions determine/design the analog and digital gauges, which, in turn, are linked with the virtual sensors installed at a number of locations on the tractor. The advantage of using a multibody dynamics approach is that virtual sensors can be described using the multibody model of the tractor. This enables a flexible approach to design a HUD unit and collect user experience on it before its implementation into a real tractor. In this study, the HUD unit includes elements that are possible to implement into a physical tractor, such as tachometer, speedometer, roll inclinometer, gear indicator, fuel gauge, and bucket height, tilt, and weight indicators. Examples of moving a certain amount of sand from one place to another are demonstrated. Therefore, this study aims to solve the following research questions: (a) How can a HUD model be build using a detailed physics-based model of a vehicle, such as a tractor?; (b) How can such a HUD unit assist drivers to perform a certain work?; and (c) How robust and modular is this HUD modeling approach to contribute to the state-of-the-art?

This paper contains five sections. The structure for the rest of the paper is organized such that Sect. II describes the multibody modeling method. Section III describes the modeling procedure for a heads-up display unit based on a detailed real-time multibody model of a tractor. Section IV provides simulation results and discussion of various tests conducted. A conclusion is provided in Sect. V.

II. MULTIBODY DYNAMICS

The equations of motion for a constrained mechanical system can be described using a multibody dynamics approach. This approach allows one to describe systems of other physical nature, such as hydraulic actuators. In this study, the multibody system is described using a semi-recursive formulation based on a velocity transformation [39] because it allows one to describe vehicles for real-time applications [32], [36].

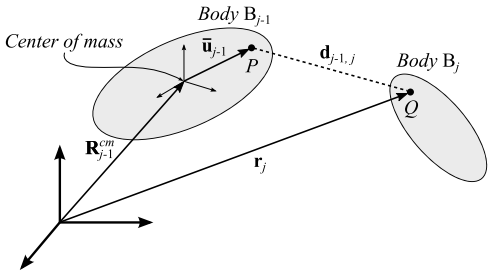

FIGURE 1. Illustration of a multibody system.

The hydraulic actuators are described using the lumped fluid theory [40]. In this study, the contacts are described using the object-oriented bounding box method [41] and penalty method [42]. Furthermore, the tires are described using the lumped LuGre tire model [43], [44].

A. SEMI-RECURSIVE MULTIBODY FORMULATION

In the semi-recursive formulation, the equations of motion are expressed in the relative joint coordinates by using a velocity transformation matrix [39]. Consider an open-loop system with N_b bodies, where the adjacent rigid bodies B_{j-1} and B_j are connected by a joint as shown in Fig. 1. Points P and Q are, respectively, the locations of joints on bodies B_{j-1} and B_j, and $\mathbf{d}_{j-1,j}$ is the relative joint displacement vector between them.

The position, $\mathbf{r}_j$, and the velocity, $\dot{\mathbf{r}}_j$, of point Q with respect to the inertial reference frame can be, respectively, written as

$$\mathbf{r}_j = \mathbf{R}_{j-1}^{cm} + \mathbf{A}_{j-1}\bar{\mathbf{u}}_{j-1} + \mathbf{d}_{j-1,j}, \tag{1}$$

$$\dot{\mathbf{r}}_j = \dot{\mathbf{R}}_{j-1}^{cm} + \tilde{\boldsymbol{\omega}}_{j-1}\mathbf{A}_{j-1}\bar{\mathbf{u}}_{j-1} + \dot{\mathbf{d}}_{j-1,j}, \tag{2}$$

where $\mathbf{R}_{j-1}^{cm}$ is the position of the origin of the body reference frame of body B_{j-1} with respect to the inertial reference frame and $\dot{\mathbf{R}}_{j-1}^{cm}$ is its time derivative, $\mathbf{A}_{j-1}$ and $\tilde{\boldsymbol{\omega}}_{j-1}$ are, respectively, the rotation matrix and skew-symmetric matrix of the angular velocity $\boldsymbol{\omega}_{j-1}$ of body B_{j-1}, $\bar{\mathbf{u}}_{j-1}$ is the position vector of point P in the body reference frame of body B_{j-1}, and $\dot{\mathbf{d}}_{j-1,j}$ is the time derivative of $\mathbf{d}_{j-1,j}$. The body reference frames are located at the center of mass of the bodies. The rotation matrix, $\mathbf{A}_j$, and angular velocity, $\boldsymbol{\omega}_j$, of body B_j can be, respectively, written as

$$\mathbf{A}_j = \mathbf{A}_{j-1}\mathbf{A}_{j-1,j}, \tag{3}$$

$$\boldsymbol{\omega}_j = \boldsymbol{\omega}_{j-1} + \boldsymbol{\omega}_{j-1,j}, \tag{4}$$

where $\mathbf{A}_{j-1,j}$ and $\boldsymbol{\omega}_{j-1,j}$ are, respectively, the relative rotation matrix and relative angular velocity between the two bodies B_{j-1} and B_j. In this study, Euler parameters are used to describe a body's rotation.

By using the principle of virtual work, the virtual power of the forces acting on a multibody system can be expressed as [39]

$$\delta\dot{\mathbf{q}}^{\mathrm{T}}\left(\mathbf{M}\ddot{\mathbf{q}} + \mathbf{C} - \mathbf{Q}\right) = \mathbf{0}, \tag{5}$$

where $\delta\dot{\mathbf{q}}$ is the virtual velocity vector, $\mathbf{M}$ is the mass matrix of the system, $\ddot{\mathbf{q}}$ is the absolute acceleration vector, $\mathbf{C}$ is the quadratic velocity vector, and $\mathbf{Q}$ is the vector of external forces and torques acting on the system. Note that $\ddot{\mathbf{q}} = [\ddot{\mathbf{q}}_1^{\mathrm{T}}\ddot{\mathbf{q}}_2^{\mathrm{T}}\ldots\ddot{\mathbf{q}}_{N_b}^{\mathrm{T}}]^{\mathrm{T}}$, $\mathbf{C} = [\mathbf{C}_1^{\mathrm{T}}\mathbf{C}_2^{\mathrm{T}}\ldots\mathbf{C}_{N_b}^{\mathrm{T}}]^{\mathrm{T}}$, and $\mathbf{Q} = [\mathbf{Q}_1^{\mathrm{T}}\mathbf{Q}_2^{\mathrm{T}}\ldots\mathbf{Q}_{N_b}^{\mathrm{T}}]^{\mathrm{T}}$. Furthermore, the virtual velocities $\delta\dot{\mathbf{q}}$ are assumed to be kinematically admissible, implying that they satisfy the equations of kinematic constraints. A velocity transformation matrix, $\mathbf{R}$, is introduced to transform the absolute coordinates into the relative joint coordinates as

$$\dot{\mathbf{q}} = \mathbf{R}\dot{\mathbf{z}}, \tag{6}$$

$$\ddot{\mathbf{q}} = \mathbf{R}\ddot{\mathbf{z}} + \dot{\mathbf{R}}\dot{\mathbf{z}}, \tag{7}$$

where $\dot{\mathbf{q}}$ is the absolute velocity vector, $\dot{\mathbf{z}}$ is the relative joint velocity vector, $\ddot{\mathbf{z}}$ is the relative joint acceleration vector, and $\dot{\mathbf{R}}$ is the time derivative of $\mathbf{R}$. For scleronomic constraints, the kinematically admissible virtual velocities can be written as

$$\delta\dot{\mathbf{q}} = \mathbf{R}\delta\dot{\mathbf{z}}. \tag{8}$$

By substituting Eqs. (7) and (8) into Eq. (5), the equations of motion for an open-loop system can be written as

$$\mathbf{R}^{\mathrm{T}}\mathbf{M}\mathbf{R}\ddot{\mathbf{z}} = \mathbf{R}^{\mathrm{T}}(\mathbf{Q} - \mathbf{C}) - \mathbf{R}^{\mathrm{T}}\mathbf{M}\dot{\mathbf{R}}\dot{\mathbf{z}}. \tag{9}$$

Equation (9) presents N_f numbers of ordinary differential equations of motion that are expressed in relative joint coordinates. The computational efficiency of this formulation is dependent on the computation of the velocity transformation matrix, $\mathbf{R}$, which in this study is obtained using an element by element technique as in [30].

For a closed-loop system, a cut-joint is introduced in each kinematic loop to make it an open-loop system, as shown above. The loop-closure constraint equations are incorporated in the equations of motion by using the penalty method [45] as explained in [39].

B. HYDRAULIC ACTUATORS

In this study, the lumped fluid theory is used to compute the pressures in a hydraulic circuit [40]. In this approach, a hydraulic circuit is divided into separate volumes where the hydraulic pressures are assumed to be equally distributed. Therefore, the effects of acoustic waves are assumed insignificant in this study. The hydraulic pressure, p_s, within a hydraulic control volume, V_s, can be computed as

$$\dot{p}_s = \frac{B_{e_s}}{V_s}\sum_{k=1}^{n_f} Q_{sk}, \tag{10}$$

where B_{e_s} is the effective bulk modulus, Q_{sk} is the sum of volume flow rates in and out of a volume V_s, and n_f is the total number of such volume flow rates.

In this study, the directional control valves are described by using a semi-empirical modeling method [46]. The volume

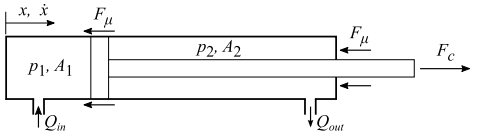

FIGURE 2. A hydraulic actuator.

flow rate, Q, through a directional control valve can be written as

$$Q = C_v U \operatorname{sgn}(\Delta p) \sqrt{|\Delta p|}, \tag{11}$$

where Δp is the pressure difference across the directional control valve, C_v is the semi-empirical flow rate constant of the valve that can be obtained from the manufacturer catalogue, and U is the relative spool position that can be described as

$$\dot{U} = \frac{U_{ref} - U}{\tau}, \tag{12}$$

where τ is the time constant and U_{ref} is the reference voltage signal for the reference spool position.

Furthermore, the force, F_c, produced by a hydraulic actuator, as shown in Fig. 2, can be written as [47]

$$F_c = p_1 A_1 - p_2 A_2 - F_\mu, \tag{13}$$

where A_1 and A_2 are, respectively, the areas of the piston and piston-rod sides of the actuator, p_1 and p_2 are, respectively, the chamber pressures on the piston and piston-rod sides, and F_μ is the total seal friction [48].

C. CONTACT MODELING

The contact model in this study is described in two steps: collision detection and collision response [49]. Collision detection is determined using the object-oriented bounding box method [41], which utilizes minimum rectangular solids as shown in Fig. 3 to circumscribe the bodies along their axes directions. In Fig. 3, the condition that two boxes E and F do not overlap can be written as

$$\mathbf{T} \cdot \mathbf{L}_i > d_{Ei} + d_{Fi}, \tag{14}$$

where

$$d_{Ei} = e_1 \mathbf{E}_1 \cdot \mathbf{L}_i + e_2 \mathbf{E}_2 \cdot \mathbf{L}_i, \tag{15}$$
$$d_{Fi} = f_1 \mathbf{F}_1 \cdot \mathbf{L}_i + f_2 \mathbf{F}_2 \cdot \mathbf{L}_i, \tag{16}$$

where $\mathbf{T}$ is the position vector between the center of the boxes, $\mathbf{L}_i$ is a separating axis in a normalized direction, e_1 and e_2, and f_1 and f_2 are, respectively, the dimensions of boxes E and F, and $\mathbf{E}_1$ and $\mathbf{E}_2$, and $\mathbf{F}_1$ and $\mathbf{F}_2$ are, respectively, the normalized axes of boxes E and F. In three dimensions, the condition shown in Eq. (14) such that the boxes do not overlap needs to hold true for all the 15 potential separating axes, implying that $i = 1 : 15$.

The collision response is determined using the penalty method [42]. Assuming a single collision point model,

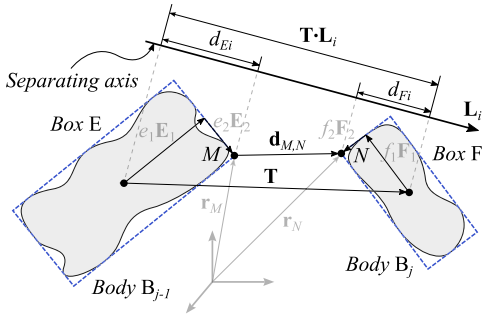

FIGURE 3. Illustration of contact modeling.

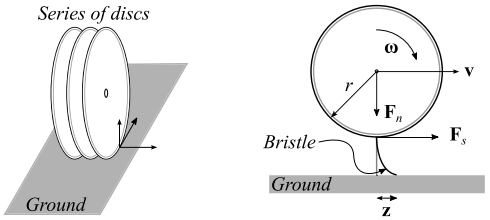

FIGURE 4. Illustration of the lumped LuGre tire model.

the normal contact force, $\mathbf{F}_n$, at the collision point can be written as

$$\mathbf{F}_n = -\left(K \left|\mathbf{d}_{M,N}\right| + C \left|\dot{\mathbf{d}}_{M,N}\right|\right) \mathbf{n}, \tag{17}$$

where

$$\left|\mathbf{d}_{M,N}\right| = (\mathbf{r}_N - \mathbf{r}_M) \cdot \mathbf{n}, \tag{18}$$
$$\left|\dot{\mathbf{d}}_{M,N}\right| = (\dot{\mathbf{r}}_N - \dot{\mathbf{r}}_M) \cdot \mathbf{n}, \tag{19}$$

where K is the coefficient of elasticity, C is the damping factor, $\mathbf{r}_M$ and $\mathbf{r}_N$, and $\dot{\mathbf{r}}_M$ and $\dot{\mathbf{r}}_N$ are, respectively, the positions and velocities of collision points M and N in the inertial reference frame, and $\mathbf{n}$ is the vector along the collision normal such that $\mathbf{n} = \frac{(\mathbf{r}_N - \mathbf{r}_M)}{|(\mathbf{r}_N - \mathbf{r}_M)|}$.

D. TIRE MODELING

In this study, the lumped LuGre tire model [43], [44] is used to model a tire as shown in Fig. 4. Furthermore, a tire is described as a series of discs as shown in Fig. 4 (on the left), where the typical forces involved are the longitudinal, vertical, and lateral forces. The lumped LuGre tire model is an extension of the Dahl model [50] and includes the Stribeck and stiction effects. Based on the lumped LuGre tire model, the friction force, $\mathbf{F}_s$, at the contact between a tire and a ground can be written as [43]

$$\mathbf{F}_s = (\sigma_0 \mathbf{z} + \sigma_1 \dot{\mathbf{z}} + \sigma_2 \mathbf{v}_r)\, \mathbf{F}_n, \tag{20}$$

where

$$\dot{\mathbf{z}} = \mathbf{v}_r - \frac{\sigma_0 \mathbf{v}_r}{g(\mathbf{v}_r)} \mathbf{z}, \tag{21}$$

$$g(\mathbf{v}_r) = \mu_c + (\mu_s - \mu_c)\, e^{-\left(\frac{|\mathbf{v}_r|}{v_s}\right)^{\frac{1}{2}}}, \tag{22}$$

where $\mathbf{z}$ is the average bristle deflection (an internal state variable), σ_0 and σ_1 are, respectively, the longitudinal lumped stiffness and damping of the rubber, σ_2 is the coefficient of viscous friction, $\mathbf{v}_r$ is the relative tangential velocity between the tire and ground, $\mathbf{F}_n$ is the normal force, μ_c and μ_s are, respectively, the normalized Coulomb and static frictions such that $\mu_c \leq \mu_s \in [0, 1]$, and $\mathbf{v}_s$ is the Stribeck velocity. Note that $|\mathbf{v}_r| = r\,|\boldsymbol{\omega}| - |\mathbf{v}|$, where r, $\boldsymbol{\omega}$, and $\mathbf{v}$ are respectively, the radius, angular velocity, and linear velocity of the tire.

III. MULTIBODY MODEL-BASED HEADS-UP DISPLAY UNIT

Using the multibody dynamics explained in Sect. II, a detailed physics-based tractor can be modeled as in this study. It should be noted that the focus of this study is to introduce a HUD unit of a tractor, which is based on a real-time multibody model. Accordingly, a semi-recursive multibody formulation that is based on a velocity transformation [39] is utilized to demonstrate a wide capability of real-time multibody models. However, the scope of this study is not limited to a single multibody formulation only. Other multibody formulations that provide real-time capabilities are also applicable, such as index-3 augmented Lagrangian semi-recursive formulation [51], [52] and double-step semi-recursive formulation [53]–[55]. It is also important to note that the used multibody formulation can be applied to wide variety of HUD studies.

A. MULTIBODY MODEL OF A TRACTOR

As a case example, a tractor is modeled using the semi-recursive multibody formulation explained in Sect. II-A. The bodies and joints used in the tractor model are shown in Fig. 5a. Modeling the mechanical system of the tractor can be divided into two parts: modeling the tractor vehicle and modeling the front-loader. The components of the tractor vehicle consist of the cabin, frame, front axle, tie rod, pivot left, and pivot right. The tie rod is used to model the steering mechanism. The components of the front-loader consist of links 1 to 6 and the bucket. The lifting of link-3 and the tilting of link-6 is controlled using hydraulic actuators as explained in Sect. II-B. The power transmission system used in the modeling of the tractor is shown in Fig. 5b.

Overall, the tractor model consists of 13 bodies and 15 joints, and a total of 28 joint coordinates. The structure consists of both open and close kinematic loops, therefore, for the closed-loop links, three cut-joints as shown in Fig. 5 and 15 loop-closure constraints are introduced. The model has nine degrees of freedom (DOFs), where six DOFs correspond to the translational and rotational axes of the tractor, one DOF corresponds to the steering mechanism, and two DOFs correspond to the lifting and tilting mechanism of the front-loader.

Furthermore, four hydraulic actuators are modeled using the lumped fluid theory, explained in Sect. II-B, to lift and tilt the front loader as shown in Fig. 5. Here, the internal dynamics of the hydraulic system are computed, and the resultant forces are combined with the force vector of the multibody equations of motion as in [56]. It should be noted that leakage is neglected in the hydraulic system model. In addition, a deformable ground (sand field) is modeled as in [36], which allows the bucket to fill physically and visually accurate sand particles. The interaction between the force points, defined on the collision geometry of the bucket, and sand field generates sand particles. Tires are modeled using the lumped LuGre tire model as explained in Sect. II-D.

B. HEADS-UP DISPLAY UNIT OF A TRACTOR

Operating a tractor can be cumbersome because its human–machine interface is not simple and requires years of on-the-job training and education. Other than driving, the primary aim in a tractor is to interact with its environment, and the present human–machine interface offers inadequate information about its surroundings and poor work visibility. HUDs can alleviate this problem by presenting more visual clues about the sensor systems of the vehicle in the field-of-view of drivers, thus, providing a quantitative picture of the surroundings [57]. However, the positioning and differences in the perception of HUD images can cause undue mental and physical workloads that can reduce the productivity of drivers through impaired concentration and fatigue [58]. Therefore, care should be taken in general to follow adequate image displaying method [58] that can reduce the cognitive load of drivers, increase their efficiency, and decrease energy costs. Furthermore, presenting machine data on a small area of a windshield impose limitations on the amount of machine information being displayed [59]. It can cause information overload, visual clutter, cognitive capture, and distorted perception of surrounding objects, which can adversely affect the driving performance [60]–[62]. Therefore, understanding drivers' information need can be crucial [5], however, it is not covered within the scope of this study.

A tractor with a front-loader can interact with its environment in several ways [63]. For example, it can load and transfer materials from one place to another, or it can collide with the objects of the environment. The loading and transferring of material are a common task for a tractor, and in such a situation, the driver has a limited information about the bucket position, bucket angle, and weight in the bucket. Therefore, a HUD unit with an effective symbology design can provide these data to improve drivers' performance and reduce their workload. Accordingly, the scope of this work covers both analog and digital gauges in the HUD unit. It should be noted that care is taken to model the design, complexity, image quality, and perceptibility of the HUD unit in an acceptable manner, keeping in mind the cognitive and sensory abilities of drivers [15].

In this study, a simple goal is demonstrated where a certain amount of sand needs to be picked from a sand pile and then dumped onto another place on the ground. In the process, a HUD unit is available to assist the driver,

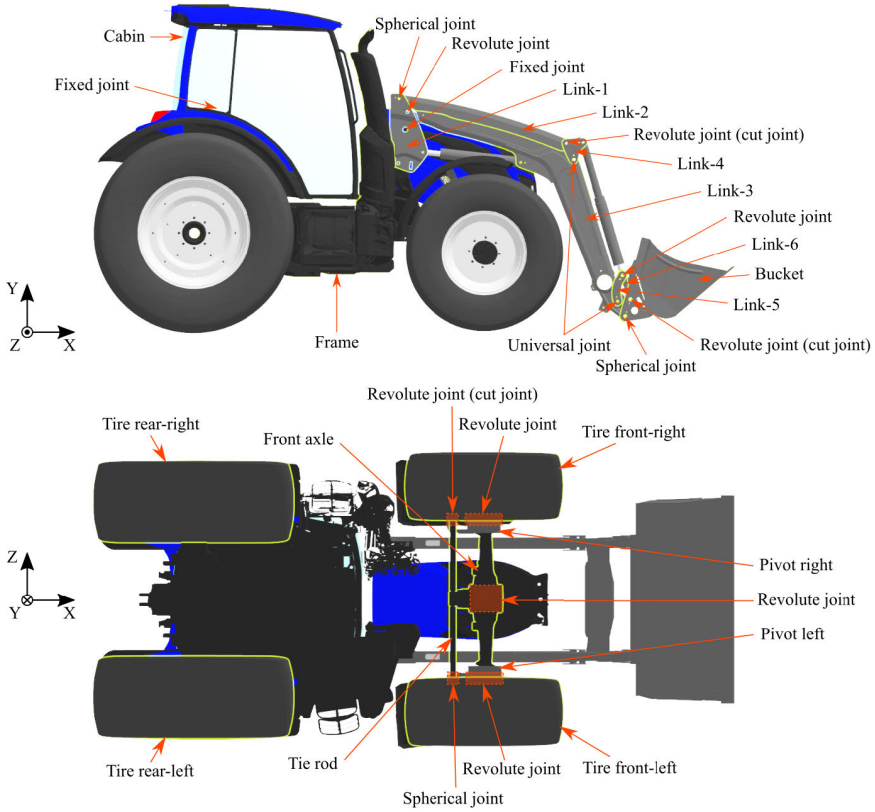

(a) Bodies and joints in the multibody model of the tractor.

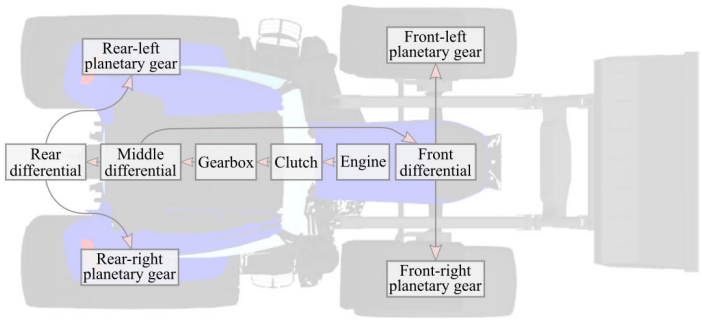

(b) Power transmission system of the tractor.

FIGURE 5. Tractor model used in this study.

for example, in picking an appropriate amount of sand. In general, the designs on a HUD are dependent on a number of factors, especially, from the field of cognitive science, such as symbology, clutter, and viewing comfort issues [60], [65].

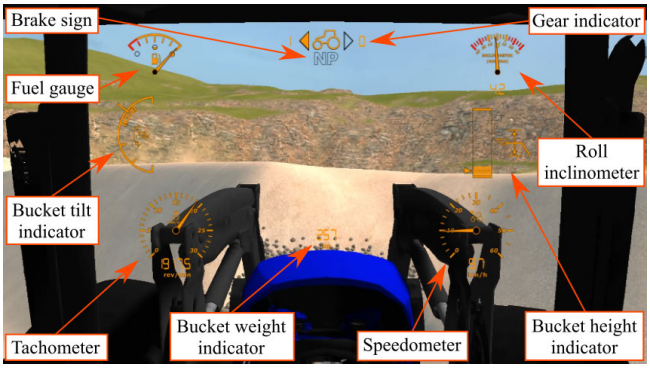

FIGURE 6. Heads-up display unit installed onto the windshield of the tractor [64].

TABLE 1. The elements of the HUD unit used in this study.

Element	Analog gauge	Digital gauge
Tachometer	✓	✓
Speedometer	✓	✓
Roll inclinometer	✓	✓
Gear indicator	✓	✓
Fuel gauge	✓	-
Bucket height indicator	✓	-
Bucket tilt indicator	✓	-
Bucket weight indicator	-	✓

However, this work is only focusing on technical aspects. Here, only one HUD unit is presented onto the windshield to demonstrate the utilization of virtual machine data, which is based on detailed physics-based models, and to assist in task completion. The elements of the HUD unit used in this study are shown in Table 1.

The design of a HUD unit is defined as a scenario, which consists of a series of tasks. Each task is associated with a set of conditions and instructions. The conditions are defined based on value boundaries and the instructions define the gauges and HUD images. These value conditions determine the display of analog and/or digital gauges. The gauges, in turn, describe the gauge type, where for analog gauges, it defines the size and position of the gauge on the windshield of the tractor; and for digital gauges, it defines the size, position, and color of the data on the windshield. Note that the gauges are linked with the data sources of the tractor model, which is defining all the required parameters. Thus, the HUD unit can present the virtual machine data during a real-time simulation. Furthermore, the value conditions can also determine the display of other HUD images, such as an out-of-fuel message, a rollover message, and gear and brake signs.

The data sources of the tractor model, which are linked with the gauges of the HUD unit, are described using virtual sensors installed at a number of locations on the tractor. Note that the virtual sensors are selected in such a way that similar physical sensors could be installed on the real tractor. The tachometer uses the engine speed and the speedometer utilizes the angular velocity and radius of the tires. The data source of the roll inclinometer is described by installing an inclinometer on the cabin of the tractor. An inclinometer is a directional accelerometer that measures the angle of the cabin with respect to the gravity force. The gear indicator utilizes the gear number of the gearbox. The fuel indicator is defined by using the fuel consumption parameter of the engine. The data source associated to the bucket height indicator is described by installing a distance sensor between a point on the front axle and a point on the bucket. The bucket tilt indicator uses data from a rotary encoder installed on the bucket. The data source of the bucket weight indicator is defined by installing a mass sensor near the teeth and inside the bucket. The mass is calculated based on the number of sand particles crossing the mass sensor at the specific location.

It should be noted that the HUD unit offers a gamified experience of the tractor model as shown in Fig. 6. Here, game logics are used to make the HUD unit more interactive during a training. For example, to achieve the goal of moving a certain amount of sand from one place to another, a number of challenges are introduced, such as limited fuel and a limited rolling angle. The HUD unit indicates the critical conditions of the fuel and roll angle by highlighting them in red in the respective analog gauges. If the tractor is out-of-fuel or a rollover has occurred, then the HUD unit shows a breakdown message and the simulation is forced to terminate. Note that a real-time simulator with a two DOFs motion platform is used to provide a realistic experience of the tractor maneuver.

As this study is concerned with the development of tool sets to model HUD units, therefore, only a quantitative evaluation procedure has been employed in this study. Simulation tests are performed by only an inexperienced tractor driver (first author). Before the simulation tests, the participant is given

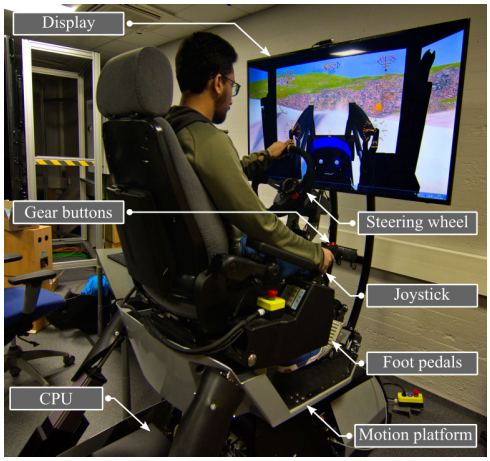

FIGURE 7. Tractor simulator installed with the heads-up display unit.

an opportunity to use the simulator to familiarize himself about the simulation environment and simulator controls. As mentioned above, the goal is to pick a certain amount of sand from a sand pile and dumped onto another place on the ground. The quantitative evaluation is carried out by measuring the amount of sand moved and the movement of the front-loader, such as lifting and tilting of the bucket. The respective gauges are made available to the driver through the HUD unit, where the recommended values of the height and tilt angle of the bucket are marked to collect the maximum amount of sand. These values are provided based on a predetermined evaluation of the sand pile and bucket geometry.

A total of 10 simulations are run to test the utility of the HUD unit and achieve the goal of moving sand, where the driver moved sand ranging from 100 kg to 600 kg, approximately. However, due to a similarity in the results, data for only four simulation tests are presented such that the amount of sand collected in the bucket are approximately 100 kg, 200 kg, 450 kg, and 600 kg. Please note that for conciseness, this paper is focused on demonstrating the utility of the HUD unit that is built using the multibody model of a tractor.

IV. TESTS AND RESULTS

This section presents the simulation results of the real-time multibody model-based HUD unit of a tractor. To test the HUD unit, the simulator setup used is shown in Fig. 7. The used tractor simulator is installed with two degrees of freedom hydraulically driven motion platform to provide a realistic experience of the tractor maneuver. Inputs provided by the driver through the steering wheel, joystick (bucket lifting and tilting), gear buttons (gear index), and foot pedals (accelerate, brake, and clutch) are fed to the central processing unit (CPU). The CPU, in turn, provides output for the display and motion platform. Additionally, the sounds of the engine and movement of the bucket are also provided as an output for a realistic experience. It should be noted that the motion signal provided to the motion platform depends on the undulating terrain of the model and the interaction of the tractor with its surroundings.

A HUD unit incorporated simulator platform can facilitate a training process. Out of a number of simulations performed, data for only four tests are shown in this section for demonstration purpose. The amount of sand collected, and the real-time ability of the system are demonstrated. Additionally, critical conditions such as limited fuel and a limited rolling angle are simulated.

A. PERFORMANCE OF THE HUD UNIT

To achieve the goal of moving a certain amount of sand from one place to another, the tractor model in all four simulation tests follow a three-dimensional maneuver. Figure 8 shows the simulation frames of the HUD unit at different instants of time for the fourth test. By following the HUD unit at 8.50 s, the height and tilt angle of the bucket are adjusted to the recommended values in the bucket height and tilt indicator gauges. The recommended values are marked on the analog gauges to collect a maximum amount of sand in the bucket. The values are predetermined based on the simulation environment, that is, the sand pile. At 10.60 s, the digging operation is performed on a pile of sand that is on the right side in the first and second simulation frames of Fig. 8. After the digging operation at 12.41 s, the bucket is lifted upward and tilted inward as visible in the simulation frame at 14.45 s. During reversing at 17.42 s, the tilt angle of the bucket is slightly adjusted, which is visible in the simulation frame at 26.08 s. At 39.29 s, the sand particles are dumped onto another place of the ground. The tractor maneuver for the fourth test is shown in Fig. 9.

The work cycle shown above demonstrates the utility of the HUD unit in performing a certain task. It provides data such as the weight, height, and tilt of the bucket, thus, it illustrates a quantitative picture of the surroundings of the vehicle. Moreover, the multibody modeling approach provides a physics-based description of the tractor model. Therefore, this multibody-based HUD model can be used in user training and in testing HUDs for various other vehicles.

B. AMOUNT OF SAND COLLECTION

For the simulation tests, the mass of sand particles inside the bucket is shown in Fig. 10a, and the tilt angle and height of the bucket are shown in Fig. 10b. In the process, the bucket is filled with approximately 450 kg, 100 kg, 200 kg, and 600 kg of sand in the consecutive tests, respectively. Otherwise, before the digging and after the dumping operations, the bucket is empty. In all the simulations, the mass inside the bucket fluctuates because of the vibration of the bucket caused either by the tractor reversing or by the hydraulic actuators. During reversing, the tests are performed carefully so that sand particles are not dropped from the bucket.

FIGURE 8. Simulation frames of the HUD unit of the tractor model at different instants of time for the fourth test.

As shown in Fig. 10b, the height and tilt angle of the bucket in every test is adjusted to the recommended value before the digging operation at around 10–11 s. However, varying lifting and tilting of the bucket after the digging process result in different amounts of sand in the bucket. Furthermore, the amount of sand moved is measured for a quantitative evaluation and it can be seen from Fig. 10a that the performance of the driver can be improved with every turn. Therefore, perhaps the HUD unit can help to get accustomed to controls and perform better.

C. REAL-TIME ABILITY OF THE SYSTEM

In this study, a complex multibody model of a tractor is demonstrated, which includes descriptions of hydraulic actuators, contact modeling, tire modeling, and deformable sand field. For all the simulation tests, the loop integration time of the system is shown in Fig. 11. In Fig. 11, the integration time in each time-step is always less than the simulation time-step (1.3 ms) indicating that the simulation step is solved before moving onto the next time-step. Thus, the results demonstrate a computationally efficient system which is real-time enabled. In order words, the real-time capability implies that an output can be received via the display and motion platform as soon as inputs are provided through the steering wheel, joystick, gear buttons, and foot pedals. Therefore, such real-time enabled system can be used in training and other product processes. Furthermore, it should be noted that the loop integration time is low when sand particles are not present, otherwise, the integration time is relatively higher. All the simulations are performed in a C++ environment

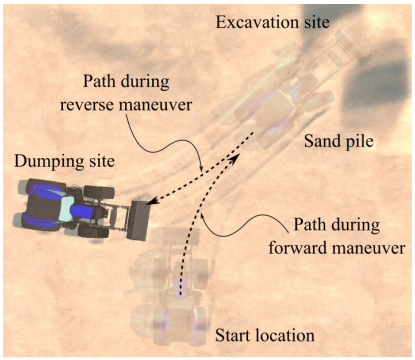

FIGURE 9. Tractor maneuver for the fourth test.

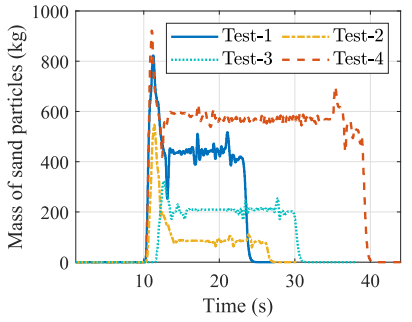

(a) Mass of sand particles in the bucket.

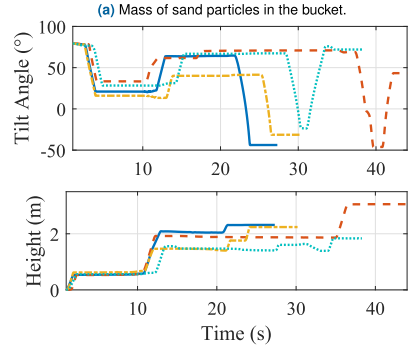

(b) Tilt angle and height of the bucket.

FIGURE 10. Data of bucket weight, tilt, and height indicators of the HUD unit during the simulation tests.

(compiler: Microsoft Visual Studio, version 14.1) and the used hardware/software is shown in Table 2.

In regard to the real-time policy in the C++ environment, the developed simulation application utilizes a *QueryPerformanceCounter* function from Microsoft libraries in the timing function under a *profileapi.h* header. This function retrieves the current value of the performance counter with

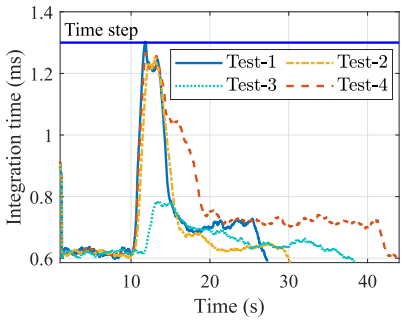

FIGURE 11. Loop integration time of the simulations.

TABLE 2. A description of the used hardware/software.

Name	System used
Operating system	Windows 10
Processor	Intel Core i7 3.41 GHz
Random access memory	64.0 GB
Graphics memory	36809 MB
Display adapter	Nvidia Quadro M2000

a high resolution of 1 µs that is used for the measurement of time-interval. On systems with a Windows XP or later operating systems, this function always succeeds and returns a nonzero value. However, it should be noted that this function is not limited for the loop integration time to reach a predefined simulation time-step at the end of a simulation step. This implies that the loop duration can exceed the real-time requirement and is left to a model designer to define a model simple enough for achieving a real-time simulation.

D. SIMULATING CRITICAL CONDITIONS

The critical conditions of limited fuel and a limited rolling angle are simulated to test the robustness of the HUD unit. Figure 12 shows the simulation frames of the HUD unit when the system is on the verge of meeting the critical conditions. Once the critical condition is met, the HUD unit displays a breakdown message and the simulation is forced to terminate. The limiting criterion for the fuel gauge is 1% of the maximum fuel and for the roll inclinometer, it is 20°.

E. DISCUSSION

The utility of the HUD unit in performing a certain task is demonstrated in Sect. IV-A. It can help to get accustomed to controls and perform better as shown in Sect. IV-B. Furthermore, the real-time capability (Sect. IV-C) and the physics-based modeling of the tractor provided a realistic experience of the tractor. Therefore, it is safe to conclude that the multibody-based HUD model introduced in this study can be used in user training, research, and testing HUDs for various vehicles.

(a) Roll inclinometer reads the maximum permissible roll angle of 20°.

(b) Fuel gauge indicates that the tractor will soon be out-of-fuel.

FIGURE 12. Simulation frames of the HUD unit while simulating critical conditions.

In conclusion, the research questions raised at the beginning of this research has been answered as follows: (a) A HUD can be modeled from a detailed multibody model of a vehicle using virtual sensing; (b) The HUD unit can assist drivers to perform certain tasks by providing a quantitative picture of the surroundings of the vehicle; (c) The proposed HUD modeling approach is robust because it can simulate critical conditions in real-time and is modular because it utilized a multibody modeling approach, thus, contributing to the state-of-the-art.

V. CONCLUSION

This study demonstrated a detailed real-time multibody model-based heads-up display unit of a tractor. The tractor was described using a semi-recursive multibody formulation and the hydraulic actuators were described using the lumped fluid theory. A HUD unit was designed based on a series of tasks that were associated with sets of conditions and instructions. These conditions and instructions determined/designed the analog and digital gauges that were linked with the virtual sensors of the tractor model. The virtual sensors were built using the multibody model of the tractor. The elements of the HUD unit were tachometer, speedometer, roll inclinometer, gear indicator, fuel gauge, and bucket height, tilt, and weight indicators.

The utility of the HUD unit was demonstrated based on a goal of moving a certain amount of sand from one place to another. In all the simulation tests, the tractor model followed a three-dimensional maneuver. The simulation frames of the HUD unit demonstrated its use in assisting a driver to meet the above-mentioned goal. The real-time capability of the system was shown where the loop integration time was always less than the simulation time-step. Such a HUD unit enabled real-time tractor simulator can facilitate a training process. Furthermore, critical conditions such as limited fuel and a limited rolling angle of the tractor were also presented. In conclusion, this study answered all the research questions raised at the beginning of this research and is contributing to the state-of-the-art.

In future work, the proposed method can be used to design HUD units for other complex mobile machines. Various goals can be set to study which goal requires more interaction with the HUD unit. In different operating situations, it can be studied that how a HUD unit contributes to a driver's workload, driving performance, and situational awareness. Moreover, a qualitative evaluation procedure can be carried out to provide more conclusive results about the efficiency and usability of the HUD model through user evaluations. Furthermore, user-centric HUD elements may facilitate a training process and product development. A HUD unit can be installed on an actual tractor and can be implemented for field testing.

REFERENCES

[1] M. Weihrauch, G. Meloeny, and T. Goesch, "The first head-up display introduced by general motors," SAE Tech. Paper 890288, 1989.

[2] J. Akyeampong, S. Udoka, G. Caruso, and M. Bordegoni, "Evaluation of hydraulic excavator human–machine interface concepts using NASA TLX," *Int. J. Ind. Ergonom.*, vol. 44, no. 3, pp. 374–382, May 2014.

[3] A. Pauzie, "Head-up display in automotive: A new reality for the driver," in *Proc. 4th Int. Conf. Design, User Exper., Usability*, Los Angeles, CA, USA, 2015, pp. 505–516.

[4] T. Deng, W. Sun, R. Zhang, and Y. Zhang, "Research on interface design of full windshield head-up display based on user experience," in *Proc. 9th Int. Conf. Appl. Hum. Factors Ergonom.*, Orlando, FL, USA, 2018, pp. 166–173.

[5] D. Beck and W. Park, "Perceived importance of automotive HUD information items: A study with experienced HUD users," *IEEE Access*, vol. 6, pp. 21901–21909, 2018.

[6] Z. An, X. Xu, J. Yang, Y. Liu, and Y. Yan, "A real-time three-dimensional tracking and registration method in the AR-HUD system," *IEEE Access*, vol. 6, pp. 43749–43757, 2018.

[7] J. Ma, Z. Gong, J. Tan, Q. Zhang, and Y. Zuo, "Assessing the driving distraction effect of vehicle HMI displays using data mining techniques," *Transp. Res. F, Traffic Psychol. Behav.*, vol. 69, pp. 235–250, Feb. 2020.

[8] S. Wang, V. Charissis, R. Lagoo, J. Campbell, and D. K. Harrison, "Reducing driver distraction by utilizing augmented reality head-up display system for rear passengers," in *Proc. IEEE Int. Conf. Consum. Electron. (ICCE)*, Las Vegas, NV, USA, Jan. 2019, pp. 1–6.

[9] A. Doshi, S. Y. Cheng, and M. M. Trivedi, "A novel active heads-up display for driver assistance," *IEEE Trans. Syst. Man, Cybern. B, Cybern.*, vol. 39, no. 1, pp. 85–93, Feb. 2009.

[10] Y.-C. Liu and M.-H. Wen, "Comparison of head-up display (HUD) vs. head-down display (HDD): Driving performance of commercial vehicle operators in Taiwan," *Int. J. Hum.-Comput. Stud.*, vol. 61, no. 5, pp. 679–697, Nov. 2004.

[11] D. R. Tufano, "Automotive HUDs: The overlooked safety issues," *Hum. Factors, J. Hum. Factors Ergonom. Soc.*, vol. 39, no. 2, pp. 303–311, Jun. 1997.

[12] A. Gregoriades and A. Sutcliffe, "Simulation-based evaluation of an in-vehicle smart situation awareness enhancement system," *Ergonomics*, vol. 61, no. 7, pp. 947–965, Jul. 2018.
[13] Y.-C. Liu, "Effects of using head-up display in automobile context on attention demand and driving performance," *Displays*, vol. 24, nos. 4–5, pp. 157–165, Dec. 2003.
[14] V. Charissis and S. Papanastasiou, "Human–machine collaboration through vehicle head up display interface," *Cognition, Technol. Work*, vol. 12, no. 1, pp. 41–50, Mar. 2010.
[15] R. Häuslschmid, "Extending head-up displays: Exploring the potential of large and 3D automotive windshield displays," Ph.D. dissertation, Ludwig Maximilian Univ. Munich, Munich, Germany, 2018.
[16] Y. Wu, M. Abdel-Aty, J. Park, and J. Zhu, "Effects of crash warning systems on rear-end crash avoidance behavior under fog conditions," *Transp. Res. C, Emerg. Technol.*, vol. 95, pp. 481–492, Oct. 2018.
[17] S. Wang, Y. Wang, Q. Zheng, and Z. Li, "Guidance-oriented advanced curve speed warning system in a connected vehicle environment," *Accident Anal. Prevention*, vol. 148, pp. 105801-1–105801-24, Dec. 2020.
[18] G. J. Heydinger, M. K. Salaani, W. R. Garrott, and P. A. Grygier, "Vehicle dynamics modelling for the national advanced driving simulator," *Proc. Inst. Mech. Eng., D, J. Automobile Eng.*, vol. 216, no. 4, pp. 307–318, Apr. 2002.
[19] R. Lagoo, V. Charissis, W. Chan, S. Khan, and D. Harrison, "Prototype gesture recognition interface for vehicular head-up display system," in *Proc. IEEE Int. Conf. Consum. Electron. (ICCE)*, Las Vegas, NV, USA, Jan. 2018, pp. 1–6.
[20] H. Wu, Y. Wang, J. Liu, J. Qiu, and X. Zhang, "User-defined gesture interaction for in-vehicle information systems," *Multimedia Tools Appl.*, vol. 79, nos. 1–2, pp. 263–288, Jan. 2020.
[21] R. Lagoo, V. Charissis, and D. K. Harrison, "Mitigating driver's distraction: Automotive head-up display and gesture recognition system," *IEEE Consum. Electron. Mag.*, vol. 8, no. 5, pp. 79–85, Sep. 2019.
[22] V. Charissis, J. Falah, R. Lagoo, S. F. M. Alfalah, S. Khan, S. Wang, S. Altarteer, K. B. Larbi, and D. Drikakis, "Employing emerging technologies to develop and evaluate in-vehicle intelligent systems for driver support: Infotainment AR HUD case study," *Appl. Sci.*, vol. 11, no. 4, p. 1397, Feb. 2021.
[23] Z. Wang, X. Liao, C. Wang, D. Oswald, G. Wu, K. Boriboonsomsin, M. J. Barth, K. Han, B. Kim, and P. Tiwari, "Driver behavior modeling using game engine and real vehicle: A learning-based approach," *IEEE Trans. Intell. Vehicles*, vol. 5, no. 4, pp. 738–749, Dec. 2020.
[24] C. Merenda, C. Suga, J. L. Gabbard, and T. Misu, "Effects of real-world visual fidelity on AR interface assessment: A case study using AR head-up display graphics in driving," in *Proc. 19th Int. Symp. Mixed Augmented Reality*, Beijing, China, 2019, pp. 145–156.
[25] S. Kim and A. K. Dey, "Simulated augmented reality windshield display as a cognitive mapping aid for elder driver navigation," in *Proc. 27th Int. Conf. Hum. Factors Comput. Syst. (CHI)*, Boston, MA, USA, 2009, pp. 133–142.
[26] C. Merenda, H. Kim, K. Tanous, J. L. Gabbard, B. Feichtl, T. Misu, and C. Suga, "Augmented reality interface design approaches for goal-directed and stimulus-driven driving tasks," *IEEE Trans. Vis. Comput. Graphics*, vol. 24, no. 11, pp. 2875–2885, Nov. 2018.
[27] M.-K. Choi, J.-H. Lee, H. Jung, I. R. Tayibnapis, and S. Kown, "Simulation framework for improved UI/UX of AR-HUD display," in *Proc. IEEE Int. Conf. Consum. Electron. (ICCE)*, Las Vegas, NV, USA, Jan. 2018, pp. 1–4.
[28] T. Hasegawa, Y. Sumiyosi, Y. Hayashi, A. Nishikawa, T. Chikuri, and O. Tsukahara, "Position correction against vehicle vibration for augmented reality on head-up display," in *SID Symp. Dig. Tech. Papers*, San Jose, CA, USA, 2019, pp. 1404–1407.
[29] M. Blundell and D. Harty, *The Multibody Systems Approach to Vehicle Dynamics*. Oxford, U.K.: Butterworth-Heinemann, 2015.
[30] J. G. De Jalon and E. Bayo, *Kinematic and Dynamic Simulation of Multibody Systems: The Real-Time Challenge*. New York, NY, USA: Springer-Verlag, 1994.
[31] Z. Zou, X. Pang, and J. Chen, "Comprehensive theoretical digging performance analysis for hydraulic excavator using convex polytope method," *Multibody Syst. Dyn.*, vol. 47, no. 2, pp. 137–164, Oct. 2019.
[32] S. Jaiswal, M. I. Islam, L. Hannola, J. Sopanen, and A. Mikkola, "Gamification procedure based on real-time multibody simulation," *Int. Rev. Model. Simul.*, vol. 11, no. 5, pp. 259–266, 2018.
[33] D. Dopico, A. Luaces, M. Gonzalez, and J. Cuadrado, "Dealing with multiple contacts in a human-in-the-loop application," *Multibody Syst. Dyn.*, vol. 25, no. 2, pp. 167–183, Feb. 2011.
[34] A. Nicolini, F. Mocera, and A. Somà, "Multibody simulation of a tracked vehicle with deformable ground contact model," *Proc. Inst. Mech. Eng., K, J. Multi-Body Dyn.*, vol. 233, no. 1, pp. 152–162, Mar. 2019.
[35] M. E. Baharudin, A. Rouvinen, P. Korkealaakso, and A. Mikkola, "Real-time multibody application for tree harvester truck simulator," *Proc. Inst. Mech. Eng., K, J. Multi-Body Dyn.*, vol. 228, no. 2, pp. 182–198, Jun. 2014.
[36] S. Jaiswal, P. Korkealaakso, R. Åman, J. Sopanen, and A. Mikkola, "Deformable terrain model for the real-time multibody simulation of a tractor with a hydraulically driven front-loader," *IEEE Access*, vol. 7, pp. 172694–172708, 2019.
[37] J. Torres-Moreno, J. Blanco-Claraco, A. Giménez-Fernández, E. Sanjurjo, and M. Naya, "Online kinematic and dynamic-state estimation for constrained multibody systems based on IMUs," *Sensors*, vol. 16, no. 3, p. 333, Mar. 2016.
[38] E. Sanjurjo, D. Dopico, A. Luaces, and M. Á. Naya, "State and force observers based on multibody models and the indirect Kalman filter," *Mech. Syst. Signal Process.*, vol. 106, pp. 210–228, Jun. 2018.
[39] A. Avello, J. M. Jiménez, E. Bayo, and J. G. de Jalón, "A simple and highly parallelizable method for real-time dynamic simulation based on velocity transformations," *Comput. Methods Appl. Mech. Eng.*, vol. 107, no. 3, pp. 313–339, Aug. 1993.
[40] J. Watton, *Fluid Power Systems: Modeling, Simulation, Analog and Microcomputer Control*. Cambridge, U.K.: Prentice-Hall, 1989.
[41] S. Gottschalk, M. C. Lin, and D. Manocha, "OBBtree: A hierarchical structure for rapid interference detection," in *Proc. 23rd Annu. Conf. Comput. Graph. Interact. Techn.*, New Orleans, LA, USA, 1996, pp. 171–180.
[42] E. Drumwright, "A fast and stable penalty method for rigid body simulation," *IEEE Trans. Vis. Comput. Graphics*, vol. 14, no. 1, pp. 231–240, Jan. 2008.
[43] C. C. D. Wit, R. Horowitz, and P. Tsiotras, *New Directions in Nonlinear Observer Design*. London, U.K.: Springer, 1999.
[44] C. C. D. Wit and P. Tsiotras, "Dynamic tire friction models for vehicle traction control," in *Proc. 38th IEEE Conf. Decis. Control*, Phoenix, AZ, USA, Dec. 1999, pp. 3746–3751.
[45] E. Bayo, J. G. De Jalon, and M. A. Serna, "A modified Lagrangian formulation for the dynamic analysis of constrained mechanical systems," *Comput. Methods Appl. Mech. Eng.*, vol. 71, no. 2, pp. 183–195, Nov. 1988.
[46] H. M. Handroos and M. J. Vilenius, "Flexible semi-empirical models for hydraulic flow control valves," *J. Mech. Des.*, vol. 113, no. 3, pp. 232–238, Sep. 1991.
[47] S. Jaiswal, E. Sanjurjo, J. Cuadrado, J. Sopanen, and A. Mikkola, "State estimator based on an indirect Kalman filter for a hydraulically actuated multibody system," *Multibody Syst. Dyn.*, pp. 1–25, Dec. 2020.
[48] S. Jaiswal, J. Sopanen, and A. Mikkola, "Efficiency comparison of various friction models of a hydraulic cylinder in the framework of multibody system dynamics," *Nonlinear Dyn.*, pp. 1–17, Apr. 2021.
[49] M. Moore and J. Wilhelms, "Collision detection and response for computer animation," in *Proc. 15th Annu. Conf. Comput. Graph. Interact. Techn.*, Atlanta, GA, USA, 1988, pp. 289–298.
[50] P. R. Dahl, "A solid friction model," Aerosp. Corp., El Segundo, CA, USA, Tech. Rep. TOR-0158(3107-18)-1, 1968.
[51] J. Cuadrado, D. Dopico, M. A. Naya, and M. Gonzalez, "Penalty, semi-recursive and hybrid methods for MBS real-time dynamics in the context of structural integrators," *Multibody Syst. Dyn.*, vol. 12, no. 2, pp. 117–132, Sep. 2004.
[52] J. Cuadrado, D. Dopico, M. Gonzalez, and M. A. Naya, "A combined penalty and recursive real-time formulation for multibody dynamics," *J. Mech. Des.*, vol. 126, no. 4, pp. 602–608, Jul. 2004.
[53] Y. Pan, S. Xiang, Y. He, J. Zhao, and A. Mikkola, "The validation of a semi-recursive vehicle dynamics model for a real-time simulation," *Mechanism Mach. Theory*, vol. 151, Sep. 2020, Art. no. 103907.
[54] Y. Pan, S. Xiang, and A. Mikkola, "An efficient high-order time-step algorithm with proportional-integral control strategy for semirecursive vehicle dynamics," *IEEE Access*, vol. 7, pp. 40833–40842, 2019.
[55] Y. Pan, W. Dai, L. Huang, Z. Li, and A. Mikkola, "Iterative refinement algorithm for efficient velocities and accelerations solutions in closed-loop multibody dynamics," *Mech. Syst. Signal Process.*, vol. 152, May 2021, Art. no. 107463.
[56] S. Jaiswal, J. Rahikainen, Q. Khadim, J. Sopanen, and A. Mikkola, "Comparing double-step and penalty-based semirecursive formulations for hydraulically actuated multibody systems in a monolithic approach," *Multibody Syst. Dyn.*, pp. 1–23, Jan. 2021, doi: 10.1007/s11044-020-09776-4.

[57] L. Morra, F. Lamberti, F. G. Pratticó, S. L. Rosa, and P. Montuschi, "Building trust in autonomous vehicles: Role of virtual reality driving simulators in HMI design," *IEEE Trans. Veh. Technol.*, vol. 68, no. 10, pp. 9438–9450, Oct. 2019.
[58] R. Li, Y. V. Chen, L. Zhang, Z. Shen, and Z. C. Qian, "Effects of perception of head-up display on the driving safety of experienced and inexperienced drivers," *Displays*, vol. 64, pp. 101962-1–101962-10, Sep. 2020.
[59] R. Häuslschmid, S. Osterwald, M. Lang, and A. Butz, "Augmenting the driver's view with peripheral information on a windshield display," in *Proc. 20th Int. Conf. Intell. User Interfaces*, Atlanta, GA, USA, Mar. 2015, pp. 311–321.
[60] N. J. Ward and A. Parkes, "Head-up displays and their automotive application: An overview of human factors issues affecting safety," *Accident Anal. Prevention*, vol. 26, no. 6, pp. 703–717, Dec. 1994.
[61] R. J. Sojourner and J. F. Antin, "The effects of a simulated head-up display speedometer on perceptual task performance," *Hum. Factors, J. Hum. Factors Ergonom. Soc.*, vol. 32, no. 3, pp. 329–339, Jun. 1990.
[62] K. G. Tippey, E. Sivaraj, and T. K. Ferris, "Driving while interacting with Google glass: Investigating the combined effect of head-up display and hands-free input on driving safety and multitask performance," *Hum. Factors, J. Hum. Factors Ergonom. Soc.*, vol. 59, no. 4, pp. 671–688, Jun. 2017.
[63] W. Yiwei, Y. Xianghai, and Z. Zhili, "Architecture modeling and test of tractor power shift transmission," *IEEE Access*, vol. 9, pp. 3517–3525, 2021.
[64] S. Jaiswal, A. Tarkiainen, T. Choudhury, J. Sopanen, and A. Mikkola, "Gamification and the marketing of agricultural machinery," in *Real-Time Simulation for Sustainable Production: Enhancing User Experience and Creating Business Value*. Evanston, IL, USA: Routledge, Jan. 2021.
[65] J. H. Iavecchia, H. P. Iavecchia, and I. S. N. Roscoe, "Eye accommodation to head-up virtual images," *Hum. Factors, J. Hum. Factors Ergonom. Soc.*, vol. 30, no. 6, pp. 689–702, Dec. 1988.

SURAJ JAISWAL was born in Kolkata, India, in July 1991. He received the B.E. degree in production engineering from Jadavpur University, Kolkata, in 2013, and the M.S. degree in mechanical engineering from the Lappeenranta University of Technology, Lappeenranta, Finland, in 2017, where he is currently pursuing the Ph.D. degree in mechanical engineering.

From 2013 to 2015, he has worked as a Design Engineer with Tata Consultancy Services Ltd., Kolkata. Since 2016, he has been working as a Junior Research Assistant with the Lappeenranta University of Technology. His research interests include multibody dynamics, non-linear Kalman filters, real-time simulation, and vehicle dynamics.

Mr. Jaiswal received the "Best Paper Award" at the 9th Asian Conference on Multibody Dynamics (ACMD 2018) held in Xian, China, during August 19–23, 2018.

RAFAEL ÅMAN was born in Karkkila, Finland, in 1978. He received the B.S. degree in mechanical engineering from the Helsinki University of Applied Sciences (Stadia), Finland, in 2002, and the M.S. and Ph.D. degrees in mechanical engineering from the Lappeenranta University of Technology, Lappeenranta, Finland, in 2007 and 2011, respectively, all in mechatronics.

From 2006 to 2016, he has worked as a Researcher on the simulation of fluid power circuits, hybrid power transmission, and energy recovery systems with the Lappeenranta University of Technology. He also has work experience as a Service Engineer in a civil engineering company. Since 2016, he has been with AGCO Corporation. He works at Valtra Inc., Suolahti, Finland. His main responsibilities have included system simulations and tractor design validation tests, as well as research and advanced engineering. As the Technical Specialist, he focuses on the use of future technologies in agricultural machinery and in their research and development processes. He has contributed to 26 scientific publications and presentations.

JUSSI SOPANEN (Member, IEEE) was born in Enonkoski, Finland, in 1974. He received the M.S. degree in mechanical engineering and the Ph.D. degree (in technology) from the Lappeenranta University of Technology, Lappeenranta, Finland, in 1999 and 2004, respectively.

From 1999 to 2006, he has worked as a Researcher with the Department of Mechanical Engineering, Lappeenranta University of Technology. From 2004 to 2005, he has worked as a Product Development Engineer for the electric machine manufacturer Rotatek Finland Ltd. From 2006 to 2012, he has worked as the Principal Lecturer in mechanical engineering and the Research Manager of the Faculty of Technology, Saimaa University of Applied Sciences, Lappeenranta. He is currently a Professor of machine dynamics with the Lappeenranta University of Technology. His research interests include rotor dynamics, multibody dynamics, and the mechanical design of electrical machines.

AKI MIKKOLA received the Ph.D. degree in the field of machine design in 1997.

Since 2002, he has been working as a Professor with the Department of Mechanical Engineering, Lappeenranta University of Technology, Lappeenranta, Finland. He is currently leading the Research Team of the Laboratory of Machine Design, Lappeenranta University of Technology. His research interests include machine dynamics and vibration, multibody system dynamics, and bio-mechanics. He has been awarded five patents and has contributed to more than 90 peer-reviewed journal articles.

Publication V

Jaiswal, S., Korkealaakso, P., Åman, R., Sopanen, J., and Mikkola, A.
Deformable terrain model for the real-time multibody simulation of a tractor with a hydraulically driven front-loader

Reprinted with permission from
IEEE Access
Vol. 7, pp. 172694–172708, 2019

IEEE Access
Multidisciplinary | Rapid Review | Open Access Journal

Received October 24, 2019, accepted November 14, 2019, date of publication November 27, 2019,
date of current version December 12, 2019.

Digital Object Identifier 10.1109/ACCESS.2019.2956164

Deformable Terrain Model for the Real-Time Multibody Simulation of a Tractor With a Hydraulically Driven Front-Loader

SURAJ JAISWAL[1], PASI KORKEALAAKSO[2], RAFAEL ÅMAN[3], JUSSI SOPANEN[1], (Member, IEEE), AND AKI MIKKOLA[1]

[1]Department of Mechanical Engineering, Lappeenranta University of Technology, 53850 Lappeenranta, Finland
[2]Mevea Ltd., 53850 Lappeenranta, Finland
[3]Valtra Inc., 44200 Suolahti, Finland

Corresponding author: Suraj Jaiswal (suraj.jaiswal@lut.fi)

This work was supported in part by the Business Finland [project: Digital Product Processes through Physics Based Real-Time Simulation—DigiPro], and in part by the Academy of Finland under Grant #316106.

ABSTRACT A real-time multibody model of an off-road vehicle can be used to analyze the dynamics of tasks, such as loading and/or transferring material from deformable ground. This analysis requires an accurate description of the mechanics, hydraulic actuators, and the terrain. The objective of this paper is to introduce a novel, real-time capable, deformable terrain/soil model that can interact with the mechanics of a multibody system model and the dynamics of a hydraulics model. To this end, a tractor is modeled by using a semi-recursive multibody formulation based on velocity transformation. The hydraulic actuation of the tractor's front-loader is modeled by using the lumped fluid theory. The tractor loads and transfers sand material from a deformable sand field (the ground), which is modeled by combining mesh-based and particle-based soil representation approaches for the real-time simulation of soil deformation. The work cycle of the tractor model follows a 3D maneuver that is used to load and transfer sand material. During the digging and dumping operations, the static sand field is converted into sand particles and vice versa respectively. For the presented work cycle, the real-time capability of the system is analyzed and determined. Furthermore, the dynamic actuator forces in the hydraulic cylinders are compared with the static actuator forces. The introduced real-time capable tractor simulation model can be utilized in product development and other product processes.

INDEX TERMS Deformable soil/terrain model, hydraulic actuators, multibody system dynamics, real-time simulation, semi-recursive formulation, vehicle dynamics.

I. INTRODUCTION

A real-time multibody system dynamics approach can be used to analyze the dynamic behavior of an off-road vehicle, such as a tractor [1]. A tractor with a hydraulically actuated front-loader can interact with its environment in two ways. It can either collide with the scene's objects and terrain, or it can load and/or transfer materials such as soil (the terrain) onto another type of machinery. To load and/or transfer material is a common task for a tractor, and for such an operation, the hydraulic actuators and the wheel/track/bucket and terrain interaction plays a major role in the tractor's dynamic performance. To achieve a real-time capable, realistic model with which to analyze the dynamics, an accurate description of the mechanical model, hydraulics model, and terrain model is needed.

In the literature, there are a large number of papers showing that multibody system dynamics can be coupled with a hydraulic system in the application of mobile machines. For example, Panetta *et al.* [2] presented a virtual tool (software) that coupled a multibody model of a tractor and a detailed hydraulic model of the suspension system in order to tune the hydro-pneumatic semi-active suspension system of the tractor. The hydraulic suspension system accounted for the dynamics of the electro-hydraulic valves, accumulator, and hydraulic actuator of the tractor. The model

The associate editor coordinating the review of this manuscript and approving it for publication was Fabrizio Messina.

was validated by comparing it against experimental data from leveling and dynamic bump tests conducted on the tractor. Baharudin *et al.* [3] demonstrated a combination of multibody system dynamics and hydraulics modeling for the real-time simulation of a hydraulically driven tree harvester. They utilized a semi-recursive formulation [4] for the dynamic modeling of the mechanical system and the lumped fluid theory [5] for modeling the hydraulic circuits. Contacts in this approach were described using the penalty approach. Jaiswal *et al.* [6] modeled a hydraulically actuated excavator to demonstrate a real-time capable, multibody simulation-based gamification procedure. They utilized the same semi-recursive formulation [4] and lumped fluid theory [5] in their study. Rahikainen *et al.* [7] introduced a monolithic formulation for a combined simulation of multibody and hydraulic dynamics by utilizing a semi-recursive formulation [8] and the lumped fluid method [5]. As a test case, they studied a four-bar linkage and a double-acting cylinder, a mechanism that is commonly used in hydraulic actuated machinery. Cook *et al.* [9] presented a generalized, multibody dynamics model of a quadtrac, which was equipped with a hydraulically powered towing winch for optimal mobility control and terrain identification. They utilized the Newton–Euler method in the system modeling. The model was used to recognize the limitation of the winch as an actuator and the amount of load it applied on the engine. Furthermore, Zou *et al.* [10] proposed a convex, polytope-based method in order to evaluate the theoretical digging performance (forces and moments) of a hydraulic excavator in the bucket force space. Newton–Euler equations were used to establish the dynamic relationships between the digging capability of the bucket and the driving capability of the hydraulic cylinder. Of the studies [2], [3], [6], [7], [9], the hydraulics modeling utilized by Baharudin *et al.* [3], Jaiswal *et al.* [6], and Rahikainen *et al.* [7] is applicable for real-time applications.

A number of studies in the literature have introduced ways to couple multibody system dynamics to terrain/soil modeling for a complex mobile machine. For example, Nicolini *et al.* [11] studied a multibody model of a small-sized tracked farming vehicle on two different types of soil: sand and compact agricultural terrain. The soil field was modeled as a rigid body and its motion was kinematically related to the vehicle so that the soil model moved under the vehicle near the tracks. The terramechanics equations of Bekker [12] and Janosi and Hanamoto [13] were utilized to describe the normal and tangential forces between the track and soil. Ma and Perkins [14] utilized the same terramechanics equations in their study. They proposed a track–wheel–terrain interaction model by using a nonlinear, finite element representation of the track segment and an adapting meshing scheme. As a test case, they studied the dynamics of a full vehicle model of an M1A1 tank on rough terrain, such as LETE sand. Sandu *et al.* [15], [16] investigated the modeling of a complex nonlinear multibody system in the presence of parametric and external uncertainties, such as vehicle–soil interaction. They utilized generalized polynomial chaos theory for the study. The methodology was illustrated on a quarter car model [16]. They demonstrated a stochastic terrain model by utilizing a truncated Karhunen–Loeve expansion [16]. However, the soil models in these studies [11]–[14] were unsuitable for real-time applications. However, Holz *et al.* [17] proposed a hybrid method for the real-time simulation of soil deformation, but not in the framework of multibody system dynamics. A high degree of soil dynamics (soil compaction and erosion) was accounted for in their study.

Dopico *et al.* [18] made an attempt to couple multibody system dynamics with terrain/soil modeling for a medium-sized wheeled excavator. In addition, they modeled the hydraulic cylinders as kinematic constraints and ignored the dynamics of the hydraulic actuators. The used multibody formulation was an index-3 augmented Lagrangian with projections of velocities and acceleration onto the constraint manifolds [19]. The contact forces were modeled as a normal force model (the Hunt–Crossley model [20]) and tangential force model [21]. The dynamic model (with 17 degrees of freedom) was real-time capable and was able to perform terrain excavation. The soft soil was modeled as a terrain mesh. However, they introduced only a simplified bucket-filling model for real-time purposes and they ignored the material flow aspect, that is, the soil model was not real-time capable.

In the literature, a number of studies have been carried out regarding soft terrain modeling for real-time applications. He *et al.* [22] aimed to standardize the experimental procedures that are used for the measurement of soil parameters and for the parameterization of terramechanics models. A comprehensive literature review was conducted to study the soil parameters, modeling procedures, experimental methods, and equipment that are used by the International Society of Terrain–Vehicle Systems community. Their study summarized the modeling techniques that are suitable for the real-time applications of terramechanics in simulation. Madsen *et al.* [23] developed a three-dimensional, physics-based, tire-terrain interaction model that can be used for off-road vehicle simulations in real time. The tire model was based on a lumped mass approach that utilized a radial spring-damper-mass distribution. The soil model utilized Boussinesq and Cerruti soil mechanics equations to compute the deformation of a volume of soil and the pressure distribution in terms of the vertical and lateral forces applied by the tire at the soil surface. In their study, numerical experiments were performed on a single soil volume node under the normal force applied by the simplified tire model on the surface of the soil. Jain *et al.* [24] focused on the description of the Rover Analysis, Modeling, and Simulation (ROAMS) system that is used to develop rover vehicles for planetary surface exploration. The ROAMS system provided real-time simulation of a planetary rover over deformable terrain. The terrain model applied the fundamental soil mechanics models, such as Mohr–Coulomb failure criterion equations [25]. Studies have also been carried out in the area of space robotics.

For example, Azimi *et al.* [26] proposed a novel approach, based on the elastoplasticity theory, to model the rigid-wheel and soft-soil interaction for rover simulation and analysis. They utilized the velocity field for soil particles (near the contact region) and the modified Drucker–Prager model to determine the normal and shear stress field in the contact area. Their study showed good agreement with the experimental data available from the literature and with the Bekker [12] and Wong–Reece [27] models. The model was compatible with multibody dynamics environments and its efficiency makes it suitable for the real-time simulation of rovers on soft soil. However, they focused on robotic systems that moved slowly, that is, with a rover speed of a few centimeters per second. Even though [22]–[24], [26] focused mainly on the wheel–terrain interaction models, the soft soil/terrain models developed by [23], [24], [26] are applicable for real-time applications, but are limited to tire–soil contacts only.

From the literature review, it can be concluded that there are a number of studies concerning terrain/soil models and hydraulics models within the multibody system dynamics framework that are appropriate for real-time applications. However, a real-time capable terrain/soil model that couples a detailed multibody dynamic system and a hydraulic system for complex mobile machines has been overlooked. Accordingly, the objective of this paper is to introduce a novel, real-time capable, deformable terrain/soil model that can interact with the mechanics of a multibody system model and the dynamics of a hydraulics model. The terrain/soil model can interact with any object, such as a bucket, along with the tires. To this end, a tractor will be described by using a semi-recursive multibody formulation based on velocity transformation [4]. The hydraulic actuation of the tractor's front-loader will be described by using the lumped fluid theory. The tractor will load and transfer sand material from a deformable sand field (ground) that will be described by combining mesh-based and particle-based soil representation methods for the real-time simulation of soil deformation. In addition, the contact model will be described by using the object-oriented bounding box method and penalty method, and the tire model will be described by using the lumped LuGre model. As a numerical example, the tractor's dynamic behavior on the deformable ground will be analyzed. Such a real-time capable simulation model can be utilized for product development and other product processes.

II. MULTIBODY FORMULATION

The equations of motion for a constrained mechanical system can be illustrated by using a multibody system dynamics approach. In multibody system dynamics, a number of formulations can be employed to construct the equations of motion, such as the augmented Lagrangian formulation [28], penalty formulation [29], recursive formulation [30], and semi-recursive formulation [4], [31]. In this study, a semi-recursive formulation based on a velocity transformation [4] is used because it provides a computationally efficient approach for vehicle applications, making it suitable for real-time applications. A combination of mesh-based and particle-based methods are used to model a deformable terrain. Lumped fluid theory [5], in turn, is used to model the hydraulic actuators. Furthermore, the object-oriented bounding box method [32] and penalty method [33] are used to model collision detection and response, and the lumped LuGre model [34], [35] is used to model the tire–ground contact.

A. SEMI-RECURSIVE MULTIBODY FORMULATION

In this study, the equations of motion are initially derived in terms of translational and rotational generalized coordinates, which are later projected onto the joint coordinate space using a velocity transformation matrix [4]. Consider two adjacent rigid bodies, B_{j-1} and B_j in an open-loop system of N_b bodies with any number of branches (tree-structure mechanisms), connected by a joint, as shown in Fig. 1. The locations of the joint on bodies B_{j-1} and B_j are denoted by points Q and P respectively. The joint relative displacement vector between points Q and P is denoted by $\mathbf{d}_{j-1,j}$.

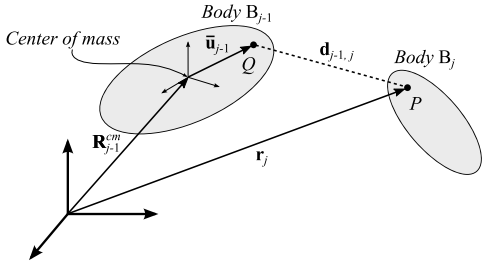

FIGURE 1. Illustration of two adjacent rigid bodies connected by a joint in an open-loop system.

The position $\mathbf{r}_j$ of point P in the global reference frame can be expressed as

$$\mathbf{r}_j = \mathbf{R}^{cm}_{j-1} + \mathbf{A}_{j-1}\bar{\mathbf{u}}_{j-1} + \mathbf{d}_{j-1,j} \tag{1}$$

where $\mathbf{R}^{cm}_{j-1}$ is the position of the body reference frame of body B_{j-1} with respect to the global reference frame, $\mathbf{A}_{j-1}$ is the rotation matrix of body B_{j-1}, and $\bar{\mathbf{u}}_{j-1}$ is the location of point Q in the body reference frame of body B_{j-1}. Note that the body reference frame is located at the center of mass of the body. The rotation matrix of body B_j can be expressed as

$$\mathbf{A}_j = \mathbf{A}_{j-1}\mathbf{A}_{j-1,j} \tag{2}$$

where $\mathbf{A}_{j-1,j}$ is the relative rotation matrix between the two bodies. In this study, body rotation is described by using the Euler parameters. Similar to (1), the velocities expression can be written as

$$\dot{\mathbf{r}}_j = \dot{\mathbf{R}}^{cm}_{j-1} + \tilde{\boldsymbol{\omega}}_{j-1}\mathbf{u}_{j-1} + \dot{\mathbf{d}}_{j-1,j} \tag{3}$$

$$\boldsymbol{\omega}_j = \boldsymbol{\omega}_{j-1} + \boldsymbol{\omega}_{j-1,j} \tag{4}$$

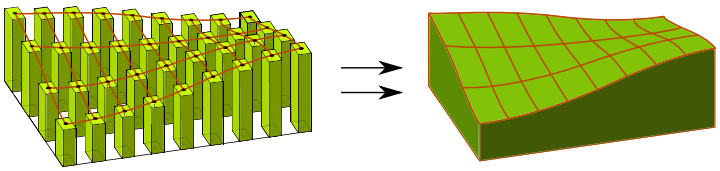

FIGURE 2. The soil model in a static state is defined as cells in a grid (heightfield). The center located on top of each soil column is referred to as the *heightfield vertex*.

where $\dot{\mathbf{r}}_j$, $\dot{\mathbf{R}}^{cm}_{j-1}$, and $\dot{\mathbf{d}}_{j-1,j}$ are, respectively, the time derivatives of $\mathbf{r}_j$, $\mathbf{R}^{cm}_{j-1}$, and $\mathbf{d}_{j-1,j}$; $\boldsymbol{\omega}_{j-1}$ and $\boldsymbol{\omega}_j$ are, respectively, the angular velocities of bodies B_{j-1} and B_j; $\mathbf{u}_{j-1} = \mathbf{A}_{j-1}\bar{\mathbf{u}}_{j-1}$. In (3), $\tilde{\boldsymbol{\omega}}_{j-1}$ is the skew-symmetric matrix of $\boldsymbol{\omega}_{j-1}$, and in (4), $\boldsymbol{\omega}_{j-1,j}$ is the relative angular velocity between the bodies.

By following the principle of virtual power, Avello *et al.* [4] proposed that the virtual power of the forces acting on a multibody system can be written as

$$\delta\dot{\mathbf{q}}^{\mathrm{T}}\left(\mathbf{M}\ddot{\mathbf{q}} + \mathbf{C} - \mathbf{Q}\right) = 0 \tag{5}$$

where $\delta\dot{\mathbf{q}}$ are the virtual velocities of dimension $6N_b$; $\mathbf{M}$ is the diagonal mass matrix of the system; and $\ddot{\mathbf{q}} = \{\ddot{\mathbf{q}}_1^{\mathrm{T}}\ddot{\mathbf{q}}_2^{\mathrm{T}}\ldots\ddot{\mathbf{q}}_{N_b}^{\mathrm{T}}\}^{\mathrm{T}}$, $\mathbf{C} = \{\mathbf{C}_1^{\mathrm{T}}\mathbf{C}_2^{\mathrm{T}}\ldots\mathbf{C}_{N_b}^{\mathrm{T}}\}^{\mathrm{T}}$, and $\mathbf{Q} = \{\mathbf{Q}_1^{\mathrm{T}}\mathbf{Q}_2^{\mathrm{T}}\ldots\mathbf{Q}_{N_b}^{\mathrm{T}}\}^{\mathrm{T}}$ are vectors of dimension $6N_b$, where $\mathbf{C}$ denotes the quadratic velocity vector and $\mathbf{Q}$ denotes the external forces and torques. Note that the terms in parentheses in (5) represent the Newton–Euler balance of inertia and external forces and torques. In (5), the internal forces (the constraint forces) do not appear as they do not produce any virtual power for a kinematically admissible velocity. Consequently, the virtual velocities, $\delta\dot{\mathbf{q}}$, are assumed to be kinematically admissible, that is, they must satisfy the kinematic constraints. The virtual velocity vector $\delta\dot{\mathbf{q}}$ of dimension $6N_b$ can be expressed in terms of vector $\delta\dot{\mathbf{z}}$ of dimension N_f, where N_f is the number of degrees of freedom of the system. Here, $\delta\dot{\mathbf{z}}$ are the virtual velocities of the joint coordinates. The velocity transformation matrix, $\mathbf{R}$, that relates the global coordinates and the relative joint coordinates, is introduced as follows

$$\dot{\mathbf{q}} = \mathbf{R}\dot{\mathbf{z}} \tag{6}$$

where $\dot{\mathbf{q}}$ is the generalized velocity vector and $\dot{\mathbf{z}}$ is the joint velocity vector. For scleronomic constraints (time independent), the kinematically admissible virtual velocities can be written as

$$\delta\dot{\mathbf{q}} = \mathbf{R}\delta\dot{\mathbf{z}}. \tag{7}$$

The acceleration equation can be expressed by taking the time derivatives of (6) as

$$\ddot{\mathbf{q}} = \mathbf{R}\ddot{\mathbf{z}} + \dot{\mathbf{R}}\dot{\mathbf{z}}. \tag{8}$$

By substituting (7) and (8) into (5), it can be expressed as

$$\delta\dot{\mathbf{z}}^{\mathrm{T}}\mathbf{R}^{\mathrm{T}}\left[\mathbf{M}\left(\mathbf{R}\ddot{\mathbf{z}} + \dot{\mathbf{R}}\dot{\mathbf{z}}\right) + \mathbf{C} - \mathbf{Q}\right] = 0. \tag{9}$$

As (9) holds true for any virtual velocity $\delta\dot{\mathbf{z}}^{\mathrm{T}}$, the virtual velocities can be eliminated and the equations of motion can be expressed as

$$\mathbf{R}^{\mathrm{T}}\mathbf{M}\mathbf{R}\ddot{\mathbf{z}} = \mathbf{R}^{\mathrm{T}}(\mathbf{Q} - \mathbf{C}) - \mathbf{R}^{\mathrm{T}}\mathbf{M}\dot{\mathbf{R}}\dot{\mathbf{z}} \tag{10}$$

which represents the N_f number of ordinary differential equations of motion expressed in terms of relative joint coordinates. Note that the way the transformation matrix, $\mathbf{R}$ in (6), is computed plays an important role in the computational efficiency of this formulation. As explained in the literature, the analytical expression of the transformation matrix $\mathbf{R}$, obtained by using an element-by-element technique, is often the most efficient method [36]. The rows of $\mathbf{R}$ corresponding to the body N_b are present in $\mathbf{R}_{N_b}$ once the zero columns are eliminated. The dimensions of $\mathbf{R}_{N_b}$ are $\left(6 \times N_{f\,b}\right)$, where $N_{f\,b}$ is the number of relative degrees of freedom found in the path that goes from the body N_b to the ground. The matrix $\mathbf{R}_{N_b}$ can be expressed as

$$\mathbf{R}_{N_b} = \left[\mathbf{R}^1_{N_b}\mathbf{R}^2_{N_b}\ldots\mathbf{R}^{P_b}_{N_b}\right] \tag{11}$$

where P_b is the number of joints in the path from the body N_b to the ground. The size of each sub-matrix, $\mathbf{R}^i_{N_b}$, is $(6 \times D_i)$, where D_i is the number of degrees of freedom of joint i. The expressions of matrix $\mathbf{R}^i_{N_b}$ for revolute, prismatic, cylindrical, universal, and spherical joint types are presented in [4].

For closed-loop systems, the equations of motion are derived by utilizing the cut-joint method and the penalty method as described by Bayo *et al.* [28]. Any closed-loop system can be expressed as an open-loop system (explained above) by simply cutting a joint in each kinematic loop and imposing the constraint conditions corresponding to the closure of the loops, as explained by Avello *et al.* [4].

B. THE TERRAIN MODEL

The terrain/soil model used in this study is a combination of grid- and particle-based methods. By using the grid-based method, the soil model is defined as cells in a grid (a heightfield), in which each cell has properties, such as the position, stiffness, and friction. Fig. 2 represents the soil model in the static state. The method used here is particularly suitable for

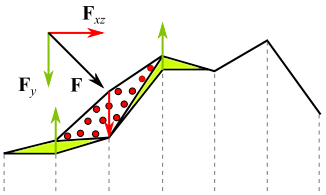

FIGURE 3. For a force F applied on the soil model, the vertical component $\mathbf{F}_y$ compresses and displaces the soil and the horizontal component $\mathbf{F}_{xz}$ generates the soil particles.

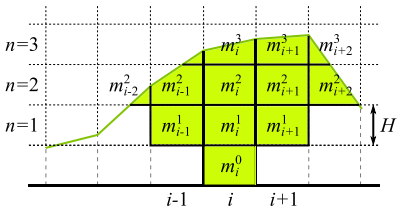

FIGURE 4. Uni dimensional automata are split into vertical slices to compute the pressure over the base of a cell.

fast collision detection and easy visualization. The vertical component of the force applied on the soil model compresses and displaces the soil, that is, it causes land compression and displacement, as shown in Fig. 3. By using the particle-based method, the soil can evolve and become unbound, which helps to describe the soil behavior. The horizontal component of the force applied on the soil model can generate the soil particles (see Fig. 3). When particles are generated, the grid height is updated based on the particles' volume. In this study, the particles have six degrees of freedom, containing both mass and inertia properties. Once the soil particles settle, they merge back to the heightfield with a volume update (that is, an accumulation of material on the ground).

1) SOIL GRID COMPRESSION AND DISPLACEMENT

In computer simulations, the evolution and visualization of the soil model's external surface is crucial. The cellular automata-based model [37], [38] is simple and it describes the soil model as cells in a grid (a heightfield) so that it can be efficiently rendered by graphics processors. The main advantage of a cellular automata model is that it can be executed in real time and it can be managed in a three-dimensional graphics environment. The system is assumed to having a constant density condition, that is, a cohesionless material forms a system with low compressibility, such as, dry sand.

Cellular automata on an $L \times L$ square grid are considered, where the variable $h(i, j)$ is the height of the system at the center of the cell (i, j). To compute the pressure over the base of one cell, the automata are split in vertical slices so that the material over a cell can be considered as a pile of blocks of height H. For simplicity, Fig. 4 shows such a representation of uni dimensional automata, where p_i^n and m_i^n are, respectively, the total pressure at the base and the weight of the n^{th} block located over the i^{th} cell. The pressure over the base of a cell is calculated by considering the pressure by their own block and the pressure received by a finite number of the closest blocks in the upper level, all of them centered over the (i, j) cell. The propagation of pressure from the layer n blocks to layer $(n-1)$ is expressed by means of a symmetric function ϕ so that

$$\left.\begin{aligned} \phi(k) = 0 \quad \forall k : |k| > 1 \\ \phi(-1) + \phi(0) + \phi(1) = 1 \end{aligned}\right\} \tag{12}$$

where $\phi(t)$ is the rate of the pressure received by the base of block i in layer n that is propagated to block $(i + t)$ in layer $(n-1)$. For real-time applications, the total weight/pressure over the base of the (i, j) cell can be written as

$$p_{ij}^0 = \sum_{n=0}^{N} \sum_{s=-n}^{n} \sum_{t=-n}^{n} a_{stn} m_{i+sj+t}^n \tag{13}$$

where

$$\left.\begin{aligned} a_{stn} = \sum_{k_1+\cdots+k_n=s} \sum_{l_1+\cdots+l_n=t} \phi^{k_1 l_1} \cdots \phi^{k_n l_n} \\ a_{000} = 1 \end{aligned}\right\} \tag{14}$$

where ϕ^i is used to denote $\phi(i)$. This leads to an efficient pressure distribution update. Note that in the presence of an external force, it is only required to add the equivalent weight to the block where the force is applied. Equation (13) only depends on the state of the cellular automata model, therefore, it can be applied to the interactive cellular automata model described below.

During soil deformation, which results from the object and soil grid interaction at some point, the previously untouched terrain in the immediate vicinity (the soil grid region) is subjected to another type of deformation, such as macroscopic patterns or avalanches. The formation of macroscopic patterns or avalanches can be modeled using cellular automata [37], [38]. In the used cellular automata model, the displacement of material (soil) can be triggered both by a large difference in height and by a large difference between the vertical forces applied to two neighboring cells.

Again, cellular automata on an $L \times L$ square grid are considered, where the variable $h(i, j)$ is the height of the system at the center of the cell (i, j). Let the scalar value of the applied vertical force on each cell be $f(i, j)$ and let F be a real function so that $F : IR \rightarrow IR$. Two new variables are introduced: h_f as the composition $h_f(i, j) = F(f(i, j))$, and the sum $h' = h + h_f$. A parameter α is introduced, which is the friction angle (the piling slope) of the system in order to simply constrain material change between the adjacent cells. In the simulation, if the calculated slope angle is smaller than the defined friction angle (the piling slope), then the material is not moved between cells without the application of external pressing force. In this study, the internal friction angle is

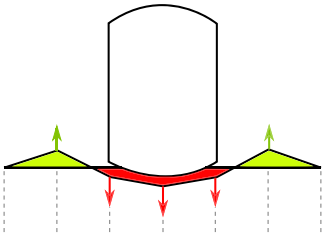

FIGURE 5. Soil compression and displacement.

considered 35°. For each cell (i, j), $\nabla h'$ is computed. For the cells where arctan $(|\nabla h'|) > \alpha$, the automata state can be updated as follows (pictorially represented in Fig. 5)

$$\left.\begin{aligned} h(i,j) &\leftarrow h(i,j) - z_+ \cdot (h'_x(i,j) + h'_y(i,j)) \\ h(i+1,j) &\leftarrow h(i+1,j) + z_+ \cdot h'_x(i,j) \\ h(i,j+1) &\leftarrow h(i,j+1) + z_+ \cdot h'_y(i,j) \end{aligned}\right\} \quad (15)$$

where z_+ is the velocity of the flowing matter, and h'_x and h'_y are the approximations to the partial derivative of $h'(x, y)$. The function F is approximated to be the height of a square column of material that weighs exactly f, as shown below

$$F(f) = \eta \frac{f}{d^2 \rho g} \quad (16)$$

where g is the acceleration due to gravity, ρ is the density of the material, d^2 is the area of the cell of the automata, and $\eta > 0$ is a parameter that allows defining how easily the force can cause the matter to be displaced. The force function F defined in (16) can integrate well with contact force models based on spring-damper equations (explained in Section II-D). The parameter η is determined based on the computation time of the simulation model in each iteration (such as the defined time step) and the amount of material that is moved between the cells. If $\eta = 0$ then there is no transfer of material between the cells. In this study, the value of η is assumed to be 4.

In this study, the parameter tuning for a given set of terrain properties is carried out case by case. This is due to the fact that the parameters are dependent on the complexity of the structure/machine and the collision geometries. The parameters are cumbersome to relate to the parameters that are usually employed to characterize soil behavior, such as the terrain cohesion or the pressure-sinkage coefficients in terramechanics models. The cellular automata-based model is consistent with actual terrain behavior. In [37], it is shown that the evolution of the surface of the cellular automata-based model is similar to the BCRE model presented by Bouchaud *et al.* [39]. Accordingly, the used cellular automata model provides a realistic and a computationally inexpensive model.

2) SOIL PARTICLE GENERATION AND REPRESENTATION

Soil particle generation is a force-based phenomenon. As shown in Fig. 3, when the horizontal component, $\mathbf{F}_{xz}$, of the force applied on the soil model is greater than the shear impulse limit, it generates soil particles. Soil failure is modeled by substituting the corresponding heightfield (static soil column) portion with soil particles, and consequently, the heightfield is lowered.

The granular soil particles are represented/simulated as rigid spherical bodies with six degrees of freedom. Their equations of motion are described by using the multibody formulation described in Section II-A. The rotations of the rigid spherical bodies are defined by using Euler parameters. In this study, all the friction is described by using the LuGre model for sliding (explained in Section II-D). The material properties — such as the contact spring and restitution coefficient, coefficient of sliding friction (friction coefficient), mass and moment of inertia of one particle system, and translational and rotational damping for the rigid spherical bodies — are introduced manually. In the soil particle representation, the degree of soil compaction (the packing of soil particles) is considered by assigning a void ratio value to all the free particles that is updated with each simulation step. This allows the soil to be represented as it appears in nature, where the overall volume of the soil is formed by its voids rather than solids. The consideration of the void ratio at the position of the soil particle allows the total volume transfer of the particle to the soil grid when the particles reach equilibrium and are merged into the soil grid (explained in Section II-B.3). This approach has a significant impact on the visual representation of the simulated soil particles.

To keep the real-time criteria, the size of the granular soil particles is determined based on the limit for the number of particles. The limit for the number of particles is determined by the complexity of the structure/machine, which includes the geometry of collision. In this study, the number of particles are limited to a maximum of 1000 particles in the bucket at a time.

3) SOIL PARTICLE MERGING

On reaching equilibrium (that is, the linear and angular velocity is below the threshold value), the soil particles that are in contact with the soil grid do not contribute to the soil dynamics. In such a situation, the soil particles are removed from the simulation and are replaced with a static volume in the soil grid by increasing the corresponding heightfield (the soil columns' height). Here, an interpolated filter kernel is applied to preserve the volume. This approach helps to achieve a real-time simulation capability by considerably reducing the total number of soil particles without affecting the soil dynamics' behavior.

C. HYDRAULIC ACTUATOR MODELING

In this study, lumped fluid theory [5] is used to describe the hydraulic pressures within a hydraulic circuit. In this method, the hydraulic circuit is partitioned into discrete volumes where the pressure is assumed to be evenly distributed. In practice, the effect of acoustic waves is assumed to be insignificant. The pressure build up (the first derivative of

pressure, p_s) within each hydraulic section of volume, V_s, can be written as

$$\dot{p_s} = \frac{B_{e_s}}{V_s} \sum_{k=1}^{n_c} Q_{sk} \tag{17}$$

where Q_{sk} is the sum of the incoming and outgoing flow in/out of a node (that is, the volume V_s), n_c is the total number of hydraulic components related to the volume V_s, and B_{e_s} is the effective bulk modulus of the hydraulic section of the volume V_s. A semi-empirical approach [40] can be used to model valves that are used to control the pressure difference, the flow rate, and the direction of flow. In this approach, the flow rate through a valve, Q, can be expressed as

$$Q = C_v U \sqrt{dp} \tag{18}$$

where C_v is the semi-empirical flow rate constant of the valve (which in many cases, such as with directional valves, can be obtained from manufacturer catalogues), dp is the pressure difference over the valve, and U is the relative spool/poppet position that can be expressed by using the first order equation as

$$\dot{U} = \frac{U_{ref} - U}{\tau} \tag{19}$$

where U_{ref} is the reference voltage signal for the reference spool/poppet position and τ is a time constant that can be read from the Bode diagram of the valve, describing the valve spool/poppet dynamics.

D. CONTACT AND TIRE MODELING

In multibody systems, the function of a contact model is to prohibit the inter-penetration of bodies. In practice, there are two steps in contact modeling: collision detection and collision response [41]. The collision between bodies is detected by using a bounding volume approach, which utilizes simple bounding volumes, such as spheres and boxes, to enclose bodies with complex geometries. In this study, the collision detection is determined by employing the object-oriented bounding box method [32]. This method uses a minimum rectangular solid to enclose the body along the direction of the axis. Fig. 6a illustrates this collision detection method in two dimensions between two bodies B_{j-1} and B_j that are enclosed in boxes E and F respectively. The two boxes do not overlap if the following condition is met, as shown below

$$\mathbf{T} \cdot \mathbf{L}_i > d_{Ei} + d_{Fi} \tag{20}$$

with,

$$d_{Ei} = e_1\mathbf{E}_1 \cdot \mathbf{L}_i + e_2\mathbf{E}_2 \cdot \mathbf{L}_i \tag{21}$$
$$d_{Fi} = f_1\mathbf{F}_1 \cdot \mathbf{L}_i + f_2\mathbf{F}_2 \cdot \mathbf{L}_i \tag{22}$$

where $|\mathbf{T}|$ is the distance between the centres of boxes E and F; $\mathbf{L}_i$ is a normalized direction; e_1 and e_2 are the dimensions of box E; f_1 and f_2 are the dimensions of box F; $\mathbf{E}_1$ and $\mathbf{E}_2$ are the normalized axes of box E; and $\mathbf{F}_1$ and $\mathbf{F}_2$ are the normalized axes of box F. In three dimensions, the boxes do not overlap if (20) holds true for all 15 potential separating axes, that is, $i = 1 : 15$.

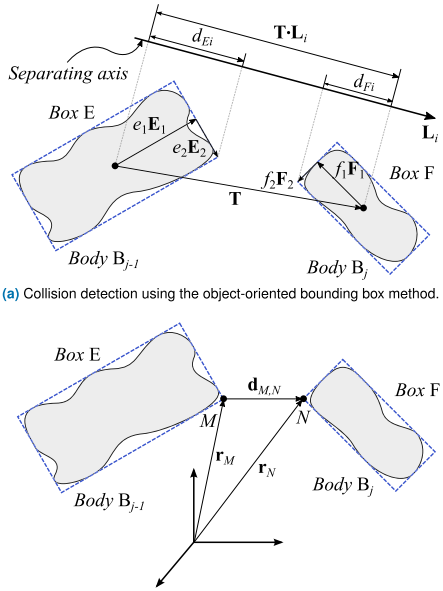

FIGURE 6. Contact modeling consists of collision detection and collision response.

In practice, the contact description based on the penalty method [33] is computationally efficient enough that it can be used in a real-time application. In this study, the geometry-based model (the single collision point model) is used to determine the contact force (the collision response) between the bodies involved. From Fig. 6b, the magnitude of the relative displacement, $\mathbf{d}_{M,N}$, and relative velocity, $\dot{\mathbf{d}}_{M,N}$, between the collision points M and N along the collision normal is derived (as in Section II-A) in the global reference frame as

$$\left|\mathbf{d}_{M,N}\right| = (\mathbf{r}_N - \mathbf{r}_M) \cdot \mathbf{n} \tag{23}$$
$$\left|\dot{\mathbf{d}}_{M,N}\right| = (\dot{\mathbf{r}}_N - \dot{\mathbf{r}}_M) \cdot \mathbf{n} \tag{24}$$

where $\mathbf{n} = \frac{(\mathbf{r}_N - \mathbf{r}_M)}{|(\mathbf{r}_N - \mathbf{r}_M)|}$ is the normal vector of the collision; $\mathbf{r}_M$ and $\mathbf{r}_N$ are, respectively, the position of collision points M and N with respect to the global reference frame; and $\dot{\mathbf{r}}_M$ and $\dot{\mathbf{r}}_N$ are their respective velocities in the global reference frame. The normal contact force, $\mathbf{F}_n$, at the collision point can be written as

$$\mathbf{F}_n = -\left(K\left|\mathbf{d}_{M,N}\right| + C\left|\dot{\mathbf{d}}_{M,N}\right|\right)\mathbf{n} \tag{25}$$

where $\left|\mathbf{d}_{M,N}\right|$ becomes the penetration distance at the contact point, K is the coefficient of elasticity, and C is the damping factor.

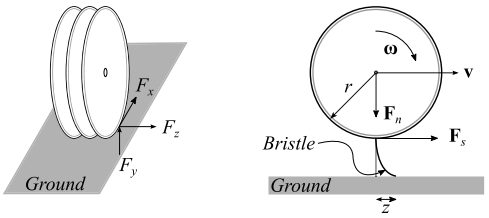

FIGURE 7. The lumped LuGre tire model.

In tire modeling, the tires are presumed to be a series of discs, as shown in Fig. 7 (on the left), where the typical forces involved are the longitudinal force F_x, lateral force F_z, and vertical force F_y. To meet the real-time criterion for this study, a tire is described by using the lumped LuGre tire model [34], [35], as shown in Fig. 7 (on the right). The approach can be seen as an extension of the Dahl model as it includes the Stribeck effect. It assumes punctual tire–ground friction contact. The lumped LuGre model proposed by De Wit *et al.* [34] can be written as

$$\dot{z} = |\mathbf{v}_r| - \frac{\sigma_0 |\mathbf{v}_r|}{g(\mathbf{v}_r)} z \tag{26}$$

$$|\mathbf{F}_s| = (\sigma_0 z + \sigma_1 \dot{z} + \sigma_2 |\mathbf{v}_r|)\, |\mathbf{F}_n| \tag{27}$$

with,

$$g(\mathbf{v}_r) = \mu_c + (\mu_s - \mu_c)\, e^{-\left|\frac{\mathbf{v}_r}{\mathbf{v}_s}\right|^{\frac{1}{2}}} \tag{28}$$

where σ_0 is the rubber longitudinal lumped stiffness, σ_1 is the rubber longitudinal lumped damping, σ_2 is the viscous relative damping, μ_c is the normalized Coulomb friction, μ_s is the normalized static friction ($\mu_c \leq \mu_s \in [0, 1]$), $\mathbf{v}_s$ is the Stribeck relative velocity, $\mathbf{F}_s$ is the friction force based on bristle deformation, $\mathbf{F}_n$ is the normal force, z is the deflection of the bristles (the internal friction state), and $|\mathbf{v}_r| = r\,|\boldsymbol{\omega}| - |\mathbf{v}|$ is the magnitude of the relative velocity, where r is the tire radius, and $\boldsymbol{\omega}$ and $\mathbf{v}$ are, respectively, the angular and linear velocity of the tire. In practice, (26) is solved by using the time integration scheme (the trapezoidal method). One of the limitations associated with this tire modeling technique is that the tire properties are assumed to be identical in the longitudinal and lateral directions. This is not the case in practice. Another limitation is that this tire model is based on a simplified LuGre model. In this study, a tire is modeled by using a series of discs while the contact patch, as predicted by a deformable tire model, is not considered. Therefore, the abrupt change in the normal contact pressure and slip distributions over the contact patch caused by the large load transfer are not considered in this tire model.

Regarding the transmission of forces between the vehicle and the terrain, in every iteration, the contact forces between the wheel and the ground are evaluated first. Then, the shape of the terrain model (explained in Section II-B) is updated based on the forces applied to the deformable terrain. Note that in the next iteration, the contact forces are re-evaluated based on the updated soil shape. Accordingly, the soil model is deformed continuously during the vehicle and terrain interaction. Prior to the evaluation of the contact forces between the wheel and the ground, the terrain is represented as static volumes in the soil grid, that is, it is considered rigid.

III. A CASE STUDY OF A HYDRAULICALLY ACTUATED TRACTOR MODEL

In this study, the tractor model shown in Fig. 8 is demonstrated as a case example. The tractor is modeled by using the semi-recursive approach, as explained in Section II-A. Fig. 8 demonstrates the connecting components of the tractor model, and the model structure is summarized in Table 1. There are eight revolute joints, three spherical joints, two universal joints, and two fixed joints, as shown in Fig. 8. The structure consists of open-loop and closed-loop links. For the closed-loop links, three cut joints are introduced at three revolute joints (marked in Fig. 8) and 15 closed-loop constraint equations are introduced for the closure of the loops. The system has nine degrees of freedom, with six degrees of freedom corresponding to the three translational and three rotational axes of the tractor, one degree of freedom corresponding to the steering mechanism, and two degrees of freedom corresponding to the lift and tilt rotational axes of the front-loader.

TABLE 1. Summary of the tractor model structure.

Name	Number
Number of bodies	13
Number of joints	15
Number of joint coordinates	28
Number of closed-loop constraint equations	15
Degrees of freedom	9

The front-loader of the tractor is operated by using hydraulic actuators. As the tractor model under consideration is subjected to product development and other product processes, a simplified version of the actual hydraulic circuit for the front-loader is utilized, as shown in Fig. 9. The circuit consists of a fixed displacement pump, two 4/3 directional control valves, and four double-acting hydraulic cylinders. The control volumes (V_P, V_1, V_2, V_3, and V_4) used in modeling the hydraulic circuit are also marked in Fig. 9. For the sake of simplicity, the circuit is assumed to be ideal, that is, leakage is not considered.

A deformable sand field is simulated by using the heightfield-based algorithm introduced in Section II-B. The dynamic performance of the tractor on this deformable sand field is analyzed when it lifts a bucket of sand from a pile of sand and dumps it in another place on the deformable ground (the sand field). This sand field model allows the correct bucket-filling process, both visually and physically (as shown in Fig. 10), that is, the bucket is filled by using the

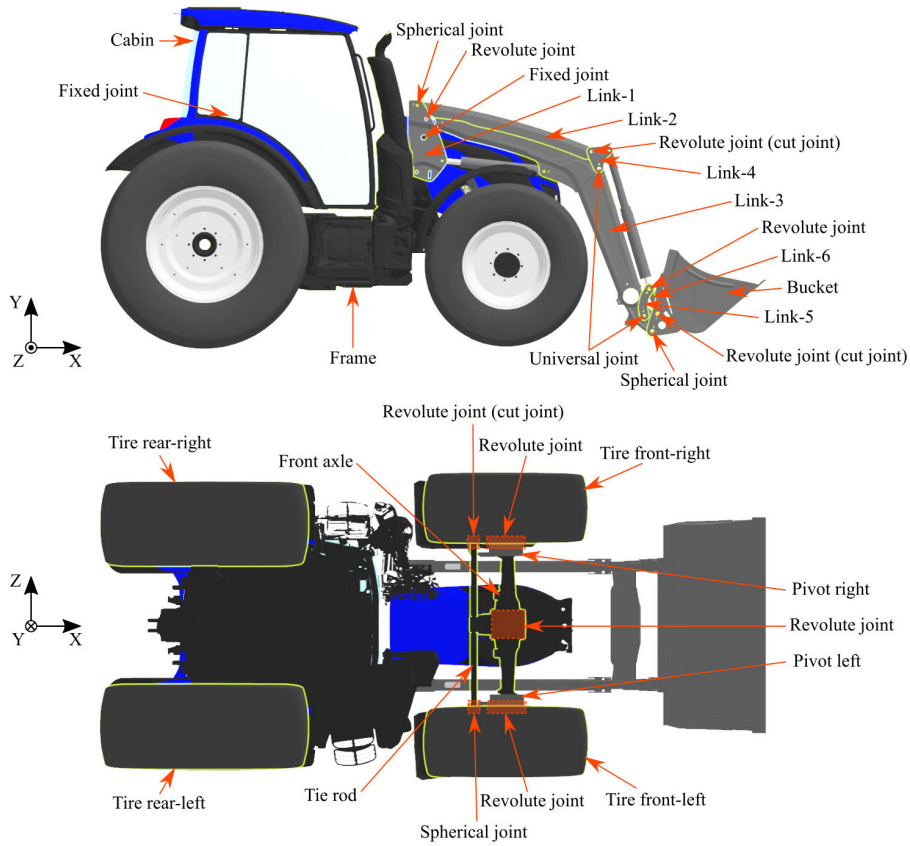

FIGURE 8. Connecting components in the tractor simulation model.

physically correct mass particles. By using the force points in the bucket, which are defined in the collision graphics of the bucket, the force at each force point is calculated independently. For the nearest cell to each force point, the direction, magnitude, and cutting force between the cells and force points are evaluated. When the cutting force reaches the penetration limit for the heightfield, particles are generated. Note that the forces at various force points on the bucket cause an uneven force distribution on the bucket, resulting in a load and moment to the structure. This study is concerned with a maximum of 1000 particles in the bucket at a time, as mentioned in Section II-B.2. Note that as the size of the particles is dependent on a number of parameters (such as the number of particles, complexity of the structure/machine, and collision geometries), the simulation result is only obtained for one kind of particle size. The size of these particles is not varied within the scope of this paper.

The nature of the terrain model introduced in this study is such that it is spatially independent, that is, the terrain in one area is independent of the terrain in another area. This implies that the computation of different areas of the terrain can be done in parallel. It does not depend on when/where the computations of different areas are performed as long as the computations are all completed before moving on to the next set of calculations. The multibody and hydraulics models are coupled, that is, a monolithic approach is used. The tractor simulation model used in this study is complex as it involves small time steps (0.0012 s), the use of hydraulics, and interaction with particle systems (in the terrain/soil model). The details about the operating system, processor, random access memory, graphics memory, and display adapter with which the simulation is performed are mentioned in Table 2. The tractor model is simulated in a C++ environment (compiler: Microsoft Visual Studio, version 14.1).

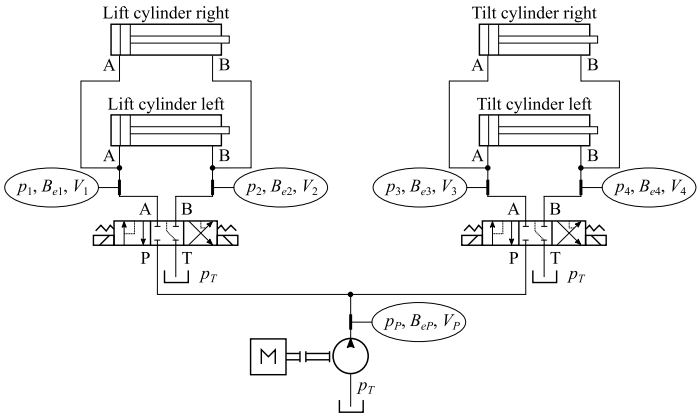

FIGURE 9. The front loader's hydraulic system.

TABLE 2. A description of the computer used for the simulation.

Name	System used
Operating system	Windows 10
Processor	Intel Core i7 3.41 GHz
Random access memory	64.0 GB
Graphics memory	36809 MB
Display adapter	Nvidia Quadro M2000

IV. RESULTS AND DISCUSSION

This section presents the simulation results of the real-time tractor on the deformable sand field. Fig. 10 shows simulation frames of the tractor model at different instants of time. In this study, the work cycle of the tractor model follows a 3D maneuver that is used to load the bucket with an amount of sand from a pile of sand and then dump it in another place on the deformable ground (the sand field). Here, the real-time capability of the system (the tractor simulation model) is analyzed. The performance of the soil/terrain model is compared with the multibody and hydraulics model, and their real-time capability is determined. The dynamic actuator forces in the hydraulic cylinders are compared with the static actuator forces (computed analytically) for the digging and dumping operation. The pressures in the hydraulic cylinders are also studied.

A. THE WORK CYCLE (THE 3D MANEUVER)

In this study, the tractor model follows a 3D maneuver, as shown in Fig. 11. At the beginning, the tractor is released from a height of 0.3 m at time 0.00 s. Then, the bucket is lifted-up (1.52 s to 2.36 s) and tilted outwards (2.96 s to 4.10 s) to the desired height and angle for the bucket to carry out the digging operation. Next, the tractor is driven forward (4.88 s to 10.81 s) towards a pile of sand along the curvature shown in Fig. 11. Note that the ground is not a flat plane, but has an undulating surface. Meanwhile, the bucket makes contact with the pile of sand at 10.12 s, digs an amount of sand until 10.85 s, and then the tractor is brought to a stop. During the collision between the bucket and the static sand field (the deformable ground), the static sand is converted into granular sand particles (10.12 s to 10.85 s). Next, the bucket is lifted up (10.56 s to 12.41 s) and slightly tilted inwards (10.32 s to 11.96 s) in order to fill the bucket with sand particles. Then, the tractor is driven in reverse (15.09 s to 34.60 s) along the curvature shown in Fig. 11. During reversing, the angle of

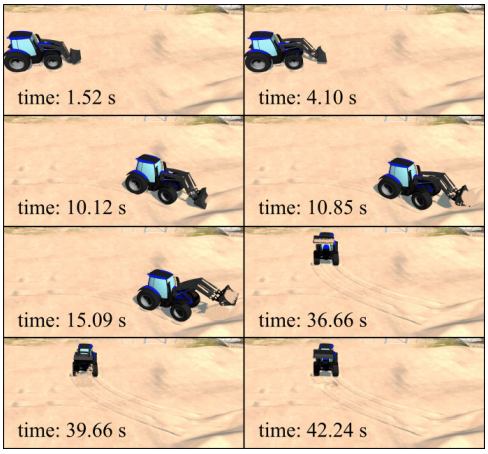

FIGURE 10. Simulation frames of the tractor model at different instants of time.

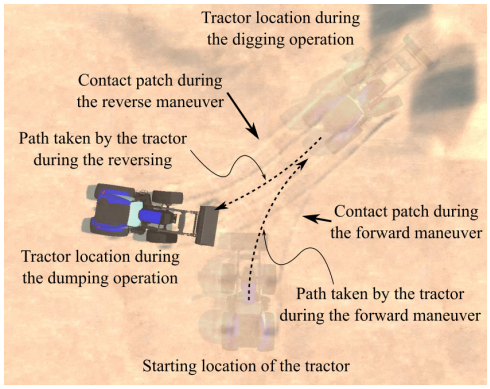

FIGURE 11. 3D maneuver of the tractor simulation model.

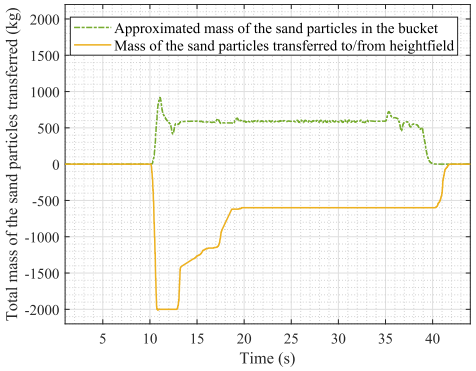

FIGURE 12. Total mass of the sand particles transferred during the simulation.

the bucket is slightly adjusted by tilting the bucket inwards (16.78 s to 17.42 s). Note that as the tires compress the soil/terrain model during the forward/backward maneuver, they make a contact patch on the undulating deformable ground, as shown in Fig. 11. Next, the tractor is brought to a stop, and the sand-filled bucket is raised (34.88 s to 36.66 s) and tilted outwards (35.00 s to 39.66 s) in order to dump the sand particles back on the ground. At last, the empty bucket is tilted inwards (40.78 s to 42.24 s) to complete the simulation process.

B. THE COLLECTION OF SAND PARTICLES

During the loading and transfer of the sand particles, the amount of sand being dug and collected in the bucket is shown in Fig. 12. During the digging operation (10.12 s to 10.85 s), the static sand field is converted into sand particles. The mass of sand particles inside the bucket before the digging (0 s to 10.12 s) and after the dumping operation (41.78 s to 44 s) is zero. Between 10.85 s to 12.85 s, the bucket is filled with approximately 600 kg of sand. Between 12.85 s to 19.72 s, the sand particles that are not collected in the bucket merge back into the sand field on reaching an equilibrium state, as mentioned in Section II-B.3. During the reversing of the tractor (15.09 s to 34.60 s), care is taken so that the sand particles are not dropped from the bucket. Note that the mass in the bucket is detected using a mass sensor. The mass sensor approximates the mass based on the number of sand particles crossing a specific location (inside the bucket) near the teeth of the bucket. The mass in the bucket (between 12.85 s to 37.20 s) slightly fluctuates around 600 kg because of tiny movements of the bucket caused by either the hydraulic actuators or the tractor's movement. Furthermore, the peaks in the curve depicting the approximated mass of the sand particles in the bucket, see between 10.50 s and 13 s and between 35 s and 38 s, should be noted. These are caused because of a sudden tilt/lift of the bucket causing the mass sensor to detect either some extra particles crossing the bucket or a loss of particles as they lose contact with the bucket. The moment the sand particles in the bucket are dumped (37.20 s to 40.28 s), they are merged back into the static sand field (40.28 s to 41.78 s) on reaching an equilibrium state.

C. REAL-TIME CAPABILITY

The tractor simulation model presented in this study is real-time capable, that is, the computation is synchronized to real time. For the presented work cycle, Fig. 13 represents the loop duration of the tractor simulation model. For the entire work cycle, the loop duration is always less than the time step (0.0012 s) of the simulation model. Therefore, the tractor simulation model is clearly real-time enabled. Note that from the time the sand particles are generated (10.12 s) until the time when they are merged back into the static sand field (41.78 s), the loop duration is higher in comparison with when no particles are generated/present.

For the work cycle presented above, the performance (measured in terms of integration time) of the soil/terrain model in comparison to the performance of the multibody and hydraulics model is shown in Fig. 13. Note that as mentioned in Section III, a monolithic approach is used for the multibody and hydraulics model. The integration time (the actual computation time) of the multibody and hydraulics model always fluctuates between 0.26 ms to 0.43 ms throughout the presented work cycle; whereas for the soil/terrain model, it varies depending upon the compression of the sand field and the generation/handling of the sand particles. As shown in Fig. 13, the integration time of the soil/terrain model is relatively low when no particles are present. At those instances, the soil/terrain model only undergoes compression because of the tires of the tractor. Otherwise, the integration time is relatively high from the moment the sand particles are generated/present. Furthermore, the integration time of the soil model depends on the number of sand particles

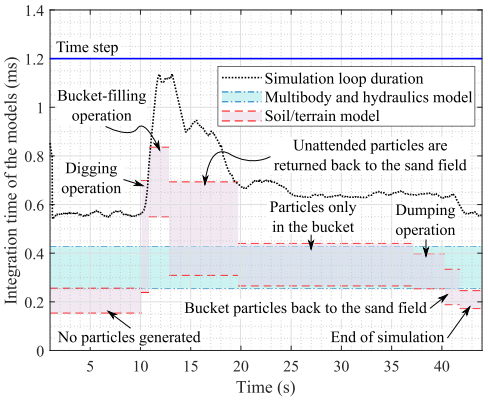

FIGURE 13. Performances of the models with respect to the simulation run time.

present/generated. A large number of sand particles results in a higher integration time. In conclusion, when no particles are generated/present, the integration time of the soil model is lower than the multibody and hydraulics model. Otherwise, the integration time of the soil model is higher, depending upon the number of sand particles generated/present and their handling. For the soil/terrain model and the multibody and hydraulics model, the integration time is always less than the time step (0.0012 s).

D. ACTUATOR FORCE AND HYDRAULIC PRESSURE IN THE HYDRAULIC CYLINDERS

This study introduced a real-time capable, deformable terrain/soil model that can interact with the dynamics of the hydraulics model along with the multibody dynamic system. Therefore, it becomes necessary to provide simulation results for the hydraulic pressure and actuator force in the hydraulic cylinders for the presented work cycle. The analysis is focused on the duration between the digging and dumping operations, that is, when the sand particles are generated/present. Such simulation results can be utilized in product development and other product processes. In the hydraulics subsystem, 4/3 directional control valves for the lift and tilt operations are modeled as an input signal for the user. For the lift operation, Fig. 14 represents the response of the hydraulics subsystem when the bucket loads and transfers approximately 600 kg of sand from a deformable ground area (the sand field). As per the presented work cycle, the important regions on the plots in Fig. 14 are highlighted in purple for the lift operation.

During the lift operation, the hydraulic pressure across the right/left hydraulic lift cylinder is shown in Fig. 14a. The actuator forces of the lift cylinders (right and left) are shown in Fig. 14b. The right and left lift cylinders have identical dynamic actuator forces. Therefore, the pressure plot is

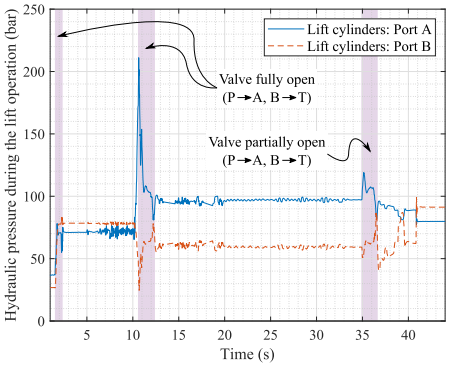

(a) Hydraulic pressure across the hydraulic lift cylinders during the lift operation.

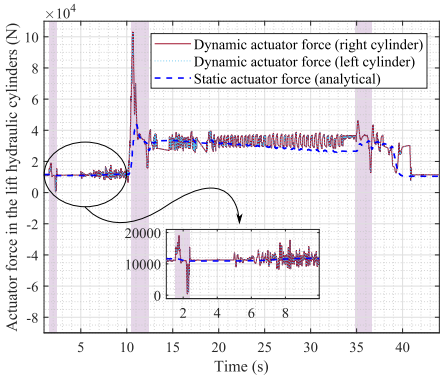

(b) Actuator forces in the hydraulic lift cylinders during the lift operation.

FIGURE 14. Simulation results for the front-loader's hydraulic lift cylinders during the lift operation.

shown for only one of the lift cylinders. Between 10.12 s and 10.85 s, a high order (of the order 100 kN), fluctuating, dynamic actuator force occurs, representing the collision of the bucket with the static sand field. During this period, a peak fluctuation in the pressure plot is also observed. The collision of the bucket with a pile of sand is a harsh operation. When the bucket is filled with sand particles (10.85 s to 37.20 s), more pressure is applied on the piston side (port A) compared with the piston-rod side (port B) (see Fig. 14a). As a result, more actuator force is applied to support the extra weight of the sand particles, as can be seen in Fig. 14b. Between 10.85 s and 37.20 s, the pressure in the lift cylinder and the dynamic actuator force fluctuates because of the mass fluctuation in the bucket. The dynamic actuator force in the lift cylinder is compared with its static actuator force, which is analytically computed without considering the dynamics of the system. It can be concluded that the dynamic actuator force showed good agreement with the static actuator force. A similar

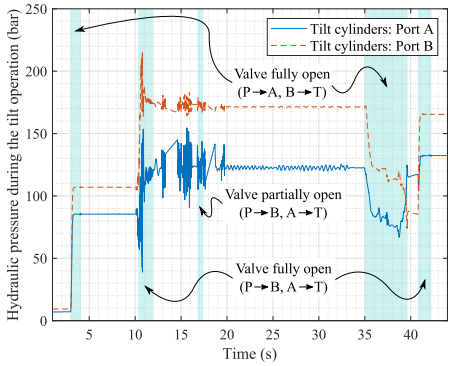

(a) Hydraulic pressure across the hydraulic tilt cylinders during the tilt operation.

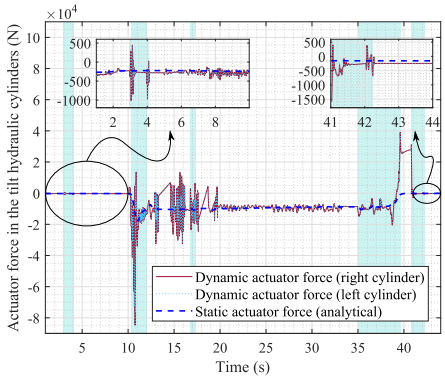

(b) Actuator forces in the hydraulic tilt cylinders during the tilt operation.

FIGURE 15. Simulation results for the front-loader's hydraulic tilt cylinders during the tilt operation.

analysis can be carried out for the tilt operation (Fig. 15) where the important regions on the plots are highlighted in cyan for the tilt operation.

V. CONCLUSION

This study demonstrated a real-time simulation approach that consists of a unique combination of multibody formulation, hydraulic actuators, and a deformable terrain/soil model. The introduced approach is ideal for the real-time analysis of the dynamics of a complex mobile machine. As a case study, a tractor was modeled by using a semi-recursive multibody formulation based on velocity transformation. A deformable sand field (the ground) was modeled by combining a mesh-based and particle-based soil representation method for the real-time simulation of soil deformation. The hydraulic actuation of the tractor's front-loader was modeled by utilizing the lumped fluid theory.

This study presented the dynamic behavior of the tractor work cycle in which the tractor dug an amount of sand from a pile of sand and dumped it in another place on a deformable ground area (the sand field). The work cycle of the tractor model followed a 3D maneuver. During the 3D maneuver, the tires made a contact patch on the undulating deformable ground as they compressed the soil/terrain model. During the digging operation, the static sand field was converted into sand particles and these were collected in the bucket of the tractor. During the dumping operation, the sand particles merged back into the static sand field on reaching an equilibrium state.

The tractor model was real-time capable as the loop duration was always less than the time step. The loop duration was higher when the sand particles were generated/present in comparison with when no particles were generated/present. This was caused by the fact that the integration time of the soil/terrain model was higher, which was dependent on the number of sand particles generated/present and their handling. In other situations, the integration time of the soil/terrain model was lower than the multibody and hydraulics model, which followed a monolithic approach. The soil/terrain model and the multibody and hydraulics model were real-time capable.

The simulated bucket and sand pile collision caused a high order fluctuating actuator force (dynamic) and a peak fluctuation in the pressure, demonstrating a similarly harsh operation as it would be in practice. When the bucket was filled with sand particles, more pressure was applied on the piston side compared to the piston-rod side (the lift cylinders), resulting in more dynamic actuator force (from the lift cylinders) to support the extra weight of the sand particles. The dynamic actuator force showed good agreement with the static actuator force. Such a real-time capable tractor simulation model can be utilized in product development and other product processes.

It should be noted that due to the lack of experimental data, no thorough validation regarding the accuracy of the tractor simulation model was provided. The validation for the physical correctness of the cellular automata model was already provided in the literature [37]. Furthermore, it has been carefully checked that the modeled tractor behaved in a logical manner. It is also worth noting that the results obtained from the hydraulics subsystem of the tractor model showed good agreement when compared to simple analytical models. This study provided a conceptual-level implementation of a possible simulation model that is focused on the entire environment.

REFERENCES

[1] M. Blundell and D. Harty, *The Multibody Systems Approach to Vehicle Dynamics*. Oxford, U.K.: Butterworth-Heinemann, 2015.

[2] G. Panetta, F. Mancarella, M. Borghi, B. Zardin, and F. Pintore, "Dynamic modelling of an off-road vehicle for the design of a semi-active, hydropneumatic spring-damper system," in *Proc. ASME Int. Mech. Eng. Congr. Expo.*, Houston, TX, USA, 2015, pp. 1–11.

[3] M. E. Baharudin, A. Rouvinen, P. Korkealaakso, and A. Mikkola, "Real-time multibody application for tree harvester truck simulator," *Proc. Inst. Mech. Eng. K, J. Multi-Body Dyn.*, vol. 228, no. 2, pp. 182–198, 2014.

[4] A. Avello, J. M. Jiménez, E. Bayo, and J. G. de Jalón, "A simple and highly parallelizable method for real-time dynamic simulation based on velocity transformation," *Comput. Methods Appl. Mech. Eng.*, vol. 107, no. 3, pp. 313–339, 1993.

[5] J. Watton, *Fluid Power Systems: Modeling, Simulation, Analog and Microcomputer Control*. Cambridge, U.K.: Prentice-Hall, 1989.

[6] S. Jaiswal, M. I. Islam, L. Hannola, J. Sopanen, and A. Mikkola, "Gamification procedure based on real-time multibody simulation," *Int. Rev. Model. Simul.*, vol. 11, no. 5, pp. 259–266, 2018.

[7] J. Rahikainen, A. Mikkola, J. Sopanen, and J. Gerstmayr, "Combined semi-recursive formulation and lumped fluid method for monolithic simulation of multibody and hydraulic dynamics," *Multibody Syst. Dyn.*, vol. 44, no. 3, pp. 293–311, 2018.

[8] J. Cuadrado, D. Dopico, M. Gonzalez, and M. A. Naya, "A combined penalty and recursive real-time formulation for multibody dynamics," *J. Mech. Des.*, vol. 126, no. 4, pp. 602–608, 2004.

[9] J. T. Cook, L. Ray, and J. Lever, "Multi-body dynamics model of a tracked vehicle using a towing winch for optimal mobility control and terrain identification," in *Proc. ASME Dyn. Syst. Control Conf.*, Minneapolis, MN, USA, 2016, pp. 1–8.

[10] Z. Zou, X. Pang, and J. Chen, "Comprehensive theoretical digging performance analysis for hydraulic excavator using convex polytope method," *Multibody Syst. Dyn.*, vol. 47, no. 2, pp. 137–164, 2019.

[11] A. Nicolini, F. Mocera, and A. Somà, "Multibody simulation of a tracked vehicle with deformable ground contact model," *Proc. Inst. Mech. Eng. K, J. Multi-Body Dyn.*, vol. 233, no. 1, pp. 152–162, 2018.

[12] M. G. Bekker, *Introduction to Terrain-Vehicle Systems*. Ann Arbor, MI, USA: Univ. of Michigan Press, 1969.

[13] Z. Janosi and B. Hanamoto, "The analytical determination of drawbar pull as a function of slip for tracked vehicles in deformable soils," in *Proc. 1st Int. Conf. Int. Soc. Terrain-Vehicle Syst.*, Turin, Italy, 1961, pp. 707–736.

[14] Z.-D. Ma and N. C. Perkins, "A super-element of track-wheel-terrain interaction for dynamic simulation of tracked vehicles," *Multibody Syst. Dyn.*, vol. 15, no. 4, pp. 347–368, 2006.

[15] A. Sandu, C. Sandu, and M. Ahmadian, "Modeling multibody systems with uncertainties. Part I: Theoretical and computational aspects," *Multibody Syst. Dyn.*, vol. 15, no. 4, pp. 369–391, 2006.

[16] C. Sandu, A. Sandu, and M. Ahmadian, "Modeling multibody systems with uncertainties. Part II: Numerical applications," *Multibody Syst. Dyn.*, vol. 15, no. 3, pp. 241–262, 2006.

[17] D. Holz, T. Beer, and T. Kuhle, "Soil deformation models for real-time simulation: A hybrid approach," in *Proc. 6th Workshop Virtual Reality Interact. Phys. Simulations*, Karlsruhe, Germany, 2009, pp. 21–30.

[18] D. Dopico, A. Luaces, and M. González, "A soil model for a hydraulic simulator excavator based on real-time multibody dynamics," in *Proc. 5th Asian Conf. Multibody Dyn.*, Kyoto, Japan, 2010, pp. 325–333.

[19] J. Cuadrado, J. Cardenal, and E. Bayo, "Modeling and solution methods for efficient real-time simulation of multibody dynamics," *Multibody Syst. Dyn.*, vol. 1, no. 3, pp. 259–280, 1997.

[20] K. Hunt and F. Crossley, "Coefficient of restitution interpreted as damping in vibroimpact," *J. Appl. Mech.*, vol. 42, no. 2, pp. 440–445, Jun. 1975.

[21] D. Dopico, A. Luaces, M. Gonzalez, and J. Cuadrado, "Dealing with multiple contacts in a human-in-the-loop application," *Multibody Syst. Dyn.*, vol. 25, no. 2, pp. 167–183, 2011.

[22] R. He, C. Sandu, A. K. Khan, A. G. Guthrie, P. S. Els, and H. A. Hamersma, "Review of terramechanics models and their applicability to real-time applications," *J. Terramech.*, vol. 81, pp. 3–22, Feb. 2019.

[23] J. Madsen, D. Negrut, A. Reid, A. Seidl, P. Ayers, G. Bozdech, J. Freeman, and J. O'Kins, "A physics based vehicle terrain interaction model for soft soil off-road vehicle simulations," *SAE Int. J. Commercial Vehicles*, vol. 5, no. 1, pp. 280–290, 2012.

[24] A. Jain, J. Balaram, J. Cameron, J. Guineau, C. Lim, M. Pomerantz, and G. Sohl, "Recent developments in the ROAMS planetary rover simulation environment," in *Proc. IEEE Aerosp. Conf.*, Big Sky, MT, USA, Mar. 2004, pp. 861–876.

[25] J. F. Labuz and A. Zang, "Mohr–Coulomb failure criterion," *Rock Mech. Rock Eng.*, vol. 45, no. 6, pp. 975–979, 2012.

[26] A. Azimi, J. Kövecses, and J. Angeles, "Wheel–soil interaction model for rover simulation and analysis using elastoplasticity theory," *IEEE Trans. Robot.*, vol. 29, no. 5, pp. 1271–1288, Oct. 2013.

[27] J.-Y. Wong and A. R. Reece, "Prediction of rigid wheel performance based on the analysis of soil-wheel stresses part I. Performance of driven rigid wheels," *J. Terramech.*, vol. 4, no. 1, pp. 81–98, 1967.

[28] E. Bayo, J. G. De Jalon, and M. A. Serna, "A modified Lagrangian formulation for the dynamic analysis of constrained mechanical systems," *Comput. Methods Appl. Mech. Eng.*, vol. 71, no. 2, pp. 183–195, 1988.

[29] E. Bayo and M. A. Serna, "Penalty formulations for the dynamic analysis of elastic mechanisms," *J. Mech., Transmiss., Autom. Des.*, vol. 111, no. 3, pp. 321–327, 1989.

[30] D. S. Bae, J. M. Han, and H. H. Yoo, "A generalized recursive formulation for constrained mechanical system dynamics," *Mech. Struct. Mach.*, vol. 27, no. 3, pp. 293–315, 1999.

[31] J. de García Jalón, E. Álvarez, F. A. de Ribera, I. Rodríguez, and F. J. Funes, "A fast and simple semi-recursive formulation for multi-rigid-body systems," *Advances in Computational Multibody Systems*, vol. 2. Dordrecht, The Netherlands: Springer, 2005, pp. 1–23.

[32] S. Gottschalk, M. C. Lin, and D. Manocha, "OBBTree: A hierarchical structure for rapid interference detection," in *Proc. 23rd Annu. Conf. Comput. Graph. Interact. Techn.*, New Orleans, LA, USA, 1996, pp. 171–180.

[33] E. Drumwright, "A fast and stable penalty method for rigid body simulation," *IEEE Trans. Vis. Comput. Graphics*, vol. 14, no. 1, pp. 231–240, Jan./Feb. 2008.

[34] C. C. de Wit, R. Horowitz, and P. Tsiotras, *New Directions in Nonlinear Observer Design*. London, U.K.: Springer, 1999.

[35] C. C. de Wit and P. Tsiotras, "Dynamic tire friction models for vehicle traction control," in *Proc. 38th IEEE Conf. Decis. Control*, Phoenix, AZ, USA, Dec. 1999, pp. 3746–3751.

[36] J. G. de Jalon and E. Bayo, *Kinematic and Dynamic Simulation of Multibody Systems: The Real-Time Challenge*. New York, NY, USA: Springer-Verlag, 1994.

[37] M. Pla-Castells, I. García-Fernández, and R. J. Martínez, "Approximation of continuous media models for granular systems using cellular automata," in *Proc. 6th Int. Conf. Cellular Automata Res. Ind.*, Amsterdam, The Netherlands, 2004, pp. 230–237.

[38] M. Pla-Castells, I. García-Fernández, and R. J. Martínez, "Interactive terrain simulation and force distribution models in sand piles," in *Proc. 7th Int. Conf. Cellular Automata Res. Ind.*, Perpignan, France, 2006, pp. 392–401.

[39] J.-P. Bouchaud, M. E. Cates, J. R. Prakash, and S. F. Edwards, "A model for the dynamics of sandpile surfaces," *J. Phys. I, France*, vol. 4, no. 10, pp. 1383–1410, 1994.

[40] H. M. Handroos and M. J. Vilenius, "Flexible semi-empirical models for hydraulic flow control valves," *J. Mech. Des.*, vol. 113, no. 3, pp. 232–238, 1991.

[41] M. Moore and J. Wilhelms, "Collision detection and response for computer animation," in *Proc. 15th Annu. Conf. Comput. Graph. Interact. Techn.*, Atlanta, GA, USA, 1988, pp. 289–298.

SURAJ JAISWAL was born in Kolkata, India, in July 29, 1991. He received the B.E. degree in production engineering from Jadavpur University, Kolkata, in 2013, and the M.S. degree in mechanical engineering from the Lappeenranta University of Technology, Lappeenranta, Finland, in 2017, where he is currently pursuing the Ph.D. degree in mechanical engineering.

From 2013 to 2015, he worked as a Design Engineer at Tata Consultancy Services Ltd., Kolkata. Since 2016, he has been working as a Junior Research Assistant at the Lappeenranta University of Technology. His research interests include multibody system dynamics, real-time simulation, and vehicle dynamics.

Mr. Jaiswal received the "On the Spot Award" for an outstanding contribution to Tata Consultancy Services Ltd., in 2013, and the "Best Paper Award" at the 9th Asian Conference on Multibody Dynamics (ACMD 2018), Xi'an, China, in August 2018.

PASI KORKEALAAKSO was born in Finland, in 1977. He received the M.S. degree in mechanical engineering and the Ph.D. degree from the Lappeenranta University of Technology, Lappeenranta, Finland, in 2002 and 2009, respectively.

From 2002 to 2010, he had been a part of several research projects financed by the Academy of Finland and the National Technology Agency of Finland (TEKES). He is currently the Co-Owner and the Technical Director at Mevea Ltd., Finland. His research interests cover topics related to multibody modeling methods, the modeling and control of hydraulically driven systems, machine–environment interaction models, and real-time simulation software development.

RAFAEL ÅMAN was born in Karkkila, Finland, in 1978. He received the B.S. degree in mechanical engineering (mechatronics) from the Helsinki University of Applied Sciences (Stadia), Finland, in 2002, and the M.S. and Ph.D. degrees in mechanical engineering (mechatronics) from the Lappeenranta University of Technology, Lappeenranta, Finland, in 2007 and 2011, respectively.

From 2006 to 2016, he worked as a Researcher on the simulation of fluid power circuits, hybrid power transmission, and energy recovery systems at the Lappeenranta University of Technology. He has work experience as a Service Engineer in a civil engineering company. Since 2016, he has been with AGCO Corporation. He works at Valtra Inc., Suolahti, Finland. His main responsibilities have included system simulations and tractor design validation tests, as well as research and advanced engineering. As a Technical Specialist, he focuses on the use of future technologies in agricultural machinery and in their Research and Development processes. He has contributed to 26 scientific publications and presentations.

JUSSI SOPANEN (M'14) was born in Enonkoski, Finland, in 1974. He received the M.S. degree in mechanical engineering and the Ph.D. degree (in technology) from the Lappeenranta University of Technology, Lappeenranta, Finland, in 1999 and 2004, respectively.

From 1999 to 2006, he worked as a Researcher at the Department of Mechanical Engineering, Lappeenranta University of Technology. From 2004 to 2005, he worked as a Product Development Engineer at Rotatek Finland Ltd., electric machine manufacturer. From 2006 to 2012, he worked as a Principal Lecturer of mechanical engineering and the Research Manager at the Faculty of Technology, Saimaa University of Applied Sciences, Lappeenranta. He is currently a Professor in machine dynamics with the Lappeenranta University of Technology. His research interests are in rotor dynamics, multibody dynamics, and the mechanical design of electrical machines.

AKI MIKKOLA received the Ph.D. degree in machine design, in 1997.

Since 2002, he has been working as a Professor at the Department of Mechanical Engineering, Lappeenranta University of Technology, Lappeenranta, Finland. He is currently leading the research team of the Laboratory of Machine Design, Lappeenranta University of Technology. His research interests include machine dynamics and vibration, multibody system dynamics, and bio-mechanics. He has been awarded five patents and has contributed to more than 90 peer-reviewed journal articles.

Publication VI

Jaiswal, S., Islam, M., Hannola, L., Sopanen, J., and Mikkola, A.
Gamification procedure based on real-time multibody simulation

Reprinted with permission from
International Review on Modelling and Simulations
Vol. 11(5), pp. 259–266, 2018

Praise Worthy Prize

This paper is available online at www.praiseworthyprize.org
International Review on Modelling and Simulations (I.RE.MO.S.), Vol. 11, N. 5
ISSN 1974-9821 *October 2018*

Gamification Procedure Based on Real-Time Multibody Simulation

Suraj Jaiswal[1], Md Iftekharul Islam[2], Lea Hannola[2], Jussi Sopanen[1], Aki Mikkola[1]

Abstract – *Gamification aims to redirect the motivating power of game mechanics towards a non-entertainment field to encourage user engagement. In the field of mechanical engineering, the gamification concept can be combined with real-time multibody simulation. The objective of this paper is to demonstrate how gamification can be used to analyze user experiences of a mobile machine. As a case study, an excavator is modeled using a semi-recursive multibody formulation. The excavator model is customizable and offers different sizes for a bucket and dipper arm's hydraulic cylinder. In the excavator model, gamification introduces game elements: goals such as filling the industrial hopper, obstacles such as utility poles, challenges such as fuel gauge, time constraint such as a timer, and fantasy element such as visualization graphics. The effect of different product features, such as the hydraulic system parameters, on the users' performance are analyzed. A product development team can utilize this information to improve the product design.*

Keywords: *Gamification, Multibody System, Product Development, Real-time Simulation, Users*

Nomenclature

$\mathbf{A}_j$	Rotation matrix of j^{th} body
A_1	Area on the cylinder side
A_2	Area on the piston side
B_{e_i}	Effective bulk modulus of i^{th} section
B_j	j^{th} rigid body
C_v	Flow rate constant
$\mathbf{C}$	Quadratic velocity vector
$\mathbf{d}_{j-1,j}$	Relative displacement vector between j^{th} and $(j-1)^{th}$ body
F_S	Force by a hydraulic cylinder
F_μ	Total friction force
$\mathbf{F}_j$	External force vector acting on j^{th} body
$\mathbf{I}$	3×3 identity matrix
$\mathbf{J}_0$	Constant inertia tensor of j^{th} body
m_j	Mass of j^{th} body
$\mathbf{M}$	Mass matrix
n_c	Total number of hydraulic inlets and outlets
p_i	Pressure within i^{th} section
P	Point location of the joint
$\dot{\mathbf{q}}$	Generalized velocity vector
Q	Point location of the joint
Q_{ij}	Ingoing or outgoing flow rate of i^{th} section
Q_v	Flow rate through valve
$\mathbf{Q}$	Generalized external force vector
$\mathbf{r}_j$	Global position vector of a point on j^{th} body
$\mathbf{R}$	Velocity transformation matrix
$\mathbf{R}_{j-1}^{cm}$	Global position vector of the origin of $(j-1)^{th}$ body
t	Time
$\mathbf{T}_j$	External torque acting on j^{th} body
$\bar{\mathbf{u}}_{j-1}$	Position vector of a point on $(j-1)^{th}$ body within its body reference coordinate system
U_{ref}	Reference voltage signal
V_i	Volume of i^{th} section
$\bar{x}_{\mathrm{B}_{j-1}}$	Coordinate of body reference coordinate system
X	X-axis of global coordinate system
X_0	Relative spool position
$\bar{y}_{\mathrm{B}_{j-1}}$	Coordinate of body reference coordinate system
Y	Y-axis of global coordinate system
$\bar{z}_{\mathrm{B}_{j-1}}$	Coordinate of body reference coordinate system
$\dot{\mathbf{z}}$	Relative joint velocity vector
Z	Z-axis of global coordinate system
δ	Virtual parameter
τ	Time constant
$\boldsymbol{\omega}_j$	Global angular velocity vector of j^{th} body

Available online by October 31th, 2018 https://doi.org/10.15866/iremos.v11i5.15267

$\boldsymbol{\omega}_{j-1,j}$	Relative angular velocity vector between j^{th} and $(j-1)^{th}$ body
~	Skew-symmetric matrix of the parameter

I. Introduction

Society's interest in games can change the traditional thinking of product design, product development, and consumer markets. The gamification concept aims to redirect the motivating power of game mechanics towards a non-entertainment field to encourage user engagement [1]. Gamification helps in monitoring the user's behavior by applying game-like criteria to strategic motives. Providing a game-like environment can help to improve productivity and end-user creativity.

Remi-Omosowon et al. [2] have applied gamification to engage users in a loading system of a warehouse environment. They introduced an interactive simulation interface to manage loading patterns, helping to check loading feasibility, share knowledge, and improve user learning. Gasca-Hurtado et al. [3] have noticed that a lack of user motivation is a prime reason for defects in a software development process. Therefore, they utilized gamification to enhance users' engagement and communication within the team. Leclercq et al. [4] have explained the role of cooperation and competition gamification mechanics in engaging users in a co-creation platform. This helped to capture the dynamics and iterative nature of user engagement. Poncin et al. [5] have explained the positive impact of challenge and fantasy game mechanics on the user's experience. They concluded that a gamified interface for a product provides a compelling playful experience leading to stronger support intensions. Komeijani et al. [6] have pointed out that designing a user-centric product helps in eliminating redundant or missing functions from the product. Therefore, Signoretti et al. [7] have proposed a modular and reusable card game helping to design user-centric services or products. They considered the user's needs, emotions, and personality, creating a highly communicative environment based on game design. Abi Akle and Lizarralde [8] have also used a card game as a pervasive and persuasive tool to identify real design needs from users' feedback, helping in (re)designing products for sustainable outcomes. Furthermore, to combine gamification with a virtual environment, Holth and Schnabel [9] have utilized an immersive virtual environment creating a direct link between the user's perceptions and the created virtual environment. Their study showed a way of creating, testing, and experiencing a virtual environment that can incorporate the strengths of various disciplines into a common platform. As can be concluded from the literature overview, there are a number of studies on gamification encouraging user engagement [2]-[4], user experience [5], user-centric products [6]-[7], designing for sustainable outcomes [8], and the collaboration of various disciplines [9]. However, studies where gamification is utilized to identify the design needs for a complex mobile machine has been overlooked. In this study, this gap can be covered by using gamification in the framework of detailed physics-based real-time multibody dynamic simulation. As demonstrated in this study, users' experience and feedback can be captured using the gamified simulation model. This information, in turn, can help the product development team in the design of the machine details. Today's real-time simulation models that are based on multibody dynamics can accurately describe systems that consist of large numbers of bodies, actuators, and contact models. The objective of this paper is to demonstrate the gamification concept in the framework of a mobile machine. To this end, an excavator will be described by employing a real-time multibody approach. In the real-time multibody model, the role of gamification is to introduce the game elements, such as goals, obstacles, challenges, time constraints, and fantasy. Users can directly test-run the virtual prototype of the initial excavator model through this gamified user interface. User feedback (user experiences) can be processed and analyzed to provide the product development team with information to improve the design of the excavator, its subsystems, or user-interface further.

II. Multibody System Dynamics

The equations of motion for a constrained mechanical system can be described using a multibody approach. Embedded technique, augmented Lagrangian formulation, penalty formulation, recursive formulation, and semi-recursive formulation are examples of formulations that can used in this approach. The semi-recursive formulation is used in this research because it leads to a computationally efficient procedure when a large number of bodies with open kinematic chains, such as an excavator, are under investigation. In this study, the semi-recursive formulation is combined with hydraulics and contact subsystem models.

II.1. Semi-Recursive Multibody Formulation

The semi-recursive formulation describes kinematics using a relative coordinate system. Consider two rigid bodies B_{j-1} and B_j connected by a joint, as Fig. 1 shows. Here, the X, Y, and Z axes represent the global coordinate system, whereas the $\overline{x}_{\mathrm{B}_{j-1}}$, $\overline{y}_{\mathrm{B}_{j-1}}$, and $\overline{z}_{\mathrm{B}_{j-1}}$ axes represent the body reference coordinate system of body B_{j-1} and are located at its center of mass. Points P and Q are the locations of the joint on body B_j and body B_{j-1}, respectively, and $\mathbf{d}_{j-1,j}$ is the relative displacement vector between points P and Q.

Following the relative coordinate system, the global position vector $\mathbf{r}_j$, the global velocity vector $\dot{\mathbf{r}}_j$, and the global acceleration vector $\ddot{\mathbf{r}}_j$ of point P can,

respectively, be written as [10]:

$$\mathbf{r}_j = \mathbf{R}_{j-1}^{cm} + \mathbf{A}_{j-1}\bar{\mathbf{u}}_{j-1} + \mathbf{d}_{j-1,j} \quad (1)$$

$$\dot{\mathbf{r}}_j = \dot{\mathbf{R}}_{j-1}^{cm} + \tilde{\boldsymbol{\omega}}_{j-1}\mathbf{u}_{j-1} + \dot{\mathbf{d}}_{j-1,j} \quad (2)$$

$$\ddot{\mathbf{r}}_j = \ddot{\mathbf{R}}_{j-1}^{cm} + \dot{\tilde{\boldsymbol{\omega}}}_{j-1}\mathbf{u}_{j-1} + \tilde{\boldsymbol{\omega}}_{j-1}\tilde{\boldsymbol{\omega}}_{j-1}\mathbf{u}_{j-1} + \ddot{\mathbf{d}}_{j-1,j} \quad (3)$$

where $\mathbf{R}_{j-1}^{cm}$, $\dot{\mathbf{R}}_{j-1}^{cm}$, and $\ddot{\mathbf{R}}_{j-1}^{cm}$ are, respectively, the global position, global velocity, and global acceleration vector of the origin of the body reference coordinate system of body B_{j-1}, $\mathbf{A}_{j-1}$ is the rotation matrix of body B_{j-1}, $\tilde{\boldsymbol{\omega}}_{j-1}$ and $\dot{\tilde{\boldsymbol{\omega}}}_{j-1}$ are, respectively, the skew-symmetric matrix of angular velocity of body B_{j-1} and its derivative, $\bar{\mathbf{u}}_{j-1}$ is the position vector of point Q within the body reference coordinate system of body B_{j-1}, and $\dot{\mathbf{d}}_{j-1,j}$ and $\ddot{\mathbf{d}}_{j-1,j}$ are, respectively, the relative velocity and relative acceleration vector between bodies B_{j-1} and B_j. It can also be noted that $\mathbf{u}_{j-1} = \mathbf{A}_{j-1}\bar{\mathbf{u}}_{j-1}$.

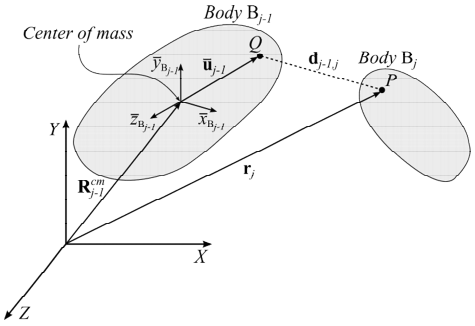

Fig. 1. Description of multibody system

The global angular velocity vector $\boldsymbol{\omega}_j$ and the global angular acceleration vector $\dot{\boldsymbol{\omega}}_j$ of body B_j can, respectively, be written in terms of the global angular velocity vector $\boldsymbol{\omega}_{j-1}$ and the global angular acceleration vector $\dot{\boldsymbol{\omega}}_{j-1}$ of body B_{j-1} as [10]:

$$\boldsymbol{\omega}_j = \boldsymbol{\omega}_{j-1} + \boldsymbol{\omega}_{j-1,j} \quad (4)$$

$$\dot{\boldsymbol{\omega}}_j = \dot{\boldsymbol{\omega}}_{j-1} + \dot{\boldsymbol{\omega}}_{j-1,j} \quad (5)$$

where $\boldsymbol{\omega}_{j-1,j}$ and $\dot{\boldsymbol{\omega}}_{j-1,j}$ are, respectively, the angular velocity and angular acceleration vector of body B_j with respect to body B_{j-1}. Using the kinematics above, the equations of motion for body B_j can be developed from the principle of virtual power in matrix form as [11]:

$$\left\{\delta\dot{\mathbf{r}}_j^{\mathrm{T}}\ \delta\boldsymbol{\omega}_j^{\mathrm{T}}\right\}\left(\begin{bmatrix} m_j\mathbf{I} & 0 \\ 0 & \mathbf{A}_j\mathbf{J}_0\left(\mathbf{A}_j\right)^{\mathrm{T}} \end{bmatrix}\begin{bmatrix} \ddot{\mathbf{R}}_j^{cm} \\ \dot{\boldsymbol{\omega}}_j \end{bmatrix} + \begin{bmatrix} 0 \\ \tilde{\boldsymbol{\omega}}_j\mathbf{A}_j\mathbf{J}_0\left(\mathbf{A}_j\right)^{\mathrm{T}}\boldsymbol{\omega}_j \end{bmatrix} - \begin{bmatrix} \mathbf{F}_j \\ \mathbf{T}_j \end{bmatrix}\right) = 0 \quad (6)$$

where $\delta\dot{\mathbf{r}}_j$ and $\delta\boldsymbol{\omega}_j$ are, respectively, the virtual translational and virtual angular velocities of body B_j, m_j and $\mathbf{A}_j$ are, respectively, the mass and rotation matrix of body B_j, $\mathbf{I}$ is the 3×3 identity matrix, $\mathbf{J}_0$ is the constant inertia tensor of body B_j, $\ddot{\mathbf{R}}_j^{cm}$ is the global acceleration vector of the center of mass of body B_j, $\tilde{\boldsymbol{\omega}}_j$ is the skew-symmetric matrix of $\boldsymbol{\omega}_j$, and $\mathbf{F}_j$ and $\mathbf{T}_j$ are the external forces and torques acting on body B_j, respectively. The equations of motion for the entire system can be expressed as [11]:

$$\delta\dot{\mathbf{q}}^{\mathrm{T}}(\mathbf{M}\ddot{\mathbf{q}} + \mathbf{C} - \mathbf{Q}) = 0 \quad (7)$$

where $\delta\dot{\mathbf{q}}$ is the dependent virtual velocity, $\mathbf{M}$ is the mass matrix, $\ddot{\mathbf{q}}$ is the generalized acceleration vector, $\mathbf{C}$ is the quadratic velocity vector, and $\mathbf{Q}$ is the generalized external force vector. To reduce the size of the system, equations of motion can be expressed using relative joint coordinates. To this end, the velocity transformation matrix $\mathbf{R}$ that relates global coordinates and relative joint coordinates is introduced as follows [11]:

$$\dot{\mathbf{q}} = \mathbf{R}\dot{\mathbf{z}} \quad (8)$$

where $\dot{\mathbf{q}}$ is the generalized velocity vector and $\dot{\mathbf{z}}$ is the relative joint velocity vector. By differentiating Equation (8) with respect to time, $\ddot{\mathbf{q}}$ can be obtained as follows:

$$\ddot{\mathbf{q}} = \mathbf{R}\ddot{\mathbf{z}} + \dot{\mathbf{R}}\dot{\mathbf{z}} \quad (9)$$

where $\ddot{\mathbf{z}}$ is the relative joint acceleration vector and $\dot{\mathbf{R}}$ is the time derivative of $\mathbf{R}$. Now, by substituting Equations (8) and (9) into Equation (7), the original form of the equations of motion can be expressed as:

$$\delta\dot{\mathbf{z}}^{\mathrm{T}}(\mathbf{R}^{\mathrm{T}}\mathbf{M}\mathbf{R}\ddot{\mathbf{z}} + \mathbf{R}^{\mathrm{T}}\mathbf{M}\dot{\mathbf{R}}\dot{\mathbf{z}} + \mathbf{R}^{\mathrm{T}}\mathbf{C} - \mathbf{R}^{\mathrm{T}}\mathbf{Q}) = 0 \quad (10)$$

Since Equation (10) is valid for any arbitrary vector of independent virtual velocities, $\delta\dot{\mathbf{z}}$ can be eliminated and

the equations of motion can be expressed in a simple form:

$$\mathbf{R}^{\mathrm{T}}\mathbf{M}\mathbf{R}\ddot{\mathbf{z}} = \mathbf{R}^{\mathrm{T}}(\mathbf{Q}-\mathbf{C}) - \mathbf{R}^{\mathrm{T}}\mathbf{M}\dot{\mathbf{R}}\dot{\mathbf{z}} \tag{11}$$

II.2. Hydraulic System Modeling

This study models a hydraulic subsystem to describe the forces provided by hydraulic actuators. In practice, pressures in a hydraulic volume can be modeled by employing lumped fluid theory, which assumes that the effect of acoustic waves is insignificant [12]. The differential equation for pressure p_i in each hydraulic section i of volume V_i can be expressed as [12]:

$$\frac{dp_i}{dt} = \frac{B_{e_i}}{V_i}\sum_{j=1}^{n_c} Q_{ij} \tag{12}$$

where B_{e_i} is the effective bulk modulus of hydraulic section i defining the compressibility, Q_{ij} is the ingoing or outgoing flow rate, and n_c is the total number of hydraulic inlets and outlets. Valves control the flow rate, pressure difference, and direction of the flow. The valves are modeled using a semi-empirical approach in which the parameters for many cases can be obtained from manufacturer catalogues. In the semi-empirical approach, the flow rate through the valve is calculated as follows [12]:

$$Q_v = C_v X_0 \sqrt{dp} \tag{13}$$

where Q_v is the flow rate through the valve, C_v is the flow rate constant defining the size of the valve, dp is the pressure difference between the volumes, and X_0 is the relative spool position that can be expressed as [12]:

$$\frac{dX_0}{dt} = \frac{U_{ref} - X_0}{\tau} \tag{14}$$

where U_{ref} is the reference voltage signal for the reference spool position, and τ is the time constant describing the valve spool dynamics. The hydraulic cylinder helps in converting hydraulic pressure into mechanical work. The force F_S produced by a hydraulic cylinder as shown in Fig. 2 can be expressed using its dimensions and pressure in each chamber as follows [12]:

$$F_S = p_1 A_1 - p_2 A_2 - F_\mu \tag{15}$$

where p_1 and p_2 are the pressure on the cylinder and piston side, respectively, A_1 and A_2 are the areas on the cylinder and piston side, respectively, and F_μ is the total friction force resulting from the contact of the seal material with the cylinder and piston wall.

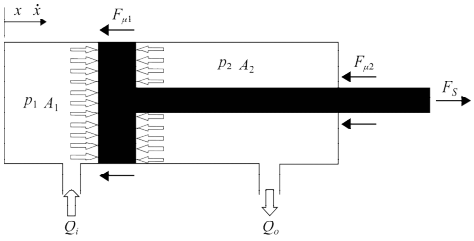

Fig. 2. Free body diagram of a hydraulic cylinder

II.3. Contact Formulation

During construction of a real-time mobile machine using multibody system dynamics, a contact subsystem also needs to be modeled. Moore and Wilhelms [13] have explained that there are two steps in contact formulation: collision detection and collision response. Collision detection determines the location and time of the collision, whereas collision response determines the contact force between the bodies involved. This research employs the object-oriented bounding box method [14] for collision detection and the penalty method [15] for collision response.

III. Gamification

The important advantage of gamification is increasing the engagement and involvement of users. This helps to create communities to improve collaboration [16]. Gamification creates challenges and new insights into regular life using the human instincts to engage in competition to learn, overcome barriers, and eventually win. Digital interaction through gamification makes the business environment more interactive and social. User-centric gamification design can increase customer satisfaction and productivity by minimizing errors to meet business goals [17]. In product development, the main aim is to introduce the experiences that people value most. The process can be done by motivating the people to reach their goal, and engaging them in product development is an excellent way of motivating them.

Leading users to have fun, explore, and use the product, developers can make their product more customer-oriented.

III.1. Elements of a Game

The role of gamification in a gamified application is to incorporate game elements. Reeves and Read [18] have identified the key game elements for a gamified experience. The key elements include goals and obstacles in the form of narrative contexts and rules that are explicit and enforced, challenges in the form of limited

resources, fantasy in the form of self-representation with avatars and three-dimensional environments, and time constraints in the form of time pressure. Other examples of game elements include badges, leaderboards, and difficulty index in the form of reputations, ranks, and levels, team play in the form of teams, playfulness in the form of feedback, and play-centric design in the form of parallel communication systems that can be easily configured. In this study, a customizable simulation model provides options for bucket and hydraulic cylinder selection. The game elements incorporated in the customized simulation model are goals, obstacles, challenges, time constraints, and fantasy. Fig. 3 represents the flowchart of the gamification procedure adopted in this study.

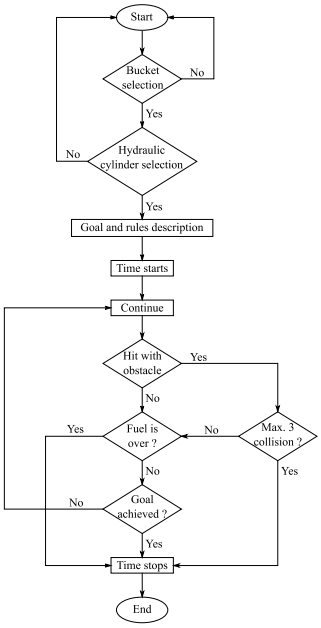

Fig. 3. Gamification procedure adopted in the study

III.2. Quantitative and Qualitative Methods of Extracting Data

The quantitative method starts with the data collection and analysis to support decisions on a particular phenomenon [19]. Game data is extracted to provide quantitative data for the study. Interviewing is one of the simplest and most practical qualitative methods of data collection [20].

There are different types of interview methods, such as narrative interviews, factual interviews, focus group interviews, and confrontational interviews [21]. This study employs semi-structured face-to-face interviews to obtain users' feedback.

III.3. Utilizing Virtual Prototype through Gamification

Dynamics deals with the forces, torque and effects of relative motions [22]. Thus, virtual prototyping with multibody system dynamics is crucial to replicate the real entity of a particular product.

To prepare a virtual prototype of a crawler type excavator, it is important to analyze the forces and motions of different parts of the excavator. This study includes different parameters to make the tasks more challenging, and system dynamics is needed in the virtual prototype of the excavator to make the model perform as intended.

IV. Case Study of an Excavator Model

Fig. 4 depicts the excavator that this study uses as a case example. The excavator is modeled using a semi-recursive approach as explained in section 2.

As Fig. 4 depicts, the model has nine bodies, 10 joints, two closed loop constraint equations, and 11 degrees of freedom. In addition, the driver controls six hydraulic cylinders to move the main boom, dipper arm, and bucket. Crawlers are modeled using particles and constraints, whereas the ground is modeled using a granular particle system.

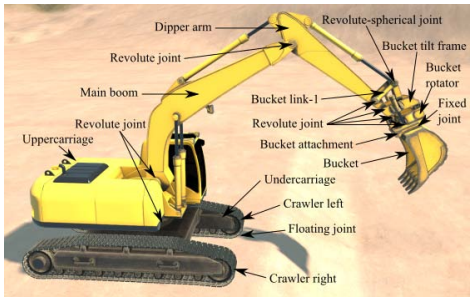

Fig. 4. Excavator model utilized in this case

IV.1. Customized Excavator Model

The excavator model under consideration can be modified. The size of the bucket and the hydraulic cylinder responsible for the movement of the dipper arm are the two customizable features. Different bucket sizes affect the amounts of particles dug, the working cycles, and fuel consumption [23].

Different hydraulic cylinder sizes affect the generated force, the torque generated by the hydro-motor, the lifting speed of the dipper arm, and fuel consumption [23]. It should be noted that the velocity and the reaction of the dipper arm have a significant effect on the working cycle time and total operation time.

Table I and Table II represent, respectively, three different sizes of buckets and hydraulic cylinders available for users.

TABLE I
DIFFERENT SIZES OF BUCKETS [23]

Size	Volume (m^3)	Mass (kg)
Small	0.318	315
Medium	0.512	450
Large	22.55	750

TABLE II
DIFFERENT SIZES OF DIPPER ARM'S HYDRAULIC CYLINDERS [23]

Size	Cylinder diameter (mm)	Piston-rod length (mm)	Mass (kg)
Small	120	1630	8
Medium	140	1650	10
Large	160	1670	12

IV.2. Task Utilized in Gamification

The excavator model described above is gamified by introducing game elements, such as goals, obstacles, challenges, time constraints, and fantasy, as section 3 explains. The game mechanics that this excavator model employs define the settings, rules, interactions, and boundary conditions of the game. However, the dynamics of this game depends on the users' behavior and their interaction with the gamified excavator model.

The goal of this gamified excavator model is to load two tons of gravel (represented as a percentage in the material indicator) into an industrial hopper. Users are free to collect gravel from anywhere on the ground.

Obstacles, such as utility poles, are placed near the industrial hopper. Users will be penalized if the bucket, dipper arm, or main boom hits the utility poles or the industrial hopper's edge, and the collision sensor reading will indicate this. Players are allowed to hit the obstacles a maximum of three times. A fuel gauge indicates the amount of fuel left. A timer measures the total time taken by the users to achieve the goal. Users have three attempts to achieve the goal. Fig. 5 illustrates the graphical user interface used to invoke the gamified experience, including all of the game elements introduced above.

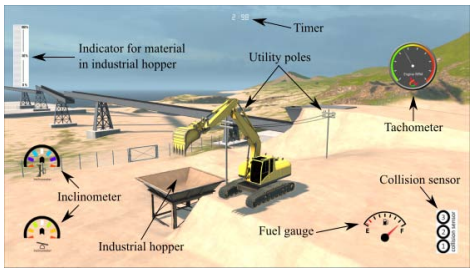

Fig. 5. Gamified graphical user interface for the excavator model

IV.3. Data Collection

This study presents data concerning the average time required to achieve the goal, the maximum number of hits with an obstacle, the average fuel consumption, the dipper arm's movement, and the selection of bucket and cylinder-piston options. A sample size of 16 users comprising of both experienced and inexperienced excavator users performed the task. In addition, semi-structured interviews were conducted to record user experiences on the trail run. The users received the questionnaires beforehand. As users' gamified experience is difficult to predict in the questionnaire, face-to-face interviews were conducted to obtain positive and negative feedback on the game.

V. Results and Discussion

This research explores the possibility of improving the excavator design through user experience. From the three successful attempts made by the users, a leaderboard was created based on the average weighted score of the time required, fuel consumption, and number of hits with obstacles. Based on the leaderboard, a comparison analysis was carried out for the arm movement, which is the distance between the center of the upper carriage and the center of the bucket. As an example, Fig. 6 compares the arm movements of the winner, the second-to-last, and the last person with respect to time in their first attempt.

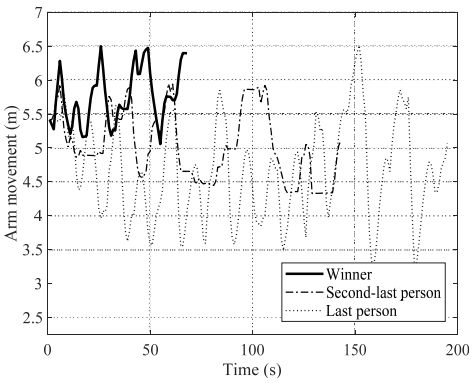

Fig. 6. Arm movement comparison between the winner, the second-to-last person, and the last person

Fig. 6 shows that the range of arm movement is 5 to 6.5 m for the winner, 4.2 to 6 m for the penultimate person, and 3.2 to 6.5 m for the last person. The winner's arm movement fluctuates rapidly but deviates relatively less compared to the second-to-last and last person. Based on the trend of the users, the more the arm movement fluctuates and the less it deviates, the less time the user consumes.

Therefore, the designer may consider this source of information for modifying the arm length, producing a more efficient design for performing a regular job. In addition, changing product features such as the size of the bucket or the size of the dipper arm's hydraulic cylinder affects users' performance. Out of all possible combinations of different sizes of buckets and hydraulic cylinders, Fig. 7 shows the percentage distribution of

these possible combinations selected by the users. It is apparent that users most frequently chose a large bucket with a large or medium hydraulic cylinder. None of the users selected a small bucket and its combinations, and they even ignored medium bucket and small hydraulic cylinder.

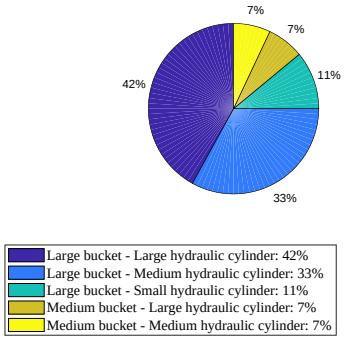

Fig. 7. Distribution of bucket and hydraulic cylinder size combinations selected by the users

As an example, Fig. 8 shows the performance of a user who chose different sizes of hydraulic cylinders in all three attempts but used a large bucket every time. For this user, the outcome was that when a medium hydraulic cylinder is chosen along with a large bucket, the time and fuel consumption was lower than when a large or small hydraulic cylinder is chosen.

A similar trend is observed for all of the other users as well. Whenever a large bucket and a medium hydraulic cylinder configuration were selected from any other configuration, the user's performance improved considerably.

Therefore, this study suggests that a large bucket and medium hydraulic cylinder may be the right combination for carrying out the regular task in hand. Similar studies can be carried out to benefit the product development team with such source of information.

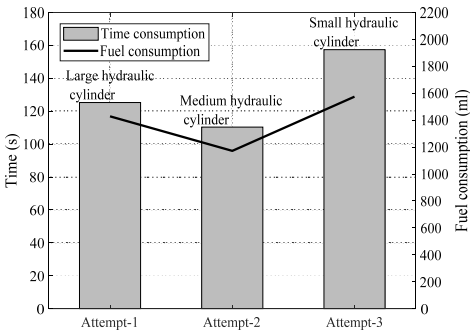

Fig. 8. Example of a user's performance with a large bucket and different hydraulic cylinder sizes

Along with the game data, this study also analyzes and discusses users' feedback from the interview process. It is noteworthy that 62% of the users found the goal to be challenging, whereas 38% found it easy. In addition, 94% of users identified the fantasy element and enjoyed the gamified experience, whereas 6% did not. The users also suggested that additional features such as a small screen inside the compartment, improved balancing system, and monitoring devices for temperature and humidity needs to be introduced.

VI. Conclusion

This study introduced a design approach in which the gamification concept is combined with a multibody dynamic system. The objective of this paper was to demonstrate how gamification can be used to analyze user experiences of a mobile machine. As a case study, an excavator was modeled using a semi-recursive formulation.

The excavator model introduced game elements such as filling the industrial hopper as the goal, utility poles as obstacles, fuel gauge as a challenge, a timer as a time constraint, and visualization graphics as the fantasy element. The excavator model offers different sizes for the bucket and the dipper arm's hydraulic cylinder. A leaderboard for the users was created based on the average weighted score of time required, fuel consumption, and the number of hits with obstacles.

Based on the leaderboard, the arm movements of the winner, the penultimate person, and the last person were compared. As a result, the more the arm movement fluctuated and the less it deviated, the less time the user consumed. In addition, changing product features such as the size of the bucket or the dipper arm's hydraulic cylinder affected user performance. A product development team can utilize this information in improving the product.

Along with the bucket or dipper arm's hydraulic cylinder, the product development team could customize numerous product features, and accordingly, select the best set of parameters. The results of this study function as a proof of concept. However, due to the limited sample size, conclusions regarding the excavator's design may be unreliable. The results from such procedures could be debatable if selection of the appropriate users for the study is not made with care. The set of users should be a combination of new, medium-experienced, and skilled users. Selecting new or medium-experienced users for the study might not provide reliable solutions.

By using a small set of users as in this study, no firm conclusion can be drawn from the users' feedback. In addition, the literature in this paper provides no information about the misuse of gamification in the context of this research work. For future research, it would be interesting to determine why different users experience/perform differently despite using exactly the same artifact under similar conditions.

References

[1] M. J. Nelson, Soviet and American precursors to the gamification of work, *Proceeding of the 16th International Academic MindTrek Conference*, pp. 23–26, Tampere, Finland, October 2012.

[2] A. Remi-Omosowon, R. Cant, and C. Langensiepen, Applying gamification principles to a container loading system in a warehouse environment, *Simulation Notes Europe SNE*, Vol. 26(Issue 2):99-104, June 2016.

[3] G. P. Gasca-Hurtado, M. C. Gómez-Alvarez, M. Muñoz, J. Mejía, Gamification proposal for defect tracking in software development process, *Proceedings of the 23rd European Conference on Software Process Improvement*, pp. 212–224, Graz, Austria, September 2016.

[4] T. Leclercq, I. Poncin, and W. Hammedi, The engagement process during value co-creation: Gamification in new product development platforms, *International Journal of Electronic Commerce*, Vol. 21(Issue 4):454-488, September 2017.

[5] I. Poncin, M. Garnier, M. S. B. Mimoun, and T. Leclercq, Smart technologies and shopping experience: Are gamification interfaces effective? The case of the smartstore, *Technological Forecasting and Social Change*, Vol. 124:320-331, November 2017.

[6] M. Komeijani, E. G. Ryen, and C.W. Babbitt, Bridging the gap between eco-design and the human thinking system, *Challenges*, Vol. 7(Issue 1):1-16, March 2016.

[7] A. Signoretti, A.I. Martins, M. Rodrigues, A. Campos, A. Teixeira, Services and products gamified design (SPGD): A methodology for game thinking design, *Proceedings of the 7th International Conference on Software Development and Technologies for Enhancing Accessibility and Fighting Info-exclusion*, pp. 62–68, Vila Real, Portugal, December 2016.

[8] A. Abi Akle, I. Lizarralde, Helping inhabitants in energy saving and getting inputs from usage for eco-design: Cooking case study, *Proceedings of the 21st International Conference on Engineering Design*, pp. 41-50, Vancouver, Canada, August 2017.

[9] J. Holth, and M. A. Schnabel, Immersive virtual environments as a tool for exploring perceptional space, *International Journal of Parallel, Emergent and Distributed Systems*, October 2017.

[10] D. S. Bae, J. M. Han, and H. H. Yoo, A generalized recursive formulation for constrained mechanical system dynamics, *Mechanics of Structures and Machines*, Vol. 27(Issue 3):293-315, January 1999.

[11] J. G. De Jalon, E. Bayo, *Kinematic and dynamic simulation of multibody systems: The real-time challenge* (Springer-Verlag, 1994).

[12] H. M. Handroos, and M. J. Vilenius, Flexible semi-empirical models for hydraulic flow control valves, *Journal of Mechanical Design*, Vol. 113(Issue 3):232-238, September 1991.

[13] M. Moore, J. Wilhelms, Collision detection and response for computer animation, *Proceedings of the 15th Annual Conference on Computer Graphics and Interactive Techniques*, pp. 289–298, Atlanta, United States of America, August 1988.

[14] S. Gottschalk, M.C. Lin, D. Manocha, OBBtree: A hierarchical structure for rapid interference detection, *Proceedings of the 23rd Annual Conference on Computer Graphics and Interactive Techniques*, pp. 171–180, New Orleans, United States of America, August 1996.

[15] E. Drumwright, A fast and stable penalty method for rigid body simulation, *IEEE Transactions on Visualization and Computer Graphics*, Vol. 14(Issue 1):231-240, January/February 2008.

[16] T. J. Brigham, An introduction to gamification: Adding game elements for engagement, *Medical Reference Services Quarterly*, Vol. 34(Issue 4):471-480, October 2015.

[17] M. Rajanen, D. Rajanen, Usability benefits in gamification, *Proceedings of the 1st International GamiFin Conference*, pp. 87–95, Pori, Finland, May 2017.

[18] B. Reeves, J. L. Read, *Total engagement: Using games and virtual worlds to change the way people work and businesses compete* (Harvard Business Press, 2009).

[19] B. Render, R. M. Stair, M. E. Hanna, T. S. Hale, *Quantitative analysis for management* (Pearson, 2015).

[20] Z. O'Leary, *The essential guide to doing research* (Sage Publications, 2004).

[21] S. Kvale, *Doing interviews* (Sage Publications, 2008).

[22] B. He, W. Tang, and J. Cao, Virtual prototyping-based multibody systems dynamics analysis of offshore crane, *The International Journal of Advanced Manufacturing Technology*, Vol. 75(Issue 1-4):161-180, October 2014.

[23] M. Mohammadi, *Parameterization and real-time simulation of an excavator*, Master's thesis, Dept. Mech. Eng., Lappeenranta University of Technology, Lappeenranta, Finland, 2017.

Authors' information

[1]Department of Mechanical Engineering, Lappeenranta University of Technology, Skinnarilankatu 34, 53850 Lappeenranta, Finland.

[2]School of Industrial Engineering and Management, Lappeenranta University of Technology, Skinnarilankatu 34, 53850 Lappeenranta, Finland.

Suraj Jaiswal received the Master of Science degree in mechanical engineering from Lappeenranta University of Technology, Finland in 2017. He is currently a PhD student at Lappeenranta University of Technology, Finland. His research interest includes multibody system dynamics, and machine dynamics.

Md Iftekharul Islam received the Master of Science degree in industrial engineering and management from Lappeenranta University of Technology, Finland in 2017. His research interest includes new product development, innovation management, and system engineering.

Lea Hannola is currently an associate professor in the department of industrial engineering and management at Lappeenranta University of Technology, Finland. Her research interest includes innovation management, especially product, service, technology, and systems design methods, sociotechnical aspects in manufacturing and smart factories.

Jussi Sopanen is currently a professor and the director of the laboratory of machine dynamics at Lappeenranta University of Technology, Finland. His research interests are dynamics and vibration of machinery, mechanical design of electrical machines, multibody system dynamics, and rotor dynamics.

Aki Mikkola is currently a professor and the director of the laboratory of machine design at Lappeenranta University of Technology, Finland. His research interest includes machine dynamics and vibration, multibody system dynamics, and biomechanics.

ACTA UNIVERSITATIS LAPPEENRANTAENSIS

943. MANKONEN, ALEKSI. Fluidized bed combustion and humidified gas turbines as thermal energy conversion processes of the future. 2020. Diss.

944. KIANI OSHTORJANI, MEHRAN. Real-time efficient computational approaches for hydraulic components and particulate energy systems. 2020. Diss.

945. PEKKANEN, TIIA-LOTTA. What constrains the sustainability of our day-to-day consumption? A multi-epistemological inquiry into culture and institutions. 2021. Diss.

946. NASIRI, MINA. Performance management in digital transformation: a sustainability performance approach. 2021. Diss.

947. BRESOLIN, BIANCA MARIA. Synthesis and performance of metal halide perovskites as new visible light photocatalysts. 2021. Diss.

948. PÖYHÖNEN, SANTERI. Variable-speed-drive-based monitoring and diagnostic methods for pump, compressor, and fan systems. 2021. Diss.

949. ZENG, HUABIN. Continuous electrochemical activation of peroxydisulfate mediated by single-electron shuttle. 2021. Diss.

950. SPRINGER, SEBASTIAN. Bayesian inference by informative Gaussian features of the data. 2021. Diss.

951. SOBOLEVA, EKATERINA. Microscopy investigation of the surface of some modern magnetic materials. 2021. Diss.

952. MOHAMMADI ASL, REZA. Improved state observers and robust controllers for non-linear systems with special emphasis on robotic manipulators and electro-hydraulic servo systems. 2021. Diss.

953. VIANNA NETO, MÁRCIO RIBEIRO. Synthesis and optimization of Kraft process evaporator plants. 2021. Diss.

954. MUJKIC, ZLATAN. Sustainable development and optimization of supply chains. 2021. Diss.

955. LYYTIKÄINEN, JOHANNA. Interaction and barrier properties of nanocellulose and hydrophobically modified ethyl(hydroxyethyl)cellulose films and coatings. 2021. Diss.

956. NGUYEN, HOANG SI HUY. Model based design of reactor-separator processes for the production of oligosaccharides with a controlled degree of polymerization. 2021. Diss.

957. IMMONEN, HEIKKI. Application of object-process methodology in the study of entrepreneurship programs in higher education. 2021. Diss.

958. KÄRKKÄINEN, HANNU. Analysis of theory and methodology used in determination of electric motor drive system losses and efficiency. 2021. Diss.

959. KIM, HEESOO. Effects of unbalanced magnetic pull on rotordynamics of electric machines. 2021. Diss.

960. MALYSHEVA, JULIA. Faster than real-time simulation of fluid power-driven mechatronic machines. 2021. Diss.

961. SIEVINEN, HANNA. Role of the board of directors in the strategic renewal of later-generation family firms. 2021. Diss.

962. MENDOZA MARTINEZ, CLARA. Assessment of agro-forest and industrial residues potential as an alternative energy source. 2021. Diss.

963. OYEWO, AYOBAMI SOLOMON. Transition towards decarbonised power systems for sub-Saharan Africa by 2050. 2021. Diss.

964. LAHIKAINEN, KATJA. The emergence of a university-based entrepreneurship ecosystem. 2021. Diss.

965. ZHANG, TAO. Intelligent algorithms of a redundant robot system in a future fusion reactor. 2021. Diss.

966. YANCHUKOVICH, ALEXEI. Screening the critical locations of a fatigue-loaded welded structure using the energy-based approach. 2021. Diss.

967. PETROW, HENRI. Simulation and characterization of a front-end ASIC for gaseous muon detectors. 2021. Diss.

968. DONOGHUE, ILKKA. The role of Smart Connected Product-Service Systems in creating sustainable business ecosystems. 2021. Diss.

969. PIKKARAINEN, ARI. Development of learning methodology of additive manufacturing for mechanical engineering students in higher education. 2021. Diss.

970. HOFFER GARCÉS, ALVARO ERNESTO. Submersible permanent-magnet synchronous machine with a stainless core and unequal teeth widths. 2021. Diss.

971. PENTTILÄ, SAKARI. Utilizing an artificial neural network to feedback-control gas metal arc welding process parameters. 2021. Diss.

972. KESSE, MARTIN APPIAH. Artificial intelligence : a modern approach to increasing productivity and improving weld quality in TIG welding. 2021. Diss.

973. MUSONA, JACKSON. Sustainable entrepreneurial processes in bottom-of-the-pyramid settings. 2021. Diss.

974. NYAMEKYE, PATRICIA. Life cycle cost-driven design for additive manufacturing: the frontier to sustainable manufacturing in laser-based powder bed fusion. 2021. Diss.

975. SALWIN, MARIUSZ. Design of Product-Service Systems in printing industry. 2021. Diss.

976. YU, XINXIN. Contact modelling in multibody applications. 2021. Diss.

977. EL WALI, MOHAMMAD. Sustainability of phosphorus supply chain – circular economy approach. 2021. Diss.

978. PEÑALBA-AGUIRREZABALAGA, CARMELA. Marketing-specific intellectual capital: Conceptualisation, measurement and performance. 2021. Diss.

979. TOTH, ILONA. Thriving in modern knowledge work: Personal resources and challenging job demands as drivers for engagement at work. 2021. Diss.

980. UZHEGOVA, MARIA. Responsible business practices in internationalized SMEs. 2021. Diss.

LUT University

ISBN 978-952-335-713-6
ISBN 978-952-335-714-3 (PDF)
ISSN-L 1456-4491
ISSN 1456-4491
Lappeenranta 2021